CO_2 LASER SURFACE TREATMENT OF MAGNESIA PARTIALLY STABILISED ZIRCONIA (MGO-PSZ) FOR IMPROVED BIOCOMPATIBILITY

HAO LIANG

SCHOOL OF MECHANICAL & AEROSPACE ENGINEERING

NANYANG TECHNOLOGICAL UNIVERSITY

2005

CO_2 Laser Surface Treatment of Magnesia Partially Stabilised Zirconia (MgO-PSZ) for Improved Biocompatibility

Hao Liang

School of Mechanical & Aerospace Engineering

A thesis submitted to the Nanyang Technological University
in fulfillment of the requirement for the degree of
Doctor of Philosophy

2005

Abstract

Magnesia partially stabilised zirconia (MgO-PSZ) is a bioinert material that exhibits high mechanical strength, excellent corrosion resistance and good compatibility with the physiological environment. It is, therefore, frequently used in high-load bearing sites such as artificial knee and bone screws in orthopaedic applications and jaw and crown in dental applications. Yet, bioinert ceramics have often failed clinically due to a lack of direct bonding with bone, that is, insufficient biointegration. Bioactivity and biointegration are the two essential aspects of good biocompatibility. Bioactivity is usually attributed to the ability to induce an apatite layer on a material's surface in physiological conditions, whilst biointegration (often osseointegration) is the ability to promote anchorage, attachment, spreading, growth and differentiation of bone cells. These interactions occur at the interface between the implant and tissue and are controlled by the surface properties of the biomaterial.

At present, the processes available to engineers for the modification of biomaterials in order to enhance biocompatibility are invariably complex and consequently somewhat difficult to control. Lasers, on the other hand, can offer not only a clean and innocuous processing technique, but one that is rapid, flexible and highly controllable. However, no work has been conducted hitherto on laser surface processing to transform the surface properties of bioinert ceramics so as to improve the biocompatibility of implants.

This current research was carried out to explore the potential of laser treatment for changing the surface properties and thereof, improving the biocompatibility of the MgO-PSZ surface. The experiments were performed with a 3 kW continuous wave (CW) CO_2 laser and the general effects thereof on the surface of the MgO-PSZ were observed. Variations in the CO_2 laser operating parameters were seen to have a significant effect on the microstructure obtained within the laser treated areas on the MgO-PSZ. Moreover, it was seen that the obtained solidification microstructures on the surface of the MgO-PSZ differed not only with changes in laser parameters, but even across the same track. This was explained by the theories of constitutional supercooling and stability morphology. Contact angle, θ, measurements revealed that CO_2 laser surface treatment of the MgO-PSZ brought about a reduction in θ, indicating that the wettability characteristics of the MgO-PSZ had been enhanced. It was subsequently deduced that the factors active in causing the observed modification in the wettability characteristics of the MgO-PSZ were the surface roughness, surface oxygen content and surface energy. By employing a novel technique the predominant mechanisms active in the wettability modification and effects of the microstructure features on the wettability characteristics was identified.

Acknowledgements

Above all, I sincerely express my heartfelt gratitude and love to my wife Zheng Yanjun for her unconditional support and selfless devotion to my academic pursuit. Furthermore, I gratefully appreciate the understanding and encouragement of my families in Wuhan, China, especially my parents.

I wish to express my sincere thanks to my supervisor, Dr. Jonathan Lawrence, for his invaluable guidance and constructive criticism throughout the course of this work. His constant support and encouragement were very helpful and have made the progress of this project go smoothly. I learned many things from him and he was always very kind to me.

Special thanks to Dr. Chian Kerm Sin (Assoc Prof), Dr. Chan Vincent, Dr Zhu Xiao, Ms Heng Chee Hoon of Tissue Engineering Laboratory who kindly provided me excellent experimental condition and valuable advises in the *in vitro* cell study of the MgO-PSZ surface.

In my work I have received considerable help from the Singapore Institute of Manufacturing Technology. In particular, I would like to thank Dr Lim Gnian Cher, Dr Low Kuang Yong David, Dr Zheng Hong Yu, Ms Tan Joo Lett, and Senior Technologist Mr. Teh Kim Ming for offering the utility of the lasers and valuable instructions.

Great acknowledgements are given to all the technicians in Materials Laboratory: Mr Leong K P; Ms Yong M Y; Ms Sandy S; Ms Chow S K; and Mr. Chang S C, for their advice and assistance on optical microscopy, XRD, SEM, EDX, contact angle, XPS analysis, and sample preparation. Many thanks also to the doctoral research students in the lab for sharing their knowledge on material treatment and analysis.

I would also like to acknowledge with much appreciation Mr Ma Dong Rui for the instructions and assistance of the osteoblast cell culture and time-consuming biological assay.

The Financial support for the project from Nanyang Techonological University is deeply appreciated by the author.

In vitro experimental work with regard to bone-like apatite formation, protein adhesion and fibroblast and osteoblast cell adhesion were performed to evaluate the biocompatibility of the CO_2 laser treated MgO-PSZ. It was found that CO_2 laser induced hydroxyl groups improved the bioactivity of the MgO-PSZ surface by way of facilitating bone-like apatite formation. The investigation of the protein adsorption revealed that the CO_2 laser treatment inhibited the adsorption of human serum albumin and promoted of human plasma fibronectin protein adsorption on MgO-PSZ, showing that the wettability characteristics of the MgO-PSZ predominantly determines the protein adsorption. Furthermore, the response of human skin fibroblast cells and hFOB human osteoblast cells response on the untreated and CO_2 laser treated MgO-PSZ were *in vitro* evaluated. The investigation of the relationships between the cell response and surface properties of the MgO-PSZ, as well as laser parameters, indicated the extent of cell response was primarily influenced by the wettability characteristics of the MgO-PSZ.

List of Publications

Journal Papers

1. L. Hao and J. Lawrence, (2003), "CO_2 laser modification of the wettability characteristics of a magnesia partially stabilised zirconia (MgO-PSZ) bioceramic", *Journal of Physics D: Applied Physics*, 36 **(11)**, 1292-1299.

2. L. Hao and J. Lawrence, (2003), "Effects of CO_2 laser radiation on the wettability and human skin fibroblast cell response of magnesia partially stabilised zirconia", *Materials Science & Engineering C: Biomimetic and Supramolecular Systems.* 23 **(5)**, 627-639

3. L. Hao and J. Lawrence, (2004) "Laser surface treatment of magnesia partially stabilised zirconia for enhanced human skin fibroblast cell response", *Journal of Laser Applications*, 16 **(1)**, 55-64

4. L. Hao, J. Lawrence, G. C. Lim and H.Y. Zheng, (2004)"Examination of CO_2 laser induced rapid solidification structures on magnesia partially stabilised zirconia and the effects thereof on wettability characteristics", *Optics and Lasers in Engineering.* 42 **(3)** 355-374

5. L. Hao and J. Lawrence, (2004),"On the role of laser induced microstructures in influencing the wettability characteristics of magnesia partially stabilised zirconia (MgO-PSZ) bioceramic", *Proceedings of the IMechE Part B, Journal of Engineering Manufacture.* 218 **(B1)**, 59-76

6. L. Hao and J. Lawrence, (2003), "CO_2 laser induced microstructural features in a magnesia partially stabilised zirconia bioceramic and the effects thereof on wettability characteristics", *Materials Science & Engineering A. Structural Materials: Properties, Microstructure and Processing***,** 364 **(1-2)**, 171-181.

7. L. Hao and J. Lawrence, (2004) "Identification of the mechanisms governing modifications of the wettability characteristics of a magnesia partially stabilised zirconia bioceramic following CO_2 laser treatment", Journal of Laser Applications, 16 **(4)**, 252-257

8. L. Hao and J. Lawrence, (2003), "On the role of microstructure form and dimension on surface energy changes in a magnesia partially stablised zirconia (MgO-PSZ) bioceramic following CO_2 laser irradiation", *Journal of Physics D: Applied Physics*, 37 **(1),** 86-92

9. J. Lawrence and L. Hao, (2004) "Bonding characteristics of selected liquid-metals with a CO_2 laser treated magnesia partially stabilised zirconia bioceramic", *Lasers in Engineering,*15 **(1-2)**, 75-90.

10. L. Hao, J. Lawrence, K.S Chian, "On the effects of CO_2 laser irradiation on the surface properties of a magnesia partially stabilised zirconia (MgO-PSZ) bioceramic and the subsequent improvements in human osteoblast cell adhesion", *Journal of Biomaterials Application,* 19 **(2)**, 81-105

11. L. Hao, J. Lawrence, D.K.Y.Low, K.S. Chian, G. C. Lim and H.Y. Zheng (2004) "The formation of a hydroxyl bond and the effects thereof on bone-like apatite formation on a magnesia partially stabilised zirconia (MgO-PSZ) bioceramic following CO_2 laser irradiation", *Journal of Materials Science: Materials in Medicine*, 15 **(9)**, 967-975

12. L. Hao, J. Lawrence, D.K.Y.Low, G. C. Lim and H.Y. Zheng (2004) "Correlation between hydroxyl bond and wettability characteristics of a magnesia partially stabilised zirconia (MgO-PSZ) following CO_2 laser irradiation", *Thin Solid Films*, 468 **(1-2),** 12-16

13. L. Hao and J. Lawrence "The adsorption of human serum albumin (HSA) on CO_2 laser modified magnesia partially stabilised zirconia (MgO-PSZ)", *Colloids and Surfaces B: Biointerfaces* 34 **(2)**, 87-94

14. L. Hao and J. Lawrence, "The improved adsorption of human plasma fibronectin on magnesia partially stabilised zirconia (MgO-PSZ) bioceramic resulting from CO_2 laser irradiation", *Journal of Laser Applications*
    Accepted for publication 14 Jul. 2004.

15. L. Hao and J. Lawrence, (2004) "On the role of CO_2 laser treatment in the human serum albumin and human plasma fibronectin adsorption on zirconia (MgO-PSZ) bioceramic surface", *Journal of Biomedical Materials Research, ,* 69A **(4)** 748-756

Conference Papers

1. L. Hao and J. Lawrence, (2003), "Laser treatment of magnesia partially stabilised zirconia (MgO-PSZ) for improved biocompatibility", *Innovation in Engineering Conference*, Singapore 25 - 26 July 2003,

2. H.R. Chew, J. Lawrence, C.K. Chong and L. Hao, (2003), "Laser treatment of selected bio-metals for improved biocompatibility", *The 22nd International Congress on Applications of Lasers and Electro-Optics: Materials Processing*, Jacksonville, FL., USA, 13-16 October 2003.

3. L. Hao, J. Lawrence, and H.Y. Zheng, (2003), "An investigation of the relationship between wettability characteristics and CO_2 laser induced microstructure features in a MgO-PSZ bioceramic", *International Conference on Materials for Advanced Technologies (ICMAT 2003)*, Singapore, 7 - 12 December 2003.

4. L. Hao, J. Lawrence, D.K.Y.Low, K.S. Chian, G. C. Lim and H.Y. Zheng (2003), "The effect of CO_2 laser irradiation on hydroxyl bond and bone-like apatite formation on a magnesia partially stabilised zirconia (MgO-PSZ) bioceramic ", *International Conference on Epithelial Technologies and Tissue Engineering*, Singapore, 4-6 Dec. 2003

5. L. Hao, J. Lawrence, H.Y. Zheng and K.M. Teh, (2004), "An analysis of the CO_2 laser treatment of a magnesia partially stabilised zirconia bioceramic and its effectiveness in promoting human skin fibroblast cell response", *International Conference on Precision Engineering*, Singapore, 2-5 March 2004.

6. J. Lawrence and L. Hao, (2004), "Bonding characteristics of selected liquid-metals with a CO_2 laser treated magnesia partially stabilised zirconia bioceramic", *1st Pacific International Conference on Applications of Lasers and Optic (PICALO 2004)*, Australia, 19-21 April 2004

7. L. Hao and J. Lawrence, (2004), "Fibroblast cell adhesion on a magnesia partially stabilised zirconia following CO_2 laser radiation", *1st Pacific International Conference on Applications of Lasers and Optic (PICALO 2004)*, Australia, 19-21 April 2004

8. L. Hao, J. Lawrence, G.C. Lim, H.Y. Zheng and K.M. Teh (2003), "Identification of the mechanisms governing modifications of the wettability characteristics of a magnesia partially stabilised zirconia bioceramic following CO_2 laser treatment", *1st Pacific International Conference on Applications of Lasers and Optic (PICALO 2004)*, Australia, 19-21 April 2004.

Press Reports

1 "Laser Treatment of Magnesia Partially Stabilised Zirconia (MgO-PSZ) for Improved Biocompatibility", Author: Hao Liang and Jonathan Lawrence, *Forward: Newsletter for Industry*, 22 May 2003, (Nanyang Technological University).

2. "Laser Treatment Improves Material's Biocompatibility" Author: Benjamin D. Butkus, *Biophotonics International*, Sep. 2003 Vol.10, P.22

Book Chapter

1. L. Hao and Jonathan Lawrence (2003) "The wettability modification of a magnesia partially stabilised zirconia using laser treatment and fundamental mechanism analysis", in *Recent Research Developments in Materials Science & Engineering*, 2, p159-184 (ISBN:81-7895-091-X) Transworld Research Network.

Contents

CO_2 Laser Surface Treatment of Magnesia Partially Stabilised Zirconia (MgO-PSZ) for Improved Biocompatibility

PART TWO
Materials Aspects

List of Figures

Chapter 6. Examination of CO_2 Laser Induced Rapid Solidification Structures on Magnesia Partially Stabilised Zirconia

Chapter 7. The Effects of CO_2 Laser Radiation on the Wettability Characteristics of Magnesia Partially Stabilised Zirconia

List of Tables

Glossary of Terms

A.

AAM ……. Acrylamide

AOCG …….. Amalgamated Oxide Compound Grout

ATCC …… American Type Culture Collection

B.

BSA …….. Bovine Serum Albumin

C.

CPD …….. Critical Point Dryer

CW …….. Continuous Wave

D.

DLC ……. Diamond Like Carbon

DLVO …..... Derjaguim Landau Verwey Overbek

DMEM …..... Dulbecco Modified Eagle's Medium

E.

EDX …….. Energy Dispersive X-ray (analysis)

F.

FAF …….. Fast Axial Flow (CO_2 Laser)

FTIR …….. Fourier Transform Infrared Spectrometer

H.

HA ……. Hydroxyapatite

HAZ …….. Heat Affected Zone

HEMA ……. Hydroxyethylmethacrylate

HPDL …..... High Power Diode Laser

I.

IAR …..... Ion Assisted Reaction

IBAD …..... Ion Beam Assisted Deposition

IBT ……. Ion Beam Texturing

L.

LCVD …….. Laser Chemical Vapour Deposition

LB ……. Langmuir Blodgett

LMS ……. Laser Surface Melting

LSA …….. Laser Surface Alloying

LSG …….. Laser Surface Glazing

LSM …….. Laser Surface Melting

LPVD …….. Laser Physical Vapour Deposition

M.

MAPLE ……. Matrix Assisted Pulsed Laser Evaporation

MgO-PSZ …..... Magnesia Partially Stabilised Zirconia

N.

NCP ……. Non-collagenic Proteins

NVP …….. N-vinylpyrrolidone

O.

ODS ……. Octadecyl Glass

P.

PBS …….. Phosphate Buffered Saline

PE …..... Polyethylene

PEEK …..... Polyetheretherketone

PET …..... Polyethylene Terephhalate

PLD ……. Pulsed Laser Deposition

PP …..... Polypropylene

PMMA …..... Polymethyl methacrylate

PSZ …..... Partially Stabilised Zirconia

PVD …..... Physical Vapour Deposition

S.

RGD ……. Arg-Gly-Asp

S.

SAM ……. Self-assembled Monolyers

SBF ……. Stimulated Body Fluids

SEM …….. Scanning Electron Microscope

SET …….. Surface Exposing Time

SF …….. Slow Flow (CO_2 Laser)

T.

TEM ..…... Transverse Electromagnetic Mode

TEOS ……. Tetraethoxysilane

TF …….. Transverse Flow (CO_2 Laser)

THR ……... Total Hip Replacement

TiPT ……. Tetraisopropyl Titanate

TZP ……... Tetragonal Zirconia Polycrystals

TTZ ……... Transformation Toughened Zirconia

U.

UHMWPE ……... Ultra High Molecular Weight Polyethylene

UV ……... Ultraviolet

X.

XPS …….. X-ray Photoemission Spectroscopy

XRD …….. X-ray Diffraction (analysis)

Y.

Y-TZP ……... Yttria Stabilised Tetragonal Zirconia Polycrystals

Nomenclature

C_L	Average liquid composition
C_O	Average equilibrium composition
D_f	Diffusion coefficient (cm^2/s)
E_y	Young's modulus (N/m^2)
ΔF_{adh}	Interfacial Free Energy of Adhesion
G	Thermal gradient (K/cm)
G_E	*van der waal* Forces
G_{VDW}	Repulsive Electrostatic Forces
L_f	Latent heat of fusion (J/kg)
R	Solidification rate (cm/s)
r	Radius (m)
r_a	Roughness factor
T	Absolute temperature (K)
T_m	Melting point (K)
T_o	Initial material temperature (K)
$\dot{T}$	Cooling rate (K/s)
t	Time (s)
t_m	Initial time to reach melting point (s)
Δt	Coherence time (s)
W_{ad}	Work of adhesion (J)
W_{adv}	Actual work of adhesion (J)
W_{ad}^d	Dispersive component of work of adhesion (J)
W_{ad}^p	Polar component of work of adhesion (J)
β	Coefficient of thermal expansion (K^{-1})
γ	Surface energy (mJ/m^2)
γ_c	Critical surface energy of wetting (mJ/m^2)
γ_{cl}	Cell Liquid Interfacial Free Energy (mJ/m^2)
γ^d	Dispersive component of surface energy (mJ/m^2)
γ^p	Polar component of surface energy (mJ/m^2)
γ_{lv}	Liquid-vapour surface energy (mJ/m^2)
γ_{sl}	Solid-vapour surface energy (mJ/m^2)
γ_{sv}	Solid-vapour surface energy (mJ/m^2)

γ_{lv}^{d}	Dispersive component of the liquid-vapour surface energy (mJ/m^2)
γ_{sv}^{d}	Dispersive component of the solid-vapour surface energy (mJ/m^2)
γ_{sv}^{p}	Polar component of the solid-vapour surface energy (mJ/m^2)
γ_{lv}^{p}	Polar component of the liquid-vapour surface energy (mJ/m^2)
θ	Contact angle (deg)
θ_a	Advancing contact angle (deg)
θ_r	Receding contact angle (deg)
θ_w	Contact angle for the wetting of a rough surface (deg)
π_{sv}	Liquid-solid surface vapour adsorption
ρ	Material density (kg/m^3)
σ	Thermal stress (N/m^2)
τ	Adhesion Tension

Introduction

Research Background

Laser Surface Treatment

It is widely recognised that the laser has some unique properties for surface treatment. The electromagnetic radiation of a laser beam is absorbed within the first atomic layers for opaque materials, such as metals, and there are no associated hot gas jets, eddy currents or even radiation spillage outside the optically defined beam area. In fact, the applied energy can be placed precisely on the surface only where it is needed; thus it is a true surface heater and a unique tool for surface engineering. The most salient advantages of laser surfacing compared to alternatives are [1]:

- Chemical cleanliness.
- Controlled thermal penetration and therefore distortion.
- Controlled thermal profile and therefore shape and location of heat affected region.
- Less after machining, if any, is required.
- Remote non-contact processing is usually possible.
- Relatively easy to automate

Surface treatment is a subject of considerable interest at present as it seems to offer the chance to save strategic materials or to allow improved components with idealised surfaces and bulk properties.

Surface Modification of Biomaterials

Biomaterial applications make use of all classes of materials: metals; ceramics; polymers and composite. These are divided roughly into three user types [2]: (i) inert or relatively inert with minimal host response; (ii) bioactive which actually stimulates bonding to the surrounding tissue and (iii) biodegradable which resorb in the body over a period of time.

The biological responses to biomaterials and devices are largely controlled by their surface properties. That is to say, the surface characteristics play a role in the functioning of biomaterial. The rationale for the surface modification of biomaterials is straightforward. The key physical properties of a biomaterial can be retained while only the outermost surface is modified to tailor to the biointeractions. Hence, if surface modification is properly carried out, the mechanical properties and functionality of the device will be unaffected, but the tissue interface-related biocompatibility can be improved [3]. Either Biological or physicochemical methods are often employed to modify the material surface. Surface engineering of biomaterials has been becoming a lucrative market.

The Application of the Bioinert Ceramic and Existing Problems

During recent decades, a vast number of materials have been tested as potential biomaterials. Ceramic implants have aroused great interest because of the failure of more traditional materials such as metal and polyethylene in total hip prosthetics. The potential of ceramics as biomaterials relies upon their compatibility with the physiological environment [4,5]. Two nearly inert ceramics most used in surgical implants, alumina and zirconia, have high-strength and exhibit minimal ion release. Zirconia ceramics have an advantage over alumina ceramics of higher fracture toughness and higher flexural strength and lower Young's modulus. Partially stabilised zirconia (PSZ) has found wide usage in medical and dental surgery. Within orthopaedic application it is commonly used as femoral head, artificial knee, bone screws and plates, whilst in dentistry it is used to manufacture dental implants, dental posts, crowns, brackets and inlays. Magnesia partially stabilised zirconia (MgO-PSZ) was the very first zirconia implant approved by the Food and Drug Administration. However, bioinert ceramics have often clinically failed due to lack of direct bonding with bone, that is, insufficient osseointegration. For an implant to be successful, close apposition of bone to the surface of implant (osseointegration) is essential.

Research Objectives

The objectives of this research were to establish the laser as a novel technique for improving the biocompatibility of MgO-PSZ implant and to solve the "loosing" problem existing in the clinical use. The bioactivity and biointegration are the two essential aspects of a good biocompatibility. Bioactivity are usually attributed to the ability to induce an apatite layer on materials surface in physiological conditions [6-8]. The osseointegration presented as the ability to promote bone cells anchorage, attachment, spreading, growth and differentiation [9,10].

The interaction between bone-implant interface depends on the surface aspects of materials which may be described according to their topography, chemistry or wettability [11]. These surface characteristics determine how biological molecules will adsorb to the surface and more particularly, determine the orientation of adsorbed molecules. They also determine the cell behaviour on contact. As previously discussed, cells in contact with a surface will firstly attach, adhere and spread. This first phase depends on adhesion proteins [11]. Different approaches are being used in an effort to obtain the desired bone-implant interface. The ideal implant should present a surface conductive to, or that will induce osseointegration, regardless of implantation site, bone quantity, bone quality, etc [9]. Consequently, much effort is being devoted to methods of modifying surfaces of existing biomaterials to achieve a desired biological response. Materials can be surface modified by using physicochemical or biochemical methods. Biochemical methods of surface modification offer an alternative or adjunct to physicochemical methods. Although there are several reports of biochemical surface modification for modulating tissue responses to cardiovascular materials, this

approach has received comparatively little consideration for orthopaedic and dental application due to the necessity of controlling the molecule delivery [12].

The physiochemical approach to modify chemistry or wettability characteristics is increasingly applied to biomaterials. In fact, biomaterial scientists have long sought a single, material-related parameter that effectively measures biocompatibility and might serve as a practical design guide. The theories of surface energy and wetting for such parameters present an attractive means to do this, as surface properties are important determinants of a biomaterial function [13]. The ability to control the surface wettability of solid substrates is important in many situations. There are some traditional approaches available for altering the surface properties and wettability characteristics of biomaterials, namely plasma modification and ion implantation. Such processes, however, are invariably complex and consequently somewhat difficult to control. In addition, plasma modification and ion implantation are not generically applicable to all kinds of biomaterials. In particular, these techniques cannot be practically applied to bioinert ceramics. Lasers, on the other hand, can offer the user not only an exceedingly high degree of process controllability, but also a great deal of process flexibility. In fact, laser radiation was found by Lawrence and Li [14] to effect significant changes in the wettability characteristics of many materials, with different types of lasers being employed to enhance the wettability characteristics of engineering materials, including composites, ceramics, metals and plastics.

Clearly, the development of a successful laser-based technique for improving the biocompatibility of bio inert ceramics used for bone-implants by way of modifying the surface properties of the materials, particularly the wettability characteristics, would be welcomed for many reasons. By varying the CO_2 laser power densities, the work investigated how the CO_2 laser effected the surface properties MgO-PSZ, such as morphology, surface roughness, O_2 surface content and rapidly solidified microstructure. It particularly analysed the change in the wettability characteristics and basic mechanisms governing this modification, since wettability characteristics is widely recognised as an important determinant of cell adhesion and biomaterial's function. Then, the bioactivity evaluation of the MgO-PSZ was conducted to find whether the bone-like apatite could form on the MgO-PSZ following CO_2 laser irradiation in the simulated body fluid and what were the functional groups for apatite nucleation. Furthermore, it investigated how the CO_2 laser modified surface properties influenced the protein adsorption and cell adhesion that would manipulate the biointegration between implant and tissue. Fig.1 elucidates the scope of this research and the feedback from the bio-evaluation to adjust the laser modification for establishing a highly controllable technique.

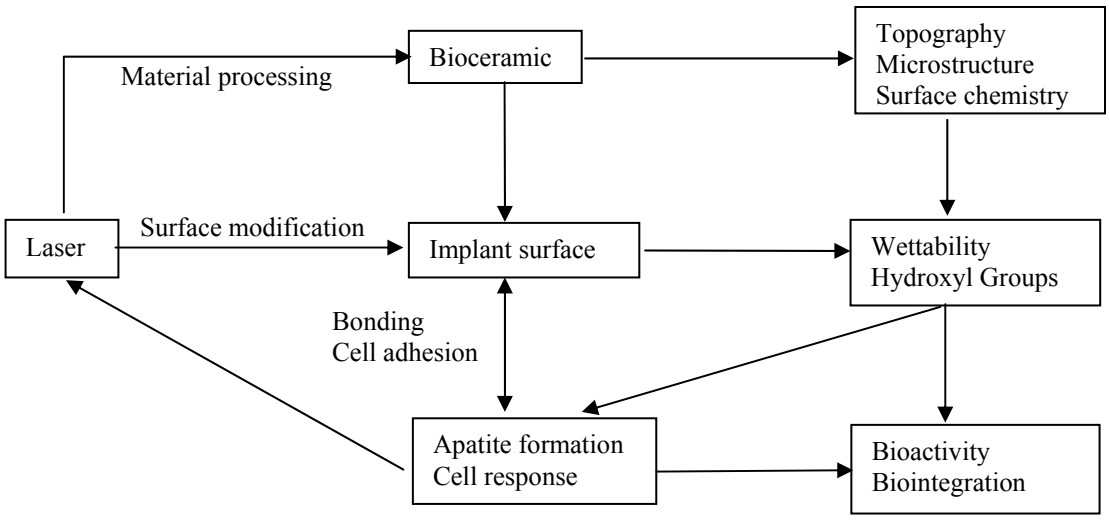

Figure 1. Laser surface processing of bioceramic for improved biocompatibility.

Thesis Organisation

This thesis describes the material characterization and biocompatibility evaluation of the untreated and CO_2 laser treated MgO-PSZ. As such, the thesis is divided into three separate parts and consists of ten distinct chapters.

Part 1. *Literature Review*. In this part of the thesis, the first four chapters elucidate the objectives of the research work and review the current work in the fields of laser materials processing, wettability and biomaterials. This literature review provides a comprehensive resource of valuable information on laser surface modification, biomaterials and the techniques currently available for the surface modification of such materials and lastly, the fundamental theories of wettability and the state-of-the-art in wettability characteristics modification and bioactivity and biointegration of orthopaedic and dental implants.

Part 2. *Materials Aspects*. In this part of the thesis, Chapter 5 describes the general effects of laser radiation on the MgO-PSZ; Chapter 6 examines and explains the CO_2 laser induced rapid solidification structures generated on the surface of the MgO-PSZ; Chapter 7 investigates the wettability characteristics of CO_2 laser treated magnesia partially stabilised zirconia (MgO-PSZ), elucidates the reasons of the changes in the wettability characteristics and identifies the predominant factor governing the modification of wettability characteristics.

Part 3. *Biocompatibility Aspects*. In this part of the thesis three chapters describe the *in vitro* experimental work regarding the bone-like apatite formation, protein adhesion and fibroblast and osteoblast cell adhesion to evaluate the biocompatibility of CO_2 laser treated MgO-PSZ. Chapter 8 finds that the laser induced hydroxyl groups improved the bioactivity of the MgO-PSZ surface by way of facilitating bone-like apatite formation. Chapter 9 investigates the human serum albumin

and human plasma fibronectin protein adsorption on MgO-PSZ and discusses the relationships between the protein adsorption and surface properties. Chapter 10 investigates the *in vitro* behaviours of human skin fibroblast cells and hFOB human osteoblast cells on the untreated and CO_2 laser treated MgO-PSZ and analysed the mechanisms active in cell response and thus deduces the main factor.

CHAPTER 1
State-of-the-art in Laser Surface Treatment

1.1. Introduction [1]

The laser has some unique properties for surface treatment. The electromagnetic radiation of a laser beam is absorbed within the first atomic layers for opaque materials, such as metals, and there are no associated hot gas jets, eddy currents or even radiation spillage outside the optically defined beam area. In fact, the applied energy can be placed precisely on the surface only where it is needed. Thus it is a true surface heater and a unique tool for surface engineering. The range of possible processes with the laser is illustrated in Fig. 1.1.

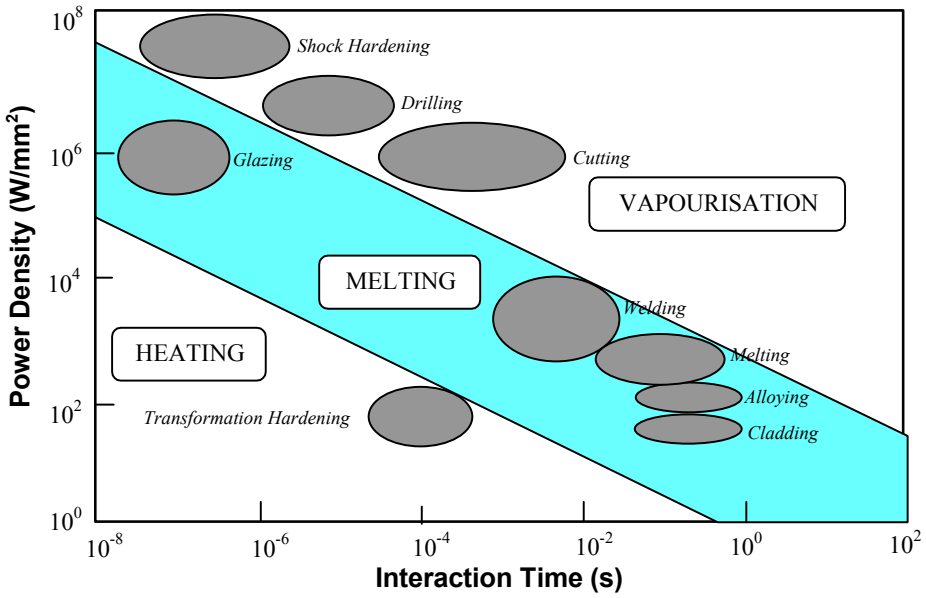

Fig. 1.1. Laser beam – material interaction spectrum [1].

Common advantages of laser surfacing compared to alternatives are:

- Chemical cleanliness.
- Controlled thermal penetration and therefore distortion.
- Controlled thermal profile and therefore shape and location of heat affected region.
- Less after machining, if any, is required.
- Remote non contact processing is usually possible.

- Relatively easy to automate

Surface treatment is a subject of considerable interest at present as it seems to offer the chance to save strategic materials or to allow improved components with idealised surfaces and bulk properties. These ambitions are real and possible but economically it is likely that this current enthusiasm will fade into a realisation that only particular parts of surfaces are vulnerable to corrosion or wear and that there is no need to cover large areas. Where large areas are required to be covered, for example for appearance, paint will probably be most cost effective, or for large area coverage by metals then electroplating is likely to be the winner; but for discrete areas the laser has few competitors and can give a wide variety of treatments as discussed here.

1.2. Contemporary Industrial Lasers

1.2.1. Introduction

Lasers are classified according to the lasing medium used into; gas lasers such as HeNe lasers, liquid lasers such as the dye laser, solid state lasers such as the ruby laser and semiconductor lasers such as the diode laser. However, not all lasers are suitable for industrial purposes due to the beam properties and output power, etc. The most commonly used industrial lasers today are the CO_2 laser, the Nd:YAG laser, the excimer laser and more increasingly, the high power diode laser (HPDL).

1.2.2. The CO_2 Laser [1,14,15]

The lasing medium in a CO_2 laser is generally composed of a mixture of carbon dioxide, nitrogen and helium gasses. The nitrogen is active in the excitation process and is added to increase the excitation efficiency and the helium, which comprises approximately three quarters of the total gas mixture, is included because it acts as an internal heat sink. The lasing transitions are due to energy levels resulting from the electronic motions, vibrational motions and rotational motions of the CO_2 molecule. Just as in single atoms, electrons in molecules can be excited to higher energy levels. Independent of the electronic state, the atomic nuclei, which are held together by molecular binding forces, will vibrate about their equilibrium position, giving rise to quantized vibrational energy levels. The energy separation between vibrational levels of the same electronic energy state generally corresponds to frequencies in the near and middle infrared range, thus each of the widely spaced electronic levels will be split into numerous vibrational sub-levels. The three possible quantized modes of vibration in the CO_2 molecule in the lowest electronic state are symmetric, bending and asymmetric vibrational motions. A molecule in any electronic-vibrational level can be capable of rotation about a number of axes in space. This rotational action will in turn lead to closely spaced, discrete energy levels, further subdividing each vibrational energy level into a series

of levels with energy separations corresponding to far infrared frequencies. Lasing transition occurs between a rotational sub-level of one vibrational level and another rotational sub-level of a lower vibrational level, where the quantized angular momentum numbers of the two rotational levels differ by exactly unity. When a gas discharge is established, CO_2 molecules are excited into higher electronic levels by colliding with excited N_2 molecules, from where they proceed to decay to a lower level. Favourable relaxation rates permit the establishment of a population inversion leading to lasing between numerous rotational levels around 10.6 μm. There are basically three major CO_2 laser designs: slow flow CO_2 Lasers (SF); fast axial flow CO_2 Lasers (FAF) and transverse flow (TF) CO_2 Lasers, which are all based on variations in the methods of cooling the carbon dioxide gas mixture.

1.2.3. The Nd:YAG Laser [1]

The Nd:YAG laser consists of a standard cavity design with neodymium (Nd^{3+}) doped in a yttrium-aluminium-garnet (YAG) crystal rod. The rod is mounted at one of the foci of an elliptical cavity, whilst at the other focus is a krypton or xenon flash lamp used to excite the crystal rod. Krypton or xenon flash lamps are used because the necessary wavelength to cause laser excitation of the crystal rod lies within the broad spectrum of their output. However, because the range of excitation wavelengths is very narrow, the part of the spectrum remaining is wasted as heat. Thus the overall operating efficiency of Nd:YAG lasers tends to be relatively low, only 0.1-2%. But, Nd:YAG lasers that incorporate a diode laser to excite (pump) the crystal rod can have an efficiency of up to 30% due to the fact that the diode laser output can produce the narrow range of wavelengths most efficient for exciting solid-state laser materials, therefore producing much less waste heat [16]. The output wavelength of Nd:YAG lasers is 1.06 μm, which is close to the visible spectrum; allowing the use of conventional optics as well as optical fibre delivery of the output beam. The laser can be operated in both continuous wave (CW) and pulsed mode with output powers currently ranging from a few watts to several thousand watts, with peak pulse powers of around 50 kW at kilohertz rates and up to 5 kW in CW mode.

1.2.4. The Excimer Laser [17,18]

The lasing medium used in excimer lasers are the rare gas halides such as ArF, KrF and XeCl. These materials are used because the diatomic molecules whilst being stable in the excited state, are not so in the ground state. Thus ‘excimer’ is contrived from the contradiction of *exci*ted di*mer*. Because of the molecules instability under equilibrium conditions the population of the ground state is low, thus enabling a population inversion to be achieved quite easily. As such, the conversion of electrical energy to optical energy efficiency of excimer lasers is relatively high, typically 10-15%, yet the overall operating efficiency of excimer lasers is only around 2%. Gaseous discharges,

electron beams and photon beams can all be used for pumping. However, because the time duration of the excited state is very short the excimer laser is operated in pulsed mode. Pulse durations are in the order of tens of nanoseconds but the average output power of the laser is generally low, typically 10-200 W, with peak energies per pulse of up to 1 J. However, 1 kW excimer lasers are currently available. Because excimer lasers emit in the short wavelength ultraviolet region of the spectrum (193-351 nm) the output beams can be focused to extremely small spots, obtaining high intensities at the workpiece.

1.2.5. High Power Diode Lasers [14,19]

Carrier injection across the junction of two semiconductor materials that had been doped with either a pentavalent or a trivalent element to create a positive charge (p-type) or a negative charge (n-type) as a means for achieving stimulated emission in semiconductors was first proposed by Von Neumann [20], with the first semiconductor injection lasers being demonstrated in several laboratories in 1962 [21]. The rapid and continuous enhancement of diode laser material and fabrication technology over the last decade has increased the average power output of the devices by two fold each year [24], giving rise today to the commercial availability of diode lasers delivering output powers in excess of 50 mW- HPDL. Indeed, output powers of up to 120 W-CW for single 10 mm experimental diode bars have been reported [25]. Because of the unique features of diode lasers; small size and low weight, which makes them easy to integrate, and because of their high efficiency and reliability, which leads to low running costs, diode lasers gained high interest as a pump source for solid-state-lasers as well as a new laser source for materials processing [19]. Already HPDL are beginning to replace technologically mature lasers in many application areas and evidence suggests that this trend will almost certainly occur in the materials processing sector.

1.3. Current Uses of Laser Surface Treatment

1.3.1. Laser Heat Treatment

The initial goal of laser heat treatment was selective surface hardening for wear reduction; it is now also used to change metallurgical and mechanical properties. There are many competing processes in the large subject of surface heat treatment. The laser usually competes successfully due to lack of distortion and high productivity. Practical uses of laser heat treatment include: hardness increase, strength increase, reduced friction, wear reduction, increase in fatigue life, surface carbide creation, etc [1]. The laser beam is defocused or oscillated to cover an area such that the average power density has a value of 10^3 and 10^4 W/mm^2. Using these power densities a relative motion between the workpiece and the beam of 5 and 50 mm/s will result in surface hardening. If surface melting

occurs and power density will produce the same effect. If no hardening or shallow hardening occurs, but deeper hardening was desired, relative motion should be decreased, an increase in power density will produce the same effect. The depth of hardening depends upon thermal diffusion and hence the heating time (D/V); where D is the spot size on the workpiece and V is the traverse speed, as well as the temperature, dependent on the specific energy (P/DV).

1.3.2. Laser Surface Alloying

The aim in laser surface alloying (LSA) is to incorporate additional alloying elements in the surface of a component with minimum change on overall dimensions as a means of improving functional properties such as wear, corrosion and oxidation resistance. The processing regime for LSA is similar to that for laser surface melting (LSM) since surface melting must be initiated yet vaporisation must normally be avoided. Hence the two techniques occupy similar processing windows on the power intensity/interaction time diagram shown in Fig. 1.1. But, unlike LSM, in LSA another material is injected into the melt pool. LSA has a number of distinct advantages over the more conventional coating methods, these are summarised below [1].

1. A dense surface layer with no porosities can be produced, with a typical thickness of 1-2000 μm.
2. The integrity of the bonding between the surface layer and the substrate is complete, and hence superior to coating techniques such as spraying or roll bonding.
3. Since the depth of penetration can be precisely controlled and the heating effect is strongly localised, there is no detrimental effect on the bulk mechanical properties such as can occur in surface diffusion techniques involving prolonged heating.
4. High vacuum conditions are not required since oxidation effects can simply be avoided by the use of an inert gas shroud. Thus there is substantial manufacturing flexibility.
5. There is no fundamental restriction on component shape.
6. Surface microstructures which are unobtainable by any of the main coating or surface treatment technologies can be produced.
7. Limited areas of a component surface can be processed without affecting surrounding areas and hence LSA is applicable to the limited area processing of critical regions of a component.

1.3.3. Laser Cladding

The purpose of laser cladding is overlay one material with another to form a sound interfacial bond without diluting the cladding metal with substrate material. This is a relative newcomer and is having to make its own market since no comparable process has previously been available for

localized cladding [22]. Unlike LSA, in laser cladding dilution is considered to be contamination of the cladding, resulting in the degradation of its mechanical or corrosion properties.

1.3.3.1. Pre-placed Powder Laser cladding [23]

Cladding with a pre-placed powder that is sufficiently adhered to the substrate is the simplest laser cladding method. This method involves traversing a defocused or restored laser beam over a powder bed, which is consequently melted and welded to the underlying substrate. Theoretical modelling of movement in the molten front has shown that the melt progresses relatively quickly through the thermally isolated powder bed until it reaches the interface with the substrate. At this point the thermal load increases due to the good thermal contact with the high thermal conductivity substrate, causing resolidification. A disadvantage of the pre-placed powder laser cladding technique is the difficulty of achieving a low dilution fusion due to the small operating window within which a fusion bond is possible.

1.3.3.2. Blown Powder Laser Cladding [23,24]

Blown powder laser cladding is one of the few cladding techniques which has a well-defined heated region, a good fusion bond with low dilution and is readily adaptable to automatic processing. This technique is carried out by scanning a defocused laser beam over the substrate whilst the cladding powder is blown simultaneously into the beam incident region thus generating a melt pool. There is a reasonably large operating window for low dilution fusion bonded cladding. This region is bounded by a dilution limit, which is dependant upon the excess powder available after the powder has been melted, an aspect ratio limit, which is dependant upon whether the runs can be over lapped without inter run porosity, and a power limit, which is dependant upon whether the power is sufficient to melt at least some of the substrate [25]. The low dilution possible with blown powder laser cladding is comparable with that of forge bonded processes, whilst the low porosity and high surface strength is similar to that obtained with welding processes. Blown powder laser cladding is essentially conducted over a small melt pool area which travels over the surface of the substrate. The thermal penetration is minimal and thus the problems associated with workpiece distortion and heat affected zone (HAZ) are reduced.

1.3.4. Laser Consolidation of Coatings

This technique makes use of coatings previously applied by alternative processes and is similar to pre-placed powder laser cladding in that the material to be processed is already on the material surface to be irradiated by the laser beam. However, the process does differ from pre-placed powder cladding as the coatings for consolidation can be used in their own right for wear and/or corrosion

resistance applications. The principal reason for employing the laser consolidation technique is to improve the coating by sealing its outer surface and reducing the porosity.

Many workers have previously demonstrated the sealing of metallic and engineering ceramic surfaces with variety materials using lasers. Ayers and Schaefer [26] investigated the laser consolidation of a variety of plasma sprayed coatings on steel and copper substrates. They found that by performing the plasma spraying in a vacuum to reduce oxidation and gas entrapment in the thin layers of the coating, corrosion resistant materials could be successfully consolidated with a CW CO_2 laser to form a non-porous surface layer. Similarly, Pangborn and Beaman [27] laser surface treated a graphite sample onto which a 50 μm thick titanium coating had been plasma sprayed. They demonstrated that the outer portion of a plasma sprayed titanium metal film could be fused by scanning with a pulsed TEA CO_2 laser, thus, the porosity of the film was sealed. Dallaire and Cielo [28] used a pulse TEA CO_2 laser to melt the surface of plasma sprayed nickel coatings. An analysis of heat transfer parameters demonstrated that the pulse length must be in the range 20-40 μs in order to fill the pores of the coating and keep the surface temperature below the boiling range.

1.3.5. Laser Chemical Vapour and Laser Physical Vapour Deposition [1]

1.3.5.1. Laser Chemical Vapour Deposition

Laser chemical vapour deposition (LCVD) can be performed by two distinct methods: thermochemical deposition and photochemical deposition. Thermochemical deposition utilises the thermal energy of the laser beam to heat specific areas of a surface of a substrate which is in an environment of a thermally degradable vapour. As such, the generated hot spot activates the deposition reaction. The process requires a vapour which is non-absorbing to the laser radiation and a substrate which is. Mazumder and Allen [29] investigated, using a suitable reaction chamber, the thermochemical deposition of TiC onto carbon steel (the TiC was formed from the reaction of titanium tetrachloride with methane). The work showed that by heating the carbon steel to approximately 1000^0C with a 400 W CO_2 laser, controlled deposits could be produced. In further work, Allen [30] deposited TiO_2 and Ni onto quartz substrates, demonstrating that that by using very short laser pulses, which heated the surface to just above the threshold temperature for the deposition reaction, very flat deposits of uniform thickness could be produced. In photochemical deposition, decomposition of a vapour phase by photolysis is achieved by means of laser radiation of particular wavelengths (193-351 nm).

1.3.5.2. Laser Physical Vapour Deposition

The technique of laser physical vapour deposition (LPVD) involves the use of lasers to either vaporise material for deposition and/or to control the location of vapour condensation by substrate heating. The vaporisation of materials for deposition can be performed by two techniques. The first method involves the simple heating and melting of coating materials using CW lasers to temperatures where a substantial amount of non-ionised vapour is produced. LPVD, usually performed in a vacuum chamber, generally results in a fairly even coverage of the substrate materials. However, typical problems associated with some level of directionality are present.

The second technique of vaporisation of materials for deposition, plasma condensation LPVD, uses short, high energy laser pulses to produce liquid and both ionised and non-ionised vapour phases. Coatings resulting from the condensation and solidification of these phases have rougher surfaces than vapour condensed deposits, and some metallic materials deposited by this process can show unusual electrical properties compared with those of the bulk material. Tagaki [31] has reported on using such a technique, employing a pulsed laser to produce a liquid/plasma, where the liquid metallic phase is allowed to solidify in a cooling gas rather than impinge on a substrate, depositing SiO_2 coatings of high purity and uniformity on pure metal and alloy substrates.

1.4. Laser Surface Melting and Glazing

Laser surface melting (LSM) aims at modifying the surface of materials in order to improve functional properties such as wear resistance or corrosion resistance. Typically the process is used to treat metals such as cast iron, stainless steel and titanium but the treatment of plasma sprayed ceramics is also possible [32]. LSM is characterised by the absence of the incorporation of any additional alloying elements to provide property enhancement of the surface layer. Property enhancement depends solely on the refinement of the microstructure that can be achieved as a result of the melting of a thin surface layer, normally less than 500 μm, followed by the relatively high cooling rate (10^4-10^8 ^{0}C/s) arising from the self quenching effect of the unaffected substrate. LSM produces a dense surface layer with no porosities, whilst the integrity of the bond between the surface layer and the substrate is complete. If, however, an extremely high cooling rate is achieved (10^6-10^9 ^{0}C/s), then laser surface glazing (LSG) occurs and a super-fine or amorphous structure is generated on the material surface. Typically the depth of this amorphous surface layer ranges from 1-10μm [33]. In terms of the cooling rate, V_c, and the critical cooling rate, V_{cr}, the conditions for glazing are [33]

$$V_c \geq V_{cr} = \frac{1-c}{\ln p}\left[\left(\frac{\nu L_f}{E}\right)\exp\left(\frac{E}{kT_m}\right)\right] \tag{1.1}$$

where, c = Constant (0.95); p = Constant (0.99); ν = Derby frequency (s^{-1}); L_f = Latent heat of fusion (J/kg); E = Atomic transition energy (eV); k = Boltzmann's constant (1.38 x 10^{-23} J/K); T_m = Melting point (K)

1.4.1. Laser Surface Melted/Glazed Layer Formation

As shown in Fig. 1.1, the power density/interaction time region for either LSM or LSG does not allow vaporisation. As a result keyholing is not achieved and Fresnal absorption of the laser beam occurs at the surface, resulting in the generated heat being dissipated into the surface of the material entirely by conduction. To improve the absorptivity of the beam coatings are often applied to the materials surface, this is especially common for metals. Once sufficient coupling is achieved and melting is initiated, a melt wave is formed which penetrates below the surface generating a melt pool. As the laser pulse is finished, or as the laser moves on to the next position on the surface for continuous processing, the melted layer will begin to cool as a result of the self quenching mechanism. In effect a point is reached where the advance of the melt front in the material is slowed down and momentarily becomes zero before the solidification front begins to advance, speeding up as is moves back towards the surface until the whole melt zone has solidified. As a consequence of the differences in temperature between different regions of the melt pool, and hence differences in surface tension, the melt pool is subject to very strong Marangoni mixing forces [34] that promote compositional homogeneity.

1.4.2. Residual Stress Generation

Residual stresses arise because of the volume changes that occur during solidification and cooling. Particular, during LSM and LSG tensile residual stresses will always be present because the melt pool is restrained by the substrate. For a melt track on the surface of a cool substrate then there is no stress when the track is liquid. On cooling the melt shrinks and the stress builds up because the substrate is already cold and acts as a restraint on the contraction of the prior molten track. This situation will prevail for materials such as aluminium in which martensitic formation is absent. For a fully restrained melt track the tensile strain is approximately given by [34]

$$\frac{\sigma}{E_y} = \frac{\delta l}{l} = \beta \Delta T \tag{1.2}$$

where, σ = Thermal stress (N/m^2); E_y = Young's modulus (N/m^2); δl = Thermal expansion over length, l (m); β = Coefficient of thermal expansion (K^{-1}); ΔT = Temperature change (K)

In some cases this gives values of the same order as the yield stress, or higher, which means that plastic deformation takes place in order to relieve the stress. As such, the deformation takes place in the form of microcracks that form along the grain boundaries or between dendrites due to liquidation cracking. When there are overlapping melt tracks there are further effects. For instance, the tensile 'bow wave' of an overlapping run can add to the prior residual stress and cause more deformation.

The generation of tensile residual stresses is altered in the case of materials such as steel, martensitic stainless steels, titanium and cast irons where the martensitic transformation is initiated at sufficiently high rates of cooling from elevated temperatures. For carbon steels there is a 4% increase in volume as the structure changes from austenite to martensite, resulting in a net compressive stress in the surface on cooling to ambient temperature. It is well established that tensile residual stresses have a deleterious effect on fatigue properties, effectively decreasing the fatigue limit of the material by the magnitude of the residual stress [34]. Subsequent heat treatment for the relief of residual stresses is possible as long as coarsening of the microstructure does not result. However, the generation of compressive residual stresses is known to be most beneficial to materials fatigue properties.

1.5. Laser Surface Treatment of Ceramics

Laser surface treatment of ceramics is a novel way of surface treating the materials without excessive changes in the surface chemistry. One objective of using laser treatment often is hardening the surface of the material so as to achieve improved surface performance and lifetime characteristics. Here a laser beam is used to carry high power levels to the surface of a material. As the light beam strikes the surface of the material being treated, the energy associated with the individual photons comprising the laser beam is rapidly transferred to the material to yield the desired results. It is generally used to increase the fracture toughness of ceramics by sealing cracks and pores, improving the friction and wear characteristics and for etching of device structures on a ceramic substrate. It is also employed to change the electrical and magnetic properties of ceramics surfaces.

1.5.1. Laser Surface Melting of Ceramics

Snow *et al* [35] were first to report that laser surface melting can be applied to a superalloy to extend the solid solution phases and to refine the dendritic structure. Schubert and Bergmann [36] have presented results for laser treated alumina samples of different purities and different surface finishes. Using an excimer laser, they found that the variation in treatment parameters affected the

surface condition, and under certain conditions the surface was generally much smoother after irradiation. The improvement was a result of melting of the surface which removed surface defects such as grinding marks and the large, interconnecting porous areas along the sintered grain boundaries.

Li *et al* [37] examined the possibility of laser fixing and sealing of radioactive contamination on concrete surfaces. Four different laser processing techniques were investigated, including direct glazing which involved using high power laser beams to scan over the contaminated concrete/cement surfaces without additional coating materials, resulting in a glazed layer on the surface which retains the radioactive contamination. It was found that operating at low traverse speed (<3 mm/s) and low power density (<200 W/cm^2) was necessary to achieve a reasonable, continuous, vitreous surface on cement-faced concrete surfaces. This resulted in a melt generated with sufficient fluidity to form a glazed layer. Armstrong *et al* [38] treated the top surface of ceramic samples of the $YBa_2Cu_3O_7$ superconductor with a single 7 ms pulse from a Nd-YAG laser. Pulsed laser melting was shown to reduce porosity of the $YBa_2Cu_3O_7$ samples, but also led to decomposition of the superconducting phase. However, heat treatment at 950°C in air restored the required orthorhombic phase and superconductivity to the laser treated surface.

Laser surface treatment has been applied successfully to produce homogeneous, pore-free and smooth surfaces with increased hardness on ceramic materials. Bradley *et al* [39] showed that a denser, uniform surface layer with solidification microstructures and which resists thermal shock, can be produced on CO_2 and diode laser-treated 60% and 85% alumina refractory materials. However, the high melting temperature and low thermal conductivity of refractory ceramics results in the development of high thermal gradients during laser processing and the generation of thermally induced cracks. By pre-heating high purity alumina ceramics in a high-temperature electric furnace prior to and during CO_2 laser treatment, Lee and ZumGahr [40]were able to eliminate cracking and produce a smooth and pore-free surface. Bradley *et al* [41] developed a flame-assisted laser surface treatment process, by applying an oxygen/acetylene welding torch to pre-heat the samples in front of a CO_2 laser beam. Triantafyllidis *et al* [42] used a diode laser was used as the pre- and post-heating source and a CO_2 laser as the main treatment source in order to reduce thermal gradients and produce a deep and crack-free surface and enhance erosion and corrosion resistance. In addition, pores were found to concentrate in the laser treated zone/untreated bulk boundary even though a pore-free surface was produced. Two distinct processes take place, leading to porosity formation at the solidifying interface: bubble motion in the molten pool due to thermocapillary forces; and pore coalescence due to this bubble motion. These two processes result in the development of fewer but larger pores in the treated zone/untreated bulk boundary compared to the initial pores in the ceramic material [43].

1.5.2. Laser Consolidation of Ceramics Coating

Zaplatiynsky [44] carried out work using a CO_2 laser on the partial melting of plasma sprayed ZrO_2 coatings of thickness 0.2 mm and 0.4 mm. With focused beam power densities of 3.5-7.5 kW/cm^2 and scanning velocities of 800 mm/min a smooth coating was generated. However, cracks were present on all the laser generated surfaces. The performance of the coatings was evaluated by means of cyclic oxidation and cyclic corrosion tests. The results obtained from the oxidation tests indicated that the laser treated samples had the same life as the untreated samples. However, despite the surface cracks, in corrosion tests the laser treated samples exhibited an almost fourfold increase in life over that of the untreated samples. Indeed, Longa and Takemoto [45] found that laser-modified coatings offered excellent corrosion resistance compared to the as-sprayed coating.

Adamski and McPherson [46] carried out the melting of ZrO_2 based protective ceramic coatings using a CO_2 laser with power densities ranging from 8.5-17 kW/cm^2. The work showed that laser treatment markedly decreased the level of structural defects and the lamellar microstructure. Similarly, Mordike and Sivakumar [47] melted ZrO_2 protective ceramic layers plasma sprayed onto a variety of bond coats using CW and pulsed CO_2 lasers. The research revealed that the pulsed laser produced a surface displaying less cracks, whilst the use of external flowing gas, such as He or Ar, resulted in increased cracking. However, the laser treated surfaces in both studies displayed the phenomenon of delayed fracture due to unrelieved thermal stresses. A study conducted by Sivakumar and Mordike [48] into the laser melting of plasma sprayed ceramic coatings based on Al_2O_3, TiO_2 and ZrO_2 using CW and pulsed CO_2 laser radiation concluded that the extent of cracking was a function of the total energy input to the surface and the thermophysical properties of the ceramic coatings. Consequently, it was suggested that, to avoid cracking in such materials when consolidating using a CO_2 laser it was essential to pre-heat the workpiece to around 800^0C.

Galasso and Veltri [49] recognised the problem of cracking when ZrO_2-20 wt%Y_2O_3 coatings were melted using a CO_2 laser, and showed that by controlling the laser power, beam size and traverse speed, vertical cracking was induced which ran from the surface of the plasma sprayed coating to the surface of the metal substrate. Such cracks perpendicular to the surface can help in accommodating the strains that occur during thermal cycling. It was also found that with a less intense beam cracking was reduced and the surface of the coating was densified. Indeed, research conducted by Jasim [50] on plasma sprayed CaO-ZrO_2 coatings showed that the optimum operating conditions were attained at low specific energy levels; resulting in a thin melt layer that solidifies to give a relatively smooth and relatively crack-free surface. Notwithstanding this, Havrda [51] were able to produce crack-free ZrO_2-SiO_2 coatings melted using a CW CO_2 laser with powers of 150-300 W and traverse speeds of around 3.6 m/min.

CHAPTER 2
Bioceramic and Surface Modification of Biomaterials

2.1. Introduction

Biomaterials have been studied for many years and defined by Ratner *et al* [3] as being nonviable materials used in a medical device and intended to interact with a biological system. There is a big demand for biomaterials to assist or replace organ functions and to improve patients' quality of life. Biomaterial applications make use of all classes of materials, metals, ceramics, polymers and composite. These are divided roughly into three usertypes [2]: (i) inert or relatively inert with minimal host response, (ii) bioactive which actually stimulates bonding to the surrounding tissue and (iii) biodegradable which resorb in the body over a period of time.

During recent decades a vast number of materials have been tested as potential biomaterials. Ceramic implants aroused great interest because of the failure of more traditional materials such as metal and polyethylene in total hip prosthetics. Three of most frequently used ceramic materials are alumina, zirconia and hydroxyapatite [3,5,52]. Hydroxyapatite is a bioactive [5] material with excellent biocompatibility properties. Unfortunately, the medical applications of hydroxyapatite are limited to small non-bearing implants, powders and coatings due to poor mechanical properties [3,52]. Alumina and zirconia are bioinert materials that exhibit high mechanical strength, excellent corrosion resistance and good biocompatibility. They are, therefore, frequently used in high-load bearing sites such as the hip (articulating ball) and the jaw (dental implant) [5].

The bulk structures of materials partly govern these properties. The biological responses to biomaterials and devices, on the other hand, are largely controlled by their surface chemistry and structure. That is to say, the surface characteristics play a role in the functioning of biomaterial. The rationale for the surface modification of biomaterials is straightforward. The key physical properties of a biomaterial can be retained while only the outermost surface is modified to tailor to the biointeractions. Hence, if surface modification is properly carried out, the mechanical properties and functionality of the device will be unaffected, but the tissue interface-related biocompatibility can be improved [3]. Either Biological or physicochemical methods are often employed to modify the material surface. Surface engineering of biomaterials has been becoming a lucrative market.

Various physicochemical methods will be induced in this chapter, among them, laser surface treatment have good potential for it unique feature.

2.2. Ceramics and Their Applications in Implants [3]

It is essential to recognise that no one material is suitable for all biomaterial applications. As a class of biomaterials, ceramics, glasses, and glass-ceramics are generally used to repair or replace skeletal hard connective tissues. Their success depends upon achieving a stable attachment to connective tissue.

Table 2.1.Types of bioceramics-tissue attachment and their classification [3].

Type of Attachment	**Example**
1. Dense, nonporous, nearly inert ceramics attach by bone growth into surface irregularities by cementing the device into the tissues or by press fitting into a defect (termed "morphological fixation").	Al_2O_3 (single crystal and polycrystalline) ZrO_2 (partially stabilised zirconia)
2. For porous inert implants, bone ingrowth occurs that mechanically attaches the bone to the material (termed "biological fixation").	Al_2O_3 (polycrystalline) Hydroxyapatite-coated porous metals
3. Dense, nonporous surface-reactive ceramics, glasses, and glass-ceramics attach directly by chemical bonding with the bone (termed "bioactive fixation").	Bioactive glass Bioactive glass-ceramics Hydroxyapatite
4. Dense, nonporous (or porous) resorbable ceramics are designed to be slowly replaced by bone.	Calcium sulphate (plaster of paris) Tricalcium phosphate Calcium-phosphate salts

The mechanism of tissue attachment is directly related to the type of tissue response at the implant-tissue interface (see Table 2.1). In recent years ceramics and glass ceramics have played an increasingly important role in implants. This has occurred because of two quite disparate uses. First, there is the use associated with improved properties such as resistance to further oxidation (implying inertness within the body), high stiffness, and low friction and wear as articulating surfaces. This requires the use of full-density, controlled, small and uniform grain size. The second, and scientifically more exciting application, takes advantage of the osteophilic surface of certain ceramics and glass ceramics. These materials provide an interface of such biological compatibility with osteoblasts (bone-forming cells) that these cells lay down bone in direct appositions of glass ceramics, which were termed bioglasses, for implant applications in orthopaedics. The model proposed for the "chemical" bond formed between glass and bone is that the former undergoes a controlled surface degradation, producing and SiO_2 rich layer and a Ca, P-rich layer eventually

crystallises as a mixed hydroxycarbonate apatite structurally integrated with collagen, which permits subsequent bonding by newly formed mineralised tissues.

2.3. Nearly Bioinert Ceramics [3,53]

The use of ceramics in medicine has increased significantly during the past decades and it is anticipated that the use of bioceramics will increase dramatically during the next. The potential of ceramics as biomaterials relies upon their compatibility with the physiological environment. Bioceramics are compatible because they are composed of ions commonly found in the physiological environment (calcium, potassium, magnesium, sodium, etc.) and of ions showing limited toxicity to body tissue (zirconium and titanium). Two nearly inert ceramics most used in surgical implants are alumina and zirconia. The characteristics of bioinert ceramics for biomedical application are shown in Table 2.2. High-strength ceramics used for implants are very inert in the body and exhibit minimal ion release. Aluminium oxide is regarded by many as the standard inert material, meaning that the remodelling of bony tissue adjacent to its surface is not altered by the presence of ions released or by immune reactions. The wettability of alumina is higher than that of the metallic implant materials. The ionic ceramic surface is in a high oxidation state, thermodynamically stable and hydrophilic, so water bonds to the surface with a relatively high strength of attachment. Minimal ion release has been noted for alumina oxide or zirconia oxide under normal conditions.

Table 2.2. Properties of bioinert ceramics [54]

Property	**Units**	**Alumina**	**MgO-PSZ**	**Y-PSZ (TZP)**
Chemical composition		99.9% Al_2O_3 + MgO	ZrO_2 + MgO (8-10 mol %)	ZrO_2 + Y_2O_3 (3 mol %)
Density	g cm^{-3}	≥ 3.97	5.74-6	>6
Porosity	%	<0.1	-	<0.1
Bending strength	MPa	>500	450-700	900-1200
Compression strength	MPa	4100	2000	2000
Young modulus	GPa	380	200	210
Fracture toughness K_{IC}	MPa m^{-1}	4	7-15	7-10
Thermal expansion coeff.	K^{-1}	8×10^{-6}	$7\text{-}10\times10^{-6}$	11×10^{-6}
Thermal conductivity	W mK^{-1}	30	2	2
Hardness	HV 0.1	2200	1200	1200

Inert bioceramics undergo little or no chemical change during long-term exposure to the physiological environment. Even in those cases where these bioceramics may undergo some long-term chemical or mechanical degradation, the concentration of degradation product in adjacent

tissue is easily controlled by the body's natural regulatory mechanisms. Tissue response to immobilised inert bioceramics involves the formation of very thin, several micrometers or less, fibrous membrane surrounding the implant material. Inert bioceramics may be attached to the physiological system through mechanical interlocking, by tissue ingrowth into undulating surfaces.

2.3.1. Alumina

High-density, high-purity (>99.5%) alumina is used in load-bearing hip prostheses and dental implants because of its excellent corrosion resistance, good biocompatibility, high wear resistance, and high strength [5,53]. Although some dental implants are single-crystal sapphires most Al_2O_3 devices are very fine-grained polycrystalline α-Al_2O_3 produced by pressing and sintering at T=1600-1700°C. A very small amount of MgO (<0.5%) is used to aid sintering and limit grain during sintering. Strength, fatigue resistance, and fracture toughness of poly-crystalline α-Al_2O_3 are a function of grain size and percentage of sintering aid (i.e. purity). Alumina has been used in orthopaedic surgery for nearly 20 years. Its use has been motivated largely by two factors: (1) its excellent biocompatibility and very thin capsule formation, which permits cementless fixation of prostheses; and its exceptionally low coefficients of friction and wear rates. Alumina on load bearing, wearing surfaces, such as in hip prostheses, must have a very high degree of sphericity, which is produced by grinding and polishing the two mating surfaces together. For example, the alumina ball and socket in a hip prosthesis are polished together and used as pair. The long-term coefficient of friction of an alumina-alumina joint decreases with time and approaches the values of a normal joint. This leads to wear on alumina-articulating surfaces being nearly 10 times lower than metal-polyethylene surfaces. The main problem with present total hip systems is loosening of the acetabular component, which is caused by wear debris.

2.3.2. Zirconia Ceramics

Alumina has outstanding biocompatibility and wear resistance, however, it exhibits moderate flexural strength and toughness. For this reason, the diameter of most alumina femoral head prostheses has been limited to 32 mm. Zirconia is also exceptionally inert in physiological environment and zirconia ceramics have an advantage over alumina ceramics of higher fracture toughness and higher flexural strength and lower Young's modulus [53]. Partially stabilised zirconia (PSZ) is a ceramic that has found wide usage in medical and dental surgery. Within medicine it is commonly used to fabricate hip ball joints, knee, thumb etc. whilst in dentistry it is used to manufacture dental implants, dental posts, brackets and inlays. Some zirconia implants for medical and dental applications are shown in Fig. 2.1.

(a) (b) (c)

Fig. 2.1. Medical-grade zirconia used as (a) femoral balls, (b) thumb and (c) dental implant [53]

2.3.2.1. Partially Stabilised Zirconia

Pure zirconia (zirconium dioxide) has a high melting point (2700º C) and a low thermal conductivity. Its polymorphism, however, restricts its widespread use in ceramic industry. During a heating process, zirconia will undergo a phase transformation process. The change in volume associated with this transformation makes the usage of pure zirconia in many applications impossible. Addition of some oxides, such as calcia (CaO), magnesia (MgO), and yttria (Y_2O_3), into the zirconia structure in a certain degree results in a solid solution, which is a cubic form and has no phase transformation during heating and cooling. This solid solution material is termed as stabilised zirconia. Partially stabilised zirconia (PSZ) is a mixture of zirconia polymorphs, because insufficient cubic phase-forming oxide (stabilizer) has been added and a cubic plus metastable tetragonal ZrO_2 mixture is obtained. A smaller addition of stabiliser to the pure zirconia will bring its structure into a tetragonal phase at a temperature higher than 1000º C, and a mixture of cubic phase and monoclinic (or tetragonal)-phase at a lower temperature. Therefore, PSZ is also called as tetragonal zirconia polycrystalline (TZP). Usually such PSZ consists of larger than 8 mol% (2.77 wt %) of MgO, 8 mol% (3.81 wt %) of CaO, or 3-4 mol% (5.4-7.1 wt %) of Y_2O_3. PSZ is a transformation-toughened material. Microcrack and induced stress may be two explanations for the toughening in partially stabilised zirconia. The microcrack explanation depends upon difference in the thermal expansion between the cubic phase particle and monoclinic (or tetragonal)-phase particles in the PSZ. Coefficient of thermal expansion (CTE) for the monoclinic form is 6.5^{-6}/º C up to 1200º C, 10.5^{-6}/º C for cubic form is. This deference creates microcracks that dissipate the energy of propagating cracks. The induced stress explanation depends upon the tetragonal-to-monoclinic transformation, once the application temperature over pass the transformation temperature at about 1000º C. The pure zirconia particles in PSZ can metastabily retain the high-temperature tetragonal phase. The cubic matrix provides a compressive force that maintains the tetragonal phase. Stress

energies from propagating cracks cause the transition from the metastable tetragonal to the stable monoclinic zirconia. The energy used by this transformation is sufficient to slow or stop propagation of the cracks. PSZ has been used where extremely high temperatures are required.

2.3.2.2. Properties and Clinical Performance [53]

Zirconia ceramics have a high density because of heavy zirconium ions, and a low microhardness and elastic modulus, together with high strength and fracture toughness compared to other ceramics including alumina. The superior mechanical strength provides the possibilities for producing ceramic ball heads of size below 32 mm.

The published results of *in vitro* wear tests demonstrated that zirconia has a superior wear resistance. Saikko [55] showed no wear of zirconia femoral heads on his hip simulator wear test against 10.9 mm ultra high molecular weight polyethylene (UHMWPE) cup, and Oka *et al* [56] demonstrated the high wear resistance of zirconia against UHMWPE and the superiority of zirconia ceramics even over alumina ceramics in terms of low wear and low friction. A significant reduction in the wear rate of zirconia ball heads compared to the metal ball heads was reported on a pin-on-disc wear test and on a hip simulator. However, there are two potential limitations for the use of zirconia as bioceramics: degradation and radiation. It is known that the phase transformation is accelerated in aqueous environment, but little is known about how this phase transformation will occur in biological environment, particularly under dynamic loadings.

The surface degradation of the zirconia balls due to the phase transformation under loading seems to be a problem, although no significant change in mechanical strength was reported in some long-term *in vivo* and *in vitro* studies. Seriously, catastrophic failure of modular zirconia ceramics femoral head components after total hip arthroplasty was reported. Since zirconia femoral heads have a short clinical history and few clinical results are available, more investigation is required to eliminate the factors which impair the clinical stability of zirconia ceramics under loading.

2.3.2.3. Magnesia Partially Stabilised Zirconia (MgO-PSZ)

Approximately 10 years ago, magnesia partially stabilised zirconia (MgO-PSZ) was introduced on the US implant market by the BioPro Inc. MgO-PSZ was the very first zirconia approved by the Food and Drug Administration and has found wide usage in medical and dental surgery [57]. Within orthopaedics application, it is commonly used as femoral head, artificial knee, bone screws and plates. Whilst in dentistry, it is used to manufacture dental posts, crowns, brackets and inlays. MgO-PSZ ceramic represents the uncompromising first choice for optimum implant performance. The combination of high strength, toughness, and stability attainable only with the MgO-PSZ makes possible superior surface characteristics.

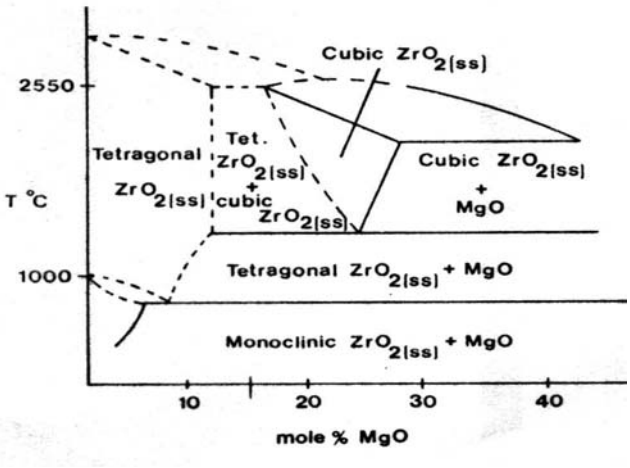

Fig. 2.2. Phase equilibrium diagram for the ZrO_2 – MgO system [58]

The phase equilibrium diagram for the ZrO_2 – MgO system [58] is shown in Fig. 2.2. There is a cubic stabilised form existing above 1400º C with MgO addition in the 15-30 mol % range. This can be quenched to room temperature, since the ZrO_2 transforms to the tetragonal form only very slowly, requiring the precipitation of MgO (Fig. 2.2). Thus one can obtain magnesia cubic stabilised zirconia. However, this material is metastable and must not be used for any length of time at temperatures below 1400º C. If the material is allowed to reach equilibrium below the critical temperature, the situation is not too desperate since the very fine MgO crystallites, 0.5-1.0 μm, are able to soften the effect of the tetragonal → monoclinic transformation by plastically deforming under the stress. Furthermore, the original cubic stabilised form can be regained by heating above 1400º C followed by rapid quenching. Because of this fortunate kinetic parameter, commercial magnesia stabilised zirconia is encountered.

MgO-PSZ belongs to the family of materials known as transformation toughened zirconia (TTZ). TTZ most commonly is formulated by alloying zirconia with stabilising oxides such as MgO, Y_2O_3, and CaO. In the TTZ family, MgO-PSZ 'ceramic alloys' are the toughest. They also have the highest surface stability when exposed to aqueous environments. Transformation toughening in zirconia results from careful manipulation of chemistry and heat treatment. The formation and retention of a metastable, tetragonal crystallographic phase provides the basis for toughening. The toughening effect arises from the preferential transformation of the tetragonal phase in the stress field of a propagating crack. The transformation to monoclinic symmetry is accompanied by a volume expansion. Resulting localised strain produces a compression 'wake' which shields the crack tip from applied tensile stress. Control of key powder characteristics is essential in attaining near zero porosity with an optimal microstructure. A proprietary sintering process yields a tailored duplex microstructure consisting of submicron tetragonal precipitates, which are coherent within a matrix of cubic grains. The resulting mechanical properties allow machining of precise tolerance

spheres with outstanding surface finish. The superior stability of the MgO-PSZ ensures high quality ceramic performance throughout the life of the product.

2.4. Surface Modification of Biomaterials

2.4.1. Introduction

Bio-integration is the ideal outcome expected of an artificial implant. This implies that the phenomena that occur at the interface between the implant and host tissues do not induce any deleterious effects such as chronic inflammatory response or formation of unusual tissues. It is, therefore, of paramount importance to design biomaterials used in implants with the best surface properties. Meanwhile, these biomaterials must process bulk properties that meet other requirements, especially mechanical properties in order to function properly in a bio-environment. As it is quite difficult to design biomaterials fulfilling both needs, a common approach is to fabricate biomaterials with adequate bulk properties followed by a special treatment to enhance the surface properties. In this way, it allows one to make ideal biomaterials with surface attributes that are decoupled from the bilk properties. Furthermore, the surface properties can be selectively modified to enhance the performance of the biomaterials. For instance, by altering the surface functionality using thin film deposition, the optimal surface, chemical, and physical properties can be attained [59]. Hence surface modification of biomaterials is becoming an increasingly popular method to improve device multifunctionality, tribological and mechanical properties, as well as biocompatibility of artificial devices while obviating the needs for large expenses and long time to develop brand new materials. It has become one of the key methods in biomaterials engineering. Usually more than one approach can satisfy the requirements of biomaterials, and the ultimate selection must take into account the process reliability, reproducibility, and products yield.

Compared to the painstaking and time consuming processes of inventing new materials, surface engineering of biomaterials can yield a more profitable return in a much shorter time. Materials can be surface modified by using biological or physicochemical methods. A few of the more widely used of physicochemical methods are briefly described here. Some of the conceptually simpler methods, such as solution coating a polymer on a substrate or metallisation by sputtering or thermal evaporation, are not elaborated upon here.

2.4.2. Radiation Grafting and Photografting [60]

Radiation is widely used in the biomaterials science for surface modification, sterilization and to improve bulk properties. The use of gamma, ultraviolet (UV) and electron beam radiation has enabled biomaterial scientist to perform bulk and surface modification that improves the biological

response of materials and subsequently, the performance of many medical devices. Radiation grafting has proven to be simple technique that enables control placement of bioactive molecules on a polymer surface. Radiation induced crosslinking has allowed the tailoring of the composition and properties of hydrogels to meet numerous biomedical applications. In addition, photocrosslinking can serve to enhance the tribological properties of load bearing components of the total artificial knee and hip. UV radiation appears to have the potential to facilitate in the situ curing of adhesives, in situ production and modification of devices, and generation of smart biomedical devices such as biochips.

2.4.3. Plasma Surface Modification of Biomaterials [61]

In the plasma surface modification process, glow discharge plasma is created by evacuating a vessel, usually quartz because of its inertness, and then refilling it with a low-pressure gas. The gas is then energised using techniques such as radiofrequency energy, microwaves, and alternating current of direct current. The energetic species in gas plasma include ions, electrons, radicals, metastables, and photons in the short-wave ultraviolet (UV) range. These energy transfers are dissipated within the solid by a variety of chemical and physical processes, to result in the surface modification. The specific advantages of plasma-deposited films (and to some extent, plasma-treated surfaces) for biomedical applications are:

- Conformal (uniform) regardless of initial surface morphology and free of voids and pinholes
- Plasma-deposited polymeric films can be placed upon almost any solid substrate, including metals, ceramics, and semiconductors.
- Exhibit good adhesion to the substrates and unique film chemistries can be produced.
- Serve as excellent barrier films because of their pinhole-free and dense, cross-linked nature.
- Plasma-deposited layers generally show low levels of leachable and chemically stable owing to their highly cross-linked nature.
- Films are easily prepared
- A mature technology for the production of these coatings
- Plasma-treated surfaces are sterile when removed from the reactor.

It would be inappropriate to cite all these advantages without also discussing some of the disadvantages of plasma deposition and treatment for surface modification. Firstly, the chemistry produced on a surface can be ill defined. Secondly, the apparatus used to produce plasma depositions can be expensive. A good laboratory-scale reactor will cost $10,000-$30,000 [3], and a production reactor can cost $100,000 or more. Third, a uniform reaction with long, narrow pores can be difficult to achieve. Finally, contamination can be a problem and care must be exercised to prevent extraneous gases and pump oils from entering the reaction zone. However, the advantages

of plasma reactions outweigh these potential disadvantages for many types of modifications that cannot be accomplished by any other method.

2.4.4. Ion Beam Processing [62]

Biomaterials modification by ion beam processing is becoming popular for improving medical device function, biocompatibility and as a new mutation breeding method. Ion-beam-base processes, such as ion implantation and ion-beam assisted deposition (IBAD) can provide beneficial surface layers with desirable properties without detrimentally affecting the bulk properties.) The ion beam method injects accelerated ions with energies ranging from $10^1$to 10^6 eV (1eV = 1.6 $\times 10^{-19}$ oules) into the surface zone of a material to alter its surface properties. It is largely, but not exclusively, used with metals and other inorganic systems. Ions formed from most of the atoms in the periodic table can be implanted, but not all provide useful modifications of the surface properties. Important potential applications for biomaterials include modification of hardness (wear), lubricity, toughness, corrosion, conductivity, and bioreaction [62].

Ion Beam Implantation Process

The primary advantage of ion implantation is selective surface modification without detrimentally affecting bulk properties. The process is also extremely controllable, reproducible and clean enough for medical devices. Because of the low substrate temperature during the ion implantation process, the product dimensions are not affected. The drawbacks of this process are high cost and the relatively shallow depth of modification. Additionally, ion implantation is a line-of-sight technique, so the uniform modification of those products with complicated geometries requires extraordinary sophisticated tooling.

Ion Beam Assisted Deposition

Ion-beam assisted deposition (IBAD) is a vacuum deposition process that combines physical vapour deposition (PVD) with ion-beam bombardment. The major feature of IBAD is bombardment with a certain energy (ranging from several hundred to several thousand eV) ion beam during the deposition of coating. IBAD is used in hydroxyapatite coating preparation, (Diamond like carbon) DLC film and C-N film and other coating. To prepare the hydroxyapatite coating on titanium (or its alloys) or alumina, IBAD is reported to be able to promote the coating/substrate adhesive strength to a much higher level than the plasma spraying method and other conventional methods. IBAD DLC films and C-N films with strong adhesive strength to the substrate had been synthesized and were proved to be biocompatible. The most attractive characteristic of IBAD is that it is able to prepare bio-coating with much higher adhesive strength to substrate comparing to a traditional coating method. Another attractive feature of the IBAD process is its superior control over coating microstructure and chemical composition. The primary

limitation to its popularisation for commercial application at present is its high cost. IBAD is reported to be able to promote the coating/substrate adhesive strength to a much higher level than the plasma spraying method and other conventional methods.

Other Ion Beam Based Processes for Biomaterials

Another ion-beam process is ion beam texturing (IBT). IBT has the ability to create desirable microfeatures and macrofeatures on the biomaterials to meet the requirement of biocompatibility *in vivo*. Ion-beam processes including plasma treatment which is based on ionised particle bombardment have been particularly successful in biomaterials modification, compared to other available surface treatment processes such as conventional coating process, nitriding, etc. This may be a result of the advantage of ion-beam process, versatility of ion species, non-equilibrium process and reliability. In general, the cost of the ion-beam process is relatively high, as it involves a vacuum chamber. However, the concerns on the life quality in many cases make the cost of the ion-beam process less problematic.

2.4.5. Other Methods [3]

Silanization

Silane reactions can be used to modify hydroxylated or amine-rich surfaces. Since glass, silicon, germanium, alumina, and quartz surfaces, as well as many metal oxide surfaces, are all rich in hydroxyl groups, silanes are particularly useful for modifying these materials. Direct evidence for surface modification on these substrates is observed by an increase in contact angles, particularly where alkyl and fluoroalkyl silanes are used. A wide range of different silanes is available, permitting different chemical functionalities to be incorporated on surfaces. The advantages of silane reactions are their simplicity and stability, which are attributed to their covalent, cross-linked structure. However, the link between a silane and a hydroxyl group is also readily subject to basic hydrolysis, and film breakdown under some conditions must be considered.

Langmuir-Blodgett Deposition

The Langmuir-Blodgett (LB) deposition method covers a surface with a highly ordered layer. Each of the molecules that assemble into this layer contains a polar head group and a nonpolar region.

Self-Assembled Monolayers

Self-assembled monolayers (SMSs) are surface coating films that spontaneously form as highly ordered structures (two-dimensional crystals) on specific.

Surface-Modifying Additives

Certain components can be added in low concentrations to a material during fabrication and will spontaneously rise to and dominate the surface.

Conversion Coating

Conversion coatings modify the surface of a metal into a dense oxide-rich layer that imparts corrosion protection, enhanced adhesivity, and sometimes lubricity to the metal.

Parylene Coating

Parylene (para-xylylene) coatings occupy a unique niche in the surface modification literature because of their frequent application and the good quality of the thin film coatings formed.

2.5. Laser Surface Modification of Biomaterials

2.5.1. Introduction

Lasers can rapidly and specifically induce surface changes in organic and inorganic. The advantages of using lasers for such modification are the precise control of the frequency of the light, the wide range of frequencies available, the high energy density, the ability to focus and raster the light, the possibilities for using both heat and specific excitation to effect change, and the ability to pulse the source and control reaction time. Treatments are pulsed (100 nanoseconds to picoseconds pulse times) and CW, with interaction times often less than 1 microsecond. Laser-induced surface alterations include annealing, etching, deposition, and polymerisation. The major considerations in designing a laser surface treatment include the absorption (coupling) between the laser energy and the material, the penetration depth of the laser energy into the material, the interfacial reflection and scattering, and heating induced by the laser.

2.5.2. Laser Patterning and Microfabrication

Laser patterning is based on the possibility of focusing an intense laser beam at certain spots on a surface, where the high beam intensity causes evaporation of the material. By this approach, pits can be produced down to ~ 1 μm, in the size range of interest to match cell sizes. By controlled motion of the beam (either by using clever optics or by sample motion), pre-designed patterns can be made. With a kinoform, it is possible to ‘laser-machine’ multiple pits in a surface at once [63].

A new method combining microphotolithographical techniques with laser excimer beam technology to create surfaces with well defined 3-D microdomains in order to delineate critical microscopic surface features governing material–cell interaction [64]. Another obvious application of this study pertains to the fabrication of cell-based biosensors. Microfabricated surfaces were obtained with micron resolution, by `microsculpturing' polymer model surfaces using a laser excimer KrF beam coupled with a microlithographic projection technique.

Most laser-based patterning techniques use UV photoablation to micromachine biological substrates, to generate mesoscopic patterns and arrays of viable cells are required to fabricate next generation tissue-based sensing devices, to build three-dimensional cellular structures for advanced tissue engineering, and to selectively separate and differentially culture micro-organisms for a variety of basic and applied research applications [65]. Recently, laser etching (or laser ablation) and microlithography have been adopted to achieve micrometer dimensions with high precision in order to develop a large number of miniaturised systems for the analysis of biological tissues. Excimer laser etching was used to microtexture a biocompatible substratum for high-contrast microscope cell analysis [66].

2.5.3. Pulsed Laser Deposition (PLD) of Biocompatible Ceramics

Pulsed laser deposition (PLD) is a new technique for the deposition of thin films of biocompatible ceramics [67]. Pulsed Laser Deposition is especially well suited to the deposition of bone-like ceramics (e.g. hydroxyapatite (HA) and calcium phosphates) onto metal, ceramic, semiconductor or polymer substrates for potential application in medical implants, prosthetic devices and biocompatible probes or sensor. Advantages of PLD for the deposition of biocompatible ceramics include the following:

- PLD is capable of depositing HA in situ in crystalline form, uncontaminated by other calciumphosphate phases.
- Simple adjustment of PLD parameters allows the deposition of amorphous films or other calcium phosphate phases, if desired.
- PLD can be conducted in both reactive and non-reactive gaseous environments, allowing control of the chemical composition of the films.
- The deposition parameters can be varied in situ to produce films of graded composition, phase, density of microstructure in order to optimise bioreactivity and resorbability.
- Adhesion of PLD-HA films exceeds the yield strength of the substrates for substrates comprising material typically used for prosthetics (e.g. Ti-6Al-4V)

The degree of control over film characteristics offered by PLD exceeds that of other known deposition techniques presently applied to production of thin films of biocompatible ceramics. It is anticipated that PLD will develop into the technique of choice for the manufacture of implant or prosthetic devices comprising biocompatible films on structurally robust substrates.

Pulsed laser ablation is a new method for deposition of thin layers of HA on to biomaterial surfaces. Differences in cell spreading were apparent which were correlated with the fluence used to deposit the HA. The optimum surface for initial attachment and spreading of osteoblasts was one of the HA films deposited using 9°J cm^{-2} laser fluence and subsequently annealed at 575°C [68]. Pulsed laser

ablation involves directing an excimer laser at a HA pellet, and creating a plume comprising a mixture of evaporated and particulate material. The evaporated material will quickly condense onto the substrate as a thin film, with macroparticles attaching onto the film surface at the same time [69]. Altering the laser fluence can control size and distribution of the macroparticles

It is possible to obtain bioactive glass thin films by PLAD even if the vaporisation is far to be congruent. The film is composed mainly of macroscopic particles directly emitted from the target and conserving the target stoichiometry. Pulsed laser ablation and deposition of bioactive glass [70,71] has been performed and the plume and film compositions have been characterised. All the elements present in the target have been found in the gaseous phase.

Plumes generated by laser ablation of HA [72] targets under diverse irradiation conditions have been analysed. Images obtained at four different laser fluences have revealed the presence of two separated emissive components in the plume for delaying times up to 1 μs after the laser pulse. The relative emission intensity between both components strongly depends on the magnitude of the fluence and so do their velocities of expansion. Spectra as recorded have shown that at low fluences, molecular species predominate over atomic ones, whereas at high fluences, atomic species are the predominant ones. Images obtained with the aid of bandpass filters have revealed that the nature of the faster emissive component in the plume is mainly atomic, whereas emission from the second one mainly arises from excited molecular radicals. Well-crystallized bioceramic HA films can be prepared by an ArF excimer laser deposition method and post deposition heat treatment [73]. The HA films on Ti, α-Al_2O_3, SiO_2/Si (100) and STO (100) substrates have a purity and crystallographic texture in the HA film.

2.5.4. Matrix-Assisted Pulsed Laser Evaporation and MAPLE Direct Write

Two techniques, Matrix-assisted pulsed-laser evaporation (MAPLE) and MAPLE direct write (MDW) were developed to deposit biomaterial thin-films [74]. MAPLE involves dissolving or suspending the biomaterial in a volatile solvent, freezing the mixture to create a solid target, and using a low fluence pulsed laser to evaporate the target for deposition of the solute inside a vacuum system. Using simple shadow masks, i.e. lines, dots and arrays, pattern features with length scales as small as 20 μm can be deposited using multiple materials on different types of substrates.

MAPLE utilises a low fluence pulsed UV laser and a frozen target consisting of a dilute mixture of the material to be deposited and a high vapour-pressure solvent. The low fluence laser pulse interacts mainly with the volatile solvent, causing it to evaporate. In the process, the solute desorbs intact, i.e. without any significant decomposition, and is then uniformly deposited on the substrate. Advantages of the MAPLE process over existing deposition techniques include:

- Allows deposition of compounds, such as biomolecules or polymers that cannot withstand the temperatures or solvents used to deposit films by other techniques.
- Deposited films are extremely smooth and uniform over large areas.
- Can use marks to prepare patterned films with feature sizes as small as ~10 μm ×10 μm.
- Solvent is removed by pumping leading to a dry process, unlike spin-coating.
- Multilayered films can be deposited without risk of dissolving the underlying layer with solvent.

MDW uses pulsed laser radiation to directly transfer material from a ribbon to a substrate. Patterns with a spatial resolution of ~10 μm can be written directly. Biomaterials ranging from polyethylene glycol to eukaryotic cells (Chinese hamster ovaries) were deposited with no measurable damage to their structures or genotype. Deposits of immobilized horseradish peroxides (an enzyme) in the form of a polymer composite with a protective coating, i.e. (polyurethane) retained their enzymatic functions. A dopamine electrochemical sensor was fabricated by MDW using a natural tissues/graphite composite.

The novelty of the MAPLE DW process is that the interaction of the incident laser pulse with the coating on the ribbon can transfer the micron-size powder, nanopowders and especially the chemical precursors to form a densely packed composite on the receiving substrate [75]. The transfer process must be extremely gentle because it is important for the low decomposition chemical precursors to transfer without reacting. In fact, the MAPLE DW process has been used to transfer whole living cells of E. Coli bacteria in patterns with the bacteria remaining viable. The combination of processing biomaterials and electronic materials by a single technique holds great potential for future sensors and interfacing to biological systems.

2.5.5. Other Laser Surface Treatments

2.5.5.1. Laser Surface Treatment for Improving Corrosion

It was found that the corrosion behaviour of NiTi samples was improved by excimer laser surface melting [76]. Laser treatment improvement resistance is explained by a combination of the homogenisation of the surface by melting, the hardening due to N incorporation and the thickening of the oxide layer. Moreover, excimer laser surface treatment in air showed a remarkable improvement in pitting corrosion resistance for 316LS bio-grade stainless steel. The results show that excimer laser surface melting can effectively eliminate carbides and second phases alike, whilst also serving the function of homogenising the microstructure. N_2 induced into the laser-treated surface could promote new precipitates and as a result lowered the corrosion resistance of 316LS stainless steel [77] and Ti-6Al-4V alloy [78]. Excimer laser surface treatment significantly increased the pitting potential of the Ti alloy, especially when the material was treated in Ar gas, while a seven-fold reduction in corrosion current was obtained when the material was treated in N_2

gas. These improvements are considered to be primarily due to the reduction of solute partitioning effect of detrimental Al segregated to the α phase.

2.5.5.2. Laser Grafting

For the purpose of improved surface hydrophilicity and biocompatibility of ethylene-propylene rubber 2-hydroxyethyle methacrylate (HEMA) and N-vinylpyrrolidone (NVP) have been grafted onto the surface of this polymer using CO_2 pulsed laser at different fluence (output power J/cm^2) as excitation source [79]. Alveolar macrophages (AMs) cultured on the surface of unmodified films showed more cell attachment with greater degree of spreading and flattening while AMs adhered onto the modified EPR appeared rounded with minimal cytoplasmic spreading and ruffling. Percentage of AMs attached to the surface of modified EPR versus graft level has also been studied. Moreover, ethylene-propylene rubber (EPR)-based vulcanizates have been surface grafted with acrylamide (AAm) and 2-hydroxyethyl methacrylate (HEMA) using CO_2-pulsed laser as excitation source [80]. Surface hydrophilicity (measured by water drop contact angle) increased for the grafted samples and comparative results indicate that the adhesion of macrophages to EPR samples modified with AAm and HEMA, with no respiratory burst and cellular damage, is significantly lower than their adhesion on unmodified surfaces which show an activated state of the attached macrophages.

2.5.5.3. Laser Treatment of Plasma Sprayed Hydroxyapatite Coating [81]

The three requirements generally expected of biomaterials coating are: crystallinity; porosity and adhesion. Crystallinity is essential because amorphous coatings are more resorbable. Porosity of the correct dimension can promote bone ingrowth for mechanical fixation. Adhesion is necessary to ensure that the coating stays intact to perform its intended function. The study found that laser treatment of plasma-sprayed coatings led to a wide range of microstructures. The porosity of the coatings was reduced significantly. Nd:YAG laser (pulsed) treatment significantly changes the characteristics of the plasma-sprayed coating microstructure in several ways. It ranges from a flat and smooth surface profile containing fine grains to an irregular surface comprising remelted particles, spherical pores and tracks.

Laser treatment of plasma-sprayed coatings basically generates a molten layer that rapidly solidifies. Lasers can perform two types of post-treatment. Firstly, an aggressive melting mode is at laser energy levels above 5 J. This is appropriated for densifying structurally porous coatings. Secondly, milder heat treatment modes at lower power induce phase transformation. This occurs without densification or melting, which often leads to porosity and cracking. Coating that are highly porous can be densified by laser treatment at higher energy, but at the expense of cracks and porosity. Coatings that have good structural integrity and adhesion but low crystallinity can be enhanced by

employing the laser at lower energy to perform only heat treatment to cause crystallisation of the amorphous structure instead of extensive melting. Operating the laser in heat-treatment mode has significant benefit to post-treatment of thermally sprayed coatings.

CHAPTER 3
Wettability in Biomaterials Science and Modification Techniques

3.1. Introduction

The wetting of a surface by a liquid and the ultimate extent of spreading of that liquid are very important aspects of practical surface chemistry. Many of the phenomenological aspects of the wetting processes have been recognised and qualified since early in the history of observation of such processes. Even with all the new information of the last 20 years, however, there still remains a great deal to learn about the mechanisms of movement of a liquid across a surface and the factors that govern such movement [13]. A more thorough understanding of the interactions and interrelationships between surfaces, interfaces, and the biological environment is required before rational prospective preparation of biomaterials from the surface chemistry viewpoint can occur.

Biomaterial scientists have long sought a single, material-related parameter that effectively measures biocompatibility and might serve as a practical design guide. The theories of surface energy and wetting for such parameters present an attractive means to do this as surface properties are important determinants of a biomaterial function [13]. The ability to control the surface wettability of solid substrates is important in many situations. Various surface processes are used for modifying the surfaces of materials depending on the actual material and the application. A number of laser-based techniques for altering the wettability characteristics of engineering materials have been investigated [14].

3.2. Wettability and Adhesion Theoretical Background

3.2.1. The Wetting Process

The term wetting in its most general sense is used to denote the displacement of air from a liquid or solid surface by water or any aqueous or molten solution [82]. When such a liquid comes into contact with a solid surface to form a solid-liquid interface, it is likely that any of the following three situations may occur:

1. The liquid could spread over the solid surface and the solid-air interface would be replaced by a solid-liquid interface. In such an instance complete wetting of the solid surface would be achieved.
2. The liquid may not spread across the solid surface at all. In this case no wetting of the solid surface by the liquid will occur.
3. The liquid could spread partially over the solid surface forming a contact angle with the surface of the solid. Here the liquid has partially wet the solid surface.

Wetting is fundamentally a thermodynamic process and the changes in free energy that may occur determine whether or not wetting will happen, at what rate it will proceed and how far it will progress against the external forces.

3.2.2. Contact Angle and Work of Adhesion

When a drop of liquid is in free space it is drawn into a spherical shape by the tensile forces of its surface tension, which results from the attractive and repulsive forces that exist between the molecules of the liquid. When such a drop of liquid is brought into contact with a flat solid surface, the final shape taken by the drop, and thus whether it will wet the surface or not, depends upon the relative magnitudes of the molecular forces that exist within the liquid (cohesive) and between the liquid and the solid (adhesive) [83]. The index of this effect is the contact angle, θ, which the liquid subtends with the solid. In practice, for wetting to occur the contact angle should be less than 90^0. If the contact angle is greater than 90^0 then the liquid does not wet the solid surface and no adhesion takes place [83]. Figure 3.1 shows a schematic view of a liquid droplet on a solid surface.

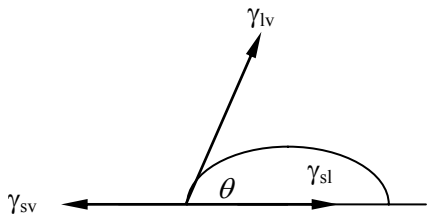

Fig. 3.1. Schematic of the wetting of a solid medium by a liquid melt [83].

The contact angle is related to the solid and liquid surface energies, γ_{sv} and γ_{lv}, and the solid-liquid interfacial energy γ_{sl}, through the principal of virtual work expressed by Young's equation:

$$\gamma_{sv} = \gamma_{lv} \cos\theta + \gamma_{sl} \tag{3.1}$$

If an equilibrium for the droplet of liquid melt shown in Fig. 3.1 is established, then the relation of θ to γ_{sv}, γ_{lv}, and γ_{sl} is described by the rearranged Young's equation:

$$\cos\theta = \frac{\gamma_{sv} - \gamma_{sl}}{\gamma_{lv}} \tag{3.2}$$

Clearly, to achieve wetting γ_{sv} should be large, while γ_{sl} and γ_{lv} should be small. Hence liquids of a lower surface tension will always spread over a solid surface of higher surface tension in order to reduce the total free energy of the system [84,85]. This is due to fact that the molecular adhesion between solid and liquid is greater than the cohesion between the molecules of the liquid [83].

Whether the drop of liquid spreads across the solid surface to wet the surface and provide a coating, or remains, as a finite drop with an equilibrium angle is dependant upon the spreading coefficient *S*. For spreading to occur spontaneously

$$S = \gamma_{lv}(\cos\theta - 1) > 0 \tag{3.3}$$

The adhesion intensity of a liquid to a solid surface is known as the work of adhesion W_{ad}, and is given by the Young-Dupre equation

$$W_{ad} = \gamma_{lv}(1 + \cos\theta) \tag{3.4}$$

Based on the nature of the attractive forces existing across the liquid-solid interface, wetting can be classified into the two broad categories of physical wetting and chemical wetting. In physical wetting the attractive energy required to wet a surface is provided by the reversible physical forces, such as the van der Waals and dispersion forces. In chemical wetting adhesion is achieved as a result of reactions occurring between the mating surfaces, giving rise to chemical bonds [86]. In either case, the driving force for wetting is the reduction of the surface free energy of the solid by the liquid (γ_{sv} - γ_{sl}). Spreading requires the additional contribution to the driving force of the free energy of the interfacial reaction [87].

3.2.3. Surface Energy and the Dispersive/Polar Characteristics

The intermolecular attraction which is responsible for surface energy, γ, results from a variety of intermolecular forces whose contribution to the total surface energy is additive [88]. The majority of these forces are functions of the particular chemical nature of a certain material, and as such the total surface energy comprises of γ^p (polar or non-dispersive interaction) and γ^d (dispersive component; since van der Waals forces are present in all systems regardless of their chemical nature). Therefore, the surface energy of any system can be described by [89]

$$\gamma = \gamma^d + \gamma^p \tag{3.5}$$

Similarly, W_{ad} can be expressed as the sum of the different intermolecular forces that act at the interface [90]:

$$W_{ad} = W_{ad}^{d} + W_{ad}^{p} = 2\left(\gamma_{sv}^{d}\gamma_{lv}^{d}\right)^{1/2} + 2\left(\gamma_{sv}^{p}\gamma_{lv}^{p}\right)^{1/2} \tag{3.6}$$

If a liquid which has both dispersive and polar forces is in contact with a solid surface where the surface energy is due to dispersion forces only, then the relationship between the contact angle and the surface energies of the liquid and solid are given by [90,91]

$$\cos\theta = \frac{2\left(\gamma_{sv}^{d}\gamma_{lv}^{d}\right)^{1/2}}{\gamma_{lv}} - 1 \tag{3.7}$$

However, by equating Equation (3.7) with Equation (3.4), the contact angle for solid-liquid systems where both dispersion forces and polar forces are present can be related to the surface energies of the respective liquid and solid by

$$\cos\theta = \frac{2\left(\gamma_{sv}^{d}\gamma_{lv}^{d}\right)^{1/2} + 2\left(\gamma_{sv}^{p}\gamma_{lv}^{p}\right)^{1/2}}{\gamma_{lv}} - 1 \tag{3.8}$$

Consequently, from Equation (3.8), one can estimate the dispersive component of a solid substrate surface energy, γ_{sv}^{d}, by plotting the graph of cos θ against $(\gamma_{lv}^{d})^{1/2}/\gamma_{lv}$. This is shown in Fig. 3.2 for a theoretical liquid system on any solid substrate.

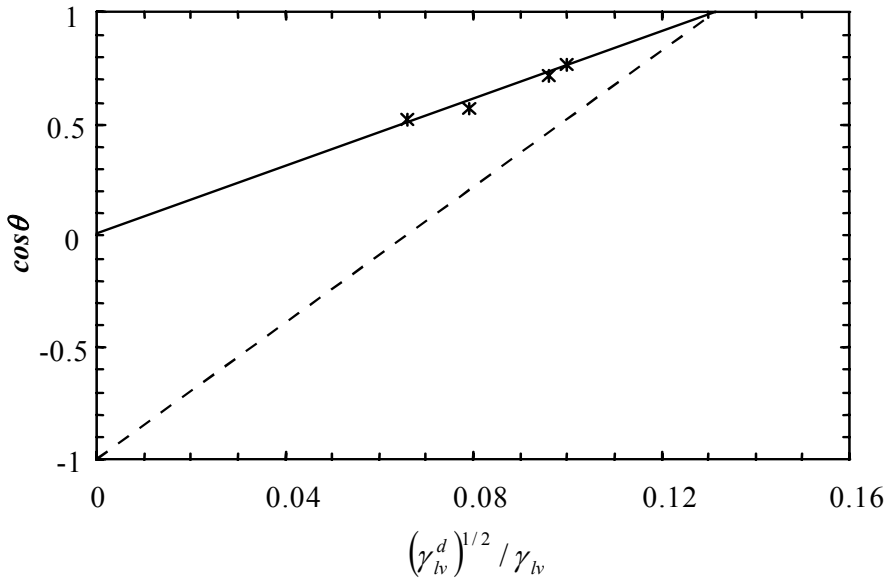

Fig. 3.2. Plot of cos θ against $\left(\gamma_{lv}^{d}\right)^{1/2}/\gamma_{lv}$ for a theoretical liquid system on any solid substrate.

Thus, according to Fowkes [89], the value of γ_{sv}^{d} is estimated by the gradient (=2 ($\left(\gamma_{sv}^{d}\right)^{1/2}$) of the line (----) which connects the origin (cos $\theta = -1$) with the intercept point of the straight line [cosθ against $\left(\gamma_{lv}^{d}\right)^{1/2} / \gamma_{lv}$](—) correlating the data point with the abscissa at cos $\theta = 1$.

In contrast, it is not possible to determine the value of the polar component of a solid substrate surface energy, γ_{sv}^{p}, directly from cos θ against $(\gamma_{lv}^{d})^{1/2}/\gamma_{lv}$. This is because the intercept of the straight line (cos θ against $(\gamma_{lv}^{d})^{1/2}/\gamma_{lv}$) is at $2\left(\gamma_{sv}^{p}\gamma_{lv}^{p}\right)^{1/2}/\gamma_{lv}$, and thus only refers to individual control liquids and not the control liquid system as a whole. However, it has been established that the entire amount of the surface energies due to dispersion forces either of the solids or the liquids are active in the wettability performance [89,92]. As such, it is possible to calculate the dispersive component of the work of adhesion, W_{ad}^{d}, by using only the relevant part of Equation (3.6) thus

$$W_{ad}^{d} = 2\left(\gamma_{sv}^{d}\gamma_{lv}^{d}\right)^{1/2} \tag{3.9}$$

If one plots a graph of W_{ad} against W_{ad}^{d} for the solid substrate, then for each particular liquid in a given system in contact with the solid surface, W_{ad}, which was determined from Equation (3.4), can often be correlated with W_{ad}^{d}, which was determined from Equation (3.9), by the straight line relationship

$$W_{ad} = aW_{ad}^{d} + b \tag{3.10}$$

Consequently, for a solid substrate the constant *a* and *b* can be deduced respectively by calculating the gradient of the best-fit straight line and by extrapolating the best-fit straight line to find the intercept point on the axis. Also, if one plots a graph of (γ_{lv}^{p}) against (γ_{lv}^{d}), then for the liquids in a given liquids system, (γ_{lv}^{p}) can often be correlated with (γ_{lv}^{d}) by the straight line relationship

$$\left(\gamma_{lv}^{p}\right)^{1/2} = c\left(\gamma_{lv}^{d}\right)^{1/2} + d \tag{3.11}$$

Again, for a solid substrate the constants *c* and *d* can be deduced respectively by calculating the gradient of the best-fit straight line and extrapolating the best-fit straight line to find the intercept point on the axis. By introducing Equation (3.10) into Equation (3.6) and rearranging, then

$$W_{ad}^{p} = (a-1)W_{ad}^{d} + b \tag{3.12}$$

or, alternatively

$$\left(\gamma_{sv}^{p}\right)^{1/2}\left(\gamma_{lv}^{p}\right)^{1/2} = (a-1)\left(\gamma_{sv}^{d}\right)^{1/2}\left(\gamma_{sv}^{p}\right)^{1/2} + \frac{b}{2} \tag{3.13}$$

By introducing Equation (3.11) into Equation (3.13) and differentiating with respect to $\left(\gamma_{lv}^{d}\right)^{1/2}$, considering that $\left(\gamma_{sv}^{d}\right)^{1/2}$ and $\left(\gamma_{lv}^{p}\right)^{1/2}$ are constant, then the following can be derived:

$$\left(\gamma_{sv}^{p}\right)^{1/2} = \frac{\left(\gamma_{sv}^{d}\right)^{1/2}(a-1)}{c} \tag{3.14}$$

Since γ_{sv}^{d} for the solid substrate can be determined previously directly from the plot of cos θ against $(\gamma_{lv}^{d})^{1/2}/\gamma_{lv}$, then it is possible to calculate γ_{sv}^{d} for the solid substrate Equation (3.14) directly.

By employing this approach it is possible to determine, from θ measurements and the control liquid surface energy properties, the changes in the wettability characteristics effected by laser treatment of a number of engineering materials in terms of surface energy [14].

3.3. The Bonding of Liquids and Solids

An essential condition for bonding is good wettability of the substrate surface by a liquid or a melt. As such, the surface tension of the liquid or melt should not be excessively high, while the substrate surface itself should be free from coarse irregularities and dirt. However, many coatings are held more firmly on a rough surface than on a completely smooth surface. In the development of the bond, the composition of the liquid or melt is of importance since it determines the surface tension and the coefficient of thermal expansion. The achievement of strong and reliable bonds between any two dissimilar materials depends on the mechanisms that come into play during the bonding process. The mechanisms for considering and promoting bonding between liquids or melts and solid substrates can be categorised generally as physical bonding, mechanical bonding, and chemical bonding. Within each of these somewhat broad categories of bonding mechanisms a number of theories exist with regard to mechanisms involved, with the category of chemical bonding providing by far the most by virtue of the vast number of possible chemical reactions that can occur between the range of dissimilar materials that can be bonded together. In practice, however, complex combinations of the various bonding mechanisms actually occur, varying according to the types of materials used. Even so, enhancement of all the mechanisms involved when preparing a material for bonding and when joining is a very important consideration in order to engineer a strong and lasting bond.

3.3.1. Physical Bonding

Physical bonding is essentially the effect that occurs when two perfectly flat surfaces are brought together to atomic interaction distances, resulting in local atomic rearrangement and consequently adhesion. A typical example of physical bonding is that of van der Waals bonding. The energy difference between the specific surface energy of one material and that of the other is the work of adhesion. The work of adhesion can yield a theoretical breaking stress similar to the strength of either of the materials used. Physical bonding provides a useful guideline to the selection of materials that will bond well together.

3.3.2. Mechanical Bonding

Mechanical bonding basically refers to the interlocking microstructure of rough surfaces to provide tensile strength and, in the case of shear, frictional strengthening. During the bonding process, the liquid or melt can flow with varying degrees of ease into cavities and asperities; a ductile metal or glass melt can conform to a rough solid substrate surface, or a vapour can deposit in surface asperities. The solid substrate surface may be roughed by means of acid or base chemical attack, grinding, grit or sand blasting, or laser treatment to enhance mechanical bonding. The effectiveness of these different surface-roughening techniques is entirely dependent upon their optimum application as well as on the specific methods and materials being used. In addition, chemical interaction between materials that are being bonded can lead to mechanical bonding. Further, the increase in the surface area of a mechanically roughened surface can affect an increase in the level of physical bonding.

The degree of mechanical bonding is often modelled on the interface ratio or undercut density. The former is the ratio of actual bonded surface to that of a flat, smooth interface and is often taken on a cross-section sample. The undercut density measures the number of re-entrant features on a cross-section per linear distance. An increase in either number usually enhances the bond.

3.3.3. Chemical Bonding

Considerable research into the various chemical mechanisms that can be present during the bonding process is in process. Although most of the research is qualitative or semi-quantitative in nature, it is providing a useful background of chemical data that is contributing to a basic understanding of the principles of chemical bonding.

A chemical bond is formed at an interface when a balance of bond energies and a continuous electronic structure are present across the interface for any two dissimilar phases. This structure occurs when a thermodynamically stable chemical equilibrium exists at the interface and is essentially achieved by chemical reactions at the interface. Generally, equilibrium compositions

(which can be determined if an equilibrium phase diagram of the two phases being bonded is available) at the interface are attained at the reaction temperature very rapidly. A chemical bond is represented by an electronic structure and a balance of bond energies across the interface whether the bonding is ionic, covalent, or metallic. These factors influence the bond microstructure. There are three main theories: the formation of intermediate oxide layer, the bonding due to oxygen bridging and the electrochemical theory.

3.4. Wettability in Biomaterial Science

From a historical perspective, Baier's proposal that critical surface energy can be directly linked to biocompatibility is perhaps the most penetrating concept among the few generalities offered to explain rules of biocompatibility. This theory, in its most general form, recognises that surface energy must control the way biologic fluids interact with materials and that this interaction, in turn, must primarily influence tissue and cell reactions. As examples, Baier pioneered the use of Zisman's critical surface tension as an indicator of blood compatibility [93,94] and bioadhesion [95,96]. Neumann *et al* employed their "equation-of-state" approach to calculate interfacial tensions from contact-angle measurements that, in turn, were used to predict cell adhesion [97] and thromboresistance [98]. Whereas concepts such as these have served as useful general guidelines or "rules of thumb" for biomaterials design, each has fallen for short of being the desired quantitative predictor of biocompatibility, particularly when applied to proteinaceous environments. Thus, the detailed physicochemical events that link surface chemistry and interfacial properties with the biological response to materials remain obscure. Tensiometric tools, which encompass a broad range of related "wetting" techniques that measure surface energy, simultaneously meet the requirements of surface sensitivity and yield results that are relevant to the hydrated physiological environment.

3.4.1. Characterisation of Biomaterial Surface

3.4.1.1. Biomaterial Interfaces [99]

Surface sensitivity is of critical importance in biomaterials surface science because only the uppermost layers are in direct physicochemical contact with the biological environment. Consequently, only the upper few molecular layers determine biocompatibility. Chemical events such as acid-base reactions, hydrogen bonding, and ion exchange occur over atomic bond-length distances. Longer-range hydrophobic forces can extend up to about 10 nm and are responsible for non-specific adsorption, adhesion, and surface-induced water structure within this zone. Surface-adsorbed proteins can have exposed regions that are specific for receptors on biological cells and

can greatly influence cell attachment, proliferation, and the response of tissue to biomaterials. Thus, the interaction of a material with the biological environment occurs at or through the narrow region termed the interface. Deeper molecular layers are effectively shielded from intimate physicochemical interaction with the liquid phase. Since these molecules are not in direct chemical contact with the external world, no primary influence on biomaterial surface properties is anticipated. Thus, the interfacial chemistry of concern to biomaterial scientists is determined by material composition within the upper nanometre or so.

3.4.1.2. Tensiometry

Tensiometry encompasses a broad range of related "wetting" techniques that measure surface energy. These include the observation of contact angles, which is perhaps the most familiar and widely applied method. Tensiometric methods have singular potential in biomaterials surface science based on the criteria of surface sensitivity, kind of analytical information obtained, and relevance of that information to biomedical problems. First, with respect to surface sensitivity, wetting measurements are sensitive only to the upper 0.5 nm or so of a surface [100,101] and are therefore among the most surface-sensitive techniques available. Second, tensiometry directly measures the fundamental energy at an interface that drives important processes such as adsorption and adhesion. This kind of information must be particularly pertinent to biomaterial problems because of the overwhelming importance of protein adsorption and cell/tissue adhesion. Third, wetting measurements can be made using proteinaceous saline solutions that are particularly relevant to biomedical applications. Special high-vacuum preparation techniques that might introduce experimental artefacts are not required.

3.4.2. Interfacial Biophysics

The physicochemical nature of biomaterial interfaces was considered, leading to the conclusion that interfacial energy is a primary determinant of biocompatibility. A colloid science theory that quantified interactions at small distances and has biomaterial applications is the so-called Derjaguim Landau Verwey Overbek (DLVO) theory [102,103], shown in the Fig. 3.3. DLVO illustrates the relationship between particle (cell) distance from the surface and repulsive (electrostatic) and attractive (namely, van der Waals) interaction energies. The basis of this theory is that attractive van der Waals potentials and repulsive electrostatic forces are additive. Formulation of these interaction potentials can be quite detailed for each case, but the qualitative predictive aspects for a macroscopic substrate are quite straightforward. From a physicochemical point of view, the kinetics of adhesion can be described as long-range interactions [89] and short-range interactions (acid-base, hydrogen bonds) [104]. Others describe these forces as dispersive and polar [105].

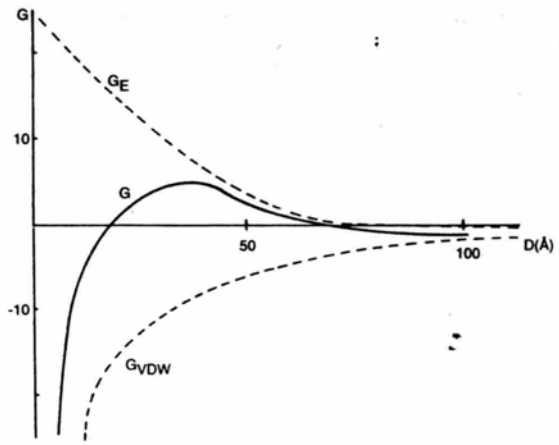

Fig. 3.3. Interaction energies between a particle (cell) approaching a solid surface [3]

The total interaction energy (G, solid line) is composed of attractive van der Waals forces (G_{VDW}) and repulsive electrostatic forces (G_E). A secondary minimum can be observed at approximately 100 Å and a primary minimum at a distance <5 Å. An energy barrier can be observed at approximately 40 Å from the surface.

$$G = G_E + G_{VDW} \tag{3.15}$$

Where D is the distance of the particle from the solid surface and G is the sum of energy forces involved in Equation (3.15); G_{VDW} is $-H.a/6D$, which represents the van der Waals interaction between a particle with a radium a and a distance D to a flat substratum; H is the Hamaker constant; and G_E *(:)* $Z_1 \cdot Z_2$ is the electrostatic interaction between a particle and a solid plate, in which Z_1 and Z_2 are the zeta potentials of the particle and the solid substratum.

Long-range interaction forces probably result in bringing a particle into the secondary minimum at approximately 100 Å from the surface, but only a little energy is needed to remove the particle from the surface again. Short-range interactions between a particle and a solid can only take place at distances <20 Å. The adhesive macromolecules in cellular membranes, however, might be able to cross the energy barrier, which is necessary to reach this primary minimum, and establish acid-base or hydrogen bond interactions with the solid substratum. The energy barrier is high for low-surface free-energy substrates (e.g. polytetrafluoroethyleen) and low or absent for high-surface free-energy substrates (e.g. glass). Particles in the secondary minimum could, theoretically, freely move over the substrate without consumption of energy, however, the adhesion would be weak compared with metabolic energy or the forces of active cellular locomotion.

3.4.3. Surface Thermodynamics: A Modelling Tool

An important conceptual tool in modelling is surface thermodynamics. A principal utility of thermodynamics is the ability to handle multicomponent systems in a phenomenological manner. One way that thermodynamics accomplishes this is by lumping a number of microscopic properties into a single, measurable parameter by the judicious assignment of a macroscopic thermodynamic property. A particular example of this that will be discussed subsequently is the assignment of an average wetting property for a biological cell. Quite clearly, biological cells are not hard spheres of uniform material but, in fact, have a nonuniform topography that is patchwise heterogeneous and studded with macromolecules exhibiting very specific biochemical properties. These ultrastructural aspects of cell membranes are assigned an average impact on the macroscopic wetting parameter in the thermodynamic model. Specific cell/substrate interactions that are known to occur between ligands and receptors are included in the overall "affinity" of the cell for substrate, but not separated from non-specific forces that cells encounter at interfaces.

3.4.3.1. Factors of Cell Adhesion and Spreading [3]

Surface hydrophobicity, or wettability is an important determinant of cell adhesion. It is related to surface free energy and is typically evaluated by water contact angle. Smaller water contact angles correspond to more hydrophilic surfaces and higher surface free energies. In general, more hydrophilic substrates support cell adhesion and spreading to a greater extent than hydrophobic materials which have low surface free energies. Substratum surface free energy is related to cell spreading, as illustrated in Fig. 3.4.

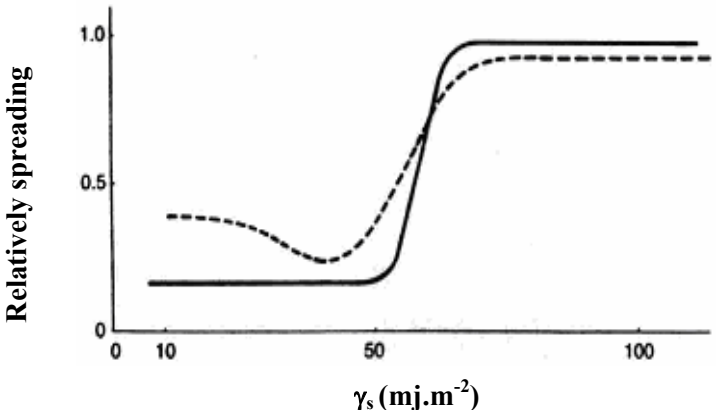

(Dotted line and solid line represents cell spreading in the absence of proteins and presence of proteins respectively)

Fig. 3.4. Cell spreading as a function of substratum surface free energy (γ_s, wettability) [106].

Poor spreading on hydrophobic substrata and good spreading on hydrophilic substrata can be observed in both the absence and presence of preadsorbed serum proteins. Specifically, work with

wettability gradient surfaces has shown that protein adsorption occurs to a greater extent on hydrophobic substrata than on hydrophilic substrata, that exchange of a preadsorbed protein by another protein occurs more readily on hydrophilic substrata than on hydrophobic substrates, that adsorption-induced conformational changes are greater on hydrophobic substrates than on hydrophilic substrates, and that cell adhesion reaches a maximum on moderately hydrophilic substrates which have a contact angles around 60 degrees. Conformation and biological activities of adsorbed adhesion proteins such a fibronectin (FN) and vitronectin (VN) have been studied in relation to substrate chemical and physical properties.

Apparently the substratum characteristics shine through the adsorbed proteins toward adhering and spreading cells. An explanation for this phenomenon can be:

1. Cell can reach the underlying substratum by pseudopodia protruding through the preadsorbed protein layer.
2. Cell consumes preadsorbed protein to make direct contact.
3. The substratum characteristics are reflected in the composition and conformation of adsorbed proteins, thus presenting different molecular groups to adhering and spreading cells.

Other parameters involved in cell adhesion are surface charge, surface topography, porosity and texture. Some workers report that negatively charged cells adhere with smaller contact areas to surfaces with higher negative charge. Others report increased adhesion between negative cells and negatively charged substrata [3]. The surface topography of a biomaterial can be classified according to roughness, texture, and porosity. However, the scale of surface roughness must be kept in mind. Roughness at the level of cell adhesion (1 μm) is different from roughness at the level of protein adsorption (50 nm). Porosity is used on a large scale to promote anchorage of biomaterials to surrounding tissue. Von Recum's group described an optimal biocompatibility using pore sizes of 1-2 μm. Smaller pore sizes caused poor adhesion and increased inflammatory response with little collagen formation. Larger pore sizes did allow ingrowth and anchorage, but caused a more severe foreign body reaction [107]. Mechanical forces around an implant, especially in combination with a rough surface, induce abundant formation of fibrous tissue, owing to the constant irritation of the cells. Firm fixation of an implant will reduce movement and thus prevent excessive fibrous tissue formation. The texture of an implant surface and its morphology can be adapted to the clinical purpose of the biomaterial by such approaches as changing the fabrication process (e.g. woven, knitted, fibrous, grooved, veloured, smooth).

3.4.3.2. Thermodynamic Aspects of Cell Adhesion and Spreading

Thermodynamically, the process of adhesion and spreading of cells from a liquid suspension onto a solid substrate can be described by Equation (3.10) [105]:

$$\Delta F_{adh} = \gamma_{cs} - \gamma_{cl} - \gamma_{sl} \tag{3.16}$$

in which ΔF_{adh} is the interfacial free energy of adhesion, γ_{cs} is the cell-solid interfacial free energy, γ_{cl} is the cell-liquid interfacial free energy and γ_{sl} is the solid-liquid interfacial free energy. If $\Delta F_{adh} < 0$, adhesion and spreading are energetically favourable, while if $\Delta F_{adh} > 0$, adhesion and spreading are unfavourable**.** Fig. 3.5 illustrates the relationship between ΔF_{adh} and substratum surface free energy (or wettability). It should be noted that hydrophobic substrata ($\gamma_s < 40$ erg.cm^{-2}) do not promote adhesion of fibroblasts. Extremely hydrophilic substrata do not promote adhesion either (e.g. high-energy methacrylates or hydrogels).

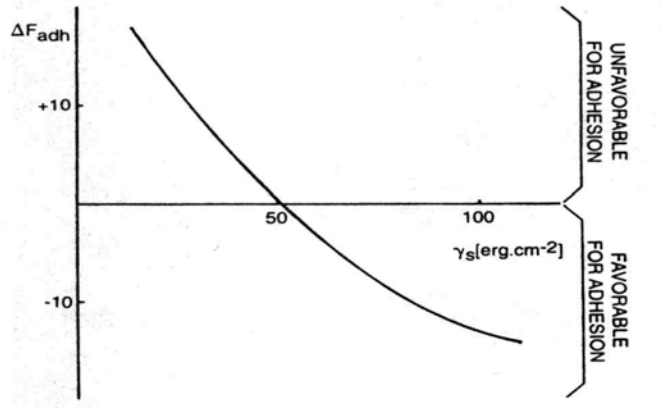

Fig. 3.5. Interfacial free energy of adhesion (ΔF_{adh}) as a function of substratum surface free energy (γ_s)[105].

Only adhesion can be described in a thermodynamic way; cell spreading, a completely different phenomenon, cannot be described in a similar way. Cellular activity such as the production of adhesive proteins and cytoskeleton transport are involved in cell spreading, interfering with thermodynamic model. Duval *et al* [108] have clearly demonstrated on a series of substrata that adhesion and spreading are indeed two separate phenomena. For example, the strength of adhesion to a substratum is not correlated with the area of contact (spreading). A cell spread on Teflon will weakly adhere and is easily removed, while a cell attached to glass for example, with one cellular extension will strongly adhere and cannot be easily removed. The type of adhesion site is crucial in this regard.

3.5. Current Methods of Wettability Modification

3.5.1. Introduction

Various methods are used to improve the surface wettability of materials and their adhesion to other materials. In the biomedical field, surface hydrophilicity, hydrophobicity and wettability are important determinants of cell adhesion and biocompatibility. Hydrophilicity is a characteristic of materials exhibiting an affinity for water. Hydrophilic literally means 'water-loving' and such materials readily adsorb water. The surface chemistry allows these materials to be wetted forming a water film or coating on their surface. Hydrophilic materials also possess a high surface tension value and have the ability to form 'hydrogen-bonds' with water. Hydrophobic describes materials possessing characteristic that have the opposite response to water interaction compared to hydrophilic materials. Hydrophobic materials ('water hating') have little or no tendency to adsorb water and water tends to 'bead' on their surfaces (i.e. discrete droplets). Hydrophobic materials possess low surface tension values and lack active groups in their surface chemistry for formation of hydrogen-bonds with water. It is related to surface free energy and is typically evaluated by water contact angle. Smaller water contact angles correspond to more hydrophilic surfaces and higher surface free energies. Therefore, the modification of the wettability of biomaterials, surface can control the adhesion of cell for improved biocompatibility.

3.5.2. Chemical Reaction

Chemical reaction can be used to leave the functional groups and change the hydrophobic or hydrophilic behaviour of materials' surface. Chemical reactions were used to attach various hydrophilic functional groups and one hydrophobic group to cross-linked polystyrene resins. These with hydrophilic groups had much better wettability by water [109].

Technically established treatments to modify the surface of silicone produced by plasma discharge and following hydrogel coating yield to a less hydrophobic surface [110,111]. The wettability measurements of Si (111) surfaces treated in aqueous HF and H_2SiF_6 solutions indicated that the HF-etched surface is hydrophobic (θ~70°), while the H_2SiF_6- treated surface is, if anything, hydrophilic (θ~55°). The Si-O-F groups detected on the H_2SiF_6-treated surface may be one of the causes for the hydrophilicity. The chain length effects of chemical modification with various normal alcohols on the wettability of silica have been studied [112]. The modifications were carried out by chemical reaction of alcohol molecules with surface silanols. The wettability of samples with modifiers of carbon number above eight markedly changes at the modification ratio of about 20%. In reactive wetting of liquid metals on ceramic substrates [113], it turns out that the volume change of ceramic substrates during reaction plays a key role in the effect of chemical reaction on wetting. If the volume of ceramic substrate decreases after reaction, the wettability is not improved by the

chemical reaction. This is the case of liquid Al wetting on SiO_2. If the volume of ceramic substrate increases after reaction, the wettability is improved by the chemical reaction. This is the case of liquid Ti wetting on Al_2O_3. The titanium dioxide chemical modification experiments resulted in an alteration of interfacial potential at pH 7.4, as well as in a marked change of wettability [114]. Peroxide treatment rendered the titanium dioxide more hydrophilic, whereas butanol treatment resulted in a more hydrophobic surface when compared to untreated control samples. The oxidation with peroxide also alters the surface chemistry of titanium dioxide.

3.5.3. Plasma Surface Modification

Plasma treatment can produce the extremes of both highly wettable and highly non-wettable (or hydrophobic) surfaces. It is possible to create hydrophobic (non-wetting) surfaces with the proper choice of gas and plasma conditions. Plasma surface modification can be used to tailor surface energies. Hydrophilic and hydrophobic surfaces can be created on polymers through interaction with gas plasma. Using oxygen to create hydroxyl functionality will increase the wettability of the surface. This has been used to enhance the performance of a catheter by the creation of a wettable surface on the polymer tubing. In a similar way, surfaces can be specifically engineered to modify protein binding and improve blood compatibility.

Most plasma cleaning operations will result in a surface that is more wettable (hydrophilic) than the starting surface. For polymers this is due to the formation of more polar functional groups created by chemical reactions within the plasma. For other materials, (glass, ceramics, metals) a more wettable surface results primarily because oily surface residues are removed. The increasement of the surface wettability is mainly due to the grafting onto the NH_3 plasma-treated PP films of nitrogen and oxygen polar groups [115]. The oxygen uptake of the surface by the ammonia plasma treatment may be due to the excitation of the residual oxygen present in the reactor or form post-oxidation of the free radicals created on the surface by plasma-surface interactions. The treatment of composite materials [116] by means of a cold plasma allows both the increase of their surface wetting properties and the improvement of their mechanical strength in terms of adhesion between fibres and matrix. The polymer superficial tension can be increased 4-5 times, corresponding to a strongly increase in wettability.

3.5.4. Ion Beam Processing

Ion-beam-based processes, such as ion implantation and ion-beam assisted deposition (IBAD) can provide beneficial surface layers with desirable properties without detrimentally affecting the bulk properties. Chemical functionality, surface texture, wettability and adhesion enhancement of polymer materials have been achieved by ion irradiation techniques. Many extensive studies have been reported regarding improving wettability of polymers and adhesion of metal/polymer and

adhesive/polymer by ion beam modification with a few megaelectron volts and a few hundred kiloelectron volts of energy.

3.5.4.1. Ion Beam Implantation Process

Wettability of organic materials was changed by ion implantation [111]. Doping effects can be obtained on electrical conductivity and wettability, induced by high dose metal implantation. Metal ion implantation in polymers form metal-doped amorphous carbon that can be called new diamond-like carbon. To date, ion implantation has been successfully applied in metal and polymer biomaterials. In metal biomaterials, physical procedures such as atomic and nuclear collisions often lead to the formation of highly disordered and sometimes amorphous structure in the near-surface region. For the polymer substrate, there are two major competing processes: chain cross-linking and chain scission, the cross-linked process creates a three-dimensionally cross-linked process creates a three-dimensionally cross-linked surface layer with much higher hardness and much improved wear resistance. That is to produce a specific functional chemical group at the surface of the polymer to improve the surface wettability, anticalcific behaviour and biocompatibility of biomaterials. Ion implantation succeeds in improving wettability, anticogulability, anticalcific behaviour of polyurethane, and critical surface tension of silicon rubber which is thought to be a primary cause for the biofouling.

3.5.4.2. Ion Assisted Reaction (IAR)

A new surface modification technique**,** ion assisted reaction (IAR) [117,118] has been developed for improving wettability of materials and enhancing adhesion to other materials. The contact angles of water drops with modified polymers were reduced more by Ar^+ ion irradiation with a flowing oxygen gas environment than without flowing oxygen gas. The hydrophilic groups were formed on the surface of polymers by chemical reaction between the unstable chains induced by ion irradiation and the oxygen gas, and the hydrophilic groups were identified as ⁻(C--O)⁻, ⁻(C=O)⁻ and ⁻(C=O)--O⁻ bonds. The enhanced adhesion between metal and modified polymers was explained by the formation of electron acceptor groups in polymer and electron donors in metal. It was found that the improved wettability of polymer surface by the IAR is greatly dependent not on change of surface morphology but on formation or increment of hydrophilic groups such as carbonyl and/or carboxyl on the polymer surface. The IAR method is also suitable process for industrial application because a large area treatment is available and time required to treatment is relatively short.

3.5.5. Radiation Grafting

Radiation grafting can be used for instance, for introducing polar groups in the bulk or on the surface of non-polar polymers, for increasing or reducing the wettability of a polymer, for

imparting a better compatibility of a polymer to a specific coating and the like. Radiation grafting and related methods have been widely used for the surface modification of biomaterials, and comprehensive review articles are available. Within this category, these types of reactions can be distinguished: grafting using ionising radiation sources (most commonly, a cobalt-60 gamma radiation source), grafting using UV radiation (photografting), and grafting using high-energy electron beams. In all cases, similar processes occur. The radiation breaks chemical bonds in the material to be grafted, forming free radicals, peroxides, or other reactive species. These reactive surface groups are then exposed to a monomer. The monomer reacts with the free radicals at the surface and propagates at a free radical chain reaction, incorporating other monomers into a surface-grafted polymer. Acrylamide (AAM), 2-hydroxyethylmethacrylate (HEMA), and N-vinylpyrrolidone (NVP) have been grafted to the surface of four vulcanizated ethylene-propylene rubbers using the simultaneous radiation method [119]. Various conditions, including differing monomer concentrations and additives, have been used. The treated rubbers have been characterised by measuring water uptake, hardness and water contact angle. In addition, some initial biocompatibility trials have been conducted, using cell attachment and growth as criteria.

A copolymer of polyethylene–polypropylene (PP/EPR) was irradiated using alpha particles under three different atmospheres [120]. It was possible to ascertain that the chemical modifications produced differ according to the atmosphere during irradiation. Indeed, it has been determined that, along with chemical modifications generated from the surface of the irradiated copolymer, an increase in its surface free energy results in greater wettability to certain liquids, such as water, formamide and diiodomethane. The drastic increase observed for the variation of total surface free energy versus alpha influence is very near form the total surface free energy obtained after the classic flaming treatment.

3.5.6. UV and Ozone

An ultraviolet (UV) -ozone oxidation process [121] is shown to be an effective adhesion pre-treatment for polyethylene (PE) and polyetheretherketone (PEEK). The data obtained indicate that the treatment gives considerable oxidation and improved wettability for PE and PEEK surface types. It produces changes in surface oxygen chemistry and free energy which improves surface polarity and wetting.

Exposing polypropylene (PP) to ozone in the presence of UV light [122] is a simple and effective way of modifying its surface to improve its wettability and adhesion. Atomic force microscopy (AFM) showed a dramatic change in the morphology and a clear increase in the adhesion force resulting from the modification of a PP film by UV/ozone exposure. A relationship has been demonstrated between a change in surface energy (measured by wetting contact angle) and the adhesion force. Exposing a polypropylene film to UV light and ozone resulted in the formation of

low-molecular-weight-oxided-materials. Also, an increase in surface energy, which is the reason for the improvement of wettability and adhesion performance of polymer, was deduced from the free-distance curve measurement. Increasing the treatment time showed an increase of surface energy and formation of droplets, which are considered, to be the aggregation of short oxidised polymer chains formed during the oxidation process. UV surface modification studies were performed in laboratory [123] using an excimer UV lamp to place oxygenated functional groups (CO, COOH and OH) on the surfaces of expanded polytetrefluoroethylene (e-PTFE). After irradiation the surface analysis indicated a reduction of fluorine groups, increases in oxygen groups, and surface wettability.

Poly (ether sulfone) and sulfonated poly (sulfone) nanofiltration membranes were modified by UV irradiation and UV-assisted graft polymerisation [124] of N-vinyl-2-pyrrolidinone (NVP) as a strategy for mitigating fouling by naturally-occurring organic compounds (NOM) found in surface waters. Exposure to UV (254 nm) alone increased membrane hydrophilicity, interpreted in terms of either θ, or surface wettability ($\cos \theta$). It was possible to increase $\cos \theta$ above 0.94. Fourier transform infrared spectrometer (FTIR) analysis suggests that this was due, in part, to the formation of surface hydroxyl groups.

3.5.7. Corona Discharge

The corona discharge is a commonly used procedure to modify surfaces of materials such as metals, glass or plastics. It is generally accepted that this treatment modifies the substrate polymer surface properties like wettability and adhesion. Jin *et al* [125] developed a method for preparing a wettability gradient on polymer surfaces using corona discharge treatment. The gradient was produced by treating the polymer sheets with the corona from a knife-type electrode whose power was changed gradually along the sample length. The polymer surfaces oxidised gradually with increasing corona power and the wettability gradient was created on the sample surfaces. One advantage of the corona discharge is that it can be initiated under atmospheric pressure. However, the corona discharge is characterised by a non-uniform field discharge and is conveniently generated in a pin-to-plane gap with its highly divergent field region adjacent to the pin.

The decrease in the contact angles (and thus the increase in wettability) along the sample length may be due to the oxygen-based polar functionalities incorporated on the surface by the corona discharge treatment. The oxygen-based functional groups produced on the PE surface increased gradually with the increase in corona power. Corona treatment has been use to modify the wettability of wood [126]. Results show that the higher the corona voltage and the longer the treatment, the higher the increase in wettability. It can also be used to decrease wettability in order to waterproof wood.

3.5.8. Electrowetting

The wettability of poly (ethylene terephthalate) (PET) films by water and aqueous solutions is increased by applying a voltage between the water and a rear electrode placed under the polymer film [127]. This electrowetting effect can decrease contact angles by more than 30° under applied voltages of 200 V_{eff}. The electrowetting effect can help the solutions to wet the solid surface.

3.6. Laser Wettability Characteristics Modification

At present, the processes available to engineers for the modification of a material's wettability characteristics are invariably complex and consequently somewhat difficult to control. Lasers, on the other hand, can offer the user not only an exceedingly high degree of process controllability, but also a great deal of process flexibility. There is a growing amount of published work that testifies to the potential of lasers for altering the surface properties of materials in order to improve their wettability characteristics. Laser radiation was found to effect significant changes in the wettability characteristics of materials.

3.6.1. Laser Surface Modification of Ceramic Materials for Improved Wettability

At present, very little published work exists regarding the effects of laser radiation on the wettability characteristics of ceramics materials. Indeed, the published work is predominantly concerned with the use of excimer laser radiation. Kappel [128] has shown that the texturing of ceramics (with an excimer laser 248 nm) can improve the adhesion strength by up to 20 %. Such an improvement is said to be due to the formation of raised microscopic protrusions over the surface.

The wettability characteristics of the selected ceramic materials: the ceramic tile (SiO_2/ Al_2O_3 – based); the clay quarry tile (SiO_2/Al_2O_3/Fe_2O_3-based); Al_2O_3 and SiO_2-TiO_2 (crystalline) were improved after HPDL treatment [129-131]. The changes in surface roughness, surface oxygen content and surface energy resulted in the enhancement of the wettability characteristics. Recently, Lawrence [132] conducted work on ceramics and metals to isolate each of these mechanisms, which permitted the magnitude of their influence to be qualitatively determined. Also, for ordinary Portland cement (OPC), surface energy, by way of microstructural changes, was seen to influence a change in the wettability characteristics, whilst surface roughness was found to play a minor role in inducing changes in the wettability characteristics.

3.6.2. Laser Surface Modification of Metallic Materials for Improved Wettability

It is recognised within the currently published work that laser irradiation of material surfaces can affect their wettability characteristics. Previously Heitz *et al* [133], Henari and Blau [134], and

Olfert *et al* [135] have found that excimer laser treatment of metals results in improved coating adhesion. The improvements in adhesion were attributed to the fact that the excimer laser treatment resulted in a smoother surface and as such enhanced the action of wetting. It was demonstrated by using contact angles that five pulses per area of CO_2 laser treatment was sufficient to produce a fully wettable surface [136]. The experimental results of CO_2 laser treatment to mild steel illustrates that the initial contact angle on the degreased-only surface was approximately 70º with a contact angle of 0º being obtained after more than 15 pulsed in each area of the raster. In addition, the investigation shows that the wettability will be influence by the surface exposing time (SET) after laser treatment. A contact angle of approximately 10º after a SET of only 1 min, indicating a degree of organic contamination after this limited time. Self-fluxing Fe-Cr-Ni-B-Si alloy powders with various Ni contents were laser clad on medium carbon steel substrates [137]. The wettability increases with increasing Ni content in the cladding alloy. Good wettability of the cladding alloy on the substrate has a beneficial effect on crack prevention in the cladding layer, because it reduces the formation of pores in the cladding layer, such pores usually being where stress concentrates and cracking initiates.

Lawrence and Li [138] compare the interaction of CO_2, Nd:YAG, HPDL, and excimer laser radiation with the surface of the mild steel studied was found to effect changes in the wettability characteristics of the material. It was observed that interaction of the mild steel with Nd:YAG and HPDL radiation brought about an improvement in the wettability characteristics of the steel. In contrast, interaction of the mild steel with CO_2 and excimer laser radiation resulted in a depreciation of the wettability characteristics of the steel. Such changes were identified as being primarily due to: (i) the generation of a smoother surface after Nd:YAG and HPDL treatment due to optimum surface melting and resolidification; (ii) the surface roughness of the mild steel increasing after interaction with CO_2, and excimer laser radiation due to excess surface melting and ablation respectively; (iii) changes in the surface oxygen content of the mild steel-increasing after interaction with CO_2, Nd:YAG, and HPDL radiation due to surface melting, and decreased after interaction with the excimer laser due to the creation of defective energy levels; and (iv) increases in γ_{sv}^{p} resulting from the melting and resolidification of the mild steel surface which thus created a different microstructure that quite possibly improved the action of wetting and adhesion [139]. However, it was found that changes in the wettability characteristics of the mild steel appeared to be predominantly influenced by the surface roughness, while the microstructure appeared to have very little effect on the mild steel's wetting properties. Additionally, surface oxygen content is also thought to play a minor role. The analysis of the mild steels revealed that surface roughness was the primary influential factor governing changes in θ and hence the wettability characteristics. Surface energy, by way of microstructural changes, was shown to influence to a lesser extent changes in the

wettability characteristics, whilst surface oxygen content, by way of process gas, was found to play a minor role in inducing changes in the wettability characteristics of the mild steels.

3.6.3. Laser Surface Modification of Polymer Materials for Improved Wettability

In general, polymer materials possess poor adhesion characteristics. Consequently it is very difficult to wet, and therefore bond, almost all polymer materials to adhesives without modifying their surface in order to improve their wettability characteristics. Much research has been carried out to study the effects of excimer laser radiation on the wettability characteristics of polymers.

Pulsed excimer lasers [140] are appropriate for the surface treatment of thermally sensitive materials, such as organic. Modifications induced on polyethylene terephthalate (PET) and other polymers surfaces in film [133], fibre [141], and sheet form [142] as well as polyparaphenylene terephthalamide (PPTA) [143] by UV lasers have been extensively studied. For the adhesive properties, chemical surface modifications inducing an improved surface wettability is related to the formation of polar and reactive chemical groups on the treated surfaces. For 193 or 248 nm wavelengths excimer laser, the lower the fluence, the higher the hydrophilicity. This is related to the lower surface oxidation at higher fluence as observed at 248 nm in air.

Laurens *et al* [144,145] concluded that a more polar surface resulted from the excimer laser treatment of polyetheretherketone (PEEK). Furthermore, these workers found that the choice of laser wavelength have a crucial influence on the resultant wettability characteristics of the PEEK.

Furthermore, comprehensive and detailed investigations by Song and Netravali [146-148] into the effects of excimer laser radiation on the interfacial characteristics of UHSPE fibres and epoxy resin revealed a considerable increase in the interfacial shear strength was attributed to the increase in surface roughness, the increase in surface oxygen content, and the increased polar nature of the fibres after excimer laser treatment. Excimer laser was also used to create morphological heterogeneities based on the surface modification of thin films of biocompatible polymer blends [149] by irradiation with an excimer laser. The UV-pulsed laser treatment of the blends is expected to induce local changes in the chemical composition and roughness of the polymer surface, depending on the way the two polymers adsorb the radiation at the near surface. It can be shown that polymer blends of polycarbonate (PC) and PMMA can be specifically patterned by excimer laser irradiation. The appearance of periodic structures around the affected areas is also reported. Both wetting and adhesion properties are enhanced by this kind of surface structure.

Surface treatment of the low-density polyethylene (LDPE) films [150] by the CO_2 laser pulsed caused a significant laser-induced oxidation onto the exposed film surfaces. The intensity of the polar groups increased with increasing the number of pulses up to two and then slightly decreased at three laser pulses. This was also confirmed with the contact angle measurements in which the

sample subjected to two laser pulses showed the highest wettability i.e. the lowest waster drop contact angle.

Lawrence [14,151] compared the interaction of CO_2, Nd:YAG, HPDL and excimer laser radiation with the surface of polyethylene (PE) and PMMA sheet. It was found to effect varying degrees of change to the wettability characteristics of the materials. It was observed that interaction of the PE and PMMA with CO_2, Nd:YAG and HPDL radiation resulted in very little change in the wettability characteristics of the materials. On the other hand, interaction of the PE and PMMA with excimer laser radiation occasioned a marked improvement in the wettability characteristics of the materials. Such changes after excimer laser treatment were identified as being primarily due to the increase in the surface oxygen content of the PE and the increase in γ_{sv}^{P}. These occurrences are believed to be the result of photo-oxidation on the PE and PMMA surfaces which, in turn, is assumed to result of photo-oxidation on the PE and PMMA surfaces which, in turn, is assumed to result in the generation of some surface oxygen containing polar functional groups, thus effecting the observed changes in the wettability characteristics of the PE and PMMA after excimer laser treatment. This study showed that under the chosen experimental laser operating parameters, changes in the wettability characteristics of the PE and PMMA were seen to vary somewhat depending upon the laser type. In particular, whether the laser radiation had the propensity to cause surface melting or ablation. As such, the influence of pulse width cannot be discounted.

3.6.4. Laser Treatment of Polymer for Improved Biocompatibility

Dadsetan *et al* [152] studied the cell behaviour of L929 fibroblasts on the laser irradiated PET surface. To modify the surface properties of the PET, CO_2 pulsed laser at the wavelength of 9.25 μm and KrF excimer laser at 248 nm with various number of pulses were used. Laser irradiation caused some changes in the chemical and physical properties of the laser-treated film surfaces, which were evaluated using different techniques. These changes may affect the cell adhesion and growth on the laser-treated PET. Therefore, cell attachment and spreading were investigated on the laser-treated PET *in vitro*. The data from *in vitro* assays showed the fibroblast cells were attached and proliferated extensively on the CO_2 and KrF laser-treated films in comparison with the unmodified PET. The results obtained from the cell behaviour studies revealed that surface morphology and wettability affected cell adhesion and spreading on the laser-treated PET.

CHAPTER 4
Bioactivity and Biointegration of Orthopaedic and Dental Implants

4.1. Introduction

Events leading to integration of an implant into bone, which in turn determine the performance of the device, take place largely at the tissue-implant interface. Development of this interface is complex and involves numerous factors. In addition to mechanical adaptation, implanted systems also have to match their physical-chemical and biological properties to those of their environment. The main requirements for a biomaterial to function properly in an osseous site include a good biocompatibility favouring bone apposition, adequate mechanical properties and the ability to assure skeletal functions, [153-155]. Thus, bioactivity and biointegration are the two essential aspects of these interactions. Bioactivity and the maintenance of skeletal functions are usually attributed to the ability to induce an apatite layer on materials surface in physiological conditions [6-8]. The close apposition between bone and an implant surface, or osseointegration, presented as the ability to promote bone cells anchorage, attachment, spreading, growth and differentiation [9,10], is another key factor for successful implantation of a biomaterial for dental and orthopaedic applications [153-155]. However, the relative importance of each of these two events is yet to be elucidated. It is widely accepted that surface chemistry and morphology exert a significant influence over these two events. Recent years have seen considerable interest in the systematic investigation of the relationship between surface chemistry [156,157] and morphology [158] and biological interfacial reactions. Ultimately, such studies may lead to an enhanced understanding of the surface chemical cues that guide the combination of apatite induction ability with attachment, growth and differentiation of bone cells and to the design of improved synthetic materials for dental and orthopaedic applications.

4.2. Bioactivity of Bone Implants

For an artificial material to bond to living bone, it is essential that the material has the ability to form a biologically active, bonelike, apatite layer on its surface in the human body. Under normal conditions, the body fluid is already supersaturated with respect to apatite, and once apatite on its

nuclei from on the surface of a material, they can spontaneously grow by consuming the calcium and phosphate ions from the body fluid. The nucleation of apatite on the surface of a material is induced by the functional groups on its surface. When some components are released from the material into the body fluid, thereby increasing the ionic activity product of apatite, they can accelerate apatite formation. Naturally, the development of bioactive materials that have improved and ultimately bone-like mechanical properties is desirable [159].

4.2.1. The Mechanism of Apatite Formation

The biological activity of most orthopaedic and dental biomaterials is related to their ability to promote the formation of a neoformed layer of carbonate apatite crystals analogous to bone mineral, this layer also associates specific bone proteins and is the starting point of bone reconstruction [160]. Orthopaedic biomaterials may be classified as “passive” or “active” with regard to their propensity to simply allow the nucleation and growth of carbonate apatite crystals from body fluids (hydroapatite, titanium oxide, neutral hydrogels, collagen), or to supply ions to build and develop this layer (bioglasses, alkaline hydroxides, Ca-P compounds, calcium carbonate). Although “active” biomaterials may appear to be more efficient immediately after implantation, their capacity to regenerate the carbonate apatite layer again and again after successive turn-over or remodelling phases seems limited. On the contrary nucleating materials can keep their properties as long as their surface remains intact,

The properties of neoformed layers are frequently compared to those of bone mineral. However, depending on the conditions of formation, the neoformed layer can be quite different. In addition its physical-chemical characteristics may evolve with time. Biological activity may be favoured in several ways, mineral ions (Sr, V, Mg, Zn) or growth factors associated with the material can enhance cell activity and multiplication, This activity is however difficult to control and appears always time dependent.

Bioactivity can be induced on surfaces of non-bioactive materials either by the formation of the functional groups that are able to induce apatite formation, or forming thin ceramic phases that have the potential to form the functional groups on exposure to a body environment [159]. Bioactive ceramics have a common characteristic at the interface with bone after integration. In fact, bioactive ceramics, including bioglass and hydroxyapatite (HA), reveal a layer of apatite at the interface, mediating integration with bone. Histological examination *in vivo* shows that this apatite layer is formed on the ceramic surface early in the implantation period and thereafter the bone matrix integrates into the apatite. Detailed characterisation indicated that this apatite layer consists of nano-crystals of carbonate-ion-containing apatite that has a defective structure and low crystallinity. These features are, in fact, very similar to those of the mineral phase in bone; hence bone-producing cells, (osteoblasts) can preferentially proliferate on the apatite, and differentiate to form an

extracellular matrix composed of biological apatite and collagen. As a result, the surrounding bone comes into direct contact with the surface apatite layer. When this process occurs, a chemical bond is formed between the bone mineral and the surface apatite to decrease the interfacial energy between them. It can be concluded that an essential requirement for an artificial material to bond to living bone is the formation of a layer of biologically active bone-like apatite on its surface in the body.

4.2.2. Functional Group

The catalytic effect of the Si-OH groups and Ti-OH groups for apatite nucleation has been proven from the observation that silica and titania gels produced by the sol-gel method form apatite on their surfaces in SBF, and these functional groups are abundant on their surfaces. Zirconia, niobium oxide, and tantalum oxide gels have also been shown to from apatite on their surface in simulated body fluids (SBF), as shown in Fig. 4.1. This indicates that Zr-OH, Nb-OH and Ta-PH groups are effective for apatite nucleation. Other assessments using self-assembled monolayers (SAM) in SBF have indicated that COOH and PO_4H_2 groups are also effective for apatite nucleation [159]. These groups have specific structures revealing negatively charge, and induce apatite formation *via* formations of an amorphous calcium compound, e.g. calcium silicate, calcium titanate, and amorphous calcium phosphate. Moreover, the efficacy of apatite nucleation of the above functional groups is determined, not by their composition alone, but in a complicated fashion that is dependent on their concentration and structural arrangement.

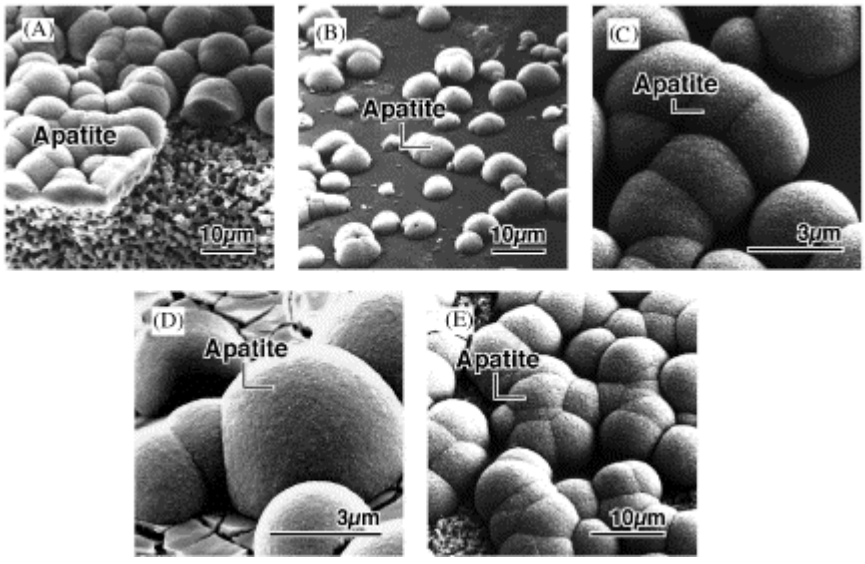

Fig. 4.1. SEM photographs of the surfaces of silica (A), titania (B), zirconia (C), niobium oxide (D), and tantalum oxide (E) gels after soaking in an SBF for 14 d [159].

4.2.3. Apatite Formation on Zirconia

Uchida *et al* [161] found that bonelike apatite formed on zirconia gel which was prepared by the hydrolysis and polycondensation of zirconium alkoxide in a SBF with ion concentrations almost equal to those in human blood plasma, in the modified SBF with higher pH values and higher concentrations of calcium and phosphate ions. Apatite formation is accelerated by increases in pH and in the concentration of calcium and phosphate ions, which is explained by an increase in the ionic activity product of the apatite in the SBF. The results suggested that zirconia ceramics might exhibit a bone-bonding ability by forming an apatite layer on their surfaces in the living body when they are modified to have many Zr-OH groups on their surfaces. Moreover, they revealed that apatite formation on zirconia gels depended on structure [162]. The experimental results showed that zirconia gel with an amorphous structure formed only a small amount of apatite on its surface even after 14 days of immersion in SBF, whereas gels with tetragonal or monoclinic structures formed quite a large amount of apatite on their surface after 3 days of immersion, and their surfaces were fully covered with apatite within 14 days of immersion. It indicated that tetragonal or monoclinic zirconia is effective in inducing apatite nucleation.

When a nano-composite of a ceria-stabilized tetragonal zirconia polycrystals (Ce-TZP) and alumina (Al_2O_3) polycrystals was subjected to chemical treatment with aqueous solutions of H_3PO_4, H_2SO_4, HCl, or NaOH at 95°C for 4 days, it formed Zr-OH surface functional groups on its surface and as a result formed apatite in SBF [163]. This type of bioactive Ce-TZP/Al_2O_3 composite is therefore expected to be useful as a bone substitute, even under load-bearing conditions.

An apatite also could form on zirconium metal surface in SBF after previous treatment with NaOH solutions with concentration above 5 M [164]. The apatite nucleation is induced by Zr-OH groups in a zirconia hydrogel layer, which forms on the metal exposure to NaOH solution.

4.3. Biointegration of Orthopaedic and Dental Implants

4.3.1. Osseointegration

Integration of the implant into the bone is a property of paramount importance in the proper functioning of the implant. Consequently, extensive studies have been carried out using different techniques to improve osseointegration. Osseointegration was defined by Branemark [165] as: A direct structural and functional connection between living bone and the surface of a load-carrying implant". The integration of a biomaterial to bone involves essentially two processes: interlocking with bone tissue and chemical interactions with bone constituents. It is essential for the efficacy of orthopaedic or dental implants to establish a mechanically solid interface with complete fusion between the material's surface and the bone tissue with no fibrous tissue interface.

The direct bonding of orthopaedic biomaterials with collagen is rarely considered, however several non-collagenic proteins have been shown to adhere to biomaterial surfaces. The direct apposition of bone mineral on biomaterial surfaces, especially those considered as bioactive, is well documented. There is thus a continuity of crystal lattice between bone mineral and apatite biomaterials. With other biomaterials a mismatch between the adjacent atomic planes will always exist, but other events such as intermediate layers, and multiple interactions must be considered [160]. The host response to implants placed in bone involves a series of cell and matrix event, ideally culminating in intimate apposition of bone to biomaterial (osseointegration). Bone cell culture models are increasingly employed to study bone-biomaterial interactions. Most of the cultures have utilized osteoblastic cells [166]. It is widely acknowledged that a major determinant of the bone-biomaterial interfacial response is the initial attachment, spreading, and growth of osteoblasts on the implant surface and that improvements in these processes may lead to faster and long-term stability [153,167] has been possible to demonstrate cellular attachment to implant surfaces, there is good evidence for new bone formation being initiated at a distance from but towards the surface of an implant rather than on the surface itself [153,167].

Cell adhesion is involved in various natural phenomena such as embryogenesis, maintenance of tissue structure, wound healing, immune response, metastasis as well as tissue integration of biomaterial. The biocompatibility of biomaterials is very closely related to cell behaviour on contact with them and particularly to cell adhesion to their surface. Surface characteristics of materials, whether their topography, chemistry or surface energy, play an essential part in osteoblast adhesion on biomaterials. Thus attachment, adhesion and spreading belong to the first phase of cell/material interactions and the quality of this first phase will influence the cell's capacity to proliferate and to differentiate itself on contact with the implant. The following part reviews bone cell adhesion and methods being investigated for controlling bone-implant interface.

4.3.2. Description of Bone Cell Adhesion [11]

The term ‘adhesion’ in the biomaterial domain covers different phenomena: the attachment phase which occurs rapidly and involves short-term events like physicochemical linkages between cells and materials involving ionic forces, van der Waals forces, etc. and the adhesion phase occurring in the longer term and involving various biological molecules: extracellular matrix proteins, cell membrane proteins, and cytoskeleton proteins which interact together to induce signal transduction, promoting the action of transcription factors and consequently regulating gene expression. Those various proteins involved in cell adhesion will be described in this first part.

4.3.2.1. Proteins Involved in Osteoblast Cell Adhesion

Extracellular matrix proteins

The extracellular matrix of bone is composed of 90% collagenic proteins (type I collagen 97% and type V collagen 3%) and of 10% non-collagenic proteins (NCP) (osteocalcin 20%, osteonectin 20%, bone sialoproteins 12%, proteoglycans 10%, osteopontin, fibronectin, growth factors, bone morphogenetic proteins, etc.). All these proteins are synthesized by osteoblasts and most are involved in adhesion. *In vitro*, other proteins such as fibronectin or vitronectin have been shown to be involved in *in vitro* osteoblast adhesion. Some other proteins with a plasmatic origin are also associated with mineralised bone matrix but their role in osteoblast adhesion is not fully defined (a2HS glycoprotein, albumin, immunoglobulin, transferrin, etc.) [168]. Some of the bone proteins have chemotactic or adhesive properties, notably because they contain an Arg-Gly-Asp (RGD) sequence which is specific to the fixation of cell membrane receptors like integrin (fibronectin, osteopontin, bone sialoprotein, thrombospondin, type I collagen, vitronectin) [168].

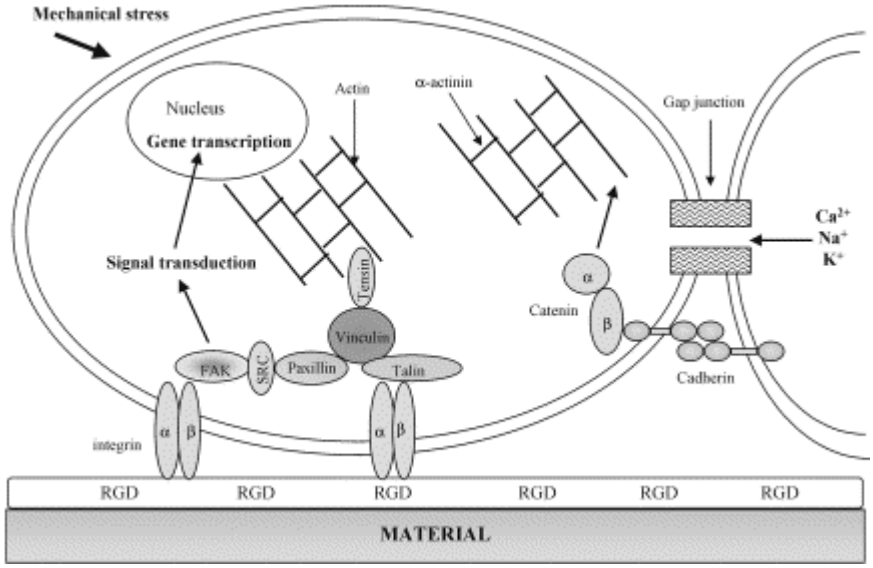

Fig. 4.2. Representation of the cell proteins involved in cell adhesion on biomaterial [11]

Cytoskeleton proteins

The sites of adhesion between tissue cultured cells and substrate surfaces are called focal contacts or adhesion plaques. Focal contacts are closed junctions where the distance between the substrate surface and the cell membrane is between 10-15 nm. This type of junction is rare *in vivo* except for endothelial cells in vessels with high hydrodynamic stress. They also appear to be analogous to sarcolemnal dense plaques of smooth muscle cells *in vivo*. The external faces of focal contacts present specific receptor proteins such as integrins. On the internal face, some proteins like talin, paxillin, vinculin, tensin are known mediating interactions between actin filaments and membrane

receptor proteins (integrins) (Fig. 4.2). Many proteins colocalize with vinculin and talin in the adhesion plaque: integrin, cytoskeletal proteins, proteases, protein kinases and phosphatases, signalling molecules, etc. These proteins are involved in signal transduction. The formation of focal contacts occurs essentially in cells with low motility and is promoted *in vitro* by extracellular matrix proteins like fibronectin or vitronectin. The architecture of the actin cytoskeleton is essential to the maintenance of cell shape and cell adhesion. If assembled in long bundles, F-actin supports finger-like protrusions of the plasma membrane known as filopodia; if assembled in the form of a mesh, it supports sheet-like protrusions known as lamellipodia. If present in bundles coupled with adhesion plaques, actin 'stress fibres' may transmit forces to the substrate [169].

Adhesion molecules

Adhesion molecules are characterized by their capacity to interact with a specific ligand. These ligands may be situated on the membrane of neighbouring cells or may be extracellular matrix proteins. Adhesion molecules belong to different families. The four main classes are selectins, immunoglobulin superfamily, cadherins and integrins.

4.3.2.2. Adhesion and Cell Migration [11]

Cell migration requires a dynamic interaction between the cell, its substrate and its cytoskeleton. Firstly, cells develop a protrusion of their leading edge to form a lamellipodium. Secondly, after formation and fixation of the lamellipodium, cells use adhesive interactions to generate the traction and energies required for cell movement. The last step of the migratory cycle is the release of adhesions at the rear of the cell followed by its detachment and retraction. Integrin have been shown to be involved in cell migration. In general, cells with a low motility form strong focal adhesions while motile cells form less adhesive structures. An intermediate level of attachment force induces a maximal migration rate. Some antiadhesive extracellular matrix proteins play a role in cell migration: tenascin, thrombospondin, laminin, muscin, proteoglycans. Migration tests on biomaterials with surface grooves demonstrated that cell migration was faster on materials with deeper grooves.

4.3.3. Osteoblast/Material Interactions

Osteoblast/material interaction depends on the surface aspects of materials which may be described according to their topography, chemistry or surface energy. These surface characteristics determine how biological molecules will adsorb to the surface and more particularly determine the orientation of adsorbed molecules [170]. They also determine the cell behaviour on contact. As previously shown, cells in contact with a surface will firstly attach, adhere and spread. This first phase depends

on previously described adhesion proteins. Thereafter, the quality of this adhesion will influence their morphology, and their capacity for proliferation and differentiation.

4.3.3.1. Morphological Aspects of Osteoblast on Biomaterials

It is known that osteoblast cell initially respond in a differential manner to material surface. The comparison of the behaviour of different cell types on materials shows that they react differently according to surface roughness [157,171]. Scanning electron microscopic examination of bone cells on materials with various surface roughness generally demonstrated that cell spreading and continuous cell layer formation was better on smooth surfaces compared to rough surfaces [168,172,173].

However, higher levels of cellular attachment have been found on rough surfaces of titanium with irregular morphologies [174-176] *in vitro*. Similarly, recent studies have shown that alkaline phosphatase specific activity is enhanced on rough Ti and Ti-6Al-4V [177,178]. Other markers of osteoblast phenotype were also found to increase on Ti or Ti alloy (osteocalcin production) [177,178]. Cells grown on rougher surfaces exhibited increased production of collagen [175,177], prostaglandin E_2 [177] and transforming growth factor β [177]. Synthesis of extracellular matrix and subsequently mineralization *in vitro* were both substantially enhanced on rough textured and porous coated titanium [179]. These differences of cell response could be attributed to either the microstructure, crystalline or chemistry, since different methods were used to get different roughness. Moreover, a complete description of the description of the surface topography (amplitude and frequency roughness parameters) of electro-eroded Ti-6Al-4V surface or pure titanium showed that the main influential characteristics of these surfaces may be their isotropic aspect and the smooth aspect of the relief due to surface fusion during the process. When the topographic is considered below the cell scale, cells appreciated their smooth surface although when the topography is considered above the cell scale, they appreciate a rough isotropic landscape formed by the numerous ‘bone-like nests’ that favour their adhesion [180].

The contact guidance phenomenon has also been described on osteoblastic cells. On smooth surfaces, bone cells were randomly oriented although they were aligned parallel to the direction of the grooves in an end-to-end fashion in 5 lm-deep grooves. In contrast, they “ignored” the surface topography on an 0.5 lm grooved surface [181]. Cells are able to discriminate among subtle differences in surface roughness. Osteoblast-like cells can discriminate not only between surfaces of different roughness but also between surfaces with comparable roughness but different topographies [175]. In a recent work, the adhesion of human osteoblasts on Ti-6Al-4V substrates with five different degrees of surface roughness was studied. Cell adhesion was correlated with roughness parameters and in particular with parameters describing the organization of the surface roughness. More so than the roughness amplitude evaluated by R_a or R_t, the developed surface or

Delta parameter describing the surface organization was the more influential parameters on human osteoblastic cell adhesion to orthopaedic alloys [182].

4.3.3.2. The Effect of Surface Chemistry on Osteoblast Adhesion on Biomaterials

Osteoblast attachment is affected by chemistry of biomaterial's surface. However, a conclusive picture has not yet emerged. Early *in vitro* cytocompatibility studies focused on the morphological aspect, growth capacity and the state of differentiation of cells on materials with various chemical compositions. The diversity of cell responses to the different materials tested highlighted the capacity of cells to distinguish the effects of subtle changes in substratum surface chemistry. For primary bovine osteoblasts, the wettability of the surface has been shown to be one of the important factors [183]. On the other hand, the functional groups present on the surface have been demonstrated to be even greater importance than the wettability for the adhesion of MC3T3-E1 osteoblasts [184]. The morphological aspect of neonate rat calvarial osteoblasts cultured on a positively or negatively charged polymer substrata was significantly different. Cell flattened out so closely onto the positively charged substrata that the ventral cell membrane was not distinguishable through the transmission electron microscope. On negatively charged substrata, the ventral cell membrane was readily visible with only focal contacts with the substrata [185]. Bone calvarial cells randomly plated on materials with patterned surface chemistry rapidly ($t < 30$ min) organized on positive charged regions in the presence of serum. After 30 min, cells started to align and spread exclusively on these regions. By day 2, cells started to extend from positive charged regions to negative charged regions due to lack of surface area available and were confluent after 4 days [157]. Analysis of focal contacts using specific labelling of actin and vinculin showed their presence only on electropolished and etched titanium surfaces but not on sandblasted ones [186].

4.4. Controlling the Bone-Implant Interface

Different approaches are being used in an effort to obtain the desired bone-implant interface. The ideal implant should present a surface conducive to or that will induce osseointegration, regardless of implantation site, bone quantity, bone quality, etc. As Kasemo and Lausmaa [187], among others, have described, biological tissues interact with mainly the outermost atomic layers of an implant. Although secondary and other by-product reactions will occur, the 'primary interaction zone' is generally about 0.1-1 nm. Consequently, much effort is being devoted to methods of modifying surfaces of existing biomaterials to achieve desired biological responses. The approaches can be classified as physicochemical and biochemical methods.

4.4.1. Physicochemical Methods

4.4.1.1. Wettability Modification

Wettability characteristics are among the physicochemical characteristics that have been altered with the aim of improving the bone-implant interface [9]. Glow discharge has been used to increase surface free energy in order to increase tissue adhesion. Polymer surfaces were modified by glow discharge to study the effect of surface treatment on cell adhesion using polyethylene, polytetrefluoroethylene, poly(ethylene terephthalate), polystyrene, and polypropylene films. The surface wettability of all the films, evaluated by the water contact angle, decreased with respect to the length of plasma treatment. For each of the polymers, a different dependence of cell adhesion on the length of plasma treatment was observed, but, in each case, the optimal water contact angle for cell adhesion was approximately 70° [188]. An experiment has been conducted involving the implantation of rats with sterilized disc-shaped quenched ethylene-tetrafluorethylenes (ETFEq), treated with oxygen and oxygen/acrylic acid plasma to modify the surfaces. Experimental results show that modification of surface chemical properties, wettability/surface tension and surface microstructure of fluoropolymers influence inflammatory cell adhesion *in vivo* and *in vitro* [189].

It has found that as the surface wettability increased, the increase in the number of the cell adhered and proliferated surface was found on the Poly (3-hydroxybutyrate-co-3-hydroxyvalerate) (PHBV) treated by chloric acid mixture solution treatment [190]. A graded oxidation process, involving UV-ozone (UVO) treatment, was used to create a poly (ε -caprolactone) (PCL) surface with a systematic variation in surface chemistry. It correlates with contact angle data and the results of the binding studies performed with mouse calvarial cells, showing that UVO treatment resulted in a PCL surface with improved wettability and cellular adhesion [191].

Polyethylene (PE) was irradiated with 15 keV O^+, P^+ and Ar^+ ions to the fluences from 3×10^{12} to 1×10^{15} cm^{-2}. In comparison with pristine PE (i) higher cell adhesion is observed on implanted PE and (ii) the cells cultivated on implanted PE are larger and their adherence is significantly more homogeneous. Highest cell adhesion was observed on PE implanted to the fluence of 1×10^{13} cm^{-2} regardless of the ion specie. It was shown that the cell adhesion is related to the wettability of the PE surface and that there exists an optimal wettability with respect to the cell adhesion.[192].

Attempts have been made to evaluate the changes in physical and chemical properties of the polyethylene terephthalate (PET) surface due to laser irradiation [193]. Both the CO_2 and KrF laser irradiation created a complicated microstructure on the PET surface accompanied by changes in surface chemistry and wettability. The results obtained from *in vitro* studies showed that the CO_2 laser-treated PET supported a larger number of more spread and flattened cells compared with unmodified PET. The degree of cell spreading was correlated with the change wettability of the KrF laser-treated PET. It seems likely that in the case of KrF laser, wettability is main parameter

affecting cell spreading, whereas both surface morphology and wettability are important in cell attachment and spreading on the CO_2 laser-treated PET.

4.4.1.2. Morphological Methods

Alterations in surface morphology and roughness have been used to influence cell and tissue responses to implants [9]. Porous coatings were developed with the rationale that, because of mechanical interlocking, bone ingrowth would increase fixation and stability of the implant. Data from retrieval studies of orthopaedic implants, however, indicate that only a relatively small portion of the available pore volume is filled with bone. In addition to providing mechanical interlocking, surfaces with grooves can induce 'contact guidance', whereby the direction of cell movement is affected by the morphology of the substrate. This phenomenon has applications in preventing epithelial down-growth on dental implants and directing bone formation along particular regions of an implant. Mineral deposits in bone cell cultures can also be altered by surfaces with pits and grooves.

When chick calvarial cells were cultured on titanium disks roughened by blasting or plasma spraying, collagenous matrix biosynthesis, alkaline phosphatase (ALP) activity, and mineral formation were elevated [179]. For osteoblast-like cloned mouse cells (MC3T3-E1) cultured on titanium plates roughened by wire-type electric discharge machining or plasma coating, proliferation and ALP activity were enhanced on the roughened surfaces [194]. Osteoblast adhesion on nanophase alumina (Al_2O_3) and titania (TiO_2) investigated *in vitro* revealed that in the presence of 10% fetal bovine serum in osteoblast adhesion on nanophase alumina (23nm grain size) and titania (32nm grain size) was significantly greater than on conventional alumina (177 nm size) and titania grain size. The explanation for the observed increase in osteoblast adhesion with decreasing alumina and titania grain size could be directly related to the greater surface area exhibited by the nanomaterial formulations. Furthermore, it implied that nanophase ceramics may promote interactions (such as adsorption, configuration, bioactivity, etc), of select serum protein(s), which, subsequently, enhance osteoblast adhesion [195]. Moreover, compared to conventional ceramics, osteoblast (the bone-forming cells) adhesion increased while fibroblast (cells that contribute to fibrous encapsulation and callus formation events which may lead to implant loosening and failure) adhesion decreased on all nanophase ceramics (alumina, titania, hydroxyapatite) tested. Nanometer grain-size topography is the nanoceramic material properties that not only promote increased select adsorption of vitronectin (a protein that mediates osteoblast adhesion) but also effect conformation(s) that enhanced subsequent osteoblast functions [196].

4.4.1.3. Surface Charge and Coating

Considering the role of electrostatic interactions in many biological events, charged surfaces have been proposed as being conducive to tissue integration. Calcium phosphate coatings have been extensively investigated because of their chemical similarity to bone mineral [9]. Two different glass layers (AP40 and RKKP) were coated to the zirconia substrates for the aim of combine the mechanical properties of zirconia and bioactivity of the glass. The osteoblast-like cells cultured on RKKP- and AP40-coated zirconia showed a higher proliferation rate, leading to confluent cultures with higher cell density and a generally better expression of osteoblast alkaline phosphatase activity in comparison with zirconia substrate [197]. Each approach, however, has drawbacks. Contradictory results with charged materials in bone have been reported; indeed both positively and negatively charged surfaces were observed to promote bone formation. Although short-term clinical results have been encouraging, dissolution of coatings as well as cracking and their separation from metallic substrates remain concerns [9].

4.4.2. Biochemical Methods [9]

Biochemical methods of surface modification offer an alternative or adjunct to physicochemical and morphological methods. Biochemical surface modification endeavours to utilize current understanding of the biology and biochemistry of cellular function and differentiation. Much has been learned about the mechanisms by which cells adhere to substrates, and major advances have been made in understanding the role of biomolecules in regulating differentiation and remodelling of cells and tissues, respectively. The goal of biochemical surface modification is to immobilize proteins, enzymes, or peptides on biomaterials for the purpose of inducing specific cell and tissue responses or, in other words, to control the tissue-implant interface with molecules delivered directly to the interface.

One approach to controlling cell-biomaterial interactions utilizes cell adhesion molecules. Since identification of the RGD sequence as mediating attachment of cells to several plasma and extracellular matrix proteins, including fibronectin, vitronectin, type I collagen, osteopontin, and bone sialoprotein, researchers have been depositing RGD-containing peptides on biomaterials to promote cell attachment. Cell surface receptors in the integrin super-family recognize the RGD sequence and mediate attachment. Because of redundancy in the affinity of integrins for adhesive proteins and because a variety of cells possess the same integrins, non-specific attachment of cells to RGD modified surfaces is a concern. Some groups are attempting to circumvent this problem by using longer peptides, having a particular conformation, rather than short tetra-, penta-, or hexa-peptides. Others are examining non-RGD peptides that may be more specific for bone cells. Furthermore, a combination of immobilized peptide and soluble growth factor(s) might be needed

to elicit specific responses. Presently, more studies are needed to develop surfaces, modified with cell attachment peptides, that are selective for only osteoblastic cells.

A second approach to biochemical surface modification uses biomolecules having demonstrated osteotropic effects. A great amount of information has been obtained about biomolecules involved in bone development and fracture healing. Many growth factors have been cloned and are recombinantly expressed. They have effects ranging from mitogenicity (e.g. IGF-I, FGF-2, and PDGF-BB) to increasing activity of bone cells (e.g. TGF- b1 enhances collagen synthesis) to osteoinduction (e.g. BMPs). By delivering one or more of these molecules, which normally play essential roles in osteogenesis, directly to the tissue-implant interface, bone formation may be promoted. Two considerations about delivering biomolecules to the tissue-implant interface are: (1) local cell populations must interact with the biomolecules for a period of time to initiate cellular events and (2) concentrations of biomolecules must exceed threshold levels for cellular activity. But, data regarding the duration of exposure or concentration needed for optimal activity of osteotropic biomolecules are lacking.

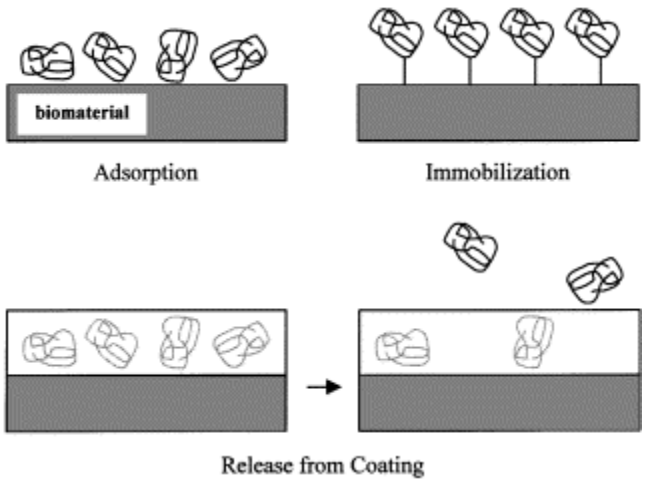

Fig. 4.3. Schematic illustration of methods for controlling retention and/or release of biomolecules at the tissue–implant interface [9].

To control exposure and concentration, retention and/or release of biomolecules from implant surfaces can be altered using different methods, including adsorption, covalent immobilization, and release from coatings (Fig. 4.3). The simplest way to deliver biomolecules to the tissue–implant interface is by dipping the device in a solution of protein before inserting it. Studies using simple adsorption indicate that delivery of TGF-β to the tissue–implant interface can improve bone formation in the periprosthetic gap and can enhance bone ingrowth into porous coatings [198]. Using a similar approach, alkaline phosphatase adsorbed on titanium implants enhanced periprosthetic bone formation [199]. One drawback with the adsorption method, however, is that it

provides little control over the delivery, including release/retention and orientation, of molecules. Proteins are initially retained on the surface by weak physisorption forces, then, depending on the implant microenvironment which varies between anatomical sites and between patients, they desorb from the surface in an uncontrolled manner to initiate desired responses. Considering the necessity of specific receptor-ligand interactions for activity of many relevant biomolecules, appropriate presentation of protein may also be needed. Although positive responses have been observed using this simple approach, there is no indication they are optimal for clinical applications.

Bonding biomolecules to implants is an alternate way of delivering them to the tissue–implant interface, albeit protein will not be released. This approach is more complicated than adsorption, because of the chemistry involved, but the activity of molecules immobilised on plastics has been shown to equal or exceed that of soluble protein [200]. For orthopaedic and dental applications, metal surfaces possess a relative paucity of functional groups needed for immobilizing molecules. The passivating oxide film on these materials does, however, have surface hydroxyl groups that provide locations for bonding using silane chemistry. This approach has been used to immobilise peptides, enzymes, and adhesive proteins on different biomaterials, including Co–Cr–Mo, Ti–6Al–4V, Ti, and NiTi [9].

CHAPTER 5
The General Effects of CO_2 Laser Radiation on Magnesia Partially Stabilised Zirconia

This chapter describes and presents the results of the experimental work that was conducted in order to establish a controllable and flexible surface process for MgO-PSZ bioceramics using a CO_2 laser. The general changes on the MgO-PSZ surface were analysed after CO_2 laser treatment. The mechanisms of crack and crater formation were discussed and the phase transformations brought about with various CO_2 laser power densities were investigated.

5.1. Introduction

The interactions between the biological environment and biomaterials take place on the materials surface. It is, therefore, of paramount importance to fabricate biomaterials with adequate bulk properties followed by a special treatment to enhance the surface properties [59]. Since the applied energy of lasers can be placed precisely on a surface only where it is needed, lasers provide the contemporary scientist and engineer with a controllable and flexible tool for surface engineering. On account of the rapid and specific modification of organic and inorganic materials, laser surface processing has aroused growing interest and has been proven to be suitable technique for modifying the surface properties of biomaterials. Its application includes laser micropatterning [63], pulsed laser deposition of biocompatible ceramics [68,70,71], improving surface corrosion of bio-metals [76-78] and treating plasma sprayed hydroxyapatite coating [81]. However, the laser has not hitherto been applied to modify directly the surface properties of the bioinert bioceramics.

5.2. Experimental Procedures

5.2.1. Material Specifications

The material investigated was a 4% MgO-PSZ obtained in sheet form with dimensions of 50 × 50 × 2.15 mm^3 (Goodfellow, Ltd). For experimental purposes, it was cut into blocks of 50 × 12 × 2.15

mm^3 with a diamond rimmed blade cutter and used as received prior to laser treatment. The properties of the MgO-PSZ are detailed in Appendix A.

5.2.2. CO_2 Laser Experimental Arrangement

A 3 kW CO_2 emitting with a wavelength of 10.6 μm was used in this study. The laser produced a transverse electromagnetic multimode (TEM_{01}) beam and was operated in the continuous wave (CW) mode. Fig. 5.1 illustrates the full arrangement with a 5-axis workstation (Trumpf, Ltd). As one can see, a series of optical units were used to deliver the CO_2 laser beam to the workpiece through the laser head, which was positioned by means of 2 linear axes (y- and z-axis) and 2 rotary axes (b- and c-axis).

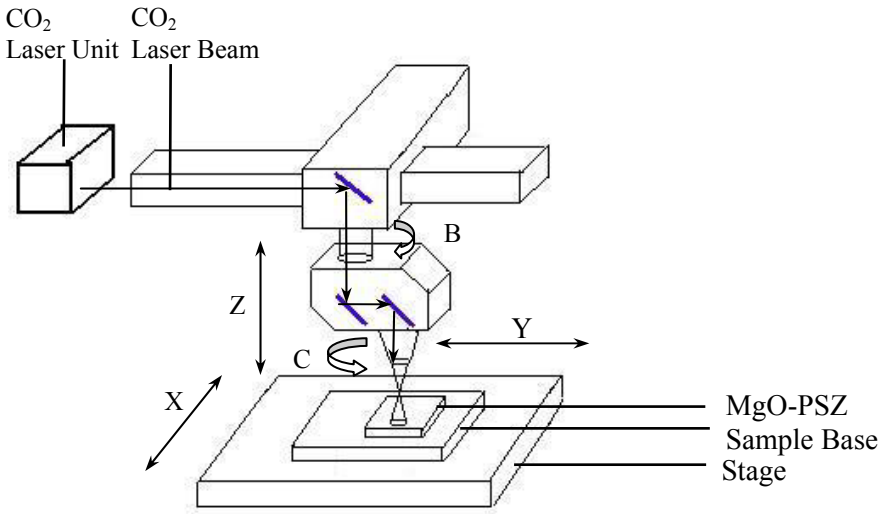

Fig. 5.1. Schematic diagram of the set-up for the CO_2 laser treatment experiments.

The laser beam is delivered to the workpiece surface using water-cooled, coated copper mirrors. Focusing was performed using a lens with a 200 mm focal length. The defocused CO_2 laser beam was traversed a single time across the surface of the MgO-PSZ samples placed on the stage using the x-axis. The fumes produced were removed with an extraction system, whilst O_2 process gas with 2-bar pressure was used to shield the laser optics and assist the surface treatment. Oxygen shielding gas was provided coaxially with the laser beam at a flow rate of 10 L/min. O_2 was selected as the process gas as previous studies by Lawrence [132] have shown it to be the most conductive gas for effective positive wettability changes.

5.2.3. Analysis Procedures

The surface and cross-section of the samples without etching were examined using optical microscopy and a scanning electron microscope (SEM), energy dispersive X- ray analysis (EDX)

and X-ray diffraction (XRD) technique. The MgO-PSZ samples were coated with Au for SEM examination. The CO_2 laser treated MgO-PSZ samples were sectioned with a cutting machine using a diamond rimmed cutting blade in order to analyse the cross-section. The sectioned samples were polished with 180, 400, 800 and 1000 grit SiC abrasive papers and then fine polished using cloths and diamond pastes to 3 μm. No etching was carried out in the studies.

5.3. The General Effects and Observations of CO_2 Laser Interaction

5.3.1. Effects of Power Density Variation

A series of experiments were conducted for a wide range of power densities with an 11 mm spot diameter, whilst the traverse speed was set at 2000 mm/min. In general, CO_2 laser treatment produced a thin affected layer on the MgO-PSZ. Power density variation was observed to have a significant effect upon the surface morphology of the MgO-PSZ.

With a relatively low power density of 0.9 kW/cm^2, the track shown in Fig. 5.2(a) was generated. As can be seen, CO_2 laser interaction under the conditions resulted in a track that appeared only partially effected. The investigation by the optical scope showed that the centre region glazed by CO_2 laser revealed a network of cracks and porosities as shown in Fig. 5.2(a-1). At a relative medium power density of 1.6 kW/cm^2, CO_2 laser radiation caused a discernible melted layer on the MgO-PSZ as shown in Fig. 5.2(b). The treated track exhibited few microcracks and porosities. The microcrystalline structures were found in the centre, while some hexagonal structures were appeared at the edge of the track (see Fig. 5.2(b-1)). The CO_2 laser glazed layer on the MgO-PSZ with the relatively high power density (2.5 kW/cm^2) is shown in the Fig. 5.2(c). As one can see, the glaze was deeply cracked across the entire width and displayed many microcracks and porosities. Under these conditions a cellular dendritic microstructure was observed at the centre of track (see Fig. 5.2 (c-1)). The different solidified microstructures on the CO_2 laser treated MgO-PSZ with various operating parameters are explained in more detail in Chapter 6.

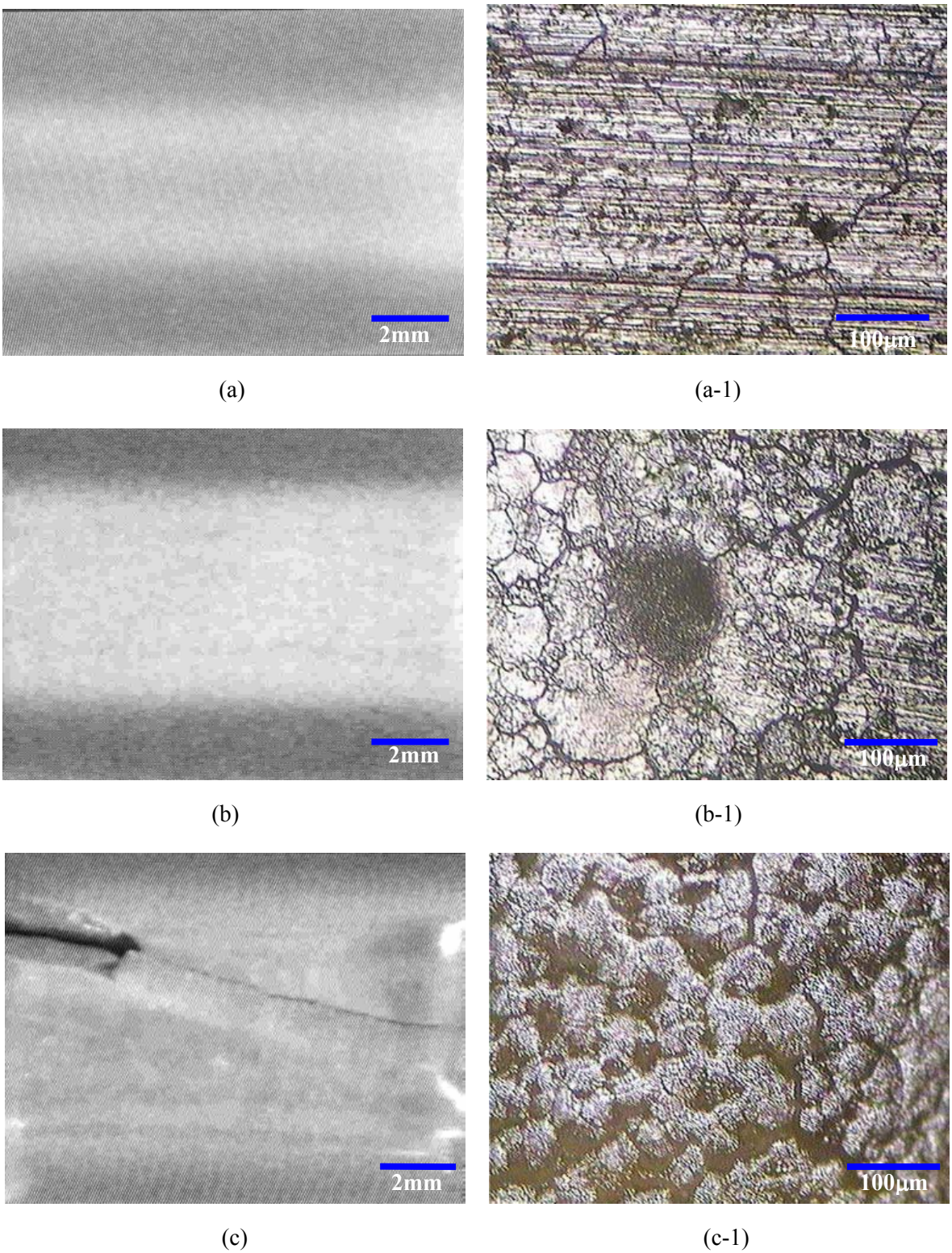

Fig. 5.2. Effects of CO_2 laser interaction on the MgO-PSZ surface at various power densities (a) treated track and (a-1) optical image power density of 0.9 KW/cm^2, (b) treated track and (b-1) optical image power density of 1.6 KW/cm^2, (c) treated track and (c-1) optical image power density of 2.5 KW/cm^2.

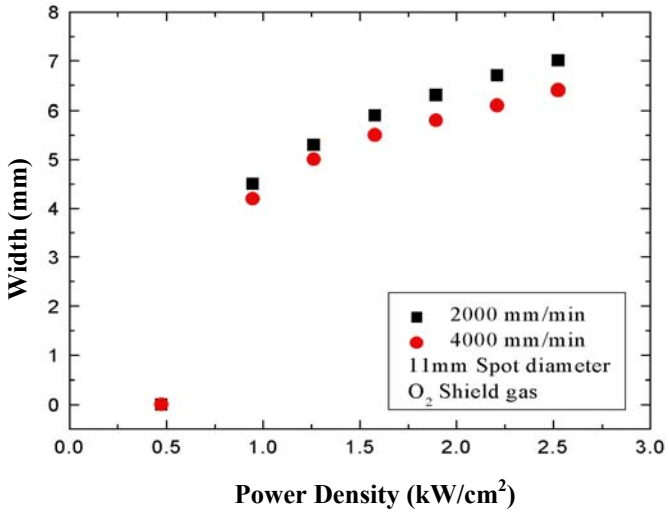

Fig. 5.3. The relationship between the widths of CO_2 laser generated tracks on the MgO-PSZ surface and laser power density.

As is evident from Fig. 5.3, the width of the CO_2 laser interaction region on the MgO-PSZ increased with power density. In the relatively low power density range (<0.47 kW/cm^2) for the given traverse speeds, few discernible effects of the CO_2 laser treatment on the MgO-PSZ were present.

5.3.2. Effects of Traverse Speed Variations

As with power density variations, changes in traverse speed affected both the surface morphology and the size of the CO_2 laser interaction region on the MgO-PSZ. A series of experiments were conducted with a wide range of traverse speeds, whilst the power densities were fixed at 0.9 kW/cm^2 and 1.6 kW/cm^2 with a laser beam spot diameter of 11 mm.

With a power density of 0.9 kW/cm^2 and a traverse speed of 2000 mm/min, the track shown in Fig. 5.4(a) was generated. As can be seen, CO_2 laser interaction under these conditions resulted in a track that appeared only partially affected. With a power density of 0.9 kW/cm^2 and a traverse speed of 4000 mm/min, the tracks shown in Fig. 5.4(b) were generated and were found to be affected less than that of the samples generated with a lower traverse speed. From the experiments it was observed that generally, as the traverse speed increased, the width of CO_2 laser treated track on the MgO-PSZ surface decreased. At this power density, the CO_2 laser treated track in Fig. 5.4(a) at a traverse speed of 2000 mm/min was wider than that shown in Fig. 5.4(b) at a traverse speed of 4000 mm/min.

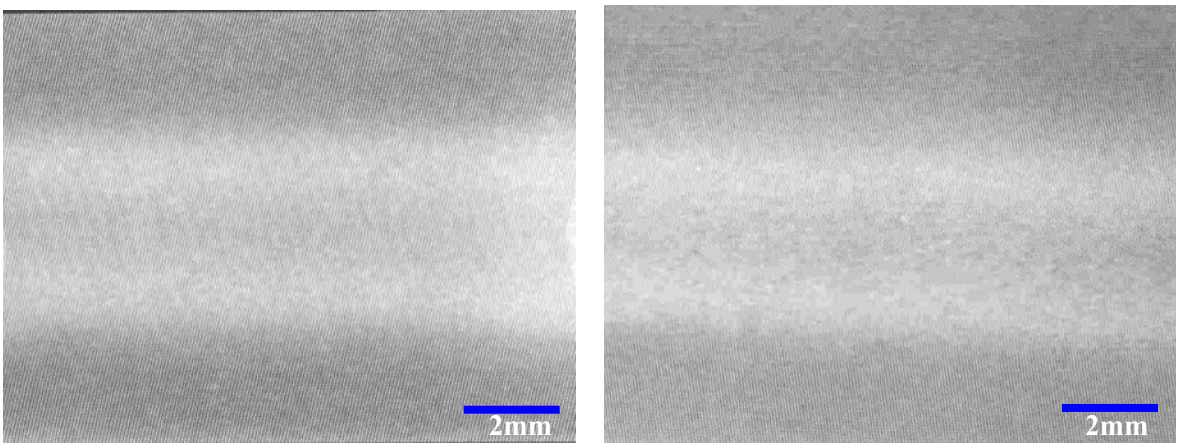

(a) (b)

Fig. 5.4. Effects of CO_2 laser interaction on the MgO-PSZ surface with 0.9 kW/cm^2 power density at (a) 2000 mm/min and (b) 4000 mm/min traverse speeds.

Fig. 5.5 shows the relationship between the width of CO_2 laser treated track on MgO-PSZ and CO_2 laser traverse speed. It is clear that the width of CO_2 laser treated track decreased as the traverse speed increased at the selected power densities.

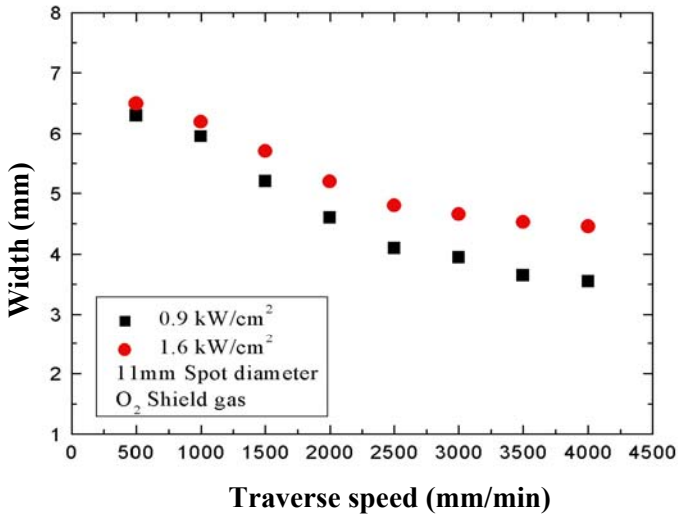

Fig. 5.5. The relationship between the widths of CO_2 laser generated tracks on the MgO-PSZ and laser traverse speed.

5.3.3. Formation of Concavity

An analysis of the surface and cross-sections of the CO_2 laser treated MgO-PSZ in Fig. 5.6 shows that concavities on the surface across the width of the CO_2 laser tracks developed.

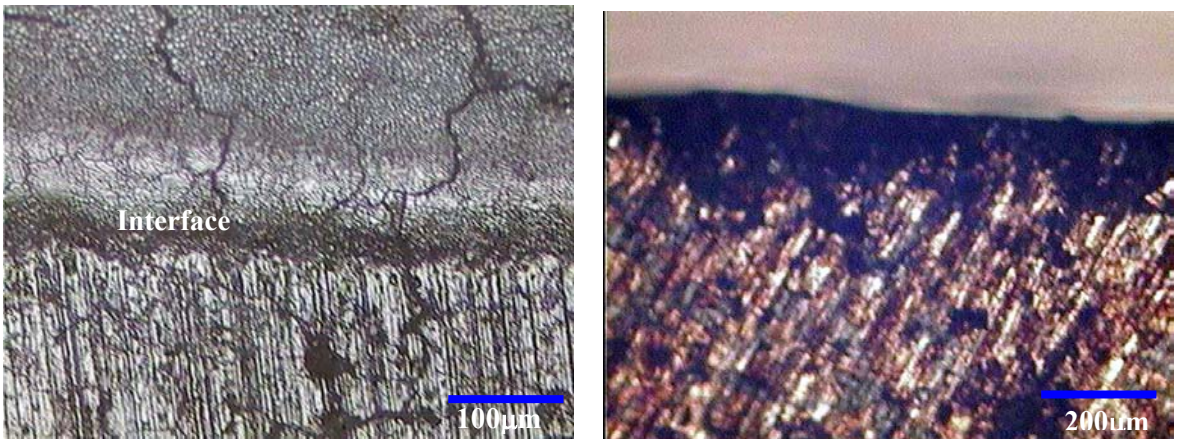

(a) (b)

Fig. 5.6.Typical optical view of (a) surface and (b) cross section of CO_2 laser treated MgO-PSZ showing the concavity in the interface region of the glaze.

The cavity formation was attributed to the surface tension induced flow of melted liquid and evaporation losses of the MgO-PSZ in the CO_2 laser processing. Previous work conducted by Liu [201] found that the extent of concavity on the plasma sprayed yttria stabilised zirconia coating resulting from CO_2 laser treatment increased with specific energy. Therefore, it is possible to obtain a melted layer with minimum or without concavity by carefully controlling the CO_2 laser processing parameters. Antou *et al* [202] also found that after *in situ* CO_2 laser remelting of plasma-sprayed yttria stabilised zirconia coating, the molten zones appeared preferentially near the singularities of the surface, and were typified by the formation of cavities.

5.3.4. Changes in Microstructure

Exposure of the MgO-PSZ to CO_2 laser irradiation results in rapid heating of the surface, for most materials typically 10^3-10^5 K/s [203], which consequently leads to the melting and resolidification of the MgO-PSZ surface. After the CO_2 laser treatment, a distinctive microstructure was generated on the MgO-PSZ surface, as can be seen in Fig. 5.7. The mechanisms of CO_2 laser induced microstructures are explained in the following chapter.

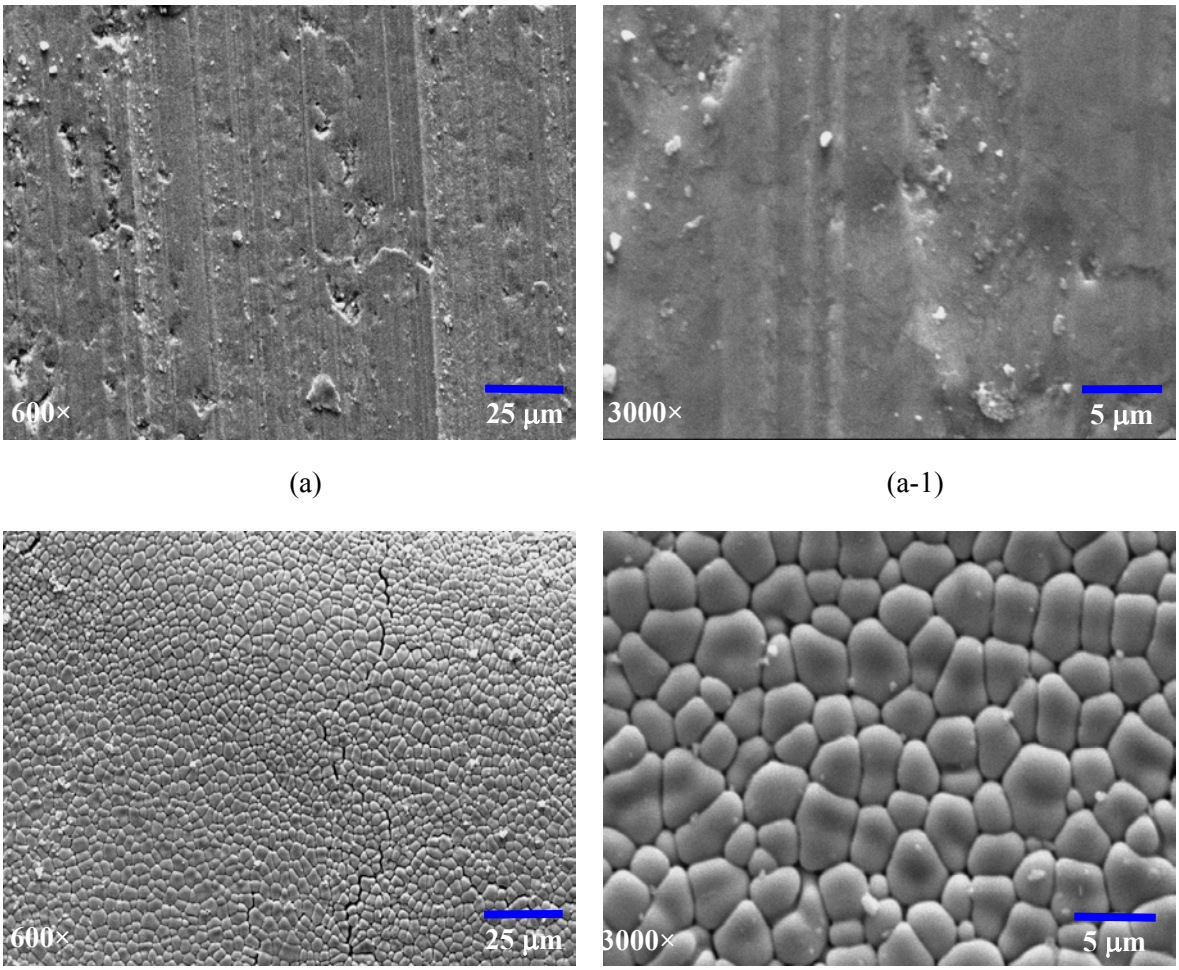

Fig. 5.7. Typical SEM surface images of the MgO-PSZ (a) before and (b) after CO_2 laser treatment (1.6 kW/cm^2, 2000 mm/min).

5.4. Discussion

5.4.1. Cracking and its Formation Mechanism

Both on the surface and within the CO_2 laser glazed track, cracks were always formed as shown Fig. 5.8(a) and (b). The formation of these cracks was mainly due to laser-induced thermal stresses. In account of the ceramic having a very high melting point and very low thermal conductivity, consequently, a large thermal gradient between the melted spot and the substrate exists. During the heating phase the stresses will be compressive and relieved by plastic deformation, thus precluding formation. At high temperatures of $T \geq 0.5\ T_{melt}$ the stress can also be relieved [204]. However, when the temperature is below this value, the stress will build up during cooling. If the fracture strength of the material is exceeded, cracking will occur in the melted layer. As shown in Fig. 5.8, the melted layer was thick. Cracks, both perpendicular and parallel to the surface were generated with the CO_2 laser parameters applied. This observation can be explained in terms of tensile

stresses producing during the cooling of the solidified layer. During the cooling of the melted layer, the temperature is nearly uniform across the thickness and so it experiences only a two-dimensional stress at the surface. Consequently, any cracks produced are perpendicular to the surface. If the temperature gradient across the depth is present along with the gradients at the surface, then the three-dimensional nature of stress results in cracks that are both perpendicular and parallel to the surface.

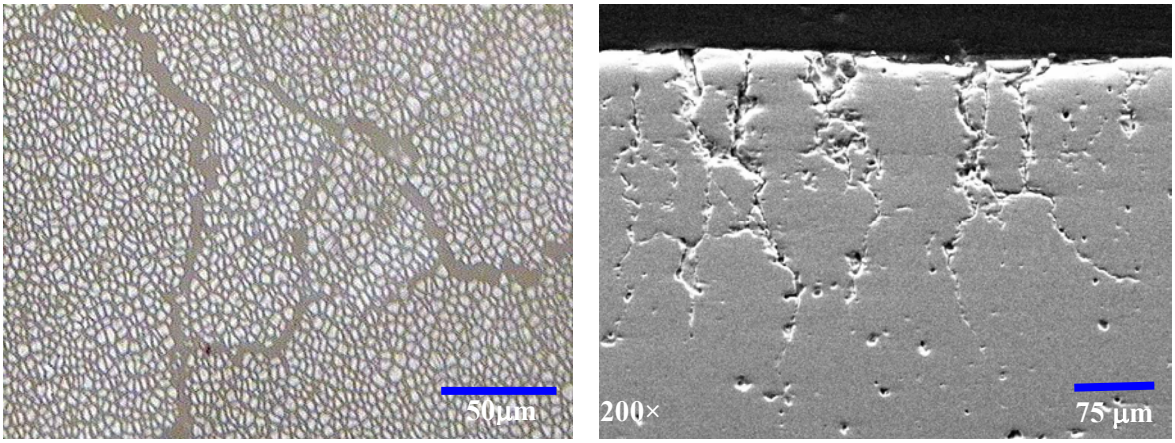

(a) (b)

Fig. 5.8. CO_2 laser treated MgO-PSZ showing cracks (a) optical surface image and cracks (b) parallel and perpendicular to the surface (SEM cross-sectional image) with power density of 1.9 kW/cm^2 and traverse speed of 4000 mm/min.

5.4.2. Craters and Their Formation Mechanism

After CO_2 laser treatment, craters were found on the MgO-PSZ surfaces as shown in Fig. 5.9. There could be two reasons for the formation of such craters. On one hand, with short interaction times or thin depths of melting, the heated gases in the small pores near the surface will expand, consequently breaking the melted layer. If insufficient time is allowed for the melt to flow and fill the pores, open crater will be left on the surface. In this case the craters are usually small and shallow. On the other hand, if the interaction time between the CO_2 laser beam and materials is long enough, then boiling of surface materials may occur. At the same time, as the melted depth increases, the pores in the deeper layer may be combined and brought up to the surface and burst to form large craters as shown in Fig. 5.9(a). Fig. 5.9(b) shows craters in the region of the cellular structure, the elongated cells are around crater. There are even finer grain structures at the middle of one crater in the region of capped hexagonal structure shown in Fig. 5.9(c). The presence of craters and closed porosity produced complex heat transfer locally resulting in the variation of microstructures associated with these defects.

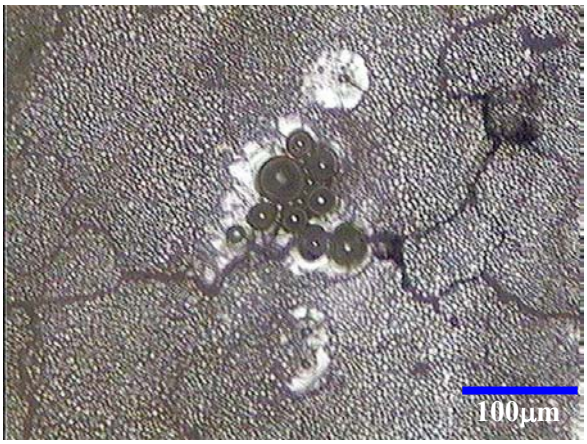

(a)

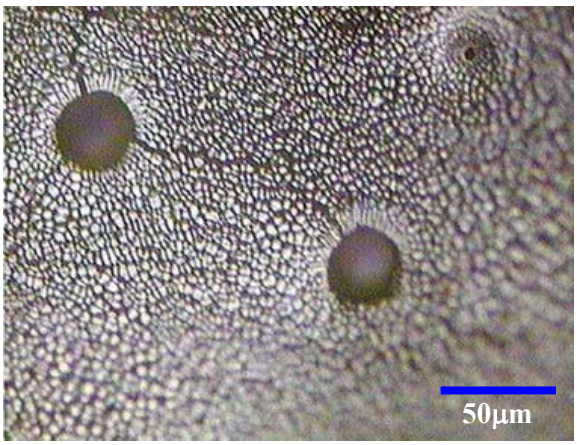

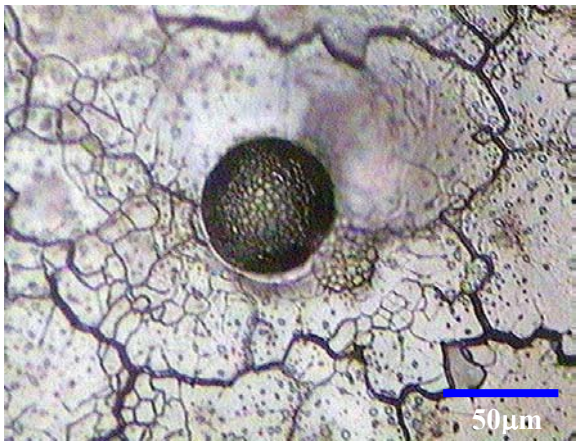

(b) (c)

Fig. 5.9. Optical views of crater on the surface of CO_2 laser treated MgO-PSZ surface (a) the pore on the surface (b) craters in the region of the cellular structure (c) one crater in the region of capped hexagonal structure.

5.4.3. Phase Transformation Effected by CO_2 Laser Irradiation

The XRD patterns of the untreated and CO_2 laser treated MgO-PSZ are given in Fig. 5.10. The peaks of the cubic and tetragonal phases are all overlapped with others. The diffraction patterns of 2 theta between 28-32° (see Fig. 5.10) are of parameter relevance and should be emphasized [205]. The peak at 29° belongs to the overlap diffraction of the (111) cubic phase and (101) tetragonal phase (denoted as c (111) and t (101)). The peaks of the cubic and tetragonal phases are all overlapped with others for the untreated and CO_2 laser treated samples (see Fig. 5.10). The peaks at 28.2 and 31.5° belong to the (111) monoclinic phase (m (111)). An increase in the peak at 29° signifies the increase in the tetragonal phase.

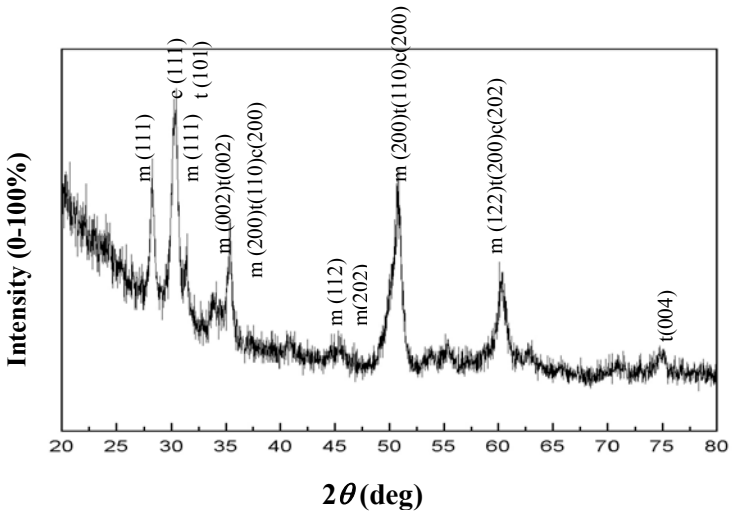

(a)

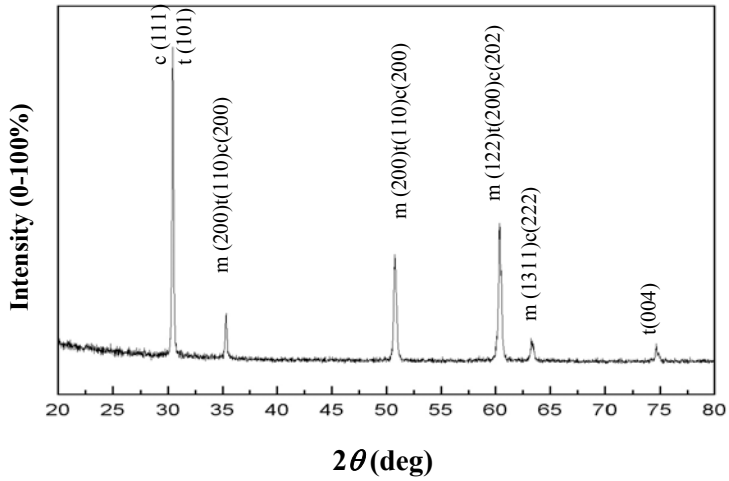

(b)

Fig. 5.10. XRD analysis of the MgO-PSZ surface (a) before and (b) after CO_2 laser treatment (1.6 kW/cm^2, 2000 mm/min)(c = cubic, t = tetragonal, m = monoclinic).

After CO_2 laser treatment, the peak at 29°, which shift to 30.5°, was seen to rise while the peaks at 28.2° and 31.5° disappeared (see Fig. 5.10), indicating that the tetragonal phase was increasing while the monoclinic phase was decreasing in MgO-PSZ surface. As shown in the Fig. 5.11, the relative intensity of the tetragonal phase on the treated MgO-PSZ increased with the power density when it was below 1.6 kW/cm^2 and then decreased slightly as the power density further increased. In contrast, the monoclinic decreased as the tetragonal phase increased.

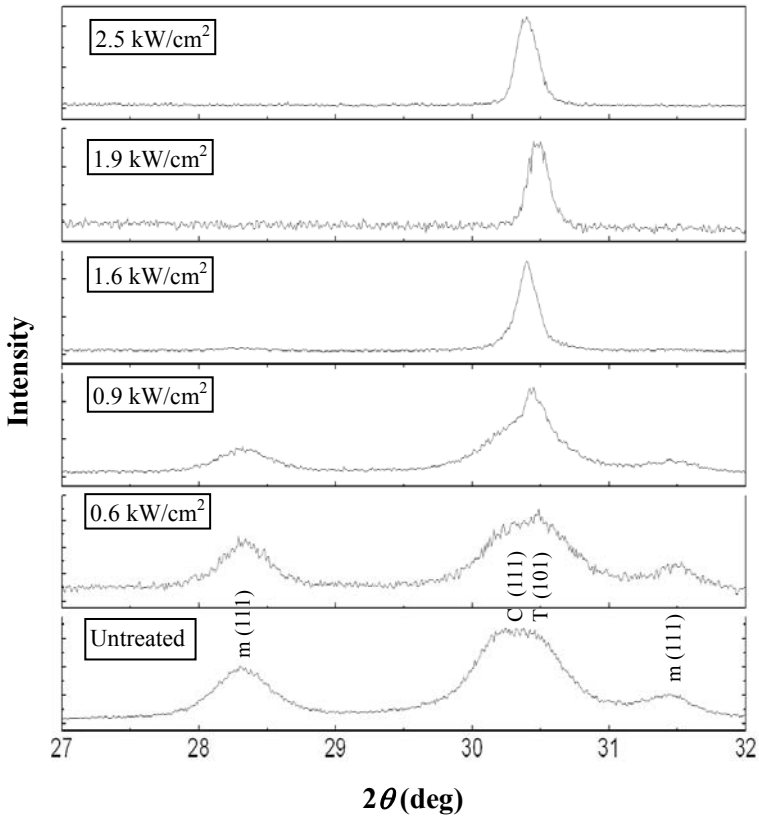

Fig. 5.11. The XRD pattern of the MgO-PSZ with various power densities at traverse speed of 2000 mm/min between 27 and 32° two-theta angle

According to the equilibrium phase diagram for MgO-ZrO_2 [206], the monoclinic phase is stable below 1240 °C and the tetragonal phase is stable between 1240 and 1400 °C. Above 1400 °C, tetragonal and cubic phases coexist, with increasing temperature, tetragonal transforms to cubic phase. From 2370 °C to the melting temperature (2600 °C) the stable phase is a cubic structure. With the increase of CO_2 laser power density, the surface temperature of the MgO-PSZ will increase and create the phase transformation on the surface. As is evident in Fig. 5.11, the decrease in the monoclinic phase is obvious whilst the tetragonal phase increases greatly when the power density is above 0.9 kW/cm^2. Indeed, the surface temperature of the MgO-PSZ during the CO_2 laser irradiation at power density of 1.6 kW/cm^2 was measured with a digital pyrometer (IGA 5 IMPAC) with temperature range of 250 – 2500 ºC. The pyrometer readings showed that the surface temperature of the MgO-PSZ was above the 2500 °C when the CO_2 laser power density was 1.6 kW/cm^2. Since the monoclinic-tetragonal transformation temperature is 1240 °C, then under these conditions the monoclinic transformed to tetragonal phase and the tetragonal phase reached the highest density. It has been reported that the CO_2 laser cladding of ZrO_2 composite coating showed higher tetragonal phase in the laser-clad ZrO_2 ceramic layer than that in the original ZrO_2 powder

[207]. Moreover, the plasma sprayed 8 wt% Y_2O_3-PSZ coating generated the metastable tetragonal phase (peak at 29°) in the as-sprayed condition after Nd:YAG laser treatment [208].

As Fig. 5.10(a) and (b) show, the X-ray spectra of the MgO-PSZ samples before and after CO_2 laser treatment possesses a zirconia phase but no MgO phase. Similar results were observed by Wen cheng *et al* [209] for injection moulded MgO-PSZ. The EDX analysis results shown in Fig. 5.12 revealed that Zr, Mg and O were still present in similar proportions on the MgO-PSZ surface before and after CO_2 laser treatment, indicating that only phase changes in the MgO-PSZ had been occasioned by CO_2 laser interaction.

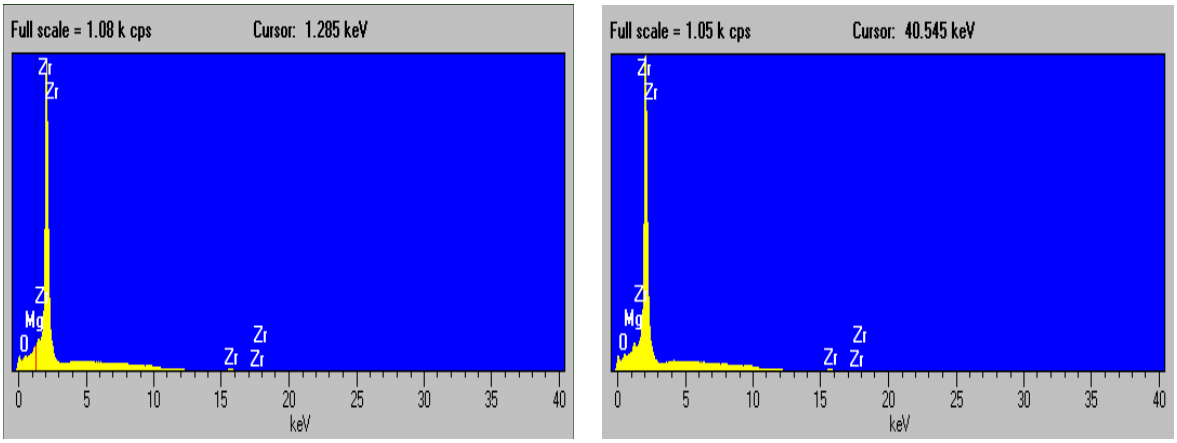

(a) (b)

Fig. 5.12. EDX analysis of the MgO-PSZ surface (a) before and (b) after CO_2 laser treatment (1.6 kW/cm^2, 2000 mm/min)

5.5. Summary

This chapter details the experiments that were performed with a 3 kW CW CO_2 laser and the general effects thereof on the surface of the MgO-PSZ. It analysed the surface morphologies and phase change generated by the various CO_2 laser parameters and briefly discussed the fundamental mechanisms. The conclusions that can be drawn are as follows:

1. It was found that CO_2 laser treatment produced a melted layer, which in turn generated a glazed track on the MgO-PSZ surface. Such effects of CO_2 laser radiation on the MgO-PSZ varied with laser power density and traverse speed. With increasing power density the melted layer was wider and displaced microcracks and various microstructures. Conversely, the widths of the melted layer decreased as the traverse speed decreased.

2. The large thermal gradient generated by CO_2 laser treatment resulted in random cracks on the MgO-PSZ surface at certain power densities. In addition, the CO_2 laser processing induced craters on the melted surface due to heated gases and the resulting burst pores.

3. An XRD analysis of the untreated and CO_2 laser treated MgO-PSZ showed an increase in the tetragonal phase and a decrease in the monoclinic phase after CO_2 laser treatment. The relative intensity of the tetragonal phase on the CO_2 treated MgO-PSZ increased with the power density due to the transformation of the monoclinic phase to tetragonal phase.

CHAPTER 6
Examination of CO_2 Laser Induced Rapid Solidification Structures on Magnesia Partially Stabilised Zirconia

In this chapter the main rapid solidification theories, namely constitutional supercooling and the theory of morphological stability are used to explain the observed microstructural changes in the MgO-PSZ resulting from CO_2 laser interaction.

6.1. Introduction

First propounded by Duwez *et al* [210] in the early 1960's, rapid solidification refers to a variety of processes which are used to modify the structures, and in turn the properties, of materials during solidification. Since the major focus of rapid solidification work has been on achieving rapid rates of heat removal during solidification, the laser beam has been viewed as an inherently suitable technique for achieving such high cooling rates. This is because the high specific rate of energy delivered to the material surface facilitates surface localised melting at a very high efficiency. That is, the major portion of the absorbed energy is used for melting, with only a small fraction going into the heating of the solid sub-surface material. This ability to maintain a cold substrate whilst melting a thin surface layer of material results in rapid quenching of the molten layer once the beam is removed. Since the majority of the heat of solidification is removed by the cold substrate, high cooling rates in the range of 106-109 K/s can be achieved [211].

Although much literature exists for laser rapid solidification processes of metals and alloys [212-214], there is very little with regard to crystalline ceramic materials [215]. The main reason for this being the inherent lack of thermal shock resistance of most ceramic materials coupled with their high melting temperatures and low thermal conductivity [216]. Nevertheless, a reasonable understanding of the formation mechanisms of solidified microstructures in ceramic materials such as the MgO-PSZ, and the influence of laser processing parameters on the microstructures of such materials during rapid solidification can be gained from a review of the basic concepts of solidification. These are principally the theory of Constitutional Supercooling and the theory of Morphological Stability.

6.2. Constitutional Supercooling Theory

In a pure material, such as a pure metal, without any solute effects only the thermal gradient controls the stability of the interface. In the presence of a positive temperature gradient ahead of the solid/liquid interface, a plane front is stable. When a negative temperature gradient is present, however, it leads to instability of the plane front and cellular or dendritic growth results [216,217]. But, for impure materials the analysis of solidification front stability is considerably more complex since the additional effect of a compositional gradient during solidification must be considered. Consequently, the constitutional supercooling cooling theory, which is basically an application of thermodynamics, is used to determine if the liquid ahead of the moving interface is undercooled with respect to its composition [217,218].

The condition where the interface is exactly at the equilibrium liquidus temperature and where every point in front of the interface is at a temperature above the liquidus, is necessary for stable plane front solidification [214,219]. However, if an instability causes a protuberance to form on the flat interface, then it will be in a superheated environment and will consequently melt back. Conversely, an unstable case presents with the temperature of the liquid in front of the interface below its equilibrium liquidus temperature. As such, it is presumed that a planar interface will be unstable if the liquid region near the interface is supercooled and that this supercooling increases with distance from the interface. Thus, if a small perturbation forms on a planar interface it will experience greater supercooling, and will therefore grow faster than the surrounding solid. Under a positive temperature gradient condition in the liquid the supercooling can be present due the solute effect. This solute-driven supercooling is known as constitutional supercooling. Constitutional supercooling, however, does not occur until there is a sufficient build up of solute atoms in the liquid in front of the interface. Constitutional supercooling will only occur if [214,219]

$$\frac{G}{R} \leq -\left[\frac{m_L C_O (1-k)}{D_f k}\right] \tag{6.1}$$

where, G is thermal gradient, R is solidification rate, m_L is slope of liquidus, C_O is the average equilibrium composition, k is ratio of equilibrium compositions in the solid and the liquid (C_S/C_L) and D_f is the diffusion coefficient.

The extent of the zone of constitutional supercooling depends upon the operative solidification parameters R and G [220-222]. At very high cooling rates, in excess of 10^6 K/s, absolute stability is possible because there is insufficient time for diffusion to occur. Under such conditions the melt solidifies without any latent heat being involved, and the melt can then solidify as either a very fine microcrystalline structure or even as a glass. During the initial stage of resolidification of the melt zone, G/R will always be large, and will therefore favour planar front solidification since the rate of

solidification is instantaneously zero at the commencement of resolidification. As the solidification rate, *R,* increases, as solidification proceeds, *G*/*R* becomes smaller and planar front solidification is no longer favoured. The characteristic result is a relatively thin planar front zone followed by directional forms of solidification.

6.2.1. Solidified Morphology in Accordance with Constitutional Supercooling

The major effects of varying thermal conditions on solidification microstructure are well known according to the theory of constitutional supercooling [214,219,223,224]. Increasing the thermal gradient-rate (*G*/*R*) ratio causes a progressive change in the solidification characteristics, ranging from fully dendritic to cellular-dendritic to cellular and finally to planar front growth. On the other hand, increasing the cooling rate ($\dot{T}$ =*G.R*) gives rise to shorter diffusion paths and finer structures. More succinctly, *G/R* controls the character of the resultant microstructure, whereas the product, *G.R* determines the scale of the microstructure. Fig. 6.1 shows a schematic summary of single-phase solidification morphologies, detailing the microstructures that can be obtained with a typical alloy material according the constitutional supercooling theory.

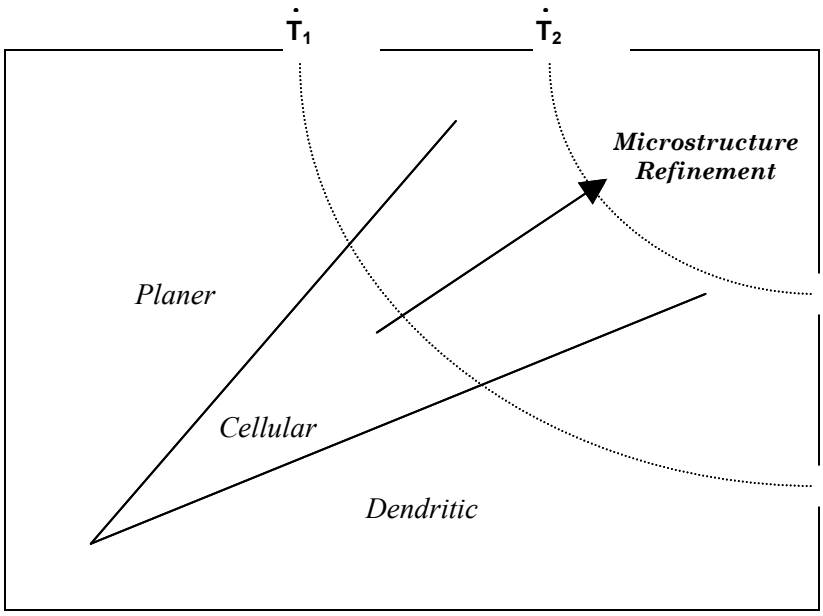

Fig. 6.1. Dependence of solidification morphology on temperature gradient (G) and solidification rate (R) [225].

6.2.2. Formation of Cell Structure

When the threshold of planar interface stability is exceeded a cellular interface is formed. But, before any such cell structure is formed several different stages have to be undergone [226]. When the degree of constitutional supercooling is small, that is *G*/*R* is slightly less than that required for

stability, the interface develops small irregularities, however, no definite structure is present. Increasing the degree of constitutional supercooling leads to the formation of fine elongated cells on the interface. On further increasing the degree of constitutional supercooling the capped-hexagonal formation becomes the stable interface shape. Finally, when marked constitutional supercooling exists, the cellular shape is developed. At even larger supercooling (G/R becomes even smaller), a transient from the cellular into cellular dendritic interface will occur [221,227,228].

6.2.3. Dendritic Growth

When the degree of constitutional supercooling is very large, that is, the ratio, G/R, becomes very small, the cells will tend to grow more rapidly than a depression, which tends to accumulate the excess solute rejected by the solidification front. This results in a transition from cellular-dendritic to dendritic microstructure [229]. The microstructural characteristics of dendrites are represented in terms of the six important length parameters: the length of the dendrite, primary dendrite arm spacing, secondary dendrite arm spacing, the diameter of the dendrite core, the spacing of the first secondary sidebranch from the dendrite tip and the dendrite tip radius. Of all these characteristics, secondary dendrite arm spacing is the most important parameter from a technological viewpoint, since it influences the mechanical behaviour of the material [230,231]. The secondary dendrite arm spacing is influenced by a great of many factors. Nevertheless, previous work by Jones [232] has shown that there exists a relationship between $\dot{T}$, and secondary dendritic arm spacing, λ_d, thus

$$\lambda_d = c\dot{T}^{-n} \tag{6.2}$$

where, c is constant and n = 1/3 to 1/2. Clearly, as Equation (6.2) shows, the secondary dendrite arm spacing decreases with the cooling rate as a result of the shorter local solidification time.

6.2.4. Preferred Growth Directions of Cellular and Dendritic Structures

Dendrites have been found to grow in specific directions, which can be crystallographically determined [214]. In cubic materials, the preferred growth directions are <001>, so that not only the primary dendrite, but also all sidebranches tend to form in these directions. Thus a cubic material will exhibit a four-fold symmetry in the side-branch formation with respect to the axis of the previous branch. The primary dendrites will tend to grow along the <001> direction which makes the smallest angle with the heat flow direction. For a hexagonal close-packed structure, since <1010> is a preferred growth orientation, a hexagonal close-packed material will exhibit a plate structure. Therefore, different crystal structures will result in completely different solidification morphological structures [233-235].

The preferred growth direction for dendrite growth exists due to the presence of interface kinetic anisotropy [214,224]. In contrast, cellular growth is very similar to planar growth in that the direction of growth of the cells is controlled by heat flow conditions. Growth crystallography influences the grain selection process as it does in planar growth but it does not play a significant role in determining the cell orientation. This type of solidification is characterised by a growth front made up of many relatively uniformly spaced cells growing parallel to one another. In addition, cellular-dendrite structures often tend to grow in the direction somewhere between the heat flow and the <001> direction.

6.3. Morphological Stability Theory

For most solidification processes at low solidification rates, the classical theory of constitutional supercooling has been used as an adequate guideline in determining the growth conditions that result in an unstable interface. However, for rapid solidification some of the assumptions and simplifications of this theory may not be valid, such as [225,236,237]:

1. Surface tension and latent heat evolution, which could stabilise the interface, are neglected.
2. The constitutional supercooling theory takes into account a layer of liquid cooler than its local melting point, but does not solve the kinetic equations for the thermal and diffusional fields to show how interface fluctuations lead to instability.
3. Local equilibrium at the interface: the equilibrium distribution coefficient is assumed to describe quantitatively the amount of solute rejected by the growing crystal.

For rapid solidification rates, however, work by Mulins [236] and Sekerka [237] has led to the development of the more comprehensive morphological stability theory. Here the time dependence of a general sinusoidal perturbation of the interface with respect to solute and heat-diffusion fields and surface tension are considered. The fundamental elements of the theory of morphological stability are [236,237]:

1. Short wavelength perturbations at high solidification rates are stabilised due to surface tension. If the thermal field is stabilising, the solidification rate for absolute stability is function of the solute content and is independent of the temperature gradient in the liquid.
2. Departures from local equilibrium at the solid/liquid interface tend to have a stabilising influence on the surface.
3. At very high solidification rates, the solute-enriched layer approaches atomic dimensions and macroscopic-transport equations used to derive the stability criterion are no longer valid.

4. When the solidification rates approach the diffusive velocity of the solute in the liquid, the assumption of local equilibrium at the solid/liquid interface is no longer valid. Complete solute trapping should occur if the solidification rate significantly exceeds the diffusive velocity.

Fig. 6.2 maps out the calculated *G* and *R* combinations that lead to homogeneous plane-front solidification as a function of copper concentration. This plot differs from Fig. 6.1 in that a new region of morphological stability is shown at high solidification rate, which is independent of temperature gradient. As anticipated, the conditions under which plane-front solidification prevails become more restricted with increasing solute content.

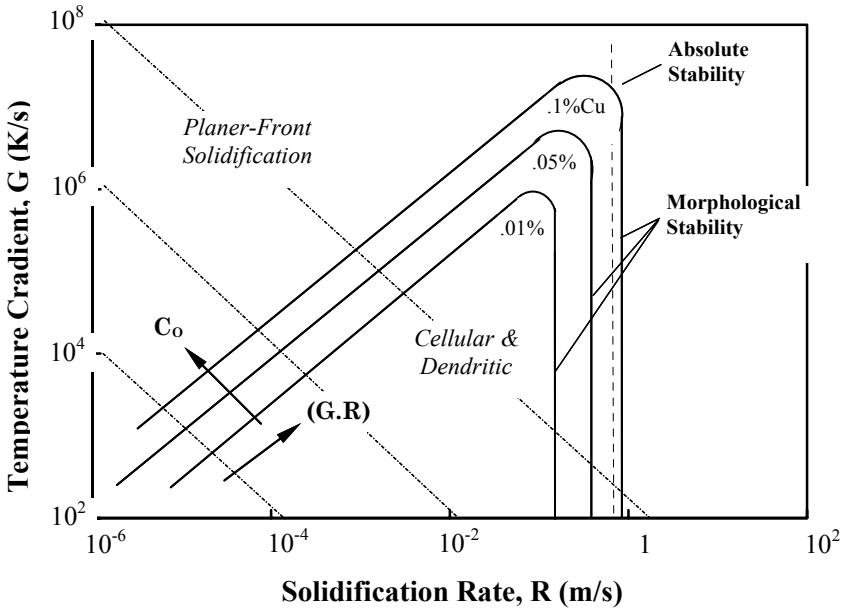

Fig. 6.2. Regimes of planar-front growth, cellular and dendritic growth as determined by liquid temperature gradient and solidification rate in an Al-Cu alloy [225].

6.4. Laser Rapid Solidification Process

A laser is an ideal tool for producing rapid solidification. The local melting and resolidification of a small portion of the surface of a material with a laser beam presents a unique opportunity for controlled crystal growth under high temperature gradient and high cooling rate. Since the properties of solidified materials depend on the solidification behaviour and the resulting microstructural characteristics, it is essential to understand the solidification behaviour in the melt pool. As discussed earlier, thermal gradient, solidification rate, G/R or T, at the solid/liquid interface significantly influence the solidification morphologies. As such, it is necessary to consider some important variables such as the temperature distribution, cooling rates, solidification rate and temperature gradients.

6.4.1. Heat Transfer Consideration

In order to determine the effects of different process parameters on the melting and rapid-cooling process resulting from high power density laser melting, it is necessary to establish a theoretical model for the melt pool to understand the laser melting processes. This can enhance our capabilities to predict and define important solidification variables such as the temperature distribution, cooling rates and temperature gradients.

If the laser surface melting process is considered to be one-dimensional, the equations of heat conduction are far simpler than for the cases of two or three dimensions. In this section, a one-dimensional thermal model developed by Kear *et al* [238] was applied to the transient-cooling processes. $\dot{T}$, is related to G and R by

$$\dot{T} = GR \tag{6.3}$$

where G and R are evaluated at the melt interface. Knowing the depth of the melt interface as a function of time, it can be evaluated to yield G and $\dot{T}$, at the interface and then be solved for R. The ratio of G/R at the melt interface is thus determined both as a function of time and as a function of depth.

6.4.2. Parametric Study

Since the properties of the solidified materials depend on the solidification behaviour and the resulting microstructural characteristics, understanding solidification behaviour in the melt pool is essential. As discussed above, thermal gradient, solidification rate, the combined forms, namely G/R or $G\dot{R}$, T, at the solid/liquid interface significantly influence the solidification morphologies, it is necessary to understand some important variables such as the temperature gradients. In this section, an analytical parametric study has been made of the transient behaviour of G, $\dot{R}$ and T, for various critical melt depths.

6.4.2.1. Temperature Gradient

For a typical material, Fig. 6.4 shows the variation of the temperature gradient, G, at the melt interface with melt depth for various absorbed power densities, F_o. The initial melt depth is assumed to be 25 μm. From this figure one can see that the temperature gradients have a maximum value at the start of solidification and approach zero as the surface solidifies. Additionally, the graph indicates that the temperature gradient is an intrinsic function of the absorbed power density.

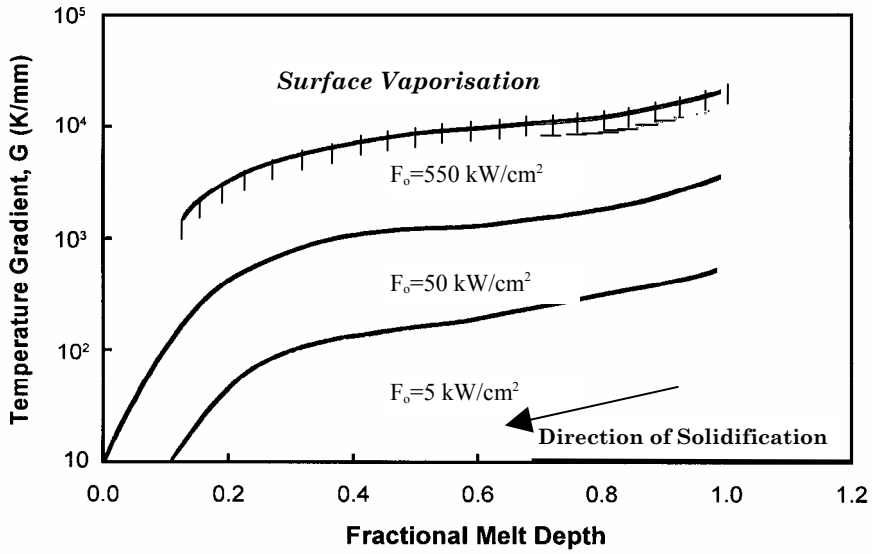

Fig. 6.4. Transient behaviour of temperature gradient, G [239].

6.4.2.2. Solidification Rate

For a given initial depth of melt that is, the depth at the cessation of laser irradiation (25 μm), the temperature at any point beneath the surface rises initially when power is removed.

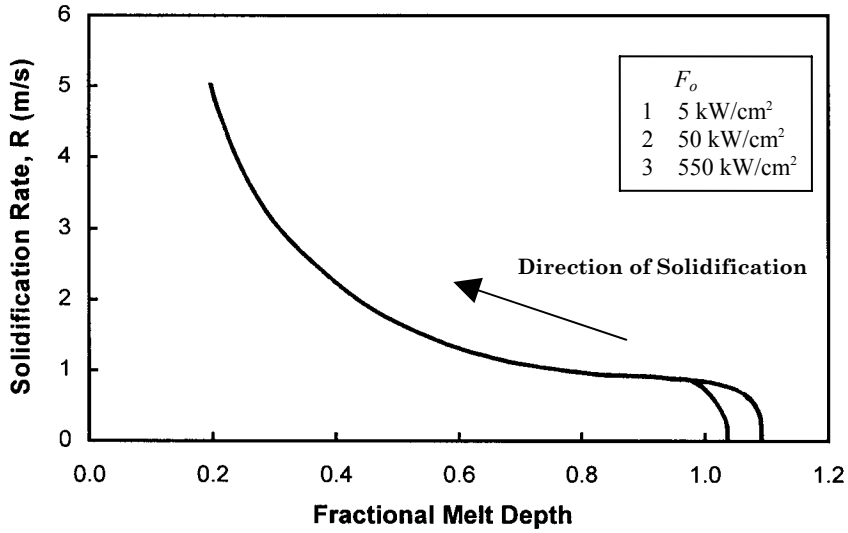

Fig. 6.5. Transient behaviour of solidification rate, R [239].

This phenomenon means that after the cessation of energy input, melting briefly continues before solidification commences. Thus, the solidification rate is initially zero. The transient behaviour of the solidification rate is given for a typical material in Fig. 6.5. As Fig. 6.5 shows, *R* at the interface starts at zero as solidification begins and goes to infinity as the surface solidifies. For a given initial melt depth, the solidification rate is essentially independent of power density after solidification has commenced.

6.4.2.3. Cooling Rate

The variation of $\dot{T}$, at the melt interface is shown in Fig. 6.6, with absorbed power density, F_o, being used as a parameter with the initial melt depth being assumed to be 25 μm. Fig. 6.6 shows that the cooling rate is strongly influenced by the absorbed power density. As in the previous discussion, the cooling rate at the melt interface starts at zero, and then tends to a constant limit as solidification proceeds to the surface.

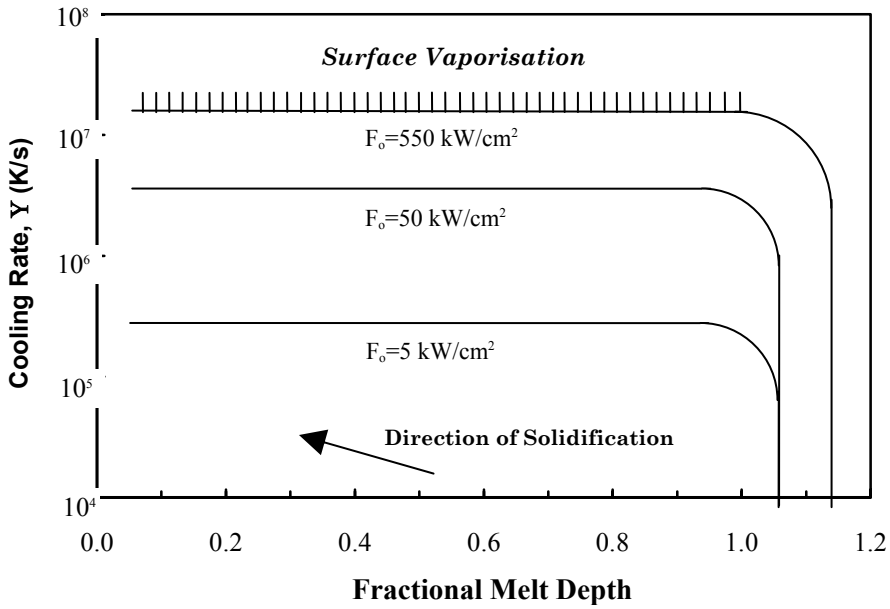

Fig. 6.6. Transient behaviour of cooling rate, $\dot{T}$ [239].

6.4.2.4. The Ratio, *G/R*

For a typical material, the ratio *G*/*R* at the interface is shown in Fig. 6.7. Again, absorbed power density is used as a parameter, with an initial melt depth of 25 μm being assumed. Characteristically, the curves begin at infinity at the onset of solidification and end at zero as solidification approaches the surface. This behaviour can be inferred from the curves of thermal gradient and the solidification rate for a constant power density. As solidification begins, the thermal gradient is large but finite, whilst the solidification rate is zero; thus the ratio, *G*/*R*, is infinite as solidification begins. As solidification approaches the surface, the thermal gradient which is continuously decreasing, tends to zero while the solidification rate, which is continuously increasing, tends to infinity. The ratio, *G*/*R*, therefore, tends to zero as the melt interface approaches the surface of the material. The ratio, *G*/*R*, increases with power density for a given depth of melt [239].

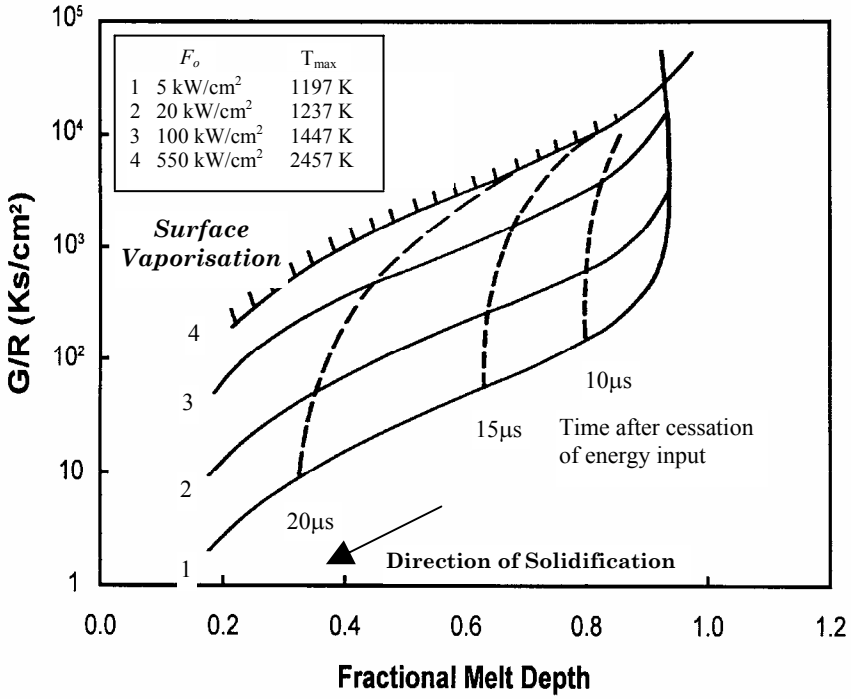

Fig. 6.7. Variation of G/R at solidification interface [239].

6.5. Solidification Microstructural Analysis of CO_2 Laser Treated MgO-PSZ

6.5.1. General Solidification Microstructural Analysis

Variations in the CO_2 laser operating parameters (power density and traverse speed) were seen to effect significantly the microstructure obtained within the laser-treated areas on the MgO-PSZ. Since the temperature distribution of the TEM_{01} beam was not homogenous, there were different degrees of CO_2 laser interactions and thus different microstructures within the treated area occurred. All microstructural features observed from the surface view using optical microscopy were evaluated without metallographic polishing or etching. For cross-section analysis, the samples were cold mounted in resin before grinding on increasing finer SiC grinding papers followed by a 1 µm finish using diamond past. The polished samples were then etched with 10 ml HNO_3 and 20 ml HF (48%) for 20 min to affect the ceramic layers.

6.5.1.1. High Power Density Induced Microstructure

Fig. 6.8(a) depicts schematically the different regions within the CO_2 laser treated track with a relatively high power density of 2.5 kW/cm^2 and a traverse speed of 2000 mm/min.

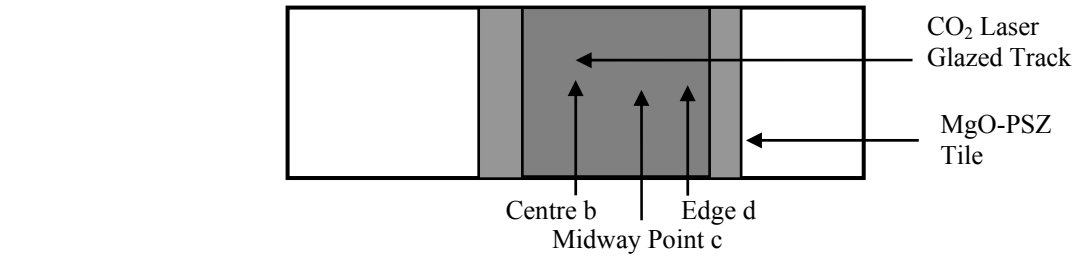

(a)

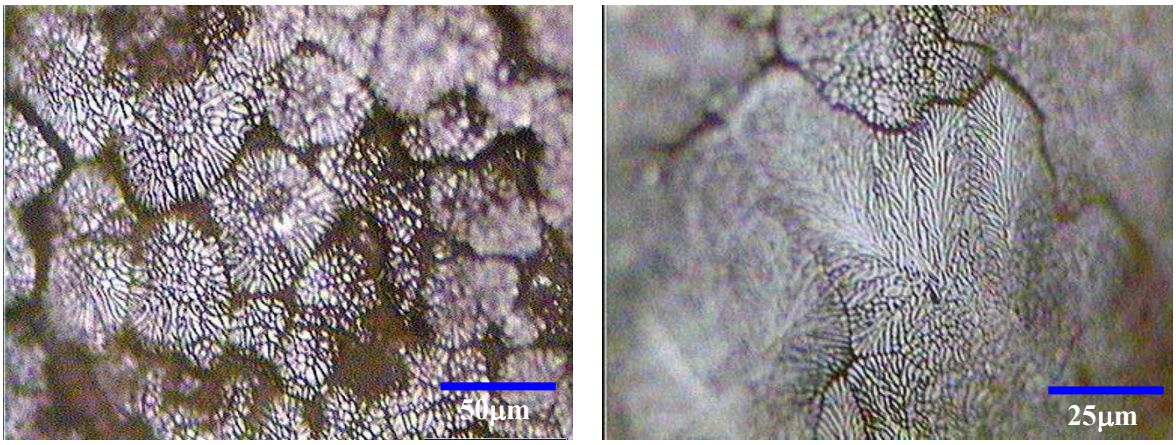

(b-1) (b-2)

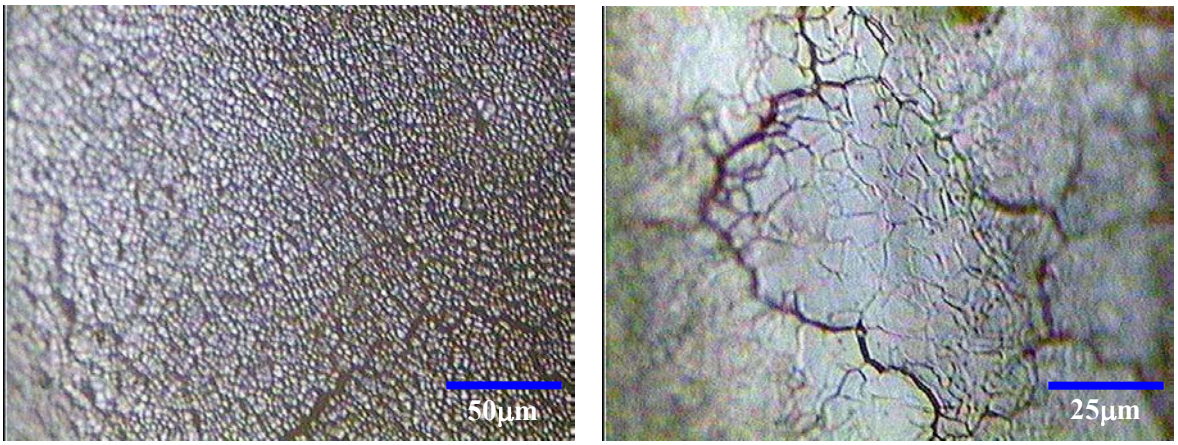

(c) (d)

Fig. 6.8. Examination of the microstructures within the CO_2 laser treated track, (a) schematic depiction of the area analysed, typical SEM surface view of the microstructures (b) in the centre, (c) at the midway point and (d) at the edge of the CO_2 laser treated track (power density of 2.5 kW/cm^2 and traverse speed of 2000 mm/min).

As one can see from Fig. 6.8, different solidified microstructures were observed in the centre Fig. 6.8(b), at the midway point Fig. 6.8(c) and at the edge Fig. 6.8(d) of CO_2 laser treated track on the MgO-PSZ. The structures described as "coral" and a few dendritic structures were found in the centre of the track, while a cellular structure was observed in midway point centre of the track and a hexagonal structure appeared at the edge as shown in Fig. 6.8(b). According to constitutional

supercooling theory, such a progressive change in the solidification characteristics within the same track, ranging from dendritic → cellular → hexagonal structure, indicated the different constitutional supercooling extent from the centre → the midway point → the edge of the CO_2 laser treated track on the MgO-PSZ surface.

In the centre of the track a few dendritic structures shown in Fig. 6.8(b-2) appeared, indicating that the *G/R* ratio is small enough to form dendritic structure. The cooling rate is so fast in the centre that secondary arms of the dendrites can be either completely absent or very short; a microcrystalline structure may be therefore formed and these spherical cells may coalescence to form a coral structure shown in Fig. 6.8(b-1), in which the perimetric cells of the coalescences grow in accord with dendritic pattern due to the relative slow scanning speed. Alternatively, the reason for the fine-grain structures may be that cellular-dendrite arms may have a slightly higher solute content than outer portions of the arms. As such, the melting point here would be lower and the thermal fluctuations would tend to cause melting just at this location. In any case, the roots of dendrite arms are often smaller in diameter than exterior portions, and even if melting in response to a thermal fluctuation were uniform; it would result in separation of the arm from the main stalk. When the arm that is separated is then carried away into slightly supercooled liquids, a new crystal is formed without a new nucleation event.

In the CO_2 laser-induced solidification process, convection flow in the melt pool provides a viable mechanism, not just for the breaking-off arms of dendrites, but also for dissipating superheat in the liquid so that the transported arm can grow. On the other hand, strong turbulent convection has added effect of bringing heat pulses to the interface. These heat pulses accelerate the melting-off of dendritic arms. Therefore, some fine-grain cellular structures as shown in the left part of Fig. 6.8(c) at the midway point on the MgO-PSZ, which show the undulate current, could come from the melted-off arms since a strong convection flow exists in the melt pool. While other cellular structures as shown in the right hand portion part of Fig. 6.8(c) at the midway point on the surface of the MgO-PSZ, which appear as a flat surface, could be the cells induced from direct solidification under supercooling. At the edge where the *G/R* ratio at the interface is just slightly less than that required for stability, i.e. the degree of constitutional supercooling is small. The hexagonal structure shown on the Fig. 6.8(d) can be easily formed to become a stable interface shape.

The cross-sectional view of the uppermost layer of the CO_2 laser modified MgO-PSZ generated with a relatively high power density is given in the Fig. 6.9. Here it is shown that a columnar dendritic structure, perpendicular to the substrate, was formed. The thickness of the columnar dendritic structure is about 120 μm at the centre region and decreases gradually toward both ends (see Fig. 6.9(a) and (b)), implying that a higher degree of laser induced solidification occurred at

the centre region than at either end. The microstructure orientation is very likely due to the fact that the temperature gradient is positive, thereby giving rise to a vertically oriented microstructure from the substrate to the melted area. In the case of *in situ* laser melting, the microstructure refinement seems to be explained by a higher overheating. The formation of this columnar dendritic structure is promising as the thermomechanical properties of the glaze are concerned [202]. Moreover, there are vertical microcracks in the melted layer along the grain boundary due to anisotropic thermal expansion mismatch (see Fig. 6.9(a)). Fig. 6.9(c) shows the grains in the unaffected substrata and the characteristic dimension the grains ranges form 40-100 μm.

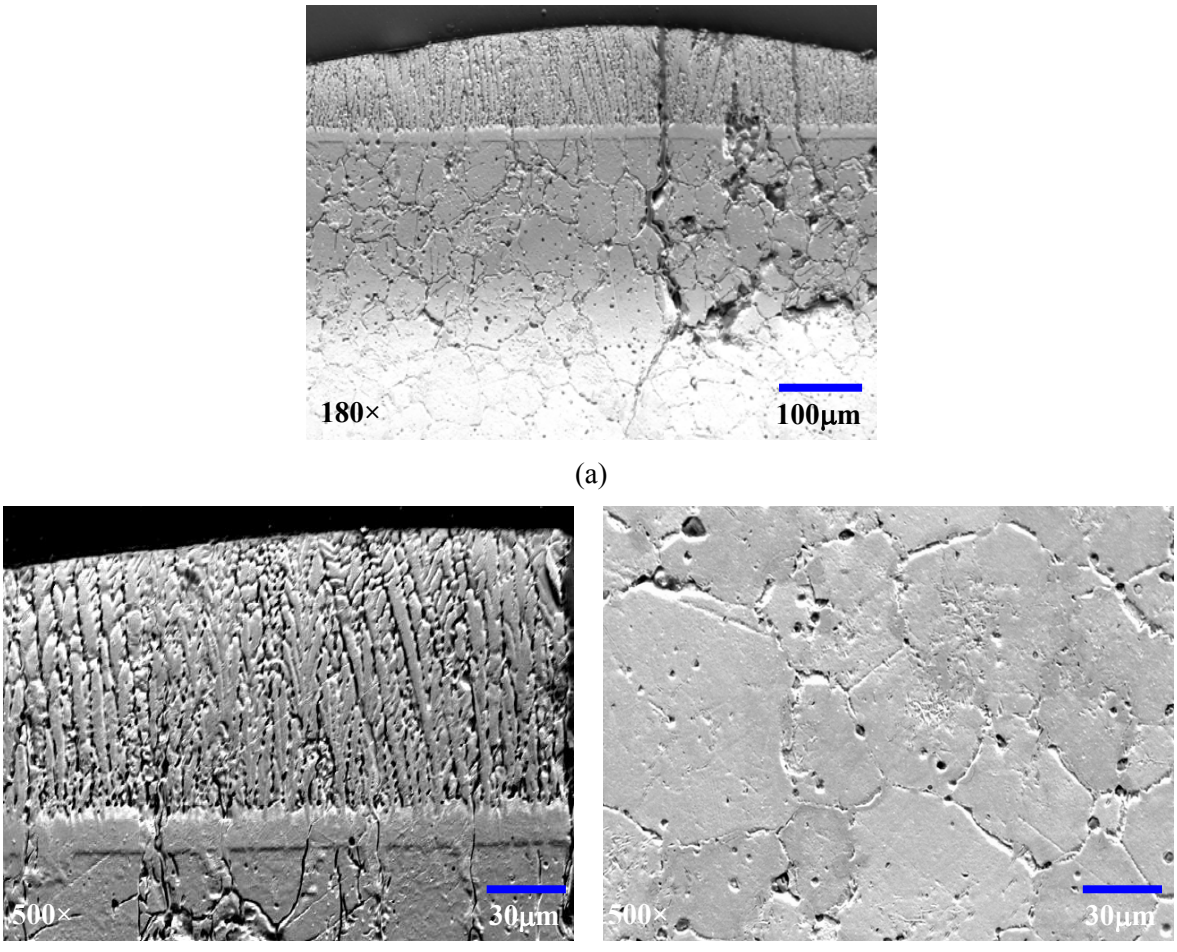

Fig. 6.9. Typical SEM cross-section view of the CO_2 laser modified MgO-PSZ surface layer (a) the centre region of the track, (b) the dendritic structures, (c) the grains in the unaffected substrata (power density of 1.6 kW/cm^2 and traverse speed of 2000 mm/min).

6.5.1.2. Low Power Density Induced Microstructure

A typical example of the microstructures within the CO_2 laser treated track obtained with a relatively lower power density of 1.6 kW/cm^2 and a traverse speed of 2000 mm/min is shown in Fig.

6.10. As one can see, different solidified microstructures were observed in the centre Fig. 6.10(b), at the midway point Fig. 6.10(c) and at the edge Fig. 6.10(d) of the CO_2 laser treated track.

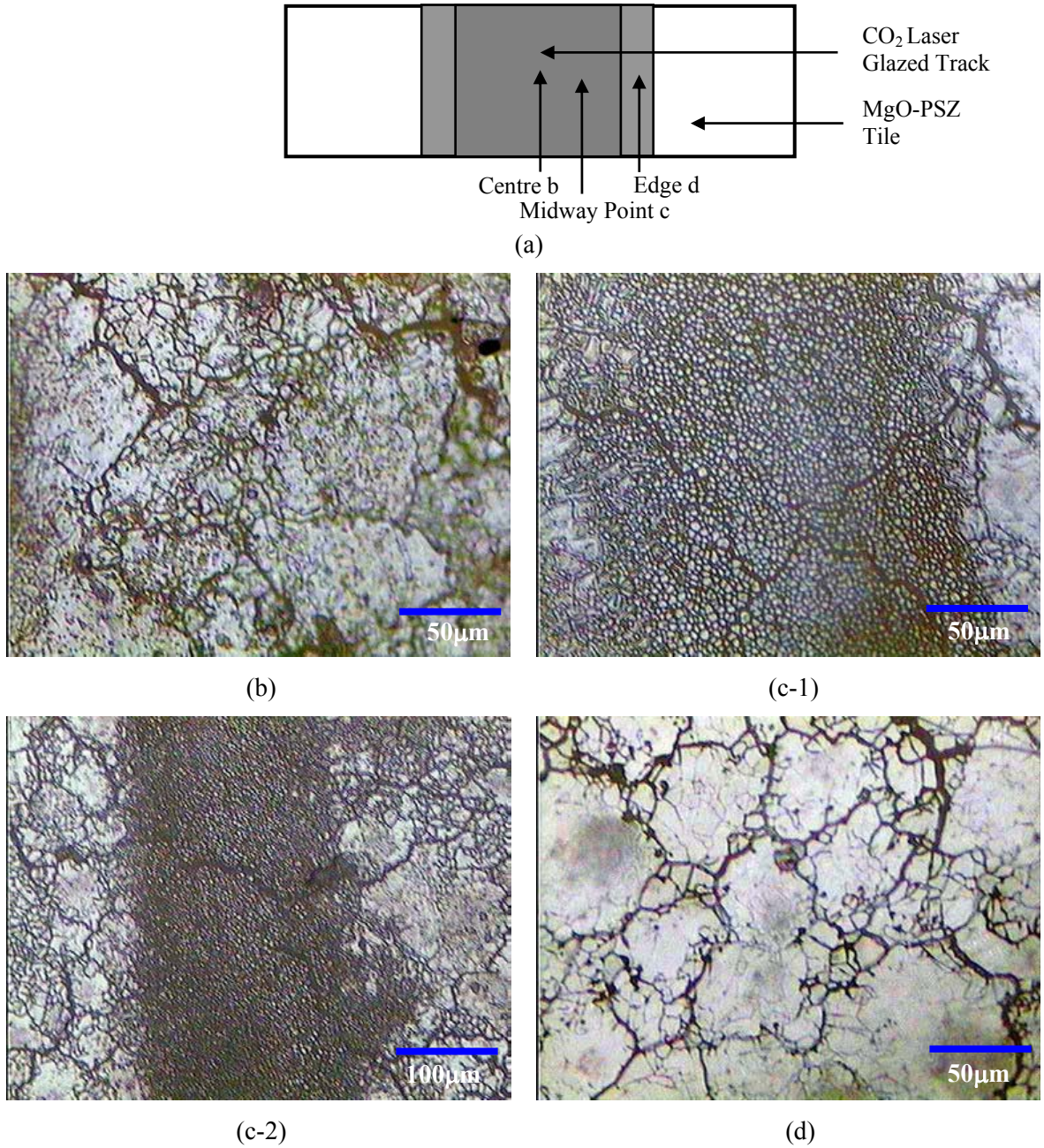

Fig. 6.10. Examination of the microstructure within the CO_2 laser treated track, (a) schematic depiction of the area analysed, typical SEM surface views of the microstructures (b) in the centre, (c) at the midway point and (d) at the edge of the CO_2 laser treated (power density of 1.6 kW/cm^2 and traverse speed of 2000 mm/min).

As can been seen from both Fig. 6.10(b) and (d), the microstructure of the hexagonal structure appeared in the centre and edge of the CO_2 laser treated track, while the cell structure formed in the midway point region shown in Fig. 6.10(c-1) and (c-2). Such solidification characteristics within

the track indicate the smallest thermal gradient-ratio is at the midway point and the maximum power density of CO_2 laser beam is at this region of the track. In the centre and at the edge, the *G/R* ratio is not sufficient to produce cellular structure and is just slightly less than that required for stability so that the hexagonal structure can be easily formed. The hexagonal structure seems more flat at the edge than in the centre, implying that the thermal gradient – ratio more favourable for planar structure formation. This indicates that the extent of constitutional supercooling is higher in the centre than that at the edge, owing to the fact that the power density of the CO_2 laser beam at the centre is higher than that of the edge (see Section 6.5.2.3).

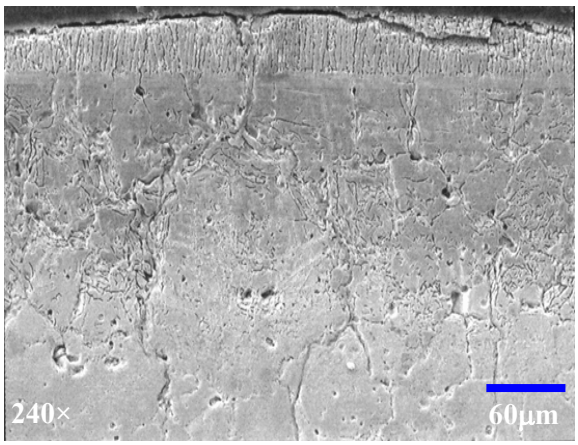

(a)

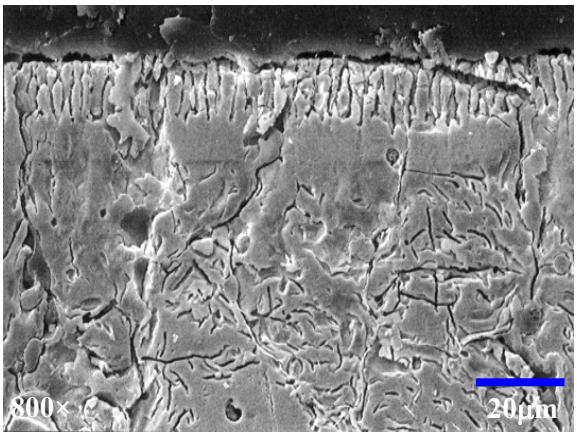

(b)

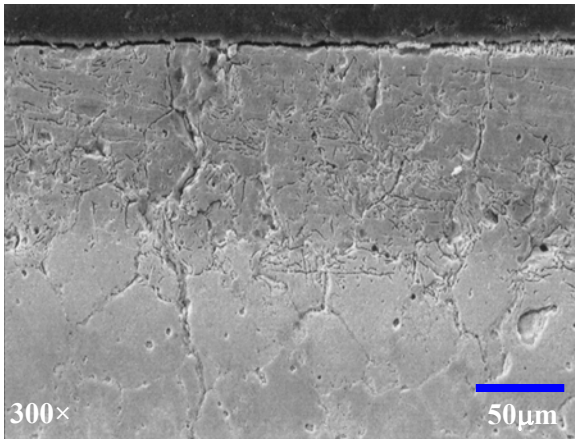

(c)

Fig. 6.11. Typical SEM cross-section view of the CO_2 laser modified MgO-PSZ surface layer (a) at the centre region, (b) at the midway point, (c) at the edge of the laser track (power density of 1.6 kW/cm^2 and traverse speed of 2000 mm/min).

The cross-section of the uppermost layer of the CO_2 laser modified MgO-PSZ with relatively low power density shows a columnar crystalline structure vertical to the substrata at the melted zone, along with irregular crystalline grain in the heat affected zone (HAZ) (see Fig. 6.11a) at the midway point of the track. The thickest section of the columnar crystalline structure at the midway point is

about 60 μm (see Fig. 6.11(a)), while the thickness of the columnar crystalline at the central region is about 20 μm (see Fig. 6.11(b)). The irregular crystalline grains typically exist at the edge of the track as shown in Fig. 6.11(c), suggesting that this region did not totally melt in the laser processing. These results reveal that the highest solidification rate is at the midway point and the lowest solidification rate is at the edge of the track.

6.5.2. The Effects of CO_2 Laser Power Density Variations

6.5.2.1. The *G/R* Ratio

From Fig. 6.8 and Fig. 6.10, it can be seen that CO_2 laser induced solidification microstructures differ not only with changes in specific energy, but even across the same track. With a relatively high power density, the *G/R* ratio in the centre of the track is small enough to produce the dendritic structure shown in Fig. 6.8(b-1), while the cooling rate is so fast that spherical cells may coalescence to form the coral structure shown in Fig. 6.8(b-2). At the midway point of the track, some cellular structures shown in the right hand portion of Fig. 6.8(c) could be induced from the direct solidification under supercooling, indicating that the *G/R* ratio at this region can cause the cell formation but not small enough to produce dendritic structure. At the edge of track, only the hexagonal structure shown in Fig. 6.8(d) formed, showing the small solidification rate and large *G/R* ratio. The higher degree of laser induced solidification at the midway point region than that at both ends revealed by the cross-section analysis (see Fig. 6.9) confirmed that highest solidification rate and smallest *G/R* ratio at the centre region. Therefore, the *G/R* ratio increases from the centre to midway point to edge region of the track as shown in the Fig. 6.8(a). With relatively low power density, cellular structure shown in Fig. 6.10(c-1) and (c-2) form at the midway point of the track and hexagonal structure is shown in the centre and edge of the track, indicating the *G/R* ratio is smallest at the midway point. The hexagonal structure in the centre shown in Fig. 6.10(b) is less planar than that at the edge of the track shown in Fig. 6.10(d), showing that the *G/R* ratio in the centre may be smaller than that at the edge. It also confirmed by the cross-section analysis (see Fig. 6.11) that the highest solidification rate at the midway point and the lower solidification rate at the edge of the track. Therefore, the *G/R* ratio is smallest at the midway point and highest at the edge region of the track shown at the Fig. 6.10(a).

6.5.2.2. Thermal Gradient and Cross-sectional Analysis

The typical CO_2 laser induced cross-sectional microstructure on the MgO-PSZ appears to consist of a columnar or dendritic structure perpendicular to the substrata (see Fig. 6.9 and Fig. 6.11). A high heat input from a laser beam facilitates surface localised melting at a very high efficiency. That is, the major portion of the absorbed energy is used for melting, with only a small fraction going into the heating of the solid sub-surface material. This ability to maintain a cold substrate whilst melting

a thin surface layer of material results in rapid quenching of the molten layer once the beam is removed. Thermal gradients at liquid-solid interface layer are very steep. In this case, melt solidification is almost a self-quenching process which allows rapid growth rate. Crystal growth takes place along the thermal gradient. The absorption coefficient of the molten oxides of the CO_2 laser radiation is high. The laser radiation is absorbed in a region within about 0.1 mm of the laser exposed external surface [26]. As shown in Fig. 6.9, the columnar dendritic structure appeared on the up-most layer with the 120 μm depth in the CO_2 laser radiation region (2.5 kW/cm^2), while the columnar structure on the up-most layer with the 60 μm depth (1.6 kW/cm^2). Moreover, heating of the internal regions of the MgO-PSZ takes place via thermal diffusion. Capillary convection also takes place in the melt and may seriously perturb the flatness of the liquid-solid interface. As such, the irregular grains in the heat affected zone could be due to the capillary convection. In fact, such columnar structures have been reported at the middle and bottom regions of the CO_2 laser clad ZrO_2 ceramics layers on steel 16MnCr5 by Ouyang *et al* [240] and on high Al_2O_3 content ceramics treated with CO_2 laser radiation previously by Bradley *et al* [241], Lee *et al* [242], and Sheih *et al* [243].

6.5.2.3. The Effects of the TEM_{01} Beam and the Resulting Temperature Distribution

The *G/R* ratio distribution across the width of the CO_2 laser treated track was indicative of a non-gaussian laser beam. Indeed, the CO_2 laser used in the experiment is a TEM_{01} multi-mode laser, the profile of which when burnt in acrylic is shown in the Fig. 6.12.

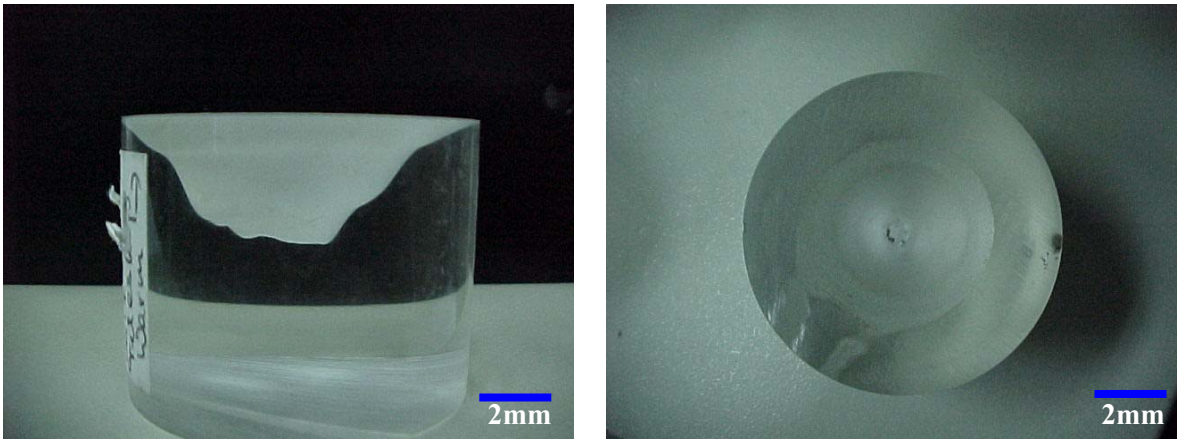

(a) (b)

Fig. 6.12. CO_2 laser beam profile burnt in acrylic (a) side view and (b) top view.

The power density distributions of the CO_2 laser appear to be multi-mode (see Fig. 6.12). It is evident that the CO_2 laser beam does not display a maximum peak in the middle of the beam, rather the peak is around the midpoint of the beam (see Fig. 6.12(a)). Also, a small part of the acrylic in the centre was not burnt out after CO_2 laser interaction, further indicating the maximum power

density is not situated in the centre. Based on the convective currents caused by a Gaussian beam profile [244,245] and the intensity distribution of a TEM_{01} beam profile, a schematic diagram of the convection currents within the CO_2 laser treated track on the MgO-PSZ was generated and is given in Fig. 6.13. From this schematic intensity distribution of the CO_2 laser beam, it is evident that the highest intensity ad hence the highest temperature is not at the centre of beam, but at the midway point near to the centre. This is in accord with the observation that the cellular structure formed at the midway point region which had the smallest *G/R* ratio (at a relatively low power density). According to the intensity distribution, the temperature in the centre is higher than that at the edge of laser beam, so the *G/R* at the centre is smaller than that of the edge. Such a *G/R* ratio distribution resulted in the formation of coral and dendritic structure in the centre and the hexagonal structure at the edge of the track (at a relatively high power density). In addition, this *G/R* ratio distribution also caused the formation of a less planar hexagonal structure in the centre than that at the edge of the track (at a relatively low power density). From an inverse analysis of the varied microstructures produced across the same CO_2 laser track, it is possible to further confirm temperature distribution over the surface of the MgO-PSZ according to the different stages of solidification exhibited in the same track.

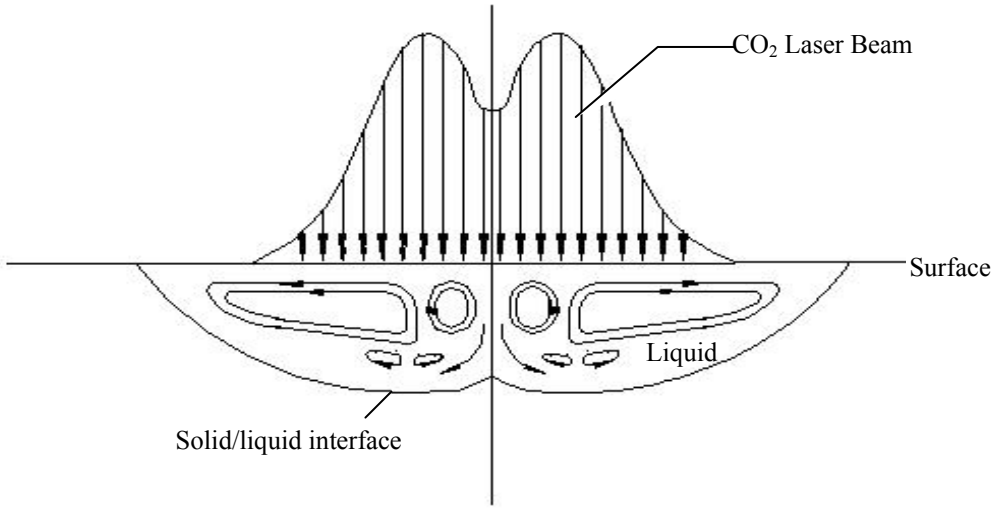

Fig. 6.13. Schematic diagram of the convection currents generated within the CO_2 laser melt pool

When a laser beam has a sufficient power density, convective currents will be generated by the surface tension gradients from the temperature gradient at the free surface. The strong turbulent convection in the centre of the TEM_{01} laser beam will be very complex and will change with the power density of the CO_2 laser beam and the diameter of beam. Because the roots of the dendrite arm are often smaller in diameter than other areas they are very susceptible to separation from the main stalk. When the arm that is separated is subsequently carried away into slightly supercooled liquid, a new crystal is formed without a new crystal is formed without a new nucleation event

[214]. As such, in the laser solidification process, convection provides a feasible mechanism not only for the breaking off of dendrite arms, but also for dissipating superheat in the liquid so that the transported arm can grow [246]. On the other hand, strong turbulent convection has the added effect of bring heat pulses to the interface that accelerates the melting off of dendrite arms [247]. Some fine-grain cellular structures as shown in the left part of Fig. 6.8(c) at the midway point on the MgO-PSZ, which show the undulate current, could come from the melted-off arms due to a strong convection flow exists in the melt pool. While a few dendrites with complete arms in the centre indicate that some regions have little and no convection. This could be attributed to the fact that the turbulent convection caused by TEM_{01} mode beam profile is very complex. Indeed, such findings have been reported by a number of workers conducting research into the laser treatment of various ceramics and alloys. The microstructure of MgO-PSZ surfaces subjected to laser radiation was characterised by Chaim *et al* [248]. Pei *et al* [207] noted that both equiaxed and dendritic microstructures were obtained in different regions of the same laser clad ZrO_2 layer, concluding that the differences were related to different cooling rates in the various regions of the laser clad ZrO_2 layer. Similar results were obtained by Liu [201] after laser sealing Y_2O_3-ZrO_2 and MgO-ZrO_2 ceramic coatings. Shih *et al* [249] observed that across a $YBa_2Cu_3O_x$ and laser clad track different microstructures were found in different regions, as did Shieh [250] across a SiO_2-Al_2O_3 laser clad track. Additionally, both workers noted that not only were cellular and dendritic microstructures visible, but also that the microstructures were much finer on the edge of the clad track than in the centre. Such differences in microstructure type and size were ascribed to the varying degrees of constitutional supercooling, which, according to McCallum *et al* [251], are inherent in laser processes. In this study, the different morphologies within one CO_2 laser treated track was observed and indicated the different stages of cell formation, due to the various extent of constitutional supercooling and the different ratios of G/R across from the centre toward the edge of the track.

6.5.3. The Effects of Other Phenomena on the Induced Solidification Microstructure

The relatively high traverse speed of CO_2 laser treatment generated the relatively high cooling rate that influenced the formation of the microstructure. Fig. 5.8(a) presents a typical solidified microstructure in the centre of a CO_2 laser track induced with a relatively high speed of 4000 mm/min and a power density of 1.9 kW/cm^2. It was found that when the traverse speed increased, the coral structure disappeared and uniform cellular crystalline structures were produced. The microstructures are distinctive when compared with those generated at low traverse speeds. This is because a further increase in the cooling rate eliminated the coalescence and growth of cells.

The craters generated in the CO_2 laser treatment influenced the thermal effects in the local region, in turn, brought about the different structures near the craters. For example, there are elongated cell around the crater in the region of cellular structure in Fig. 5.9(a) and (b) and even finer grain

structures appears at the middle of the crater in the region of hexagonal structure Fig. 5.9(c). The reason for these is associated with the presence of craters and closed porosity. The existence of these defects produced complex heat transfer locally resulting in the variation of microstructures.

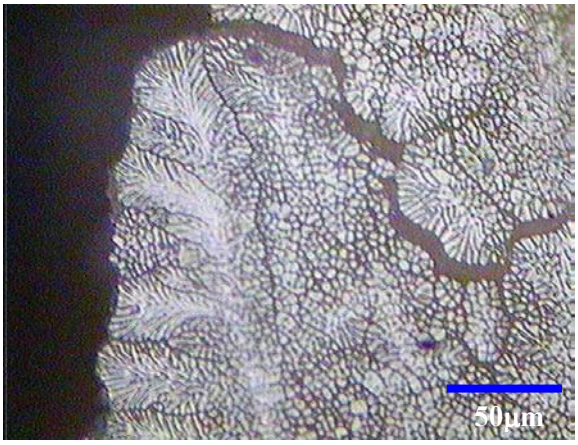

Fig. 6.14. Dendritic structures located near the crack (2.5 kW/cm^2 power density and 2000 mm/min traverse speeds).

The generated cracks in the CO_2 laser treatment influenced the thermal gradient in the region. Fig. 6.14 shows very obvious dendritic structures along the edge of the crack occurred near to the centre region of the CO_2 laser treated track, while the cell crystal formation took place far away on the edge of the crack. This indicates that the convection happened at the centre of the track and stopped at the edge of crack, where dendrites formed and secondary arms were complete. The orientation of dendritic growth is toward the edge of crack.

6.6. Summary

In this chapter the theories relating to laser rapid solidification were introduced to explain the different solidified microstructures generated in the CO_2 laser surface processing of the MgO-PSZ. The main conclusions can be made as follows:

1. It was seen that the obtained solidification microstructures on the surface of the MgO-PSZ differ not only with changes in laser parameters (power density and traverse speed), but even across the same CO_2 laser treated track.

2. With a relatively high power density, “coral” and dendritic microstructures occurred in the centre of laser treated track, while fine-grain structures from melted-off arms of dendrites and cells from direct solidification under supercooling were found at the midway point of the track and hexagonal structures were found at the edge of the track. Such different microstructures within the CO_2 laser treated track were due to the high degree of constitutional supercooling at

the centre and the midway point and low level of constitutional supercooling at the edge of the track.

3. With a relatively low power density, the hexagonal microstructure appeared at both the centre and the edge of the CO_2 laser treated track, while the cell structure formed at the midway point region. This indicates that the highest extent of constitutional supercooling resulted in the cell structure and took place at the midway point. The lower extent of constitutional supercooling resulted in the hexagonal structure observed in the centre and at the edge of the laser treated track on the MgO-PSZ surface.

4. The intensity distribution of a TEM_{01} CO_2 laser beam resulted in different temperatures and different G/R ratios within the CO_2 laser treated tack, and in turn induced the various microstructures across the track.

CHAPTER 7
The Effects of CO_2 Laser Radiation on the Wettability Characteristics of Magnesia Partially Stabilised Zirconia

This Chapter investigates the modification of the wettability characteristics of the MgO-PSZ bioceramic following CO_2 laser irradiation. To study the wettability characteristics, contact angles between a set of test liquids and the surface of the CO_2 laser treated MgO-PSZ were measured in comparison with the untreated MgO-PSZ. The influential factors active in wettability characteristics were analysed and primary mechanism was deduced.

7.1. Introduction

Since the applied energy of lasers can be placed precisely on a surface only where it is needed, lasers provide the contemporary scientist and engineer with a controllable and flexible tool for surface engineering. The interactions between the biological environment and biomaterials take place on the materials surface. Hence, it is of paramount importance to fabricate biomaterials with adequate bulk properties followed by a special treatment to enhance the surface property [59].

From a historical perspective, Baier's proposal that critical surface energy can be directly linked to biocompatibility is perhaps the most penetrating concept among the few generalities offered to explain rules of biocompatibility. This theory, in its most general form, recognises that surface energy must control the way biologic fluids interact with materials and that this interaction, in turn, must primarily influence tissue and cell reactions [13]. Neumann and co-workers employed their "equation-of state" approach to calculate interfacial tensions from contact-angle measurements that, in turn, were used to predict cell adhesion [252] and thromboresistance [253]. The wettability and interfacial interactions in bioceramic-body-liquid system were investigated and low adherence was observed at the interface between the Al_2O_3 and ZrO_2 and the body liquids [254].

To date, much research has been carried out to study the effects of excimer laser radiation on the wettability characteristics of polyethylene terephthalate (PET) in film [133] and sheet [142] forms, as well as polyparaphenylene terephthalamide (PPTA) [143]. Moreover, it was shown that the surface of biocompatible polymer blends of polycarbonate (PC) and polymethyl methacrylate

(PMMA) could be specifically patterned by excimer laser radiation [149]. Both wetting and adhesion properties are enhanced by this kind of surface structure. Kappel [128] has shown that the texturing of ceramic (with an excimer laser 248 nm) can improve the adhesion strength by up to 20 %. Such an improvement is said to the formation of raised microscopic protrusions over the surface. Lawrence and Li have demonstrated practically of employing different types of lasers to effect changes in the wettability characteristics of ceramics [130,131,255] metals [256] and polymers [151]. Surface treatment of the low-density polyethylene (LDPE) films [150] by the CO_2 laser pulses caused a significant laser-induced oxidation and the sample subjected to two pulse showed the highest wettability. Yet, despite a growing amount of work conducted with engineering materials and biopolymers, no work has been conducted on the laser process for the wettability modification of bioinert ceramic so far.

7.2. Experimental Procedures

The material specification and CO_2 laser experimental arrangement are detailed in Section 5.2.1 and 5.2.2. The MgO-PSZ was irradiated using the defocused TEM_{01} mode CO_2 beam with a beam spot diameter of 11 mm and laser output power range from 0.6 kW to 2.4 kW.

7.2.1. Wettability Characteristics Analysis Procedure

To investigate the effects of CO_2 laser irradiation on the wetting and surface energy characteristics of the MgO-PSZ, a set of sessile drop control experiments were carried out using glycerol, formamide, etheneglycol, polyglycol E-200 and polyglycol 15-200 with known total surface energy, γ_{lv}, dispersive, γ_{lv}^{d} and polar, γ_{lv}^{p} component values [257] detailed in Table 7.1.

Table 7.1. Total surface energy (γ_{lv}), dispersive (γ_{lv}^{d}) and polar (γ_{lv}^{p}) components for the selected test liquids [257].

Liquid	γ_{lv} **(mJ/m^2)**	γ_{lv}^{d} **(mJ/m^2)**	γ_{lv}^{p} **(mJ/m^2)**
Glycerol	64.0	34	30
Formamide	58.3	32.3	26.0
Etheneglycol	48.3	29.3	19.0
Polyglycol E-200	43.5	28.2	15.3
Polyglycol 15-200	36.6	26.0	10.6

The contact angles, θ, of the test liquids on the untreated and CO_2 laser treated MgO-PSZ were determined in atmospheric condition at 25°C using a sessile drop measure machine (First Ten

Ångstroms, Inc). In order to estimate the influence of contaminant layers on the measurement results, the specimens of the untreated MgO-PSZ were cleaned with acetone in an ultrasonic bath for 2 h, rinsed with distilled water several times and dried in a vacuum oven at 90°C for 12 h. The test liquids were used to measure θ for the cleaned sample. It was observed that the value of θ on the cleaned sample are 1.5°, 1.2°, 1.0°, 0.9° and 0.8° for glycerol, formamide, etheneglycol, polyglycol E-200 and polyglycol 15-200 respectively lower than that of the received sample without the cleaning. It is deemed that the contaminant on the surface of the MgO-PSZ has only a slight influence on θ. Since the contaminant is a minor factor active in the wettability characterisation, it is reasonable to preclude of cleaning pre-treatment for practical application of CO_2 laser treatment. In order to explore the potential of CO_2 laser treatment as an industrial and economical processing for altering the wettability characteristics of MgO-PSZ, the work was conducted in a normal atmospheric environment without pre-cleaning. Each measurement of θ lasted for 3 mins with profile photographs of the sessile drop being obtained every minute and a mean value being subsequently determined. After the test liquid drops for each liquid attached and rested on the MgO-PSZ surface, the drops consistently reached an equilibrium state in around 6 s. Thereafter they remained motionless and the magnitude of the θ changed little with time. On average only ± 0.5° deviation of the θ for each test liquid was observed during the 3 mins of measuring when photographs were taken every minute; indicating that the shape of the drop was stable in its equilibrated state. The difference between the θ value on the left hand side and the right hand side of the sessile drop is very small, which generates a ± 0.36° deviation. In turn, the average total deviation for the θ measurement was ± 0.86°.

7.3. The Effects of CO_2 Laser Radiation on Wettability Characteristics

7.3.1. Contact Angle

An optical micrograph of a sessile drop of glycerol placed on a MgO-PSZ sample before and after CO_2 laser irradiation with the θ results are shown in Fig. 7.1. Additionally, as Table 7.2 shows, with all the control liquids used the MgO-PSZ experienced a significant reduction in θ as a result of interaction with the CO_2 laser beam. Since the contaminant has been proved to be a minor factor active in the wettability characterisation, a sharp reduction of θ should be the effect of CO_2 laser treatment instead of pollution elimination. Due to the similar trend of the change in θ of the test liquids for the untreated sample and CO_2 laser treated samples with various power densities as shown in the Table 7.2, the glycerol was used as a typical liquid expressing the change in θ and thus the wettability characteristics of the MgO-PSZ for the concise statement.

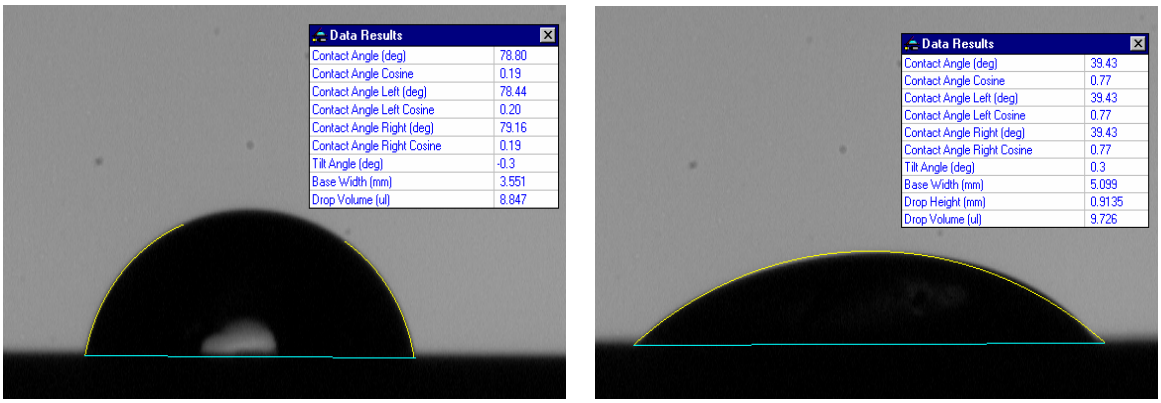

(a) (b)

Fig. 7.1. Contact angels for glycerol on (a) the untreated MgO-PSZ and (b) CO_2 laser treated MgO-PSZ (power density of 1.6 kW/cm^2 and traverse speed of 2000 mm/min).

Table 7.2. Mean values of contact angles formed between the untreated and laser treated MgO-PSZ for various power densities (traverse speed of 2000 mm/min) and the selected test liquids at 25^{0}C.

Test Liquid	**Contact Angle, θ (deg)**					
	Untreated	**CO_2 Laser treated (kW/cm^2)**				
		0.5	**0.9**	**1.6**	**1.9**	**2.5**
Glycerol	79	76	62	40	50	54
Formamide	73	71	57	36	44	50
Etheneglycol	61	60	48	29	38	41
Polyglycol E-200	53	51	40	26	33	36
Polyglycolycol 15-200	35	33	28	19	22	27

7.3.2. The Effect of Surface Oxygen Content

The observed increase in the wetting performance of the MgO-PSZ would have certainly been influenced by the increase in the oxygen content of the MgO-PSZ surface as a result of the CO_2 laser treatment, since this is known to increase the likelihood of wetting [14,146,147,258,259]. Wetting is governed by the first atomic layers of the surface of a material, thus, in order to determine accurately the element content of O_2 on the surface of the MgO-PSZ, it was necessary to examine the surface using X-ray photoemission spectroscopy (XPS).

As can been seen from the Fig. 7.2, augmentation of the surface oxygen content of the MgO-PSZ after interaction with the CO_2 laser beam is observed. The values obtained shows that the oxygen content increased from an initial value of 41.6 at% to 64.3 at%, while the θ of glycerol decreased from an initial value of 79° to 40°. As one can see, an overall increase of some 22.7 at% in the amount of O_2 on the this CO_2 treated MgO-PSZ sample could have occurred due to the oxidisation

of the MgO-PSZ surface during melting. When the oxygen content increased to value of the 64.3 at%, the θ decreased to its minimum value. This indicates that O_2 enrichment of the CO_2 laser treated MgO-PSZ surface was active in promoting wetting and adhesion, as well as bonding.

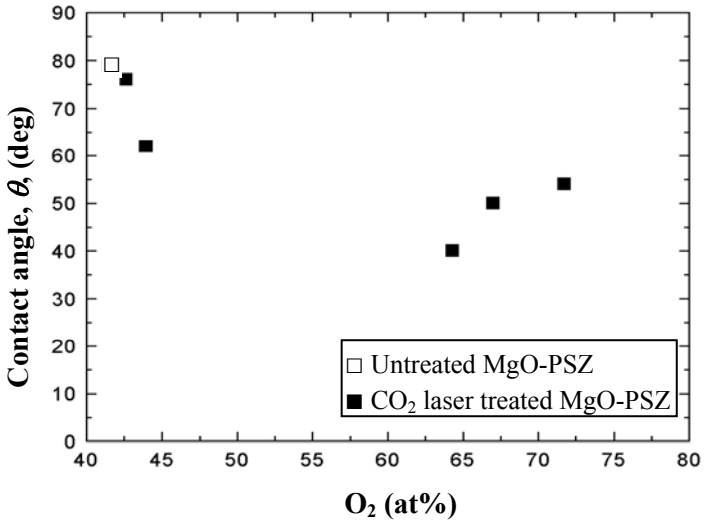

Fig. 7.2. Relationship between the θ (glycerol) of the untreated and CO_2 laser treated MgO-PSZ and oxygen content.

Such a finding is similar to that of Song *et al* [146,147], who observed that surface oxygen content increased after laser treatment and in turn, effected a reduction in the θ. Nevertheless, when the oxygen content is higher than the point at 64.3 at%, the θ increased despite the further increase of oxygen content. This suggests that other mechanisms are active and more dominant and so cause the θ to increase.

7.3.3. The Effect of Surface Roughness

By varying the CO_2 laser operating parameters it was possible to obtain a narrow range of surface roughness values. The values of θ for glycerol in contact with the CO_2 laser treated MgO-PSZ samples were obtained at various points across the narrow range of surface roughness values. After CO_2 laser treatment, the roughness of the MgO-PSZ surface increased with the power density. This might be the result of turbulent convection in the melt pool caused by the TEM_{01} mode of CO_2 laser beam. A model similar to that for heterogeneous solid surfaces can be developed in order to account for surface irregularities, being given by Wenzel's equation [260]:

$$r_a\left(\gamma_{sv}-\gamma_{sl}\right)=\gamma_{lv}\cos\theta \qquad (7.1)$$

where r_a is the roughness factor defined as the ratio of the true to apparent surface areas, θ is the contact angle for the wetting of a rough surface. If r_a is large, that is the rougher surface, then $\cos\theta$ is large and θ decrease for the wetting surfaces ($\theta < 90°$). So, when r_a increases the θ decreases as $\theta < 90°$.

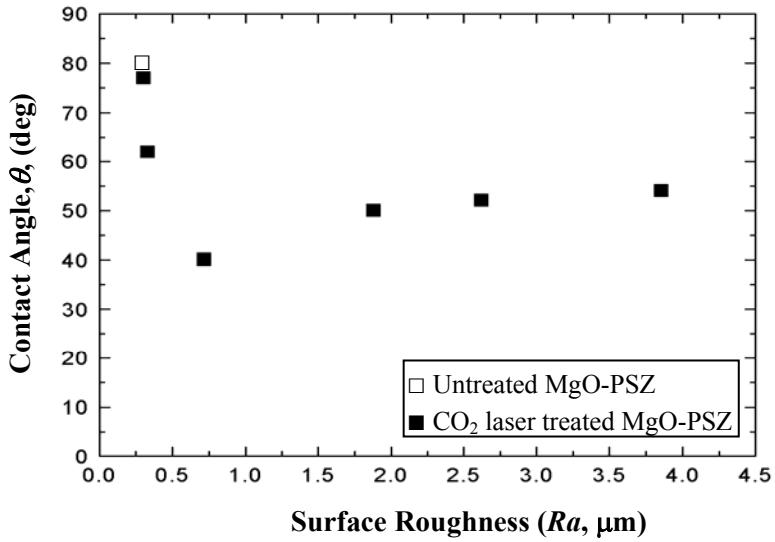

Fig. 7.3.Relationship between θ (glycerol) on untreated and CO_2 laser treated MgO-PSZ and R_a

The surface roughness (R_a) of the MgO-PSZ was measured by a profilometer (Surface Tester, SV-600). Five measurements were made at different places across the laser treated track on each sample and mean values were obtained. As one can see from Fig. 7.3, the surface of the untreated MgO-PSZ sample was very smooth, with an average roughness value (R_a) of around 0.295 μm. As shown in Fig. 7.3, CO_2 laser treatment results in θ to a minimum of 40° at R_a of 0.717 μm from an initial maximum θ of 79° in the untreated state at R_a of 0.295 μm. Indeed, this observation is in accord with Equation (7.1), an increase in R_a ought to effect a decrease in θ when it is below 90°, signifying that the alternation of R_a contribute the reduction of θ for the MgO-PSZ after CO_2 laser treatment. However, it is also worth remarking that the increase in R_a of the MgO-PSZ occasioned after laser treatment is very small, only about 0.4 μm, and not proportional to the considerable reduction of θ. In fact, it should be noted that in this work the CO_2 laser treatment effects changes in many other surface properties besides R_a. Furthermore, the significant increase in R_a from 0.717 to 3.854 μm occasioned with a slight increase in θ from 40 to 54° contradicts Equation (7.1) and previous finding [261] that the higher surface roughness is corresponding to the lower θ on the ZrO_2. Consequently, postulation that other factors such as changes in the surface energy and the surface oxygen content play a more predominant role than surface roughness in the decrease of θ

for the CO_2 laser treated MgO-PSZ is not unreasonable. This is explained in more detail in Section 7.5.

7.3.4. The Effects of Solidified Microstructures and Surface Melting on Wettability Characteristics

To analyse the effects of solidified structures on the wettability performance of the MgO-PSZ, a series of wetting experiments using glycerol were conducted to determine the θ for the different microstructures generated in a range of CO_2 laser power densities.

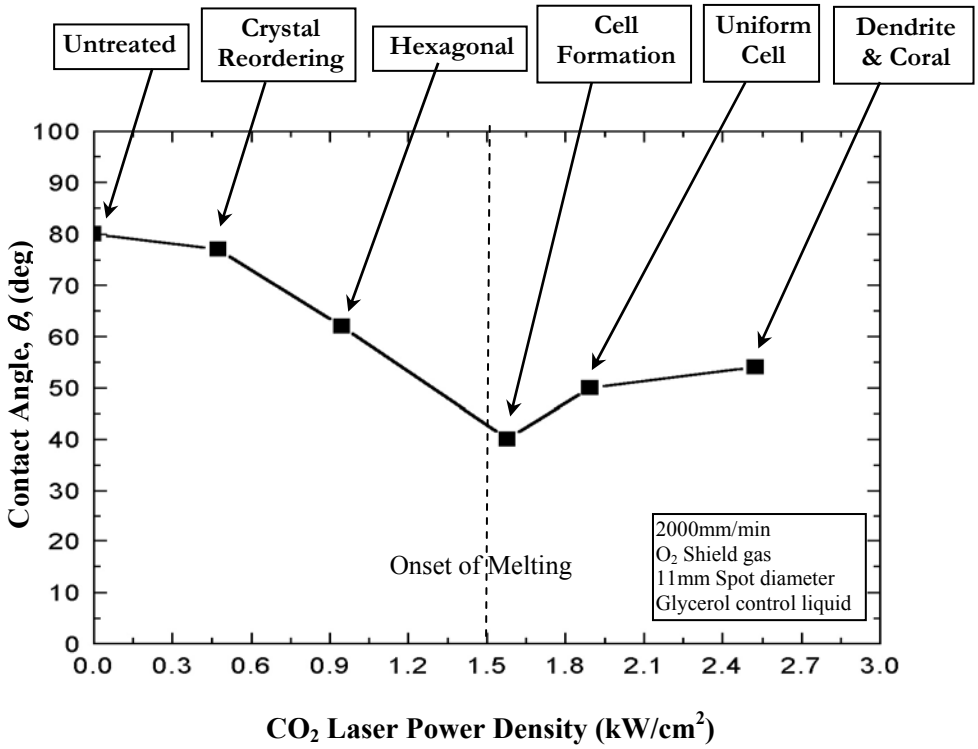

Fig. 7.4. Relationship between contact angle on the untreated and CO_2 laser treated MgO-PSZ and power density and solidified structure.

As discussed in the Chapter Six, the hexagonal structure, cell structure and dendritic structure were formed on the CO_2 laser treated MgO-PSZ samples. In order to simplify the analysis, the structures were defined according the main structures on the MgO-PSZ after CO_2 laser treatment as shown in the Fig. 7.4. As one can see from Fig. 7.4, the surface structures of the MgO-PSZ play a significant role in θ. The mere reordering of the crystals occurred at power densities below around 0.5 kW/cm^2 appears to have only a slight effect on θ, reducing it from 79° to 76°. In contrast, at around 0.9 kW/cm^2 θ decreases markedly from 77° to 62°, with a hexagonal structure being generated on the MgO-PSZ. With further increases in power density to around 1.6 kW/cm^2, θ decreases from 62° to 40°, with some cells beginning to form in the region due to the high temperature peak caused by the

intensity distribution of the CO_2 laser beam spot. One reason for this sharp reduction in θ may be related to the onset of melting at this power density, which would consequently imply that melting is an essential prerequisite for a significant reduction in θ. Further increase in power density resulted first in an increase in θ from 40° to 50°, corresponding with the formation of uniform cell structures and then to 54°, at which point dendrites and coral structures were observed. Indeed, work conducted by Zhang *et al* [262] found that considerable improvement in the bond strength of a Si_3N_4 ceramic could be realised only when excimer laser treatment of a structural alloy steel (SAE 4340) resulted in surface melting. Similarly, Lawrence [263] observed a sharp reduction in θ at the point of melting for an Al_2O_3/SiO_2 based oxide compound after high diode power laser (HPDL) treatment. In general, the CO_2 laser radiation induces the microstructural change and consequently causes a reduction of the θ on the MgO-PSZ. The θ begins to decrease significantly when the hexagonal structure forms on the MgO-PSZ. The onset of melting and cell formation creates a sharp decrease of θ.

7.4. Surface Energy and its Component Parts

The θ values for untreated and CO_2 laser treated MgO-PSZ with various power densities were shown in Table 7.2. It is possible to adequately estimate the dispersive component of the MgO-PSZ surface energy, γ_{sv}^{d}, by plotting the graph of cos θ against $(\gamma_{lv}^{d})^{1/2}/\gamma_{lv}$ according to Equation (3.8). Thus, according to Fowkes [89], the value of γ_{sv}^{d} is estimated by the gradient (= $2(\gamma_{sv}^{d})^{1/2}$) of the line which connects the origin (cos θ = -1) with the intercept point of the straight line (cos θ against $(\gamma_{lv}^{d})^{1/2}/\gamma_{lv}$) correlating the data point with the abscissa at cos θ = 1. Fig. 7.5 shows the best-fit plot of cos θ against $(\gamma_{lv}^{d})^{1/2}/\gamma_{lv}$ according to Equation (3.8) for the untreated and CO_2 laser treated MgO-PSZ-experimental control liquids system. From Fig. 7.5 the values of γ_{sv}^{d} for the untreated and CO_2 laser treated MgO -PSZ could be calculated.

Comparing the ordinate intercept points of the untreated and CO_2 laser treated MgO-PSZ-liquid systems in Fig. 7.5, it can been seen clearly that for the untreated MgO-PSZ, the best-fit straight line intercepts the ordinate closer to the origin. In case of a 0.5 kW/cm^2 power density, the best-fit straight line intercepts the ordinate relatively close to the origin. This is noteworthy since intercept of the ordinate close to the origin is characteristic of the dominance of dispersion forces acting on the MgO-PSZ material-liquid interfaces of the untreated and low power density treated sample, resulting in poor adhesion [89,90]. On the other hand, the best-fit straight line of samples treated at higher laser power density intercept the ordinate considerably high above the origin. The highest intercept point is found for the sample treated with laser parameters of 1.6 kW/cm^2 power density

and a traverse speed of 2000 mm/min. An interception of the ordinate above the origin is indicative of the action of polar forces across the interface, in addition to dispersion forces, hence improved wettability and adhesion is promoted [89,90]. Furthermore, because none of the best-fit straight lines intercept below the origin, it can be said that the development of an equilibrium film pressure of adsorbed vapour on the MgO-PSZ surface (untreated and CO_2 laser treated) did not occur [90].

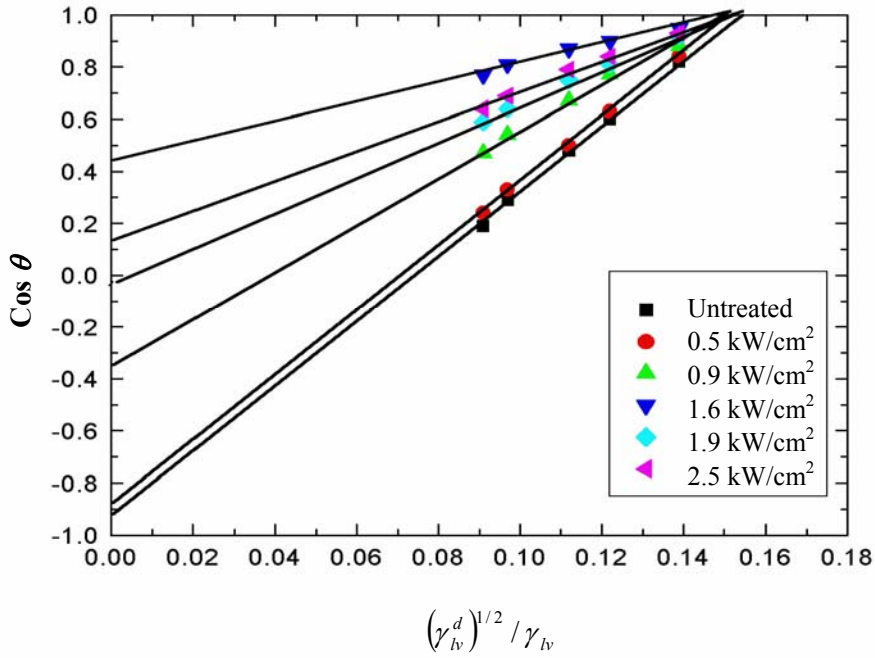

Fig. 7.5. Plot of cos θ against $\left(\gamma_{lv}^{d}\right)^{1/2}/\gamma_{lv}$ for the MgO-PSZ in contact with the wetting test control liquids, before and after CO_2 laser treatment of various parameters.

It is not possible to determine the γ_{sv}^{p} value of the MgO-PSZ directly from Fig. 7.5. This is because the intercept of the straight line (cos θ against $(\gamma_{lv}^{d})^{1/2}/\gamma_{lv}$) is at $2\left(\gamma_{sv}^{p}\right)\left(\gamma_{lv}^{d}\right)^{1/2}/\gamma_{lv}$, and so only refers to individual control liquids and not the control liquid system as a whole. Even so, it has been established that the entire amount of the surface energies due to dispersion forces either of the solids or the liquids are active in the wettability performance [89,92]. As such, it is possible to calculate the dispersive component of the work of adhesion, W_{ad}^{d}, by using only the relevant part of Equation (3.6) thus

$$W_{ad}^{d} = 2\left(\gamma_{sv}^{d}\gamma_{lv}^{d}\right)^{1/2} \tag{7.2}$$

Table 7.3 shows the values of W_{ad} calculated using Equation (3.4) and the values of W_{ad}^{d} calculated using Equation (7.2) for both the untreated and CO_2 laser treated MgO-PSZ with various power densities. Fig. 7.6 and Fig. 7.7 show the best-fit straight line plots of W_{ad} against W_{ad}^{d} for the

MgO-PSZ when it is both untreated and laser treated. From the plots of W_{ad} against W_{ad}^{d} one can see that the experimental results reveal that for each particular control liquid in contact with both the untreated and CO_2 laser treated MgO-PSZ surfaces, W_{ad}, determined from Equation (3.4), can be correlated with W_{ad}^{d}, determined from Equation (7.2), by the straight line relationship

$$W_{ad} = aW_{ad}^{d} + b \tag{7.3}$$

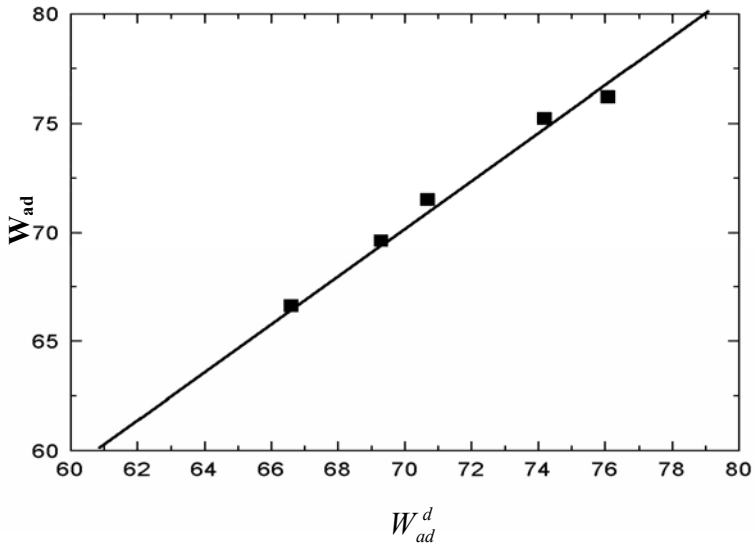

Fig. 7.6. Plot of W_{ad} against W_{ad}^{d} for the untreated MgO-PSZ.

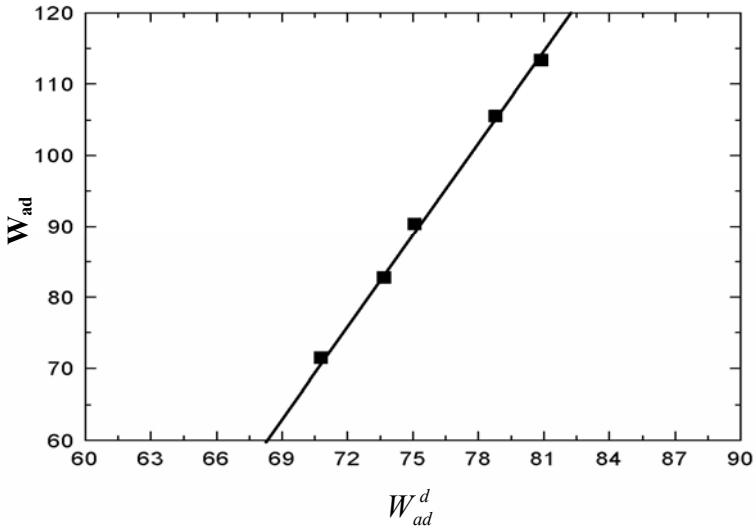

Fig. 7.7. Plot of W_{ad} against W_{ad}^{d} for the CO_2 laser treated MgO-PSZ (1.6 kW/cm^2 and 2000 mm/min).

Consequently, from the best-fit straight line in Fig. 7.6, the constant *a* was found to be 1.11 for the untreated MgO-PSZ. For the CO_2 laser treated MgO-PSZ, *a*, was deduced as being 4.25 from the

best-fit straight line in Fig. 7.7. Similarly, the values of *a* for various laser parameters shown in Table 7.3 were determined by W_{ad} and W_{ad}^{d}.

Table 7.3. Values of W_{ad} and W_{ad}^{d} of test liquids and the determined constant a from the plots of W_{ad} against W_{ad}^{d} for the untreated (UT) and CO_2 laser treated MgO-PSZ with various power densities.

Power Density (kW/cm^2) \ Liquids	a	Work of adhesion (W_{ad})					Dispersive work of adhesion (W_{ad}^{d})				
		Glyc	Form	Ethel	P1	P2	Glyc	Form	Ethel	P1	P2
UT	2.41	76.2	75.2	71.5	69.6	66.6	76.1	74.2	70.7	69.3	66.6
0.5	2.37	79.4	77.5	72.5	70.9	67.3	77.2	75.2	71.6	70.3	67.5
0.9	3.03	92.8	89.8	80.7	77.0	68.8	77.7	75.7	72.1	70.7	67.9
1.6	4.25	113.3	105.5	90.3	82.7	71.4	80.9	78.8	75.1	73.7	70.8
1.9	3.42	105.0	98.5	86.5	80.0	70.6	80.5	78.4	74.7	73.3	70.4
2.5	3.17	101.8	95.6	84.5	78.7	70.3	77.7	75.2	71.6	70.3	67.5

Note: Glyc: glycerol; Form: formamide; Ethel: etheneglycol; P1: polyglycol e-200, P2: polyglycol 15-200

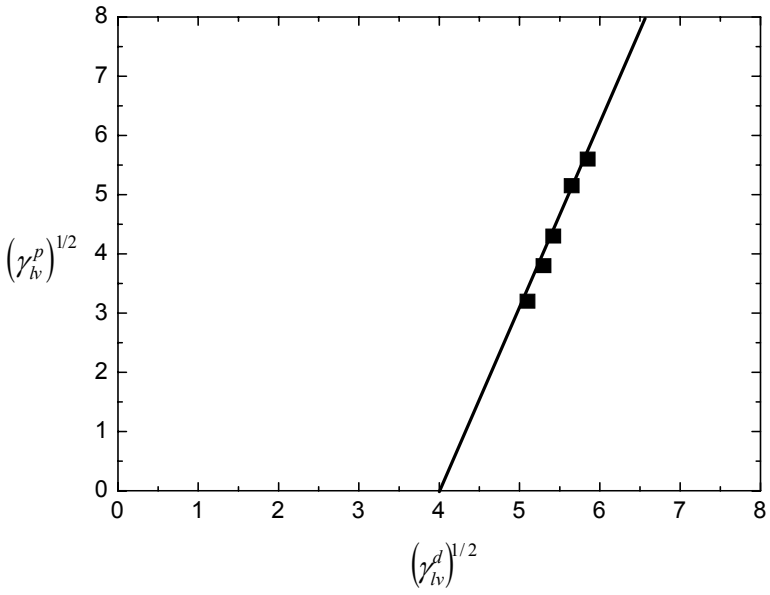

Fig. 7.8. Plot of $\left(\gamma_{lv}^{p}\right)^{1/2}$ against $\left(\gamma_{lv}^{d}\right)^{1/2}$ for the test control liquids.

Also, as Fig. 7.8, for the control test liquids used a linear relationship between the dispersive and polar components of the control test liquids surface energies was observed which satisfied the Equation (7.4).

$$\left(\gamma_{lv}^{p}\right)^{1/2} = 2.9\left(\gamma_{lv}^{d}\right)^{1/2} - 11.14 \tag{7.4}$$

By introducing Equation (7.2) into Equation (3.6) and rearranging, then

$$W_{ad}^{p} = (a-1)W_{ad}^{d} + b \tag{7.5}$$

or, alternatively

$$\left(\gamma_{sv}^{p}\right)^{1/2}\left(\gamma_{lv}^{p}\right)^{1/2} = (a-1)\left(\gamma_{sv}^{d}\right)^{1/2}\left(\gamma_{sv}^{p}\right)^{1/2} + \frac{b}{2} \tag{7.6}$$

By introducing Equation (7.4) into Equation (7.6) and differentiating with respect to $\left(\gamma_{lv}^{d}\right)^{1/2}$, considering that $\left(\gamma_{sv}^{d}\right)^{1/2}$ and $\left(\gamma_{lv}^{p}\right)^{1/2}$ are constant, then the following can be derived:

$$\left(\gamma_{sv}^{p}\right)^{1/2} = \frac{\left(\gamma_{sv}^{d}\right)^{1/2}(a-1)}{2.9} \tag{7.7}$$

Since γ_{sv}^{d} has already been determined for the untreated and laser treated MgO-PSZ from Fig. 7.5, then it is possible to calculate γ_{sv}^{p} for untreated and CO_2 laser treated MgO-PSZ using Equation (7.7). The values of γ_{sv}, γ_{sv}^{d} and γ_{sv}^{p} of the untreated and CO_2 laser treated MgO-PSZ are shown in Fig. 7.9. As one can see from Fig. 7.9, CO_2 laser treatment of the surface of the MgO-PSZ leads to an overall increase in the γ_{sv}, whilst, more importantly, also significantly increasing the γ_{sv}^{p}. The increase in γ_{sv} of the MgO-PSZ was primarily attribute to the increased γ_{sv}^{p}, since γ_{sv}^{d} was almost similar for all the samples. The increase, in particular the increase in γ_{sv}^{p}, had a positive effect upon the action of wetting and adhesion [92], since primarily both dispersion and polar forces were active to a greater extent [89,264]. The changes in the surface energy are thought to be due to the fact that CO_2 laser treatment of the MgO-PSZ results in the partial vitrification of the surface, a transition that is known to effect an increase in γ_{sv}^{p} [254], thus an improvement in the wettability characteristics and an increase in the adhesion at the interface in contact with the control liquids. This conclusion is in strong agreement with the findings of Agathopoulos *et al* [254], who from wettability analysis of SiO_2-TiO_2 in various states, from fully crystalline through to completely vitrified, found that as the vitrification of the material increased, the γ_{sv}^{p} increased. It is important to note that because of the long range ionic interactions between the MgO-PSZ and the test liquids, it is highly likely that the thermodynamically defined total solid surface energy, will be higher than

the sum of the γ_{sv}^{d} and γ_{sv}^{p}. Indeed, the derivation that leads to Equation (3.8) can only be done under the specific assumption that the ionisation potentials are all equal and that dipole-dipole random orientation interactions dominate over dipole-induced dipole random interactions. Although the increase in (excess) surface free energy will probably be less than the increase in the total lattice energy, on the other hand an absorbed liquid layer may shield the ionic fields substantially. As such, all the data derived from Equations (3.5), (3.8) and (7.7) should be considered as being semi-empirical. Notwithstanding this, as the studies by many researchers[129,131,254], it is reasonable to conclude from the data obtained from Equations (3.5), (3.8) and (7.7) that CO_2 laser treatment of the MgO-PSZ has caused an increase γ_{sv}^{p} at surface.

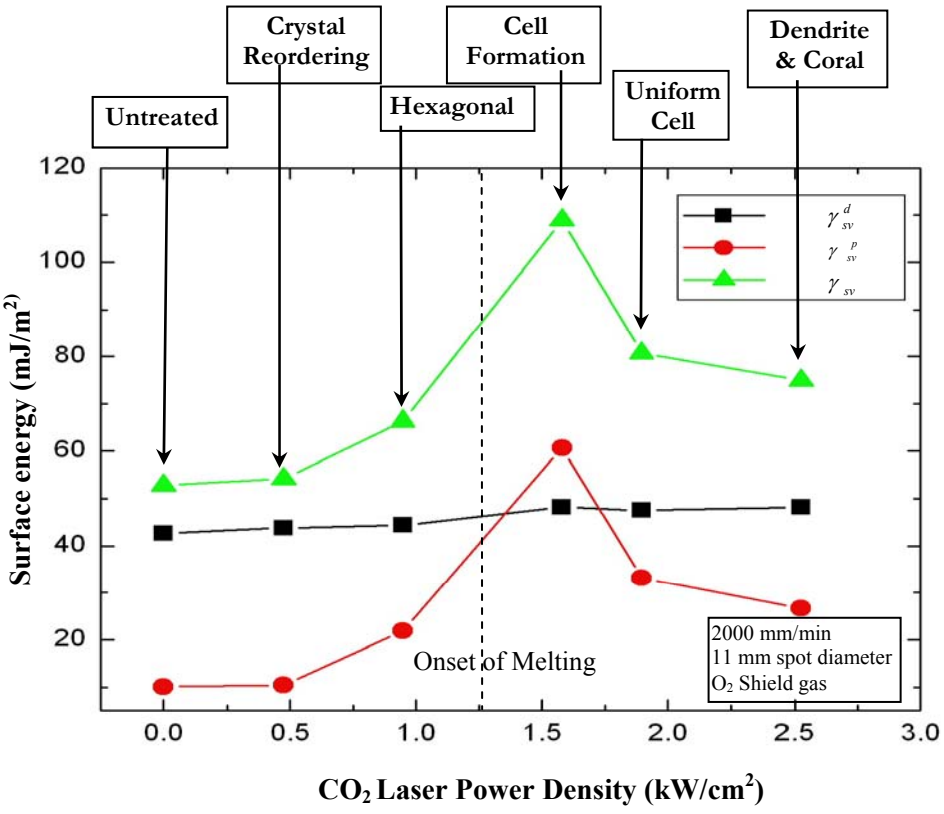

Fig. 7.9. Relationship between surface energy (γ_{sv}^{d}, γ_{sv}^{p} and γ_{sv}) of the CO_2 laser treated MgO-PSZ and power density

Moreover, as can be seen from Fig. 7.9, γ_{sv} and γ_{sv}^{p} changed depending on the microstructures obtained at different laser parameters. However, the dispersive energy γ_{sv}^{d} just has a very slight increase. At the point of the sample treated by low power density, mere crystal reordering appeared on the surface of the MgO-PSZ and obtained few change of surface energy comparing with untreated one. When hexagonal microstructure was shown on the surface of the MgO-PSZ, the

obvious increase in γ_{sv} and γ_{sv}^{p} was shown in Fig. 7.9. At the point of the sample treated by medium power density, the cell formation on the MgO-PSZ surface reached the maximum value of γ_{sv} and γ_{sv}^{p}. It suggests that the onset of melting accompanied the cell formation. With the increase of power density, the uniform cell microstructure on the surface of the MgO-PSZ cause γ_{sv} and γ_{sv}^{p} decreased from the maximum value. When the coral and dendritic microstructures appear on the surface of the MgO-PSZ, γ_{sv} and γ_{sv}^{p} had a further reduction from the maximum place.

7.5. Identification of the Predominant Mechanisms Active in Wettability Characteristics

The different CO_2 laser power densities brought about differences in surface roughness, microstructure, surface oxygen content and surface energy simultaneously. All these surface properties influenced the wettability characteristics of the MgO-PSZ. It is essential to identify the effect of each factor and find the predominant mechanism active in governing the wettability characteristics of the MgO-PSZ. Fig. 7.10 shows the relationship of the wettability characteristics ($\cos\theta$ for glycerol) and the influential factors of the roughness, the γ_{sv}^{p} and oxygen content. As evident from Fig. 7.10, the rougher surface of the modified sample has a higher value of $\cos\theta$ than the smooth, untreated one. However, the change in $\cos\theta$ is not proportional to the alteration in the surface roughness, with $\cos\theta$ increasing sharply up to a roughness 0.717 μm, then, decreasing despite a considerable increase in surface roughness. Therefore, other mechanisms, namely the oxygen content and the γ_{sv}^{p}, may play a more predominant role in influencing the wettability of the CO_2 laser treated MgO-PSZ than just the surface roughness. As is apparent from Fig. 7.10, $\cos\theta$ increased with an increasing surface oxygen content below 63.4 at%. This is in accord with the established theory for the relationship between the oxygen content of materials and their wettability. Nonetheless, when the value of the surface oxygen content exceeds 63.4 at%, $\cos\theta$ decreases, thus, oxygen content is not a major factor active in changing the wettability of the MgO-PSZ. A clear relationship between the value of $\cos\theta$ and the γ_{sv}^{p} observed in Fig. 7.10, and Fig. 7.11 reveals that an increase in the γ_{sv}^{p} will cause a rise in $\cos\theta$. So, it is deemed that the γ_{sv}^{p} influences the wettability characteristics of the MgO-PSZ. Indeed, it was found by Lawrence [263] that surface energy was the most predominant factor governing the wetting characteristics of the SiO_2/Al_2O_3-based ceramic following with irradiation of high power diode laser (HPDL).

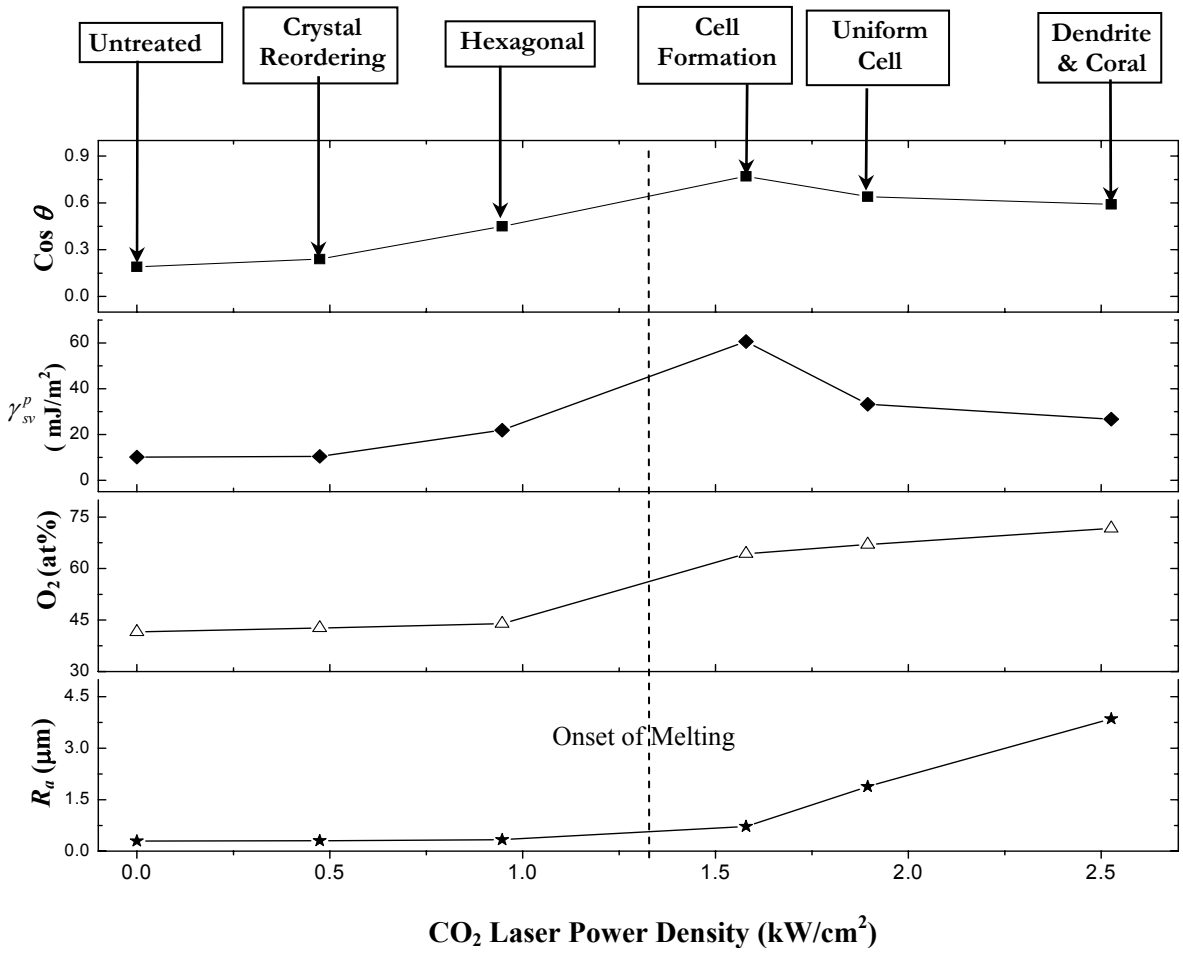

Fig. 7.10. Relationship between cos θ for glycerol and the surface roughness, the surface oxygen content, the γ_{sv}^{p} and microstructures of the untreated and CO_2 laser treated MgO-PSZ.

The foregoing results are a clear indication that interaction of the CO_2 laser beam with the MgO-PSZ resulted in a decrease in θ formed between the control liquids and the material. Such changes in the wettability characteristics are influenced primarily by: modifications to the surface roughness; changes in the surface oxygen content and changes to the surface energy of the MgO-PSZ. Firstly, CO_2 laser treatment of the surface of the MgO-PSZ generated a rougher surface and thereby reduced θ. Secondly, the increase in the surface oxygen content of the MgO-PSZ resulting from CO_2 laser treatment will be influential in the promotion of wetting, because an increase in surface oxygen content inherently effects a decrease in θ and *vice versa*. Lastly, an increase in γ_{sv}^{p} resulting from the melting and resolidification of the surface of the MgO-PSZ occurred. This naturally created a different microstructure that quite possibly improved the action of wetting and adhesion.

But, from the above discussion it is not clear whether the surface roughness, the surface energy (by way of microstructural changes) or the oxygen content alone, or a combination thereof, are the

principal factors influencing the observed changes in the wettability characteristics of the MgO-PSZ after CO_2 laser surface treatment. Consequently, several stages of polishing were used to isolate the various influential factors detailed above and thus analyse and qualitatively quantify the effect each one had on the wettability characteristics of the MgO-PSZ. In the first stage, the surfaces of the untreated MgO-PSZ and CO_2 laser treated MgO-PSZ (1.6 kW/cm^2) with the largest change in θ were ground with a grinding paper (180 Grit SiC) for 3 mins, whilst still retaining the CO_2 laser treated microstructure. In this way it was possible to investigate the effects of the oxygen content, since it exists within the first atomic layers of the material. In order to evaluate the influence of CO_2 laser induced microstructure, an intermediate grinding stage using grinding paper (400 Grit SiC) was used to remove the microstructure. In the final stage, both the untreated and the CO_2 laser treated samples were ground down further with the grinding paper (800 Grit SiC) to study the effect of surface roughness. The observed changes to surface roughness, oxygen content and θ (Glycerol) effecting by these steps are given in Table 7.4.

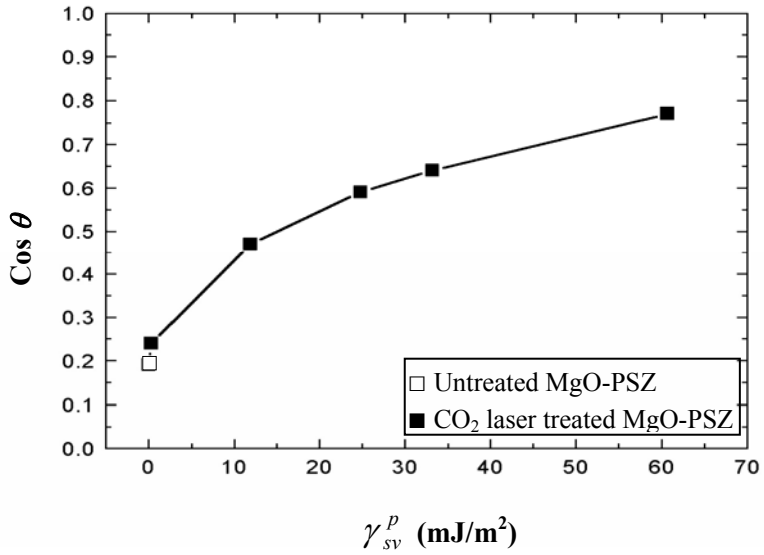

Fig. 7.11. Relationship between cos θ for glycerol and γ_{sv}^{p} on the untreated and CO_2 laser treated MgO-PSZ.

After the first grinding, a large difference in θ for glycerol was observed between the untreated and the CO_2 laser treated samples was still present, with θ increasing slightly from 39.4° to 43.7° for the CO_2 laser treated sample, while θ for the untreated sample increased from 79 to 82° (Table 7.4). From this observation it is reasonable to suggest that the retained CO_2 laser induced microstructure in the CO_2 laser treated MgO-PSZ could be the mechanism responsible for the large different θ from the untreated sample. Furthermore, the oxygen content of the CO_2 laser treated sample was found to have reduced from 64.3 to 42.0 at%, a level similar to that of the untreated sample, 42.2 at%. It is, therefore, quite possible that the decreased oxygen content could be the factor influencing

the general increase in θ. It is interesting to note that although the surface roughness of the CO_2 laser treated sample increased from 0.72 μm to 1.90 μm, the value of θ increased, thus implying that surface roughness does not have as great an influence on the wetting characteristics of the MgO-PSZ as that of the oxygen content. This proposition was borne out somewhat when the samples were ground further. In this subsequent stage, the CO_2 laser induced microstructure and heat affected zone (HAZ) were removed from the CO_2 laser treated sample. The surface oxygen content on the untreated and CO_2 laser treated samples were practically the same as the original untreated value of 41.6 at%. Significantly, θ for the CO_2 treated samples was 77.3°; close to the original untreated value of 79.1°. Basically the removal of the CO_2 laser induced microstructure alone appears to have brought about an increase in θ to around the original level, since the oxygen content was almost same value in both ground stages. Such findings reveal unequivocally that microstructure is by far the predominant mechanism governing the wettability characteristics of the MgO-PSZ. The effect of the surface roughness was studied through a further step. This step generated a smoother surface by reducing the R_a from 1.72 to 1.40 μm. For the CO_2 laser treated sample, this step caused θ to change slightly from 77.3 to 77.9°. For the untreated sample, the final ground stage caused Ra to change considerably, reducing from 0.30 to 0.08 μm. But as one see from Table 7.4, θ only increased very marginally from 79.1 to 82.3°. Despite the magnitude change in R_a, θ had varied only slightly in this range of surface roughness. Such a finding indicates that changes in R_a have an insignificantly reflected by the corresponding change in θ. Consequently, it is reasonable to assume that the surface energy difference brought about by microstructural changes is the primary influential factor governing changes in θ and in turn, the wettability characteristics of the MgO-PSZ. What is more, surface oxygen content, was also found to influence changes in the wettability characteristics of the MgO-PSZ but to a much lesser extent, whilst surface roughness was shown to play a very minor role in inducing changes in the wettability characteristics of the MgO-PSZ.

Table 7.4.The contact angle, surface roughness and oxygen content on the untreated and laser treated MgO-PSZ following the polishing steps

Polishing Steps	**Untreated**			**CO_2 Laser treated**		
	R_a (μm)	**Oxygen content (%)**	**θ (glycerol)**	**R_a (μm)**	**Oxygen content (%)**	**θ (glycerol)**
Unpolished	0.30	41.6	79.1°	0.72	64.3	39.4°
180 Grit SiC (3 min)	0.22	41.5	81.9°	1.90	42.0	43.7°
400 Grit SiC (3 min)	0.08	41.7	82.3°	1.46	41.8	77.3°
800 Grit SiC (3 min)	0.06	41.8	82.3°	1.23	41.7	77.9°

7.6. The Roles Played by Microstructures in Terms of Crystal Size and Phase in Effecting Surface Energy Changes

The surface energy has been identified as the main mechanism governing the modification of wettability characteristics of the MgO-PSZ and is varied with the surface microstructure. It is believed that the changes in surface energy of the MgO-PSZ were attributed to the change in microstructures by the form of crystal sizes and phase changes.

7.6.1. The Role of Crystal Size on Surface Energy

After CO_2 laser radiation, the modified surface of the MgO-PSZ exhibits a typical microstructure of rapid solidification. In the previous XRD analysis, it was found that the peak at 30.5 assigned as the (101) plane of the tetragonal lattice varied considerably with CO_2 laser power density. Moreover, the intensity of the peak at 30.5° assigned as (111) plane of the tetragonal lattice overwhelms the others, which indicated the tendency of crystal orientation. The crystal size in the direction perpendicular to the *hkl* plane, D_{hkl}, is expressed by the Scherrer equation [265],

$$D_{hkl} = \frac{K\lambda}{\beta \cos\alpha} \tag{7.8}$$

where λ is the wavelength of the X-ray (1.54056 Å for K_α line of Cu in this experiment), α is the Bragg angle, β is the expansion of the XRD peak caused by the crystal size, and K is the Scherrer constant. We take the full-width half-maximum (FWHM) of the peak at (111) in the XRD analysis as β, the crystallite size as D_{hkl}, and the K for 0.91, the crystallite sizes in the untreated and CO_2 laser treated MgO-PSZ at various power densities are listed in Table 7.5.

Table 7.5. Crystallite size calculated from the XRD of the untreated and CO_2 laser treated MgO-PSZ on the basis of Scherrer equation

Power density (kW/cm^2)	**FWHM**	**α**	**D (nm)**
Untreated	4.187	15.26°	34.7
0.5	3.489	15.25°	41.6
0.9	2.318	15.22°	65.4
1.6	1.396	15.20°	103.1
1.9	2.415	15.24°	60.1
2.5	2.268	15.18°	64.0

As shown in Table 7.5, the crystal sizes in the MgO-PSZ following CO_2 laser radiation are consistently larger than the untreated sample, implying that the crystal grew after CO_2 laser radiation. A high heat input from a laser beam facilitates surface localized melting at a very high efficiency. That is, the major portion of the absorbed energy is used for melting, with only a small fraction going into the heating of the solid sub-surface material. This ability to maintain a cold substrate whilst melting a thin surface layer of material results in rapid quenching of the molten layer once the beam is removed. Thermal gradients at liquid-solid interface layer are very steep and cause crystal growth taking place along the thermal gradient. The power density of the laser treatment has a significant effect on the crystal size. Generally, the crystal sizes in the MgO-PSZ increase with the increasing power density, with the largest crystal size of around 103.1 nm occurring at a power density of 1.6 kW/cm^2. Furthermore, it found that the crystal size varies similarly as surface energy with power density as shown in Fig. 7.12, signified that the crystal size is correlated with the surface energy of the MgO-PSZ.

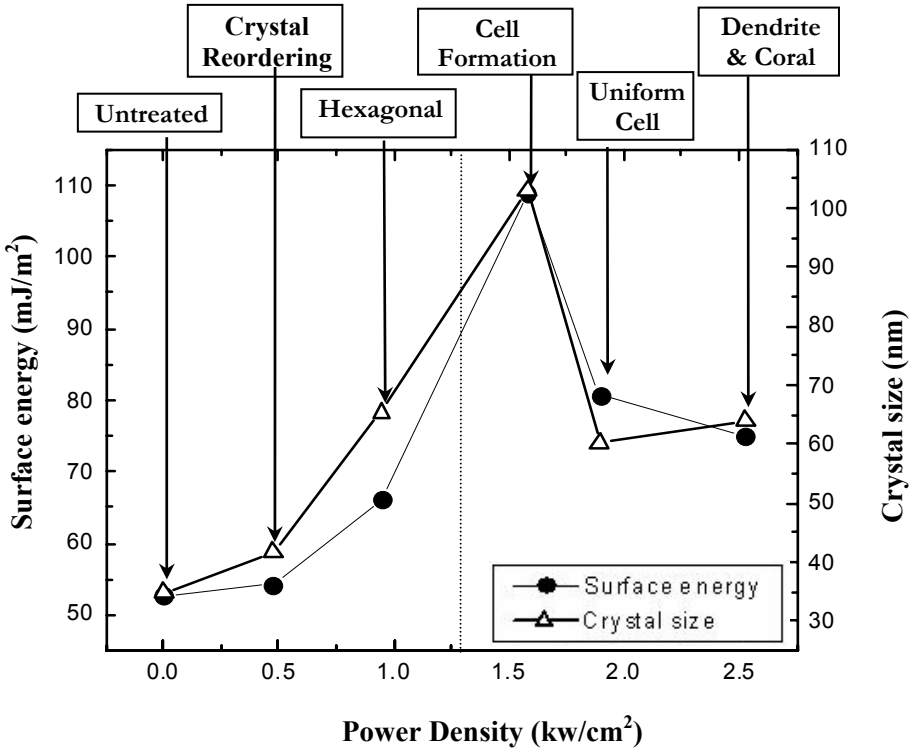

Fig. 7.12. Relationship between surface energy and crystal size of the CO_2 laser treated MgO-PSZ and power densities (at traverse speed of 2000 mm/min)

According to the classical theory of nucleation and growth in solids [266], a crystallite nucleate in the form of critical embryos grows by accreting atoms from the surroundings. Assuming the embryo has a spherical shape of radius *r*, the free surface energy of an unstrained spherical particle, *G*, is expressed as,

$$G(r) = \frac{4}{3}\pi r^3 G_V + 4\pi r^2 \gamma_t \tag{7.9}$$

where G is the free energy of an spherical particle, G_v is the free energy per unit volume of an crystal, and γ_t is the surface energy of the tetragonal crystal. So, by assuming the number of crystals in the CO_2 laser treated surface is n in unit area, the tetragonal crystal, the total surface energy of tetragonal MgO-PSZ, γ_{sv}, considering that half of the surface of the crystal is covered by the neighbour crystals, may be estimated by the expression

$$\gamma_{sv} = \frac{1}{2} n\pi r^2 \gamma_t = \frac{1}{8} n\pi D^2 \gamma_t \tag{7.10}$$

where D is crystal size. Since the main crystals remain as tetragonal structure in the MgO-PSZ, it is reasonable to assume that γ_t does not change with the crystal size. In the CO_2 laser processing, the n could be the same as the crystal grows. Thus, γ_{sv} is proportional to D^2, which is in accordance with the linear relationship between $\gamma_{sv}^{1/2}$ and D as shown in Fig. 7.13. As such, the larger crystal size can be attributed to the increase in the surface energy of the MgO-PSZ. Indeed, Man *et al* [262,267] found that excimer laser treatment induced a conical structure, a microscale of peak and valley structure, provided extra adherent surface area for a strong adhesion joint on Si_3N_4 and LT35 surface. The joint strength increased with the height of the cones and the laser energy density. Kappel [128] showed that the improved adhesion strength occasioned by excimer laser texturing of ceramics is due to the formation of raised microscopic protrusions over the surface.

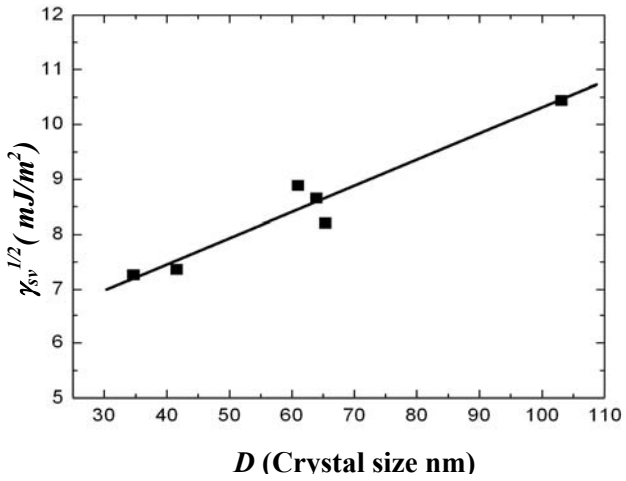

Fig. 7.13. Relationship between $\gamma_{sv}^{1/2}$ and crystal size (D) of the MgO-PSZ

7.6.2. The Role of Phase Change on Surface Energy

The previous XRD analysis revealed that the (101) tetragonal phase increased and (111) monoclinic phase decreased in the CO_2 laser interaction layer on the MgO-PSZ. Furthermore, the relative intensity of the tetragonal phase increased when power density was below 1.6 kW/cm^2 and then decreased slightly as the power density increased further. The MgO-PSZ treated at 1.6 kW/cm^2 power density has the highest surface energy (108.9 mJ/m^2) as discussed previously and corresponds to the highest intensity of the tetragonal phase. When the power density is at 1.9 and 2.5 kW/cm^2, the surface temperature of the MgO-PSZ increased to well above the melting temperature, thereby generating more cubic phase and reducing the tetragonal phase. Associated with this phenomenon, the surface energy begin to decrease from 108.9 to 80.7 and 74.9 mJ/m^2. These phase changes could be represented by the different microstructures on the treated MgO-PSZ with various power densities. It is noticed that tetragonal intensity varies similarly as the surface energy with the CO_2 laser power density, indicating that the tetragonal intensity is closely correlated with the surface energy of the MgO-PSZ. In fact, it has been found that at T = 0 K, the surface energy of the (101) tetragonal phase is 45% higher than that of the (111) monoclinic phase and 95% higher than that of the (111) cubic phase [268]. Therefore, it is believed that the phase change (increase in tetragonal phase and decrease in monoclinic phase) resulted in the higher surface energy of the MgO-PSZ following the CO_2 laser irradiation.

7.7. Summary

The results presented in this chapter are a clear indication that CO_2 laser surface treatment of the MgO-PSZ brought about a reduction in the θ formed between the MgO-PSZ and the control liquids, indicating that the wettability characteristics of the material were modified. The extent of this wettability characteristics modification was varied by manipulation of the CO_2 laser parameters. The main conclusions could be made as follows:

1. Changes in the wettability characteristics of the magnesia partially stabilised zirconia (MgO-PSZ) were attributed to the following factors: (i) an increase in surface roughness; (ii) incorporation of oxygen at MgO-PSZ surface resulting from CO_2 laser treatment and (iii) the increase in the polar component, γ_{sv}^{p}, of the surface energy resulting from the melting and resolidification of the MgO-PSZ surface.

2. The changes in γ_{sv}^{p} resulted from the melting and solidification of the MgO-PSZ surface and its value varied with the solidified microstructure. The cellular microstructure obtained by the CO_2 laser induced rapid solidification corresponded to the maximum value of γ_{sv}^{p}.

3. Further analysis revealed that surface energy, by way of microstructure, was the primary influential factor governing changes in θ and hence the wettability characteristics of the MgO-PSZ. Incorporation of oxygen at the surface was also shown to influence, to a lesser extent, changes in the wettability characteristics, whilst surface roughness was found to play a vary minor role in inducing changes in the wettability characteristics of the MgO-PSZ.
4. The surface energy increase as the crystal size and tetragonal phase increase in the MgO-PSZ surface after the CO_2 laser treatment.

CHAPTER 8

The Formation of a Hydroxyl Bond and the Effects Thereof on the Bioactivity of a MgO-PSZ Bioceramic Following CO_2 Laser Irradiation

In this chapter a Fourier Transform Infrared Spectrometer (FTIR) was used to analyse OH groups on the MgO-PSZ following CO_2 laser irradiation. The bioactivity of the CO_2 laser modified MgO-PSZ has been investigated in simulated body fluids (SBF) with ion concentrations almost equal to those in human blood plasma. Subsequently the effect of the CO_2 laser treatment on the OH groups, the correlation between OH groups and polar surface energy and the effect of the OH groups on the apatite formation were studied.

8.1. Introduction

The biological activity of most orthopaedic and dental biomaterials is related to their ability to promote the formation of a neoformed layer of carbonate apatite crystals analogous to bone mineral, this layer also associates specific bone proteins and is the starting point of bone reconstruction [160]. Under normal conditions, the body fluid is already supersaturated with respect to apatite, and once apatite nuclei form on the surface of a material, they can spontaneously grow by consuming the calcium and phosphate ions form the body fluid. The nucleation of apatite on the surface of a material is induced by the functional groups on its surface. When some components are release from the material into the body fluid and thereby increase the ionic activity product of the apatite, they can accelerate apatite formation [161].

The integration between bioinert ceramic and tissue is a critical problem. There have been considerable efforts for improving the bioactivity of alumina and zirconia inert bioceramics. It has been revealed that a zirconia gel forms an apatite on its surface in SBF, indicated that the Zr-OH group is able to induce apatite nucleation [161]. Furthermore, the investigation of apatite-forming ability of zirconia gels with different structures exhibits that specific structures of Zr-OH group in tetragonal or monoclinic zirconia are effective for inducing apatite nucleation [162,269,270]. For

the purpose of the apatite formation, the chemical treatment has been used to produce the Zr-OH group on a zirconia/alumina composite with high strength and fracture toughness subjecting the composite to H_3PO_4, H_2SO_4, HCl or NaOH aqueous solution treatments [163] and on zirconium metal treated with aqueous NaOH [164].

8.2. Surface Hydroxyls on Zirconia

It is well known that, when exposed to the atmosphere, the surface of most oxidic systems become covered by a hydrated layer that builds up to compensate, at least in part, the coordinative instauration of the surface ions brought about by the truncation of the crystallites. The surface hydrated layer is normally made up, in varying proportions, of hydroxyl groups belonging to the coordination sphere of one or more surface cations and of undissociated water molecules coordinated to surface cations acting as Lewis acid centres. Relative amounts and stability towards thermal activation *in vacuo* of the two species in the surface hydrated layer depend primarily on the nature of the oxide system and on the crystal planes constituting the termination of the crystallites [271]. In general, the second component of the hydrated layer (i.e. undissociated coordinated water molecules) may represent up to ≈ 50 % of the layer, is far less resistant to vacuum activation than surface OH groups (it is normally eliminated by ≈ 473 K), and is much less useful for the characterization of the surface features. In fact it is almost invariably associated with two unresolved v(OH) bands at $\bar{\nu} \geq 3500$ cm^{-1}, and with a broad δ(OH) band, centred at ≈ 1630 cm^{-1} on all oxidic systems and on all crystal planes. Surface hydroxyls are, in contrary, more useful for characterization work, as they are more sensitive to the coordinative and/or structural configuration of the surface cations to whose coordination sphere they are associated. Spectral data on the surface hydrated layer of m-ZrO_2 has reported that in general, an abundant component of undissocated water on m-ZrO_2; as well as two families of "free" surface hydroxyls absorbing at ≈ 3775 cm^{-1} (termed [OH]H) and ≈ 3675 cm^{-1} (termed [OH]L) respectively [271]. The two OH bands have usually been assigned to OH groups bonded respectively to one and more than one (possibly three) Zr^{4+} ions.

8.3. Bonelike Apatite Formation

Histological examinations *in vivo* show that an apatite layer is formed on the ceramic [159] surface early in the implantation period and thereafter, the bone matrix integrates into the apatite. Detailed characterisation indicates that this apatite layer consists of nano-crystals of carbonate-ion-containing apatite that has a defective structure and low crystallinity. These features are, in fact,

very similar to those of the mineral phase in bone and hence, bone producing cells (osteoblasts) can preferentially proliferate on the apatite and differentiate to form an extracellular matrix composed of biological apatite and collagen. As a result, the surrounding bone comes into direct contact with the surface apatite layer. When this process occurs a chemical bond is formed between the bone mineral and the surface apatite to decrease the interfacial energy between them. It can be concluded from these findings that an essential requirement for an artificial material to bond to living bone is the formation of a layer of biologically active bone-like apatite on its surface in the body [159].

8.3.1. Apatite Formation

It has been shown that the induction period for apatite formation decreases appreciably with an increase in pH or an increase in concentration of calcium or phosphate ions in the SBF [161]. This is attributed to an increase in the apatite ionic activity product (IP) of the SBF with an increase in the concentrations of the ions that constitute the apatite. Formation of hydroxyapatite ($Ca_{10}(PO_4)_6(OH)_2$) from its constituent ions is given by the following equation:

$$10Ca^{2+} + 6PO_4^{3-} + 2OH^- \leftrightarrow Ca_{10}\left(PO_4\right)_6\left(OH\right)_2 \tag{8.1}$$

The IP of the hydroxyapatite in an aqueous solution is, therefore, given by the following equation:

$$IP = \left(\alpha_{Ca^{2+}}\right)^{10}\left(\alpha_{PO_4^{3-}}\right)^6\left(\alpha_{OH^-}\right)^2 = \left(\gamma_{Ca^{2+}}\right)^{10}\left(\gamma_{PO_4^{3-}}\right)^6\left(\gamma_{0H^-}\right)^2\left[Ca^{2+}\right]^{10}\left[PO_4^3\right]^6\left[OH^-\right]^2 \tag{8.2}$$

where α is the activity and γ the activity coefficient. Square brackets ([]) represent ionic concentration. The relative supersaturation (σ) is given by the following equation:

$$\sigma = \frac{IP^{1/\nu} - K_{SO}^{1/\nu}}{K_{SO}^{1/\nu}} = \left(\frac{IP}{K_{SO}}\right)^{1/\nu} - 1 \tag{8.3}$$

where K_{so} is the solubility product and ν the number of ions in the molecule, i.e. for the apatite. The calculated IP of apatite in SBF is 6.2×10^{-96} at 37ºC, which indicates that the SBF is already highly supersaturated with respect to the apatite. Equations (8.2) and (8.3) show that the IP, i.e. The degree of the supersaturation of the apatite, increases with an increase in pH or an increase in the calcium- or phosphate-ion concentration of the SBF. The increased degree of the supersaturation increases the nucleation rate of the apatite, which results apparently in an increase in the quantity of deposited apatite. Once the apatite nuclei are formed, they grow spontaneously by consuming the calcium, phosphatase and hydroxyl ions from the surrounding fluid.

8.3.2. Functional Groups for Apatite Nucleation [159]

The catalytic effect of the Si-OH groups and Ti-OH groups for the apatite nucleation has been proven by the observation that silica and titania gels produced by the sol-gel method form apatite on their surfaces in SBF, and these functional groups are abundant on their surfaces. Zirconia, niobium oxide, and tantalum oxide gels have also been shown to form apatite on their surfaces in SBF. This indicates that Zr-OH, Nb-OH, and Ta-OH groups are effective for apatite nucleation. Other assessments using self-assembled monolayers (SAM) in SBF have indicated that COOH and PO_4H_2 groups are also effective for apatite nucleation. However, it has been suggested that the efficacy of apatite nucleation of the above functional groups is determined, not by their composition alone, but in a complicated fashion that is dependent on their concentration and structural arrangements. For example, a silica gel that has been derived by hydrolysis and polycondensation of tetraethoxysilane (TEOS) in water in the presence of polyethylene glycol (PEG-silica) loses its apatite-forming ability on heat treatment at temperatures above 900ºC, owing to a decrease in the number of Si-OH groups. Silica gels, which are derived in water in the absence of polyethylene glycol or in the presence of polyacrylic acid, have an equivalent number of Si-OH groups as the PEG-silica, but these show no apatite-forming ability, presumably because of the different arrangement of the Si-OH groups. However, silicate ions dissolved from silica gel can induce apatite formation, independent of the source silica gels.

A titania gel prepared from tetraisopropyl titanate (TiPT) assumes an amorphous, anatase, or rutile structure, when it is heat-treated at 500ºC, 600ºC and 800ºC, respectively. Among these, the anatase gel forms apatite most effectively, followed by the rutile gel; however, the amorphous gel forms no apatite, even though it has much more abundant Ti-OH groups than the anatase and rutile gels [270]. Sodiumor calcium-containing titania gels can release sodium or calcium ions on immersion in SBF to increase the IAP, and thereby provide much more favourable conditions for apatite nucleation than for a pure titania gel. However, even these gels do not form apatite if they do not assume the anatase structure. Similarly, pure zirconia gel and zirconia gels containing sodium or calcium form apatite in SBF only when they assume a tetragonal and/or a monoclinical structure [272]. Concerning this structural dependence, it has been suggested that the Ti-OH or Zr-OH groups in anatase or the tetragonal/monoclinic structures may provide effective epitaxial nucleation sites for apatite crystals. For example, the arrangement of oxygen ions in the anatase structure along the (100) plane fits well to that of the hydroxide ions in HA along the (001) plane [270,272].

8.3.3. Mechanism of Apatite Nucleation by Functional Groups [159]

A model of bioglass apatite formation on a simple binary sodium silicate ($20Na_2O{\cdot}80SiO_2$ in mol%) glass was investigated. This glass releases Na^+ ions into SBF via an exchange with the H_3O^+ ions in the fluid to form Si-OH groups on its surface. The Si-OH groups formed immediately combine with

Ca^{2+} ions in the fluid to form an amorphous calcium silicate on the glass surface. After a long soaking period, this calcium silicate combines with phosphate ions in the fluid to form an amorphous calcium phosphate with a low Ca/P atomic ratio, and this phase later transforms into bone-like apatite crystal, increasing its Ca/P ratio and incorporating minor ions such as Na^+, Mg^{2+}, and Cl^-. In a different model, the sodium titanate releases Na^+ ions via exchange with the H_3O^+ ions in the fluid to form Ti-OH groups on its surface in the SBF. The Ti-OH groups formed immediately combine with Ca^{2+} ions in the fluid to form amorphous calcium titanate. This calcium titanate later combines with phosphate ions in the fluid to form amorphous calcium phosphate with a low Ca/P ratio. The calcium phosphate transforms into apatite, which exhibits a Ca/P ratio of 1.65, and contains a small concentration of Mg and Na, similar to bone mineral. Additionally, it was found that the complex process of apatite formation is well interpreted in terms of the electrostatic interaction of the functional groups with the ions in the fluid. The Ti-OH groups formed on the surface of sodium titanate after soaking in SBF are negatively charged and, hence, combine selectively with the positively charged Ca^{2+} ions in the fluid to form calcium titanate. As the calcium ions accumulate on the surface, the surface gradually gains an overall positive charge. As a result, the positively charged surface combines with negatively charged phosphate ions to form amorphous calcium phosphate. This calcium phosphate spontaneously transforms into the apatite, because the apatite is the stable phase in body environment. A similar electrostatic mechanism for apatite formation might hold for the other functional groups described above that are effective for apatite nucleation, because all these functional groups have isoelectric zero points at pH values much lower than 7 and thus, should be negatively charged in the living body.

It is observed that even sintered HA forms a bonelike apatite layer on its surface in the living body, and bonds to bone through this apatite layer although HA has none of such functional groups for the apatite nucleation as described above. When HA sintered at 800ºC is soaked in an SBF, observations of its surface show that the Ca/P ratio increases from 1.67 to 1.87 within 3 h. The HA then decreases its Ca/P ratio to 1.41 within the next 6 h, forming an amorphous calcium phosphate, and then gradually increases its Ca/P ratio to 1.65, forming nano-sized bone-like apatite. During this process, the zeta potential of the surface of the HA varies with soaking time. HA is negatively charged immediately after soaking in the SBF, owing to its surface OH^- and PO_4^{3-} ions, and selectively combines with the positively charged Ca^{2+} ions in the fluid to form Ca rich calcium phosphate. As the calcium ions accumulate, the surface imparts a positive charge, and thus combine with the negatively charged phosphate ions in the fluid to form amorphous calcium phosphate with a low Ca/P ratio. This phase is metastable, and eventually transforms into stable bone-like apatite. It is has been reported that the bioactivity of HA decreases with increasing sintering temperature. This can be interpreted in terms of the degree of negative charge on its surface and the rate of bone-like apatite formation.

8.4. Experimental Methods

The CO_2 laser processing procedures, material characterisation techniques and wettability analysis of the untreated and CO_2 laser treated MgO-PSZ are detailed in Section 5.2.2, Section 5.2.3 and Section 7.2.1. The surface energy characterisation and the microstructures and crystal size analysis are detailed in Section 7.4 and Section 7.6.1 respectively.

8.4.1. FTIR Analysis

The optical adsorption spectra were measured at room temperature by means of a FTIR (Bio-Rad, US) spectrometer over the 500-5000 cm^{-1} range at a resolution of 1 cm^{-1}.

8.4.2. Soaking in Simulated Body Fluid

The samples were soaked in an acellular simulated human body fluid (SBF) [159], having an ion concentration nearly equal to that of human blood plasma. This solution, whose composition is reported in Table 8.1, was prepared by dissolution of high purity reagents in distilled water, and was buffered at 7.25 with 50 mM tris-hydroxymethyl amino ethane and 45 mM hydrochloric acid. The untreated and CO_2 laser treated samples with various power densities were washed by distilled water and immersed in 30 mL SBF in a polyethylene bottle at 37ºC, without stirring. After 14 days they were removed from the solution, gently washed in distilled water, and dried at room temperature. The soaked samples were then characterised by SEM and energy dispersive X-ray analysis (EDX). The samples for SEM observations were simply dried and covered by a thin gold layer to guarantee the conductivity.

Table 8.1. Ionic concentration and pH of simulated body fluid in comparison with those in human blood plasma [159]

Ion	Concentration	
	Simulated body fluid (SBF) (mM)	**Blood plasma (mM)**
Na^+	142.0	142.0
K^+	5.0	5.0
Mg^{2+}	1.5	1.5
Ca^{2+}	2.5	2.5
Cl^-	148.8	103.8
HCO_3^-	4.2	27.0
HPO_4^{2-}	1.0	1.0
SO_4^{2-}	0.5	0.5
pH	7.40	7.40

8.5. Results and Discussion

8.5.1. Spectral Analysis and Hydroxyl Group

The main regions in the 750-950 cm^{-1} range are ascribed to ZrO_2 stretching modes as shown in the Fig. 8.1, owing to the fact that it is similar to infrared (IR) peak of the 20 mol% Al_2O_3 doped ZrO2 nanoparticles reported previously [273] and the IR peak of the Al_2O_3 - ZrO_2 nanopowders after laser ablation [274].

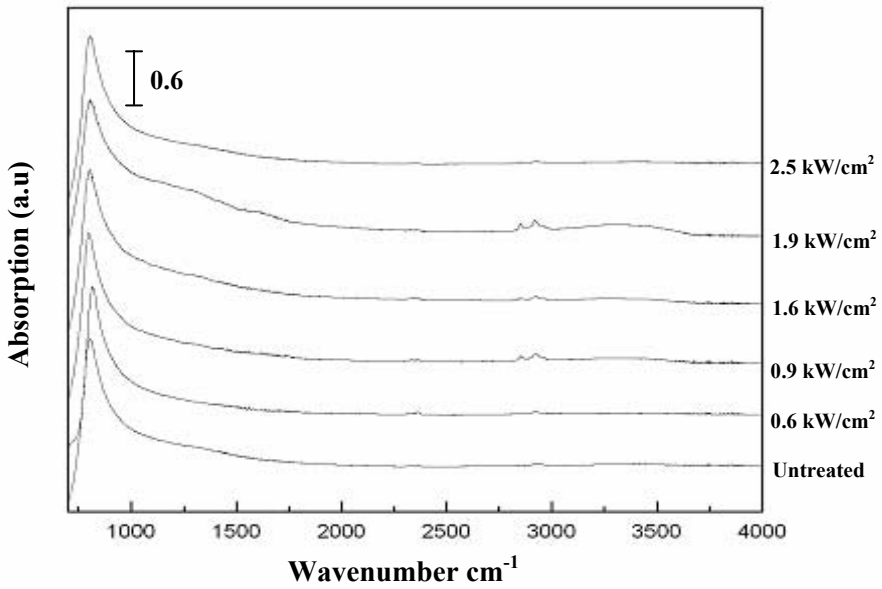

Fig. 8.1. Infrared spectra of the untreated and CO_2 laser treated MgO-PSZ with different power densities at traverse speed of 2000 mm/min.

The vibration around 3300 to 3500 cm^{-1} in the FTIR spectra (see Fig. 8.2) could be attributed to the OH groups. Indeed OH stretching vibrations around this region have been observed by other workers on Al_2O_3 - ZrO_2 nanopowders after Nd:YAG laser ablation [274] and on the Fe-doped crystals after laser irradiations [275]. As one can see from Fig. 8.2, the absorption coefficient of the OH group on the MgO-PSZ in this region increased after CO_2 laser irradiation and varied with the power density employed. For the untreated sample and the CO_2 laser treated sample (power density of the 0.6 kW/cm^2), the absorption peaks from 3200 to 3600 cm^{-1} are not obvious, indicating that no OH groups bonded on these samples. In contrast, the absorption peaks at this region can be clearly observed on the samples following the CO_2 laser irradiation with power densities of 0.9, 1.6, and 1.9 kW/cm^2, denoting that OH groups existed on these sample. The highest absorption coefficient of OH groups was obtained on the sample that had been treated at 1.9 kW/cm^2. This finding shows that the OH groups increased with the CO_2 laser power density used. This relationship was also

seen by Zeng *et al* [276] on the OH groups bonded onto copper after CO_2 laser treatment. However, the absorption peaks in this region on the sample treated with a CO_2 laser power density of 2.5 kW/cm^2 was not obvious, suggesting that the OH bond does not increases linearly with the CO_2 laser power density. The explosive evaporation due to the superhigh temperature on the MgO-PSZ surface treated at this power density caused the water vaporisation and disappearance of the OH band. The phenomena of losing OH groups was also found on the human dentin after Er:YAG laser irradiation [277].

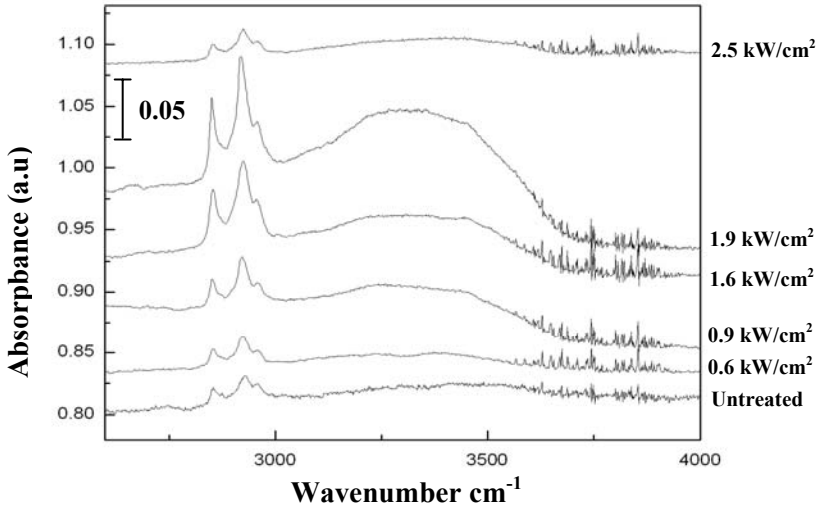

Fig. 8.2. Infrared spectra of the hydroxyl groups presents on the surface of the untreated and CO_2 laser treated MgO-PSZ with different power densities at traverse speed of 2000 mm/min.

CO_2, a weak acid, is known to absorb on ZrO_2 in the form of both carbonate and bicarbonate species [278]. Carbonate structures are formed via the interaction of CO_2 with zirconium cations in the lattice, as well as with a surface oxygen atom, whereas bicarbonate structures are formed via the interaction of CO_2 with hydroxyl group. The peak from 2800 to 3000 cm^{-1} testified to the existence of carbonate structures on the MgO-PSZ surface. The change of carbonate structures has the same trend as the OH groups discussed above.

The formation of the hydroxyl groups on the MgO-PSZ is due to the reactions of the zirconia with water vapour in air during CO_2 laser processing. Hydroxyl ion is a common impurity in insulating crystals and by interacting with other impurities, it gives rise to new complexes. The OH-stretching frequency is a very sensitive probe of the hydroxyl environment. Proper thermal treatments and isotopic substitutions allowed to assign the stretching mode absorption lines to the defects in which OH^- is embedded and to supply possible models for them [278].

Crystal growth from the melt is commonly carried out in air atmosphere as air always contains a certain degree of humidity from which OH^- ions are incorporated into the lattice [279]. CO_2 laser irradiation is a thermal process. When the laser fluence exceeds the ablation threshold, the irradiated surface experiences melting, followed by evaporation, whereupon the particles emit from the surface. At a higher fluence, the amounts of particles increases and they break out quickly from the superheated surface to produce a high density vapour plume wherein a portion of the particles are ionised due to the thermal ionisation. Therefore, the main reactions occur in the melt ceramic and vapoured flume:

$$ZrO_2 \Leftrightarrow Zr^{4+} + 2O^{2-} \tag{8.4}$$

So, the following oxido-reduction reactions occur at the melt-atmosphere interface:

$$O^{2-} \rightarrow \frac{1}{2}O_2 + 2e^- \tag{8.5}$$

$$H_2O + e^- \rightarrow \frac{1}{2}H_2 + OH^- \tag{8.6}$$

the whole reaction being

$$O^{2-} + 2H_2O \rightarrow 2OH^- + H_2 + \frac{1}{2}O_2 \tag{8.7}$$

Finally, the OH^- ions produced according to reaction (8.4) would be incorporated with one, two and three and four surface Zr^{4+} respectively. According to the classification proposed by Tsyganenko *et al* [280], the OH groups bonded in the spectral ranges at ≈ 3770 cm^{-1} and ≈ 3680 cm^{-1} are typical one and three surface Zr^{4+} cations respectively in tetragonal zirconia while the OH groups at ≈ 3775 cm^{-1} and 3675 cm^{-1} bonds respectively one and more than one (possible three) surface Zr^{4+} ion.

According to the microstructure analysis discussed, it has been found that the surface melting was occasioned on the MgO-PSZ treated by the CO_2 laser treatment with 1.6 kW/cm^2 power density. Consequently, the Zr^{4+} ion and OH^- were produced and reaction between these ions brought about the Zr-OH group on the MgO-PSZ. The relatively high amounts of the hydroxyl groups bonded onto the modified samples with 1.6 and 1.9 kW/cm^2 were associated with the melting and chemical reaction on the MgO-PSZ surface.

8.5.2. The Correlation Between OH Groups and Wettability Characteristics

The values of the surface energy have been calculated for the MgO-PSZ treated by the various power densities in detail (see Chapter 7) and are shown in Table 8.2. It is found that the absorption

coefficient of the OH group (see Fig. 8.2) and γ_{sv}^{p} on the MgO-PSZ increased after CO_2 laser irradiation (see Table 8.2) and varied with the power density employed.

Table 8.2. Determined surface energy values for the MgO-PSZ before and after CO_2 laser treatment of various power densities (traverse speed of 2000 mm/min).

Surface energy		**Untreated**	**CO_2 Laser Treated (kW/cm^2)**				
			0.5	**0.9**	**1.6**	**1.9**	**2.5**
Dispersive Component	γ_{sv}^{d} (mJ/m^2)	42.7	43.8	44.4	48.2	47.5	48.2
Polar Component	γ_{sv}^{p} (mJ/m^2)	10.1	10.4	21.9	60.7	33.2	26.7
Total surface energy	γ_{sv} (mJ/m^2)	52.8	54.2	66.3	108.9	80.7	74.9

The untreated sample and the samples treated with the lower power densities had relatively low absorption peaks of the OH groups and lower γ_{sv}^{p}. On the other hand, the relatively high absorption peaks of the OH groups and higher surface energy existed on the samples following the CO_2 laser irradiation with power densities of 1.6, and 1.9 kW/cm^2. Moreover, when the OH groups decreased on the sample treated at the power density at 2.5 kW/cm^2, there was a corresponding decreased in the γ_{sv}^{p}. It is also interesting to notice that the melting of the MgO-PSZ was the fundamental reasons for the induction of the OH groups and improvement of the surface energy. This finding implied that there was correlation between the OH groups and γ_{sv}^{p}. Indeed, Takeda *et al* found that the surface OH groups governed the wettability of commercial glasses [281] and adsorption properties of metal oxide films [282]. The previous study [283] indicated that in the case of cassiterite its wettability strongly depends on the acid-base interactions (polar component) resulting from the presence of OH groups and physically adsorbed water on it. For the surface of the 'dry' cassiterite its surface free energy practically results only from Lifshitzvan der walls (dispersive component) intermolecular interactions. Most metal oxides are hydroxylated under normal conditions, i.e. at room temperature and when water or its vapour has had access to the surface. It was stated that the acid-base component of surface energy of the zirconia probably depends on the density of OH groups on the surface of the solids studied [284]. Indeed, the acid-base component of surface energy presented the majority of the forces as the functions of the particular chemical nature of a certain material, and as such corresponding to γ_{sv}^{p} [285]. Therefore, it is deemed that the CO_2 laser induced hydroxyl groups could be a major factor influencing the γ_{sv}^{p}, in turn, the wettability characteristics of MgO-PSZ.

8.5.3. The Effects of CO_2 Laser Treatment on Apatite Formation onto MgO-PSZ in SBF

As one can see from Fig. 8.3, there are very small sediments on the untreated MgO-PSZ and CO_2 laser treated MgO-PSZ with the power density of 0.6 kW/cm^2.

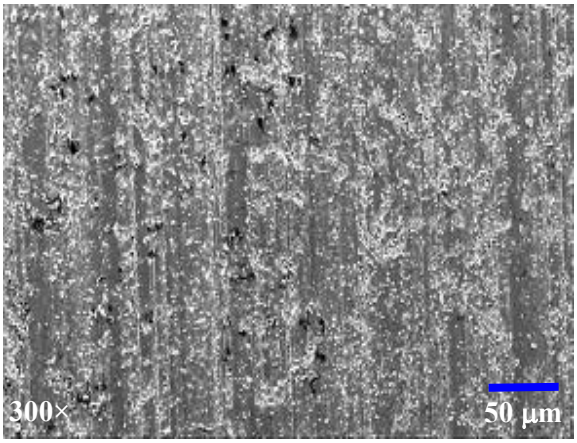

(a)

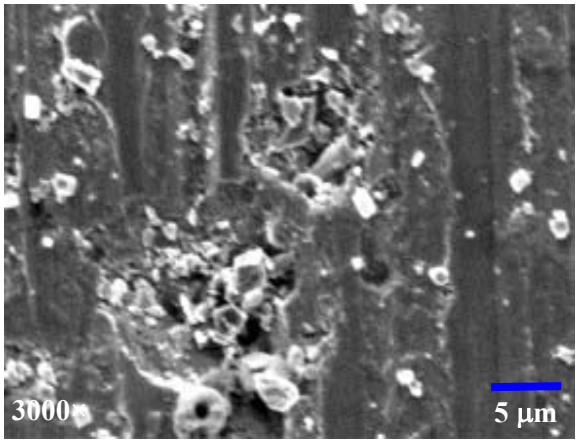

(a-1)

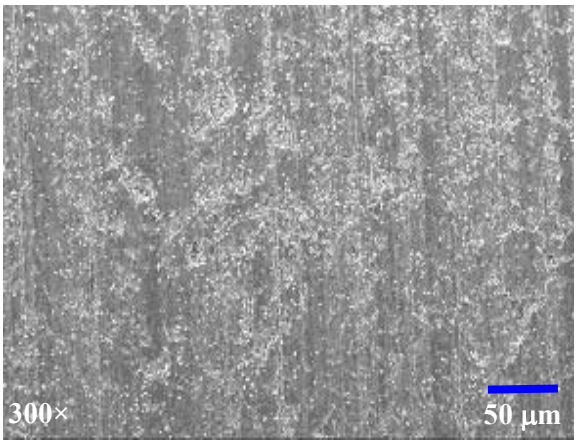

(b)

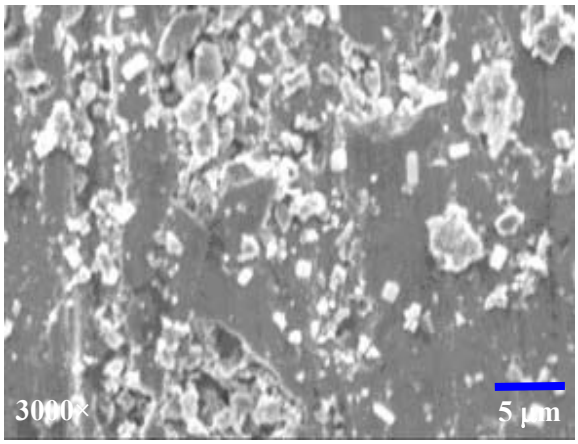

(b-1)

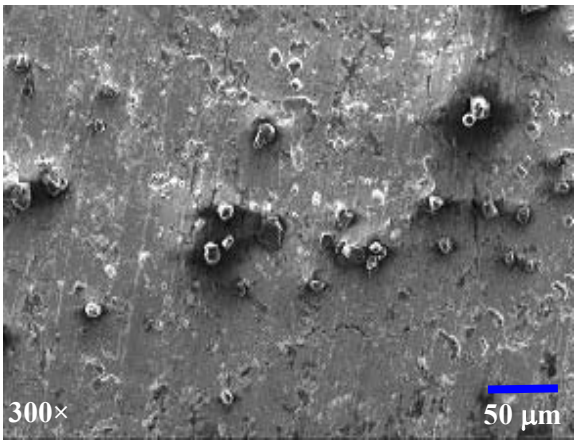

(c)

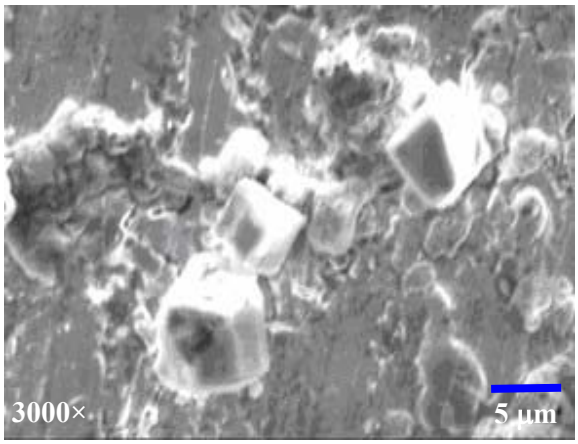

(c-1)

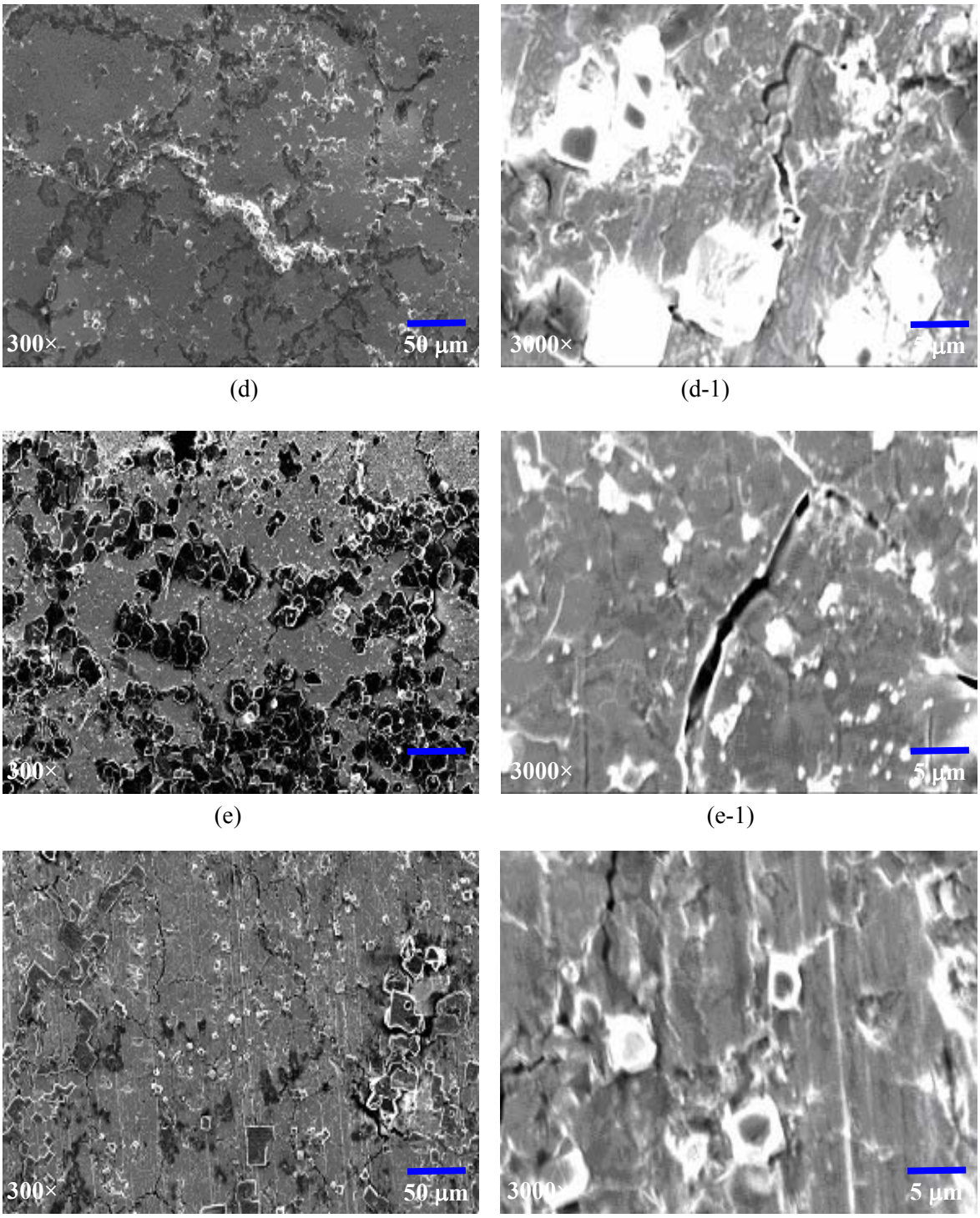

Fig. 8.3. SEM images of the MgO-PSZ soaked in the SBF (a) Untreated (b) 0.6 kW/cm^2, (c) 0.9 kW/cm^2, (d) 1.6 kW/cm^2, (e) 1.9 kW/cm^2, (f) 2.5 kW/cm^2.

On the other hand, some obvious sediments were found on the CO_2 laser treated samples with the power densities of 0.9 kW/cm^2, 1.6 kW/cm^2, 1.9 kW/cm^2 and 2.5 kW/cm^2. The highest amount of the sediments is observed on the sample treated at 1.9 kW/cm^2 as shown in Fig. 8.3. The EDX analysis shows that most particles on the soaked surface are NaCl sediments as the element of Na

and Cl as shown in the Fig. 8.4(a). Apatites were only found on the samples treated at power densities of the 1.6 kW/cm^2 and 1.9 kW/cm^2. As shown in Fig. 8.4(a), only a few apatites formed on the sample treated at a power density of 1.6 kW/cm^2 with only a small amount of Ca element shown in the EDX analysis given in Fig. 8.4(a). But, on the sample treated with a CO_2 laser power density of 1.9 kW/cm^2, some apatites were observed. One of them is shown in Fig. 8.4(b) with the Ca:P about 1.65. This Ca:P ratio exhibits the calcium phosphate transforms into apatite [159].

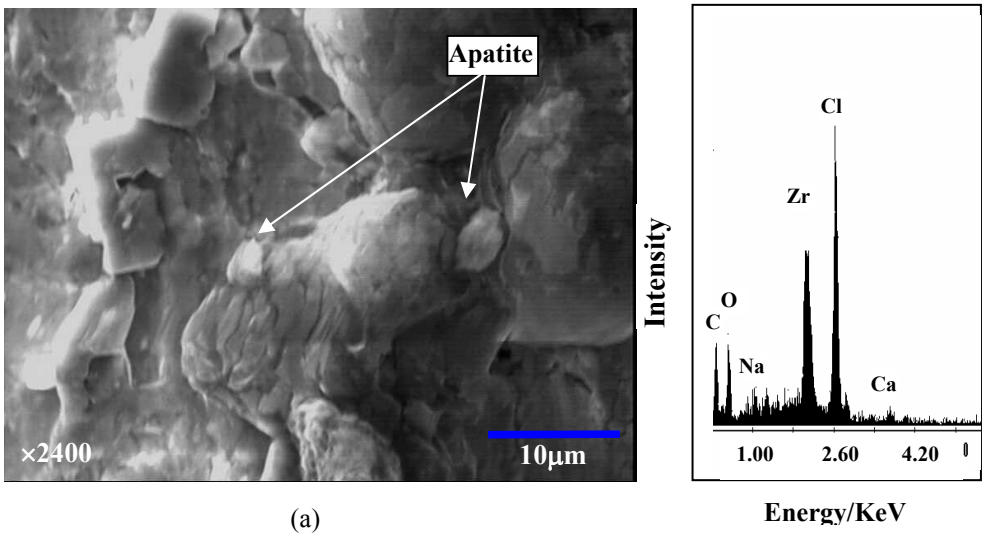

(a)

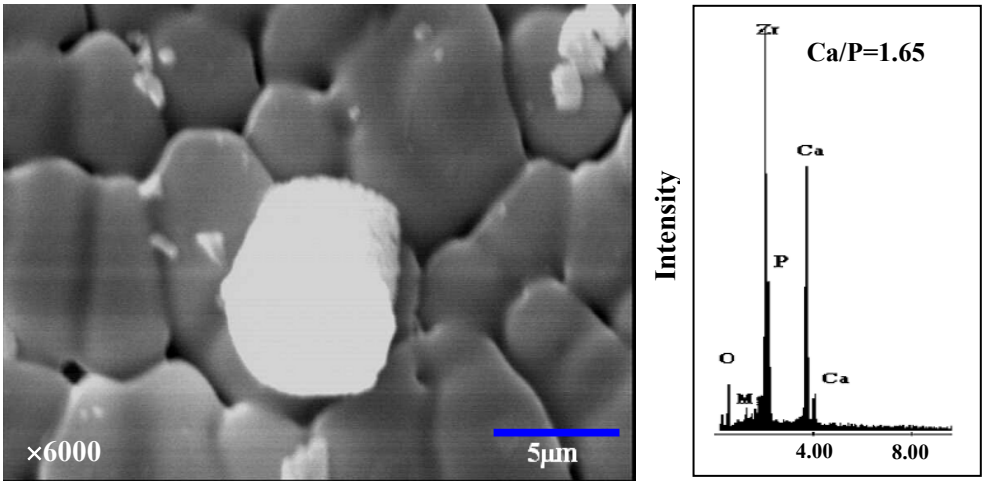

(b)

Fig. 8.4. SEM image and EDX analysis of the apatite formed on the MgO-PSZ treated at the power density of (a) 1.6 kW/cm^2 (b) 1.9 kW/cm^2.

There was no occurrence of apatite formation on the untreated and certain CO_2 laser treated samples (0.6, 0.9, 2.5 kW/cm^2) with few hydroxyl groups. On the other hand, some apatites formed on CO_2 laser treated samples (1.6 and 1.9 kW/cm^2) with some hydroxyl groups. This finding suggests that the hydroxyl group on the MgO-PSZ could be the predominant factor governing the

formation of the apatites. The hydroxyl groups on the MgO-PSZ surface certainly generate Zr-OH groups which have been shown to be functional groups for the formation of the apatite [161], it is suggested that Zr-OH functional groups formed on the samples in the CO_2 laser processing at certain parameters and such functional groups naturally brought about the nucleation of the apatite on these samples in the simulated body fluid environment. The nucleation of the apatite could yield the apatite formation and bone-bonding ability to the MgO-PSZ modified to have Zr-OH groups on the surface.

As shown in Table 8.2, the CO_2 laser treated MgO-PSZ at relatively high power density have the higher surface energy than the untreated one and the samples treated at relatively lower power density. It has found that there are more sediments and apatites on the surface with the higher surface energy than that on the surface with the lower surface energy. In the process of Ca-P precipitation, the variations of Gibbs function (ΔG) of the MgO-PSZ with the higher surface energy should be greater, compared to that of the MgO-PSZ surface with lower surface energy. This finding, agreeing with the study by Feng *et al*[286], suggested that the adsorption and reaction would be more easily occurred on the surface with the higher surface energy, especially polar component of surface energy which would be beneficial to the chemical force and bonding.

8.6. Summary

The bioactivity of the CO_2 laser modified MgO-PSZ has been investigated in simulated human fluids (SBF) with ion concentrations almost equal to those in human blood plasma. The effects of CO_2 laser irradiation on the hydroxyl groups and bonelike apatite formation has analysed. The conclusions can be drawn as follows:

1. It has been demonstrated that the CO_2 laser treatment could improve the bioactivity of the MgO-PSZ surface by generating functional group to facilitate the formation of bonelike apatites.
2. The apatite formed readily on the MgO-PSZ with relatively high amounts of hydroxyl groups, which were generated by CO_2 laser treatment with power densities of 1.6 kW/cm^2 and 1.9 kW/cm^2. No apatite was observed on the untreated and CO_2 laser modified samples (0.6 kW/cm^2, 0.9 kW/cm^2 and 2.5 kW/cm^2) that exhibited few hydroxyl groups. These observations indicate that Zr-OH groups on the MgO-PSZ surface are the functional groups required to facilitate apatite formation.
3. The surface melting on the MgO-PSZ induced by CO_2 laser processing provides the Zr^{4+} ion and OH^- ion. The incorporation of Zr^{4+} ion and OH^- ion creates the Zr-OH group on the surface. However, the power density at 2.5 kW/cm^2 could generate the explosive evaporation and in turn lose the water and OH band.

4. It was found that there was correlation between the OH group and γ_{sv}^{p} of the MgO-PSZ. The improvement of γ_{sv}^{p} probably depends on the relative density of OH groups on the MgO-PSZ following CO_2 laser treatment.

CHAPTER 9

Human Serum Albumin and Human Plasma Fibronectin Protein Absorption on a MgO-PSZ Bioceramic Following CO_2 Laser Irradiation

This chapter provides understanding of the fundamental interaction between proteins and the MgO-PSZ and useful information for the subsequent cellular interactions. Human serum albumin was chosen as the test protein since it is the most abundant protein and plasma, while human plasma fibronectin was chosen as the cell-adhesive protein. Ellipsometry was used to investigate the albumin and fibronectin adsorption on the untreated and CO_2 laser modified MgO-PSZ bioceramic. The relationships between the protein adsorption and surface properties of the MgO-PSZ are discussed.

9.1. Introduction

The particular properties of surfaces, as well as the specific properties of individual proteins from the surrounding fluid, contribute to the organization of the absorbed protein layer. The nature of this layer in turn determines the cellular response to the adsorbed surfaces [287].

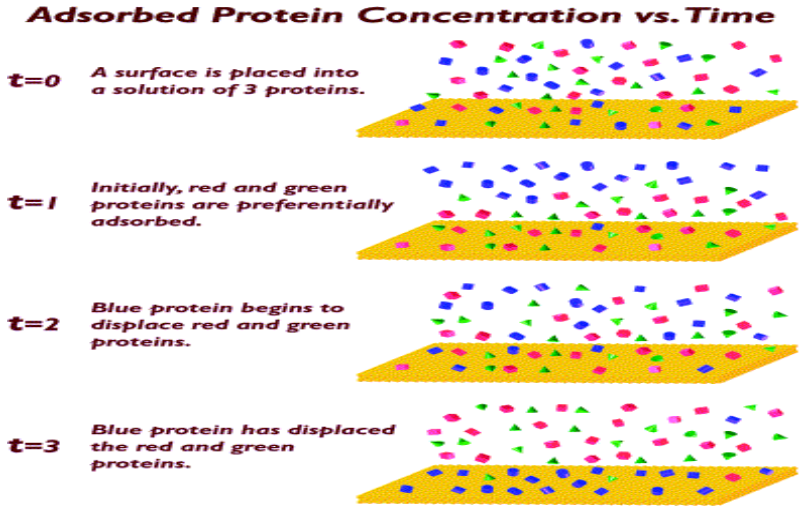

Fig. 9.1. Adsorbed protein concentration vs. time [288]

The adsorption of proteins onto a biomaterial surface from the surrounding fluid phase is rapid, with the surface properties of the biomaterial determining the type, amount, and conformation of the adsorbed proteins [289]. As Fig. 9.1 shows, a surface placed in a protein mixture will be covered with a layer of adsorbed proteins in a matter of seconds. The concentration of proteins in the adsorbed film is typically different from their solution concentration and can change with time. In this example, initially the 'red' and 'green' proteins are preferentially adsorbed. With increasing adsorption time (minutes to hours) the red and green proteins are displaced by the 'blue' protein [288].

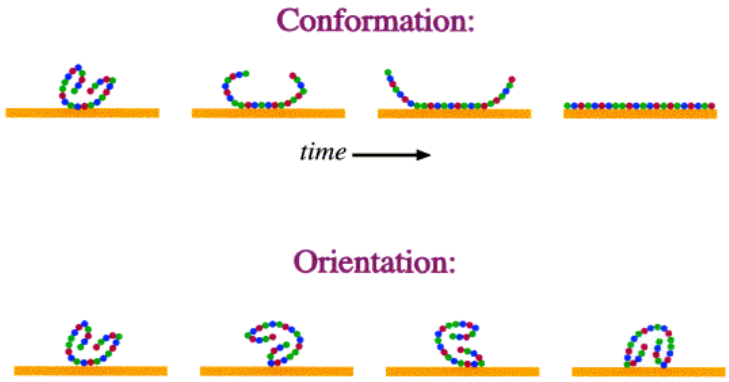

Fig. 9.2. A schematic diagram depicting the conformation and orientation of adsorbed proteins [288].

The structure and composition of the adsorbed protein layer determine the type and extent of the subsequent biological reactions, such as the activation of the coagulation and immune response [290-292], and osseointegration [293]. The adsorption of the protein layer may also be critical in terms of providing attachment sites for bone cells such as osteoblasts and their progenitors [294]. The composition of the adsorbed protein layer (i.e. the type and concentration of the proteins present in the adsorbed film) can differ from the fluid phase composition and can change with time adsorbed. This is shown schematically in Fig. 9.1 using three different proteins (red, green and blue). Initially the surface concentration of 'red' and 'green' proteins is higher than their solution concentration, with time the red and green proteins are displaced from the surface by the 'blue' protein. In addition to the time-dependent compositional changes, each absorbed protein can undergo conformational and orientational changes, as shown schematically in Fig. 9.2. The top schematic shows a protein denaturing with increasing adsorption time. The bottom schematic shows a protein adsorbing to the surface in different orientations. Upon adsorption, a protein can retain the conformation or structure it has in the biological environment or it may conformationally change in response to local environments. The nature of the surface strongly influences the composition and recognisability of the adsorbed protein layer, which in turn affects the subsequent cellular

interactions. Thus, to understand the biological response to a material, especially *in vitro*, one must fully understand the nature of the adsorbed protein film that forms on that material [288].

An important fact to highlight is that different surfaces provide very different opportunities for protein binding. Thus, both the exact mixture of proteins on the surface and their conformational state will be different, depending on the original surface properties, e.g. how the surface binds water. The latter lies behind the common observation that, e.g. hydrophilic and hydrophobic surfaces bind proteins differently. On very hydrophilic areas toward the surface, and with intact water shells, while on very hydrophobic surfaces, the proteins are more likely to bind with their hydrophobic segments closes to the surface, and without intervening water shells [63].

When the protein layer has been established (it is probably never totally static, but rather subject to slow dynamic changes in composition and conformational state, since the composition of the bioliquid outside the surface changes over the whole healing period), living cells appear on the stage. They are biological aggregates from 100 to 10,000 times larger than the proteins and enormously much more complex in structure and function. They interact with the proteins covered surface via their cell membrane, and via membrane-bound proteins and receptors. The surface specificity of the cell-surface interaction derives, at least partly, from how the protein layer is composed and organised, which in turn depends on how the surface binds water, ions, and different biomolecules. There is thus no need of a direct cell-surface contact for a surface specific cell interactions could be the eventual formation of newly organised tissue at the interface verses a chronic inflammatory response to the material, for example.

The molecules involved in cell adhesion and spreading include extracellular matrix molecules, transmembrane receptors and intracellular cytoskeletal components. Among the extracellular matrix proteins shown to mediate cell attachment to substrates, fibronectin is protein found in many extracellular matrices and in blood plasma. By virtue of fibronectin being a ubiquitous molecule, which, among other functions, also serves as an attachment molecule between substrate and cell membrane of anchorage-dependant cells. It is known that the ligand fibronectin connects to the cell membrane *via* integrin receptors. The activation of integrins triggers cytoplasmic reactions, and thereby, stimulates the intracellular signalling pathway and subsequently the cellular function and such as proliferation and differentiation [294]. On the other hand, human albumin is a non-adhesive protein for osteoblasts [295]. Albumin is the major protein component of serum. It functions as a carrier protein for a range of small molecules, lipids, etc., and as a pH buffer. Albumin dominates the adsorption of phenomena on medical implants in the first stage of contact with body fluids, since it is the most abundant protein in serum and plasma and has a high mobility. Human serum albumin or bovine serum albumin (BSA) coatings are often used as a passivating agent to prevent the adhesion of cells and thrombus formation [296]. However, a previous study illustrated that BSA can favour or inhibit the adhesion of a neuroblastoma cell line (NB2a) and endothelial cells on

fluorinated ethylene propylene films (FEP) depending on the chemical fictionalisation of these substrates [297]. It has been found that the variable behaviour of serum albumin toward cells adhesion promotion is related to its conformation on chemically distinct substrates [296].

9.2. Previous Work Investigating the Effects of Surface Properties on Protein Adsorption

9.2.1. The Effect of the Wettability Characteristics on Protein Adsorption

Janocha *et al* [298] found that the amount of adsorbed protein decreased with increasing surface energy of the substrate. The interfacial energy of the solid–liquid interface increases for substrates of high surface energy, which indicates that the decrease of interfacial energy is not the only driving force of this adsorption but also an expulsion of the proteins from the solution takes place (hydrophobic interaction). The investigation of competitive protein adsorption showed that collagen and BSA in single component solution adsorbed onto a hydrophobic surface two times more than that onto a hydrophilic surface. The competitive adsorption between collagen and BSA showed that serum albumin preferentially adsorbed onto a hydrophobic surface, while collagen on a hydrophilic surface. In the binary solution of BSA (1mg/ml) and collagen (0.1 mg/ml), nearly 100% of the protein adsorbed onto the hydrophobic surface was BSA, but on the hydrophilic surface only about 6% was BSA. Surface affinity was the main factor controlling the competitive adsorption [299].

The surface wettability of biomaterials affects the ability of cells to reorganise preadsorbed fibronectin and to form their own matrix by secreted fibronectin. Moderate wettable and hydrophilic surfaces are ideal for better interactions with cells while hydrophobic substrata inhibit early and late matrix formation. It is possible that there is a critical value in the strength of fibronectin adsorption which regulates the ability of cells to construct a fibronectin matrix [300]. The model using defined hydrophilic and hydrophobic surfaces has shown that fibroblasts on hydrophilic surfaces may reorganise fluorescent fibronectin in extracellular matrix-like configurations whereas on hydrophobic surfaces almost no rearrangement of fluorescent fibronectin takes place. The morphology of cell spreading and the organization of fibronectin receptors and actin filaments were examined to gain better insight into the initial stages of cell-material interaction. The ensuing cell proliferation was measured in order to further describe the biological reactivity of other surfaces in context with fibronectin organization [301].

It was found that the ability of fibroblasts to form their own extracellular matrix was inhibited on the hydrophobic octadecyl glass (ODS) in comparison to hydrophilic glass, where significant amounts of fibronectin were deposited in fibrils and clusters. This result was corroborated by the impaired morphology of cells on ODS, visualised by staining of actin micro-filaments and the

fibronectin receptor. Moreover, cell growth was significantly inhibited on the hydrophobic surface. In contrast to these findings, cell morphology and proliferation was not impaired on hydrophilic glass. Precoating of both substrata with fibronectin could restore the cell morphology and enhanced the proliferation on the hydrophobic ODS [302]. It also was found that cell interactions with hydrophobic polymer substrata are enhanced considerably when modified with hydrophilic and sterically demanding poly(ethylene glycol) PEG moieties at a low surface coverage due to enhanced biologic activity of adsorbed and intercalated adhesive proteins such as fibronectin [302].

9.2.2. The Effect of Surface Morphology on Protein Adsorption

It has been demonstrated that protein can "sense" the nanotopography similarly to the cells at micrometer scales. The topography is therefore an important parameter, which has to be taken into account in the general biomaterial field because the structure of the surface at a nanometer scale can influence the response of biological materials [303]. Nanostructures are created by local anodic oxidation on titanium using the atomic force microscope. A remarkable specificity of the actin filament adsorption on the nanostructure height is noticed. F-actin is observed to have a low adsorption on nanostructures of a height of 4 nm and the adsorbed proteins appear to be randomly oriented. In contrast high protein adsorption is observed for structure height between 1 and 2 nm, moreover the filaments adsorb preferentially parallel to the nanostructured pattern [304]. Protein A (one standard protein for immunology tests) shows no adsorption difference on parallel 1 nm high nanostructures on Si. The non- specifically bounded IgG also shown no preferential adsorption on or outer the nanostructures covered with proteins A. In contrast, the F-actin adsorbs preferentially along 1nm high lines on Si [303]. Even so, protein adsorption studies on modified surfaces using human fibrinogen showed that the extent of both initial protein adsorption and retention was remarkably independent of surface morphologies over the 5 to 100 nm mean roughness employed. Protein adsorption was observed to be significantly affected by the nature of surface chemistry [305].

9.3. Experimental Procedures

The CO_2 laser processing procedures, material characterisation techniques and wettability analysis of the untreated and CO_2 laser treated MgO-PSZ are detailed in Section 5.2.2, Section 5.2.3 and Section 7.2.1. The surface energy characterisation and the microstructures and crystal size analysis are detailed in Section 7.4 and Section 7.6.1 respectively.

9.3.1. Protein Adsorption

The proteins used for this study were human serum albumin and human plasma fibronectin (Calbiochem, Inc). Prior to the adsorption of 1mg/ml albumin in phosphate buffered salines (PBS), MgO-PSZ samples were rinsed with deionised water. The individual samples were transferred into a 24-well tissue culture plate. Thereafter, 2.5 ml of prepared albumin solution was added into each well. Adsorption proceeded for 1 h in an incubator at 37 ° C. After adsorption was complete, the samples were dried with N_2 and immediately transferred to an ellipsometer for measurement of the adsorbed protein layer. The above procedure was repeated with a 0.2 mg/ml concentration fibronectin in PBS.

9.3.2. Ellipsometric Measurement

Human plasma fibronectin were measured using an automatic ellipsometer equipped with a 632.8 nm helium-neon laser (Gaertner, Inc). The thickness and refractive indices of protein films were determined using an ellipsometer computer program with an accuracy of ± 3Å. Four ellipsometer measurements at different locations on each sample were taken and the average value was calculated.

9.4. Results

9.4.1. Surface Roughness and Oxygen Content

The CO_2 laser treatment brought about a consistently rougher surface on the MgO-PSZ compared with the untreated sample, with R_a increasing as the CO_2 laser power density increased (see Fig. 9.3).

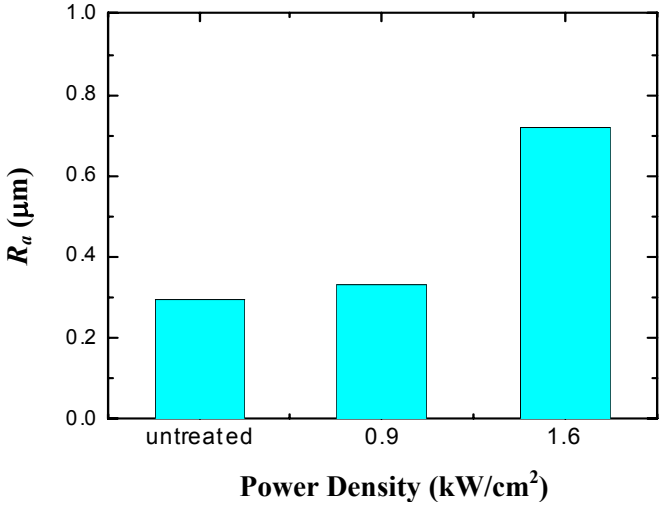

Fig. 9.3. The relationship between R_a and CO_2 laser power density (2000 mm/min)

An XPS analysis revealed that the O_2 surface content of the MgO-PSZ increased with the CO_2 laser power density, as shown in Fig. 9.4.

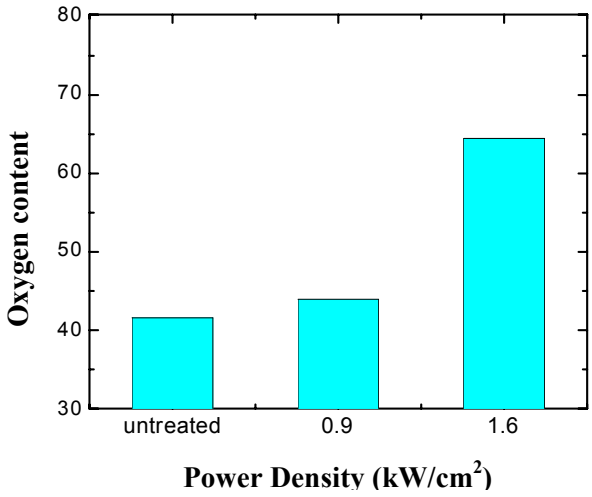

Fig. 9.4. The relationship between surface oxygen content and CO_2 laser power density (2000 mm/min)

9.4.2. Microstructure Effected by CO_2 Laser Irradiation

It was found that the microstructures generated on the MgO-PSZ surface varied with the different CO_2 power densities applied, as shown in Fig. 9.5. The defined microstructures according to the main structure on the MgO-PSZ were hexagonal structure (0.9 kW/cm^2) and cellular structure (1.6 kW/cm^2) as shown in Fig. 9.5(b) and (c).

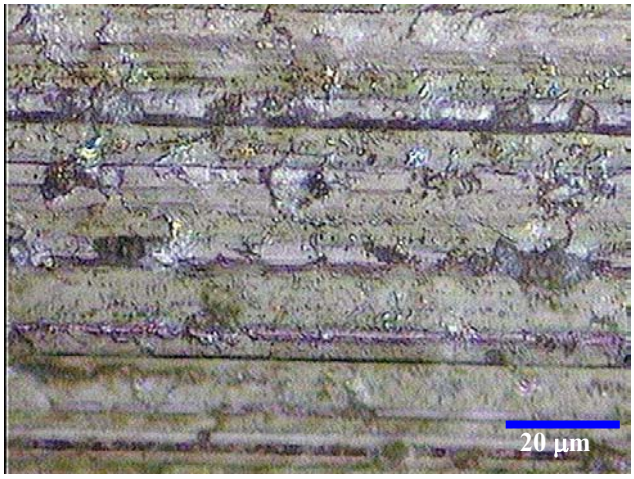

(a)

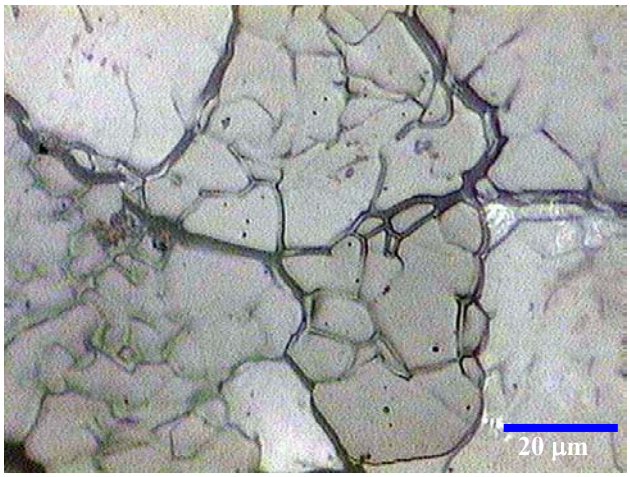

(b)

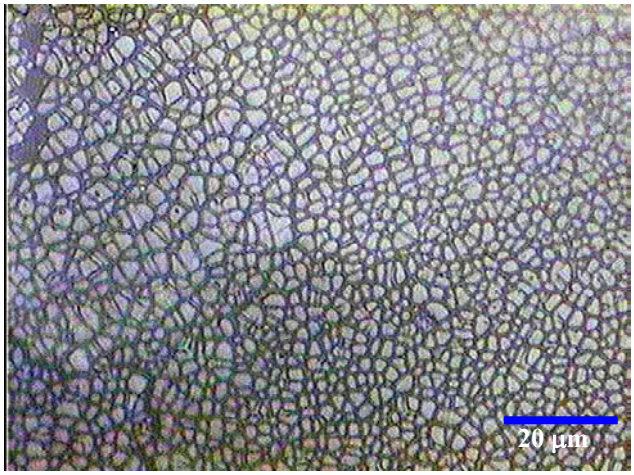

(c)

Fig. 9.5. Optical images of the morphology of (a) the untreated MgO-PSZ and the CO_2 laser treated MgO-PSZ with power densities of (b) 0.9 kW/cm^2, and (c) 1.6 kW/cm^2.

9.4.3. Wettability Characteristics and Surface Energy Analysis

The increased value of $\cos\theta$ denotes higher wettability characteristics of a material. As one can see from Fig. 9.6, the wettability of the MgO-PSZ increased with the CO_2 laser power density. In order to state concisely the change in θ and thus the wettability characteristics of the MgO-PSZ, the glycerol was used as a typical liquid due to the similar trend of the change in θ of the test liquids for the samples before and after CO_2 laser treatment.

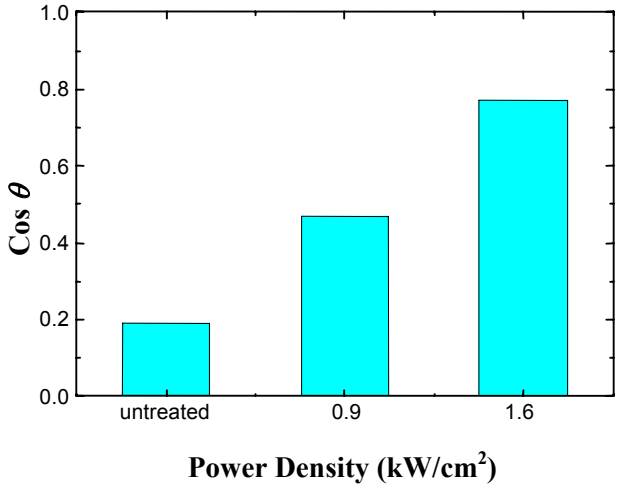

Fig. 9.6. The relationship between the wettability characteristics (cos θ) of the MgO-PSZ and the CO_2 laser power density

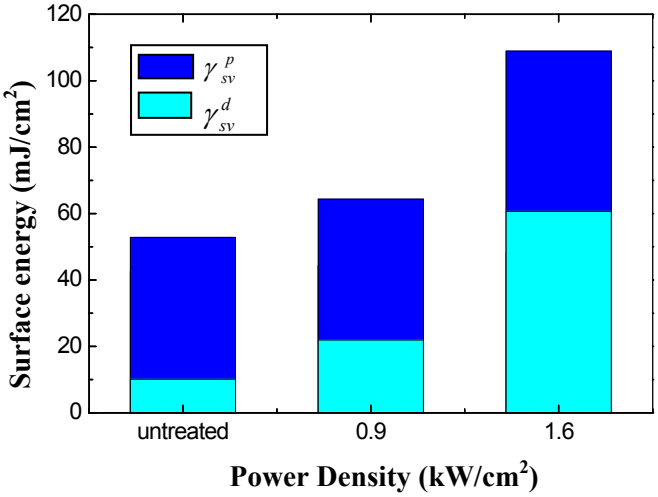

Fig. 9.7. The relationship between the γ_{sv}^{d}, γ_{sv}^{p} (and γ_{sv}) of the MgO-PSZ with CO_2 laser power density

The procedures for the surface energy analysis were described previously in Chapter 7 and the determined values of the untreated and CO_2 laser treated MgO-PSZ (at various CO_2 laser power densities) are given in the Fig. 9.7. As is evident from Fig. 9.7, CO_2 laser treatment increased γ_{sv} of the MgO-PSZ by primarily increasing γ_{sv}^{p}; since γ_{sv}^{d} was similar for all the samples.

9.4.4. Protein Adsorption Analysis

The thickness of the adsorbed albumin and fibronectin layer, which indicates the amount of the adsorbed protein on the untreated and CO_2 laser modified MgO-PSZ, are shown in the Fig. 9.8.

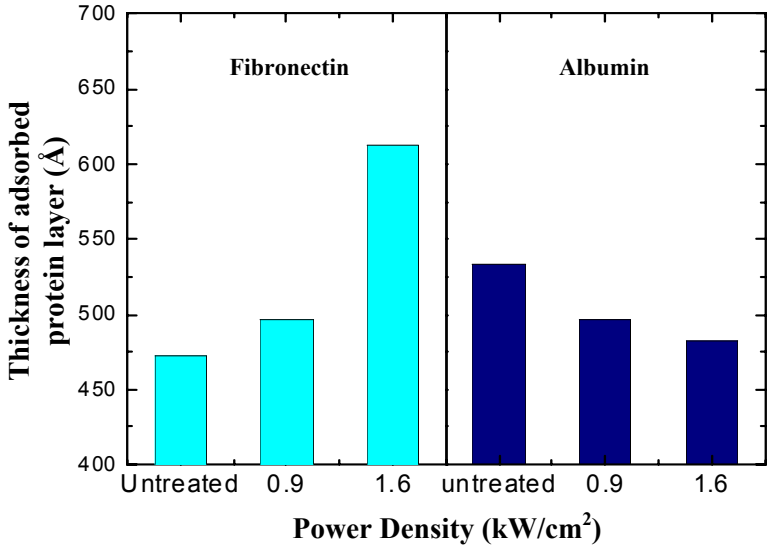

Fig. 9.8. Thickness of the adsorbed fibronectin and albumin layer on the untreated and CO_2 laser treated MgO-PSZ with different CO_2 laser power densities.

It was found that the thickness of the albumin layer on the untreated MgO-PSZ is higher than that on the CO_2 laser modified sample as shown in Fig. 9.8, whereas the thickness of the fibronectin layer is less on the untreated sample than that on the modified sample. The CO_2 laser power density applied in the experiments is negatively correlated to the amounts of albumin, while positively correlated with the fibronectin (see Fig. 9.8).

9.5. Discussion

The results showed that the CO_2 laser treatment promoted the adsorption of the fibronectin on the MgO-PSZ and the amount of the adsorbed fibronectin was positively correlated with the CO_2 laser power density applied in the experiments, as shown in Fig. 9.8. While the thickness of the adsorbed human serum albumin layer on the untreated MgO-PSZ is higher than that on the CO_2 laser modified MgO-PSZ and was negatively correlated with the CO_2 laser power densities. The finding is perhaps not so surprising as various CO_2 laser power densities brought about the different extent change in wettability characteristics and surface roughness of the MgO-PSZ. It is known that the protein adsorption is influenced by the surface chemistry (wettability characteristics) [306] and the surface topography [303].

9.5.1. The Effect of Surface Roughness

The experimental results given in Fig. 9.9 reveal that the amount of fibronectin adsorption increased, while the amount of albumin adsorption decreased with the surface roughness of the

MgO-PSZ. The relationship between the albumin adsorption and surface roughness given in Fig. 9.9 are consistent with the findings of other researchers in so far as bovine serum was adsorbed preferentially onto the smooth substratum [287,307], indicating that the surface roughness of the MgO-PSZ is one of the factors active in the albumin adsorption. However, it was explained that the roughing of Ti surface created hydrophilic surface [308] and the increase in surface hydrophilicity of Ti resulted in lower albumin adsorption [307]. Since it has proved that the surface roughness plays only a minor role in the wettability characteristics of MgO-PSZ following CO_2 laser treatment, it is reasonable to postulate that the wettability characteristics of the MgO-PSZ could play a more important role than the surface roughness in the albumin adsorption.

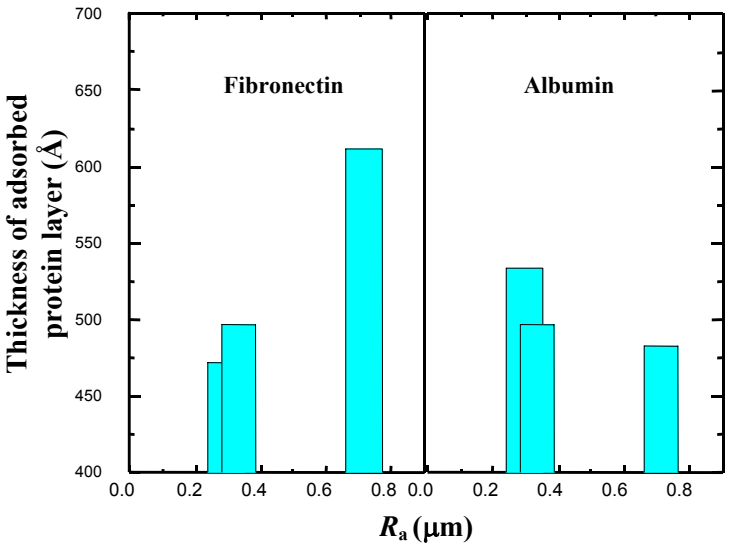

Fig. 9.9. The relationship between the thickness of the adsorbed (a) albumin and (b) fibronectin layer and R_a of the MgO-PSZ

The relationship between the fibronectin adsorption and surface roughness given in Fig. 9.9 is in agreement with previous reports. Deligianni *et al* [287] find that the rough Ti alloy adsorbed much more fibronectin than the smooth one. The much higher affinity of rough substrata to fibronectin could be the driving force for preferential adsorption of fibronectin. However, others researchers have reported that the amounts of immobilised fibronectin on the rough titanium were 50% lower than those adsorbed on smooth one [309]. This decrease was noticed when the roughness was produced by polishing or sandblasting, followed by acid attack, this is an indication that the chemical or mechanical manufacturing process, used to achieve the surface texture, might influence the protein adsorption behaviour of a surface [309]. So, a simple conclusion would be difficult to execute for the relationship between the amplitude of surface roughness and fibronectin adsorption. It must be noted that in this work the CO_2 laser treatment effects changes in other surface properties besides roughness, since surface roughness is only one of the factors affecting protein adsorption. It

is most likely that the surface roughness plays a role in the fibronectin adsorption, but its effects correlate to and are less than the wettability characteristics of the MgO-PSZ.

9.5.2. The Effects of Wettability Characteristics

The previous results are a clear indication that interaction of the CO_2 laser beam with the MgO-PSZ brought about a decrease in contact angle, in turn, improved the wettability characteristics. Such changes in the wettability characteristics are influenced primarily by: the increased surface roughness (see Fig. 9.3); the increased in surface oxygen content (see Fig. 9.4) and surface oxidation; increased the surface energy, by way of microstructures, (see Fig. 9.5), especially polar surface components (see Fig. 9.7). Among them, the surface energy was found to be the main mechanism governing the wettability characteristics of the MgO-PSZ.

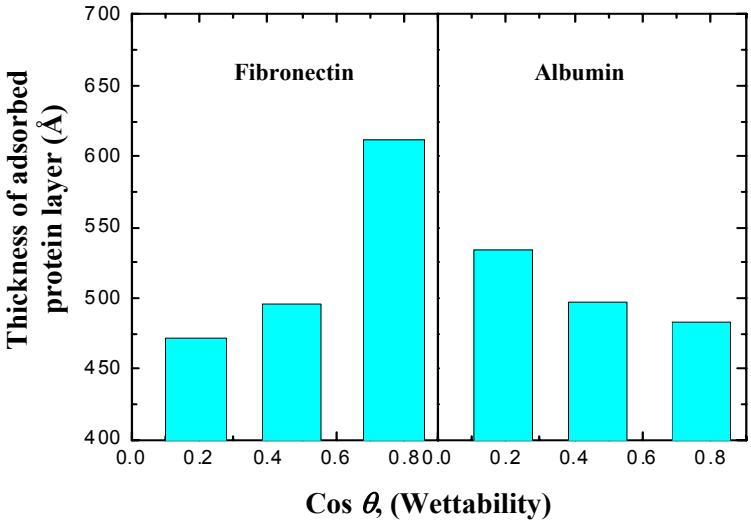

Fig.9.10. The relationship between the thickness of the adsorbed fibronectin layer and wettability characteristics (cos θ) of the MgO-PSZ

As one can see from Fig.9.10, as the wettability of the MgO-PSZ increased, the adsorbed amounts of fibronectin increased, while the adsorbed amounts of albumin decreased. The results of the albumin adsorption are consistent with the previous finding that the increase in surface hydrophilicity of Ti results in lower albumin adsorption [307], showing that the wettability characteristics of the MgO-PSZ could be the main factor active in the albumin adsorption. The results of the adsorption of fibronectin show that it increased on the hydrophilic surface. The previous investigation [310] on the extent of fibronectin adsorption as compared to its biological activity on hydrophobic and hydrophilic surfaces suggested the possibility that fibronectin was adsorbed in two different conformations when incubated with the surfaces a low concentrations, with the more active conformation on the hydrophilic surfaces. The results showed the anti-plasma

fibronectin antibody appeared to bind to the conformation of fibronectin adsorbed on hydrophilic surfaces much better than the conformation of fibronectin adsorbed on hydrophobic surfaces [310]. Therefore, the wettability characteristics of the MgO-PSZ could be the predominant mechanism governing the fibronectin adsorption. It is noticeable that considerable change in the γ_{sv}^{p} instead of minor difference in γ_{sv}^{d} (see Fig. 9.7) was the main mechanism governing the wettability characteristics after CO_2 laser irradiation, indicating that the albumin and fibronectin adsorption on the MgO-PSZ surfaces was probably due to the polar and chemical interactions [311].

9.6. Summary

In this study, the surface properties of a magnesia partially stabilised zirconia (MgO-PSZ) bioceramic were modified using CO_2 laser treatment in order to mediate the albumin and fibronectin protein adsorption with the aim being to favour the bonding between implant and bone interface. An ellipsometer was applied to investigate the protein adsorption on the untreated and CO_2 laser modified MgO-PSZ. The conclusions can be drawn as follows:

1. The CO_2 laser treatment brought about a lower amount of adsorbed albumin layer and a higher amount of the adsorbed fibronectin layer on the MgO-PSZ. Such interactions would be of benefit to the osteoblast cell adhesion since albumin is the no-cell adhesive protein while fibronectin is the cell adhesive protein.
2. The surface roughness and wettability characteristics influenced the adsorption of the protein adsorption. The albumin adsorption decreased, while the fibronectin increased with the increased surface roughness and wettability characteristics of the MgO-PSZ. The effect of the surface roughness is correlated with the wettability characteristics and less than that of the wettability characteristics on the protein adsorption. What is more, the considerable change in the γ_{sv}^{p} and thereof its effect on protein adsorption implied that the albumin and fibronectin adsorption on the MgO-PSZ surfaces was probably due to the polar and chemical interactions.

CHAPTER 10
In Vitro Cell Response on the CO_2 Laser Modified Magnesia Partially Stabilised Zirconia

The chapter investigates the in vitro behaviours of human skin fibroblast cells and hFOB human osteoblast cells on the untreated and CO_2 laser treated MgO-PSZ. The fibroblast cell adhesion and growth was analysed. The evaluations of osteoblast cell adhesion and proliferation were also conducted to analyse the effect of surface properties on the osteoblast cell adhesion and growth. This study discusses the mechanisms active in the fibroblast and osteoblast cell response and thus deduces the main factor.

10.1. Introduction

A large number of groups have studied the interaction of biomaterials with cultured cells because cell compatible materials are thought to be very important in many biomedical applications [106,312-314]. Surface chemistry and/or topography ultimately effect the nature and the strength the interactions occurring at the biomaterial-biological environment (e.g. water and ion sorption, protein adsorption, cell adhesion, mobility, spreading and proliferation). Numerous *in vitro* experiments have shown that the cell behaviour is influenced by the physicochemical properties of polymer surfaces such as wettability, chemistry and roughness [315-317]. The rudimentary problem in biomaterials is the translation of the desirable biomedical properties that define biocompatibility for a particular end application into materials properties that lead to the correct selection, design, or synthesis of an appropriate material for that use. This is a particularly difficult problem with respect to surface properties because structure-function relationships connecting biomedical function to surface chemistry and interfacial properties are not yet generally available. Elucidating these structure-function relationships is a fundamental challenge of modern biomaterials surface science. The biological response to artificial materials is primarily driven by interfacial phenomena at biomaterial surfaces and wetting measurements directly probe these interfacial properties. Wettability, as measured in surface energies or tensions, must be in some way connected to surface chemistry, as described in compositional terms, because it is those functional groups residing at a

given surface with specific chemical reactivity that most profoundly distinguish one surface from any other [99]. Zirconia-based bioceramics are frequently used in the high-load bearing sites such as artificial knee and bone screws in orthopaedic application and dental post crown in dental application [318]. However, these materials do not naturally form a direct bond with bone, thereby suffering from a lack of osseointegration [195]. When orthopaedic/dental implants are surgically placed within the body, they are exposed to blood, extracellular fluids, and various cell types (for example, osteoblasts, osteoclasts, fibroblasts, endothelial cells, etc.) [319]. The cellular behaviour on a biomaterial is an important factor determining the biocompatibility. Osteoblasts and fibroblasts are anchorage-dependent cells that must adhere to substrate surfaces prior to undergoing subsequent cell functions such as proliferation, synthesis of collagen and other extracellular matrix proteins, etc. Cell adhesion is one of the initial events essential to subsequent proliferation and differentiation of cells before tissue formation. The first physiological process that occurs within the initial stages of exposure is the adsorption of biomolecules onto the surface this is usually followed by cellular interactions. The whole process of adhesion and spreading of the cell after contact to biomaterials consists of cell attachment, growth of filopodia, cytoplasmic webbing and flattening of the cell mass, and the ruffling of peripheral cytoplasm, which progress in a sequential fashion [313]. The development of bone-implant interfaces depends on the direct interactions of bone matrix and osteoblasts with the biomaterial. There is a substantial body of literature based on the premise that improved initial attachment of osteoblasts or osteoblast precursor cells to orthopaedic implant surfaces may lead to improved bone integration of the implant and longer-term stability [320]. Osteoblast adhesion is a prerequisite for bone-biomaterial interaction and depends on the surface aspect of materials. Cell in contact with a material surface will firstly attach, adhere and then spread. The quality of this adhesion will influence their morphology and their future capacity for proliferation and differentiation. The attachment of anchorage-dependent cells such as osteoblasts to biomaterial surfaces is a complex process involving cell attachment and spreading [321], focal adhesion formation, and extracellular matrix formation and reorganisation [322].

10.2. Experimental Procedure

The CO_2 laser processing procedures, material characterisation techniques and wettability analysis of the untreated and CO_2 laser treated MgO-PSZ are detailed in Section 5.2.2, Section 5.2.3 and Section 7.2.1. The surface energy characterisation and the microstructures and crystal size analysis are detailed in Section 7.4 and Section 7.6.1 respectively.

10.2.1. Cell Culture

Human skin fibroblast cells and human osteoblast cell were used to evaluate the cell response on the MgO-PSZ. The human skin fibroblast cells were derived directly from human skin samples. The cells were cultured in Dulbecco's Modification of Eagle's Medium (DMEM) containing 10% fetal bovine serum and 100IU/mL penicillin, 100 μg/mL streptomycin (Gibco, Inc.). They were incubated at 37ºC in a humidified atmosphere of 5% CO_2. The human osteoblastic cell line hFOB 1.19 was obtained from American Type Culture Collection (ATCC, Inc.). These cells were cultured in a medium containing a 1:1 mixture Dulbecco's Modified Eagle's medium without phenol red and Ham's F12 medium with 2.5 mM L-glutamine (D-MEM/F-12 Medium), supplemented with 10% fetal bovine serum (ATCC, Inc) and 0.3 mg/ml G418 (Calbiochem, Inc.) at 37°C in a humidified, 5% CO_2 incubator. Osteoblasts at passage numbers 2-4 were used in this experiment.

10.2.2. Cell Adhesion and Growth Analysis

The MgO-PSZ samples were placed in a 24-well tissue culture polystyrene plate (NUNC, Inc.). The samples were sterilised in 70% alcohol and rinsed in phosphate buffered saline (PBS) solution. The fibroblast cell suspension of 1×10^5 cells/ml was prepared before seeding. The 0.5 ml cell suspension seeded on the samples and then maintained in the incubator for 7 days. To analyse the osteoblast cell attachment and morphology, one untreated sample and one CO_2 laser modified sample (power density of 1.6 kW/cm^2) were used in the assessment of cell morphology. The specimens were seeded with the 0.5 ml cell suspension of 1×10^5 cell/mL and analysed under SEM after 24 hours cell culture. For a 7-day osteoblast cell adhesion analysis, the suspension of 4×10^5 cell/mL were prepared before seeding. The samples were rinsed by PBS and then were seeded with 0.5 mL cell suspension. The cells were then cultured with cell culture medium and then maintained in the incubator for one week. The cell culture medium was changed every 3 days. For determination of osteoblast cell proliferation, the specimens were seeded with the 0.5 ml cell suspension of 1×10^5 cell/ml and cultured for 14 days. Osteoblast cells were detached by trypsinization and counted using a hematocytometer.

10.2.3. Microscopic Analysis

After culturing, the cells were fixed in 2.5% glutaraldehyde solution for 1 h, washed with PBS and then dehydrated in increasing concentrations of alcohol (70%, 85%, and 100%). The fibroblast cells were dried at room temperature and osteoblast cells were dried in the critical point dryer (CPD030, BAL-TEC, GmbH). Then the samples examined with a SEM (5600LV, JEOL, Ltd.) after sputter gold coating. For the cell adhesion analysis, three images were taken for the each sample at different areas and a typical one was chosen for the analysis.

10.2.4. Statistics

Statistical analysis was performed with a SPSS v.12 software package (SPSS/PC, Inc.). Data are reported as mean ± SD at a significance level of $p<0.05$. After having verified normal distribution and homogeneity of variances, one-way ANOVA and Scheffé's post hoc multiple comparison tests were done.

10.3. Fibroblast Cell Adhesion on CO_2 Laser Treated MgO-PSZ

10.3.1. The General Effects of CO_2 Laser Treatment

The attached fibroblast cells on the untreated MgO-PSZ and CO_2 laser treated MgO-PSZ were examined using SEM as shown in Fig. 10.1.

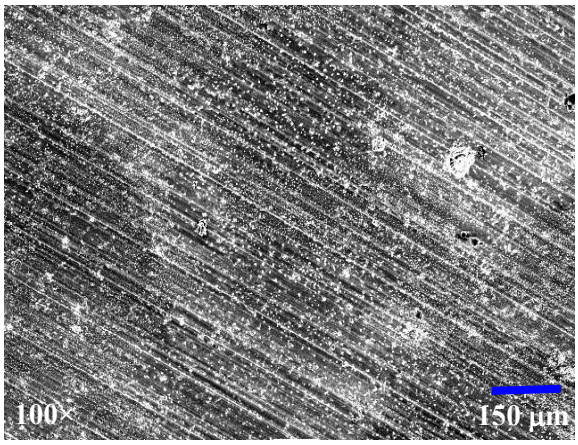

(a)

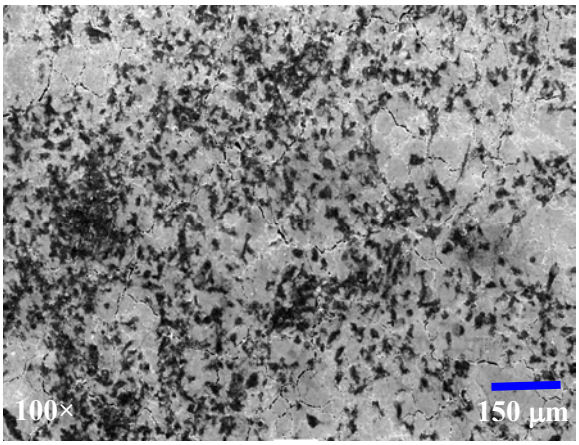

(b)

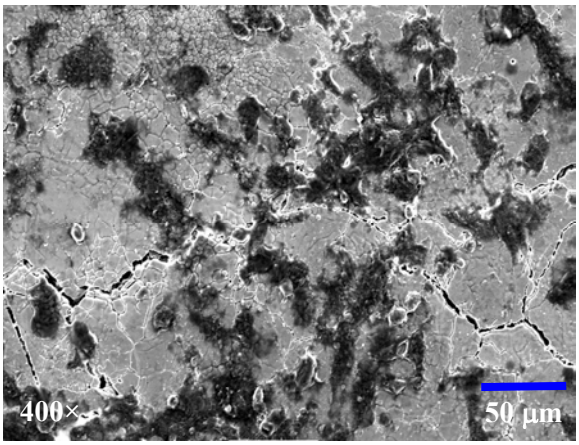

(c)

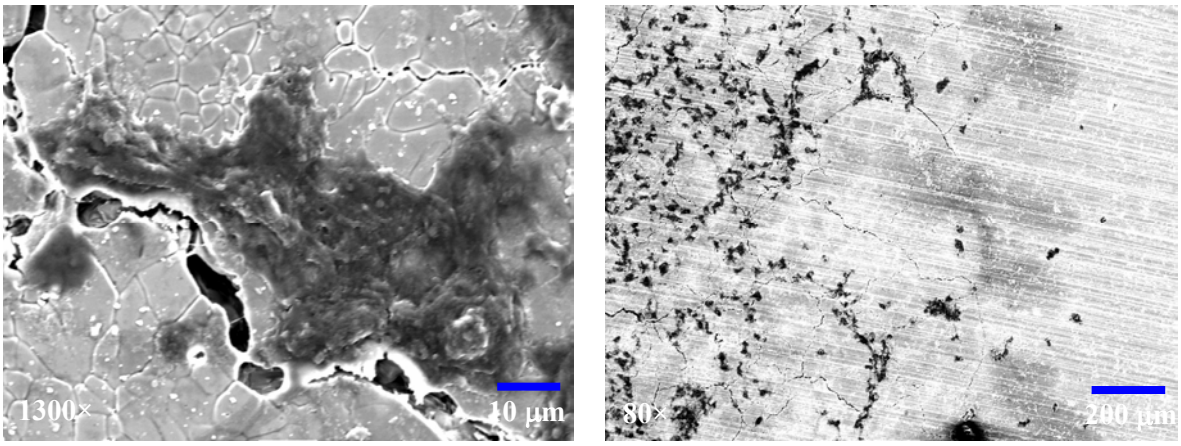

(d) (e)

Fig. 10.1. SEM micrographs of human skin fibroblast cells cultured on the (a) the untreated MgO-PSZ, and (b, c, d) in the centre and (e) at the edge of CO_2 laser treated MgO-PSZ (with power density of 1.6 kW/cm^2 and traverse speed of 2000 mm/min).

As can be seen in Fig. 10.1(a), no cells appeared on the surface of the untreated MgO-PSZ, showing that the surface was not favourable for cell adhesion. However, augmentation and adhesion of the fibroblast cells were found on CO_2 laser treated MgO-PSZ. Some of cells (see Fig. 10.1(d)) could be considered as flattened and spread, indicating the final stage of the cell adhesion on the CO_2 laser treated MgO-PSZ. The interface at the edge of the CO_2 laser treated track (see Fig. 10.1(e)) revealed that only a few cells were present at this region. Thus, it found that CO_2 laser treatment brought about the improved cell response to the MgO-PSZ.

10.3.2. The Effects of Power Density Variation

Fig. 10.2 shows the attachment of human fibroblast cells on the surface of the MgO-PSZ treated with various laser power densities and reveals that the degree of fibroblast cell adhesion and growth in terms of cell coverage area varied with the CO_2 laser power density. As before, no cells attached onto the untreated sample whilst cells adhered onto the CO_2 laser treated sample (see Fig. 10.2). On the MgO-PSZ treated with a power density of 0.5 kW/cm^2 in the Fig. 10.2(b), cell adhesion was sparse and occurred in various locations on the CO_2 laser treated track. When the CO_2 laser power density reached at 0.9 kW/cm^2 (see Fig. 10.2(c)), more cells adhered on more locations on the MgO-PSZ. In Fig. 10.2(d) and (e), very densely packed cells appeared on the CO_2 laser treated MgO-PSZ with power densities of 1.6 kW/cm^2 and 1.9 kW/cm^2 respectively.

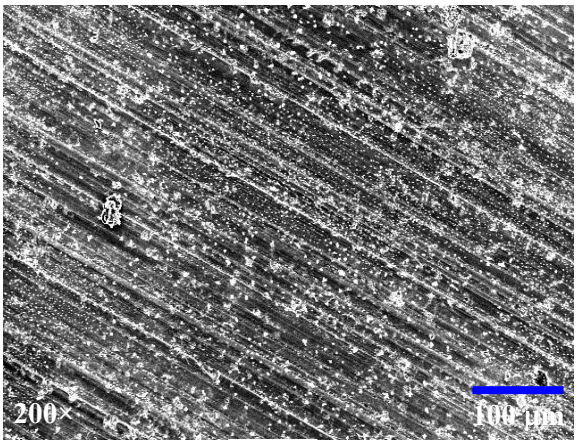

(a)

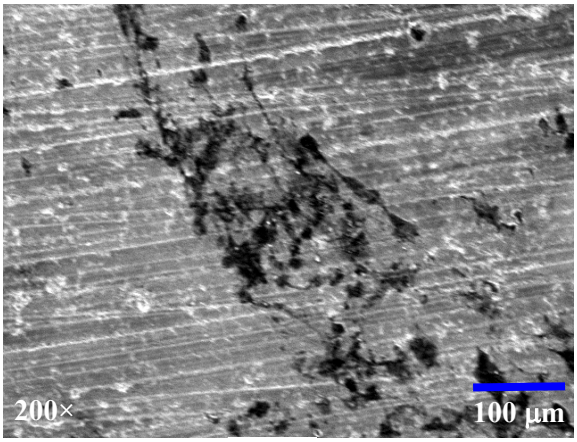

(b)

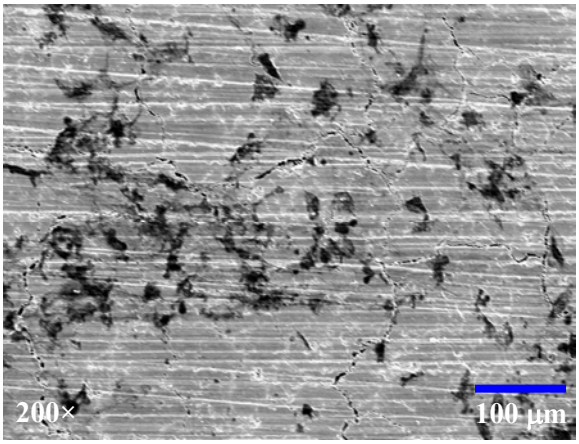

(c)

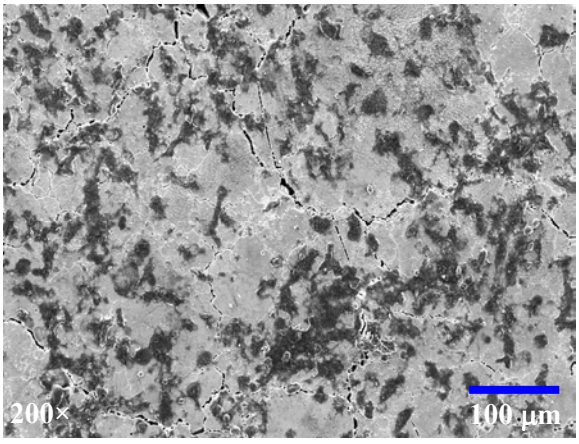

(d)

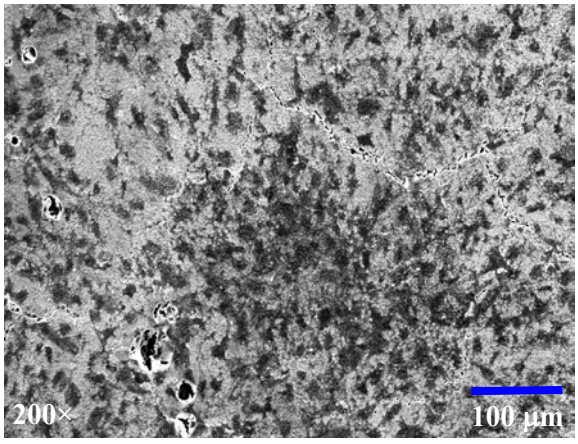

(e)

Fig. 10.2. SEM micrographs of human fibroblast cells on the (a) untreated MgO-PSZ and CO_2 laser-treated MgO-PSZ at traverse speed at 2000 mm/min with power densities of (b) 0.5 kW/cm^2, (c) 0.9 kW/cm^2, (d) 1.6 kW/cm^2, and (e) 1.9 kW/cm^2.

To quantify and indicate the fibroblast cell adhesion and growth, the cell cover density is defined by the ratio of the fibroblast cell adhesion area to the whole surface area shown in the three typical

SEM images and is presented by the average value. Thus, the fibroblast cells covered about 0 % of the area on the untreated surface as shown in Fig. 10.3(a), whereas the cells covered more area on the CO_2 laser treated MgO-PSZ. Following CO_2 laser treatment, there was a cover density about 12 % at 0.6 kW/cm^2 (see Fig. 10.3(b)), 20 % at 0.9 kW/cm^2 (see Fig. 10.3(c)), 65% at 1.6 kW/cm^2 (see Fig. 10.3 (d)), 70% at 1.9 kW/cm^2 (see Fig. 10.3(e)).

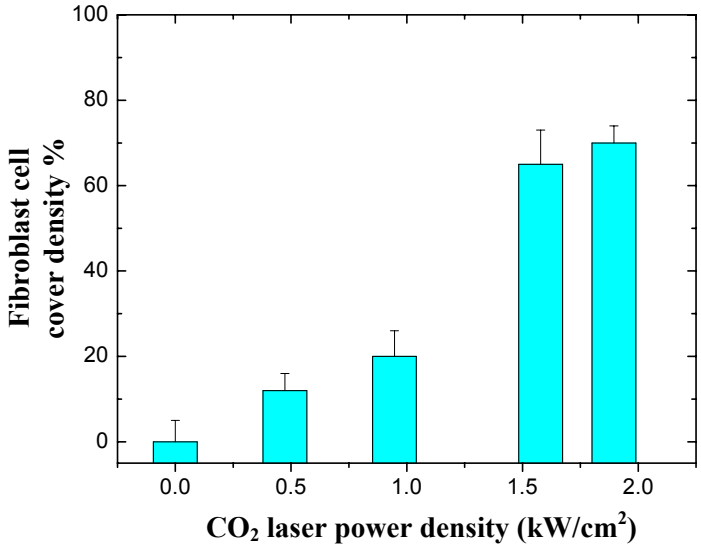

Fig. 10.3.The relationship between the cover density of the hFOB human osteoblast cells and CO_2 laser power density

10.3.3. The Effects of Wettability Characteristics on Fibroblast Cell Adhesion

As discussed in the Section 7.4, the CO_2 laser treatment brought about the changes in surface properties in terms of the surface roughness, surface oxygen content, phase transformation, solidified microstructures, and surface energy. The modifications of the wettability characteristics are attributed to these surface changes of the MgO-PSZ and primarily determined by the surface energy.

The differences in wettability characteristics and γ_{sv}^{p} are postulated to be the determinant factor governing the differences in the fibroblast cell adhesion on the MgO-PSZ before and after CO_2 laser treatment. As evident in Fig. 10.1, the CO_2 laser treated MgO-PSZ (1.6 kW/cm^2) with high wettability (γ_{sv} =108.9 mJ/m^2) favoured the cell adhesion (see Fig. 10.1(b)), while the untreated MgO-PSZ with low wettability (γ_{sv} = 52.5 mJ/m^2) did not support the cell adhesion (see Fig. 10.1(a)). It is assumed that the MgO-PSZ with high wettability characteristics supported fibroblast cell adhesion to a greater extent than the untreated material with low wettability characteristics. This is also particular apparent when one considers Fig. 10.1(e) that some cells appeared on the CO_2 laser treated region and few cells adhered on the untreated region.

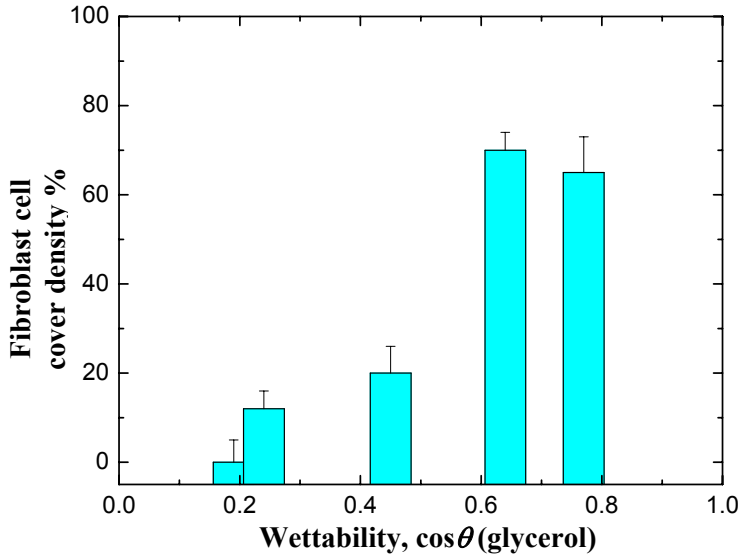

(a)

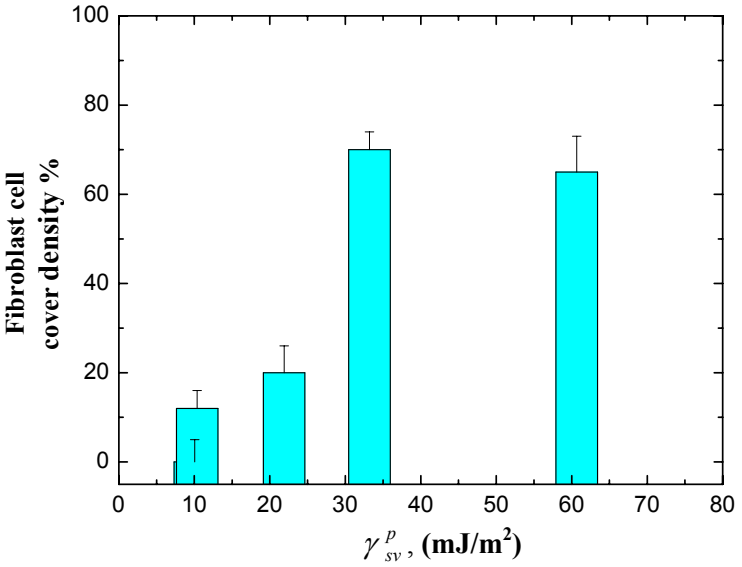

(b)

Fig. 10.4. The relationship between the cover density of the human skin fibroblast cells and (a) wettability characteristics and (b) γ_{sv}^{p}

The values of cos θ (glycerol) are used to express the wettability characteristics of the MgO-PSZ. An increase in cos θ corresponds to an increase in wettability characteristics. Fig. 10.4(a) shows the relationship between the fibroblast cell cover density that presents the cell adhesion and growth and the wettability characteristics (cos θ) of the MgO-PSZ. As is evident from Fig. 10.4(a), the fibroblast cell cover density increases generally as wettability characteristics increases. In the experimental condition applied, the fibroblast cells did not adhere on the untreated MgO-PSZ with the lowest wettability characteristics. The cell cover density increases slightly when the cos θ

increases from 0.18 to 0.50, then increases sharply to the maximum extent when cos θ increases to 0.60. When the cos θ increased further, the cell cover density does not increase anymore. As the results in Chapter 7 have shown, the change in wettability characteristics was primarily influenced by the surface energy of the MgO-PSZ, especially γ_{sv}^{p}. As one can see from Fig. 10.4, the fibroblast cell cover density generally increases with the γ_{sv}^{p}. This implies that γ_{sv}^{p} influenced the behaviour of the fibroblast more strongly compared to γ_{sv}^{d}. Thus, γ_{sv}^{p} presenting chemical reaction primarily determines the fibroblast cell adhesion.

10.3.4. The Effects of Topography on Fibroblast Cell Adhesion

The study by Ruardy *et al* [323] has shown that the adhesion of human skin fibroblast on the physicochemical chemical characterised gradient surfaces is dependent not only on the wettability characteristics, but also on its roughness. In this study, the CO_2 laser treatment generated a consistently rougher surface on the MgO-PSZ compared with the untreated sample and R_a increased with the power density as shown in Fig. 10.5.

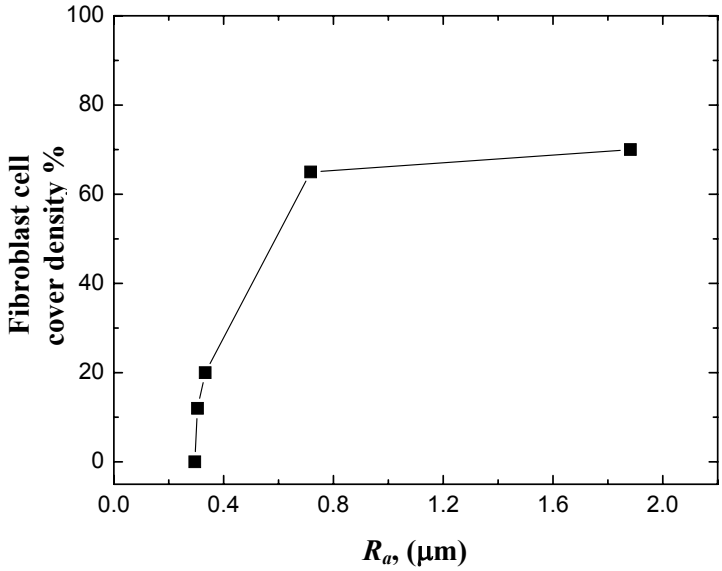

Fig. 10.5. The relationship between the cover density of the human skin fibroblast cells and R_a

As shown in Fig. 10.5, the CO_2 laser treated MgO-PSZ with rougher surface has higher fibroblast cell cover density compared with the smooth untreated sample. It is interesting to note from Fig. 10.1(e) that a few human fibroblast cells spread and directed themselves according to the line of the cracks. But no evidence shows that the fibroblast cell adhesion depends on the cracks at the MgO-PSZ surface. It was thought that the groove generated by the crack could be the influential factor governing the direction of the fibroblast cell spread.

10.3.5. Discussion of Fibroblast Cell Response

The study has shown that the CO_2 laser treatment brought about a better response of the human skin fibroblast cell on the MgO-PSZ. The changes in wettability characteristics and surface roughness generated by the CO_2 laser treatment are the factors influencing the adhesion and growth of the human skin fibroblast on the MgO-PSZ. As discussed previously, the surface roughness is also one of the influential factors on the wettability characteristics, but it just plays a minor role on the wettability characteristics. It is postulated that the wettability characteristics, presenting the physicochemical property of the MgO-PSZ, is the main mechanism governing the fibroblast cell adhesion. The previous analysis has found that the γ_{sv}^{p} is the determinant factor influencing wettability characteristics and can represent the change of the wettability characteristics.

The relationship between ΔF_{adh} (the interfacial free energy of cell adhesion) and substratum surface free energy (or wettability) shown in Fig 3.5 shows that substrata with γ_{sv} below 50 mJ/cm^2 does not favour the cell adhesion, whilst the favourable adhesion force increases with the γ_{sv} of substrata in the range of 50 to 100 mJ/cm^2. This could explained that no cells adhered on the untreated sample (53.3 mJ/cm^2), while some cells adhered on the CO_2 laser treated MgO-PSZ (108.9 mJ/cm^2) (see Fig. 10.2). The relationship between fibroblast cell adhesion and total surface energy of the MgO-PSZ observed in the Fig. 10.6 has a similar trend in terms of cell adhesion change as the previous studies shown in Fig. 3.5. As one can see from Fig. 10.6, CO_2 laser treatment resulted in higher surface energy and better attachment of human skin fibroblast cells on the MgO-PSZ surface than on the untreated MgO-PSZ . For the samples treated with a power density lower than 0.9 kW/cm^2, the γ_{sv} and fibroblast cell adhesion improved slightly. For the sample treated with a relatively medium power density (0.9 -1.6 kW/cm^2), the γ_{sv} and adhesion of the cells increases sharply. As discussed previously, melting occurred in this range and crystal cell microstructure form on the surface of the MgO-PSZ. After γ_{sv} decreased on the MgO-PSZ treated at the relatively higher CO_2 laser power density (> 1.6 kW/cm^2), the cell attachment increased a little bit. Therefore, the fibroblast cell adhesion, closely correlated with the γ_{sv}, shows a similar change with the γ_{sv} depending on the CO_2 laser power density when it is lower than 1.6 kW/cm^2. It is noted that there is not a total linear relationship between the fibroblast cell adhesion and surface energy. The fibroblast cell adhesion on the MgO-PSZ with surface energy of 80.7 mJ/cm^2 is higher than that on the MgO-PSZ with surface energy of 108.9 mJ/cm^2. This finding suggests that the cell adhesion preferred on the MgO-PSZ with moderate wettability characteristics. Indeed, some works has shown that neurite formation of PC-12 cells [125] and was increased more various types of cells (Chinese hamster ovary, fibroblast, and endothelial cells) [324] onto the positions with moderate hydrophilicity of the wettability gradient surface than onto the more hydrophobic or hydrophilic positions.

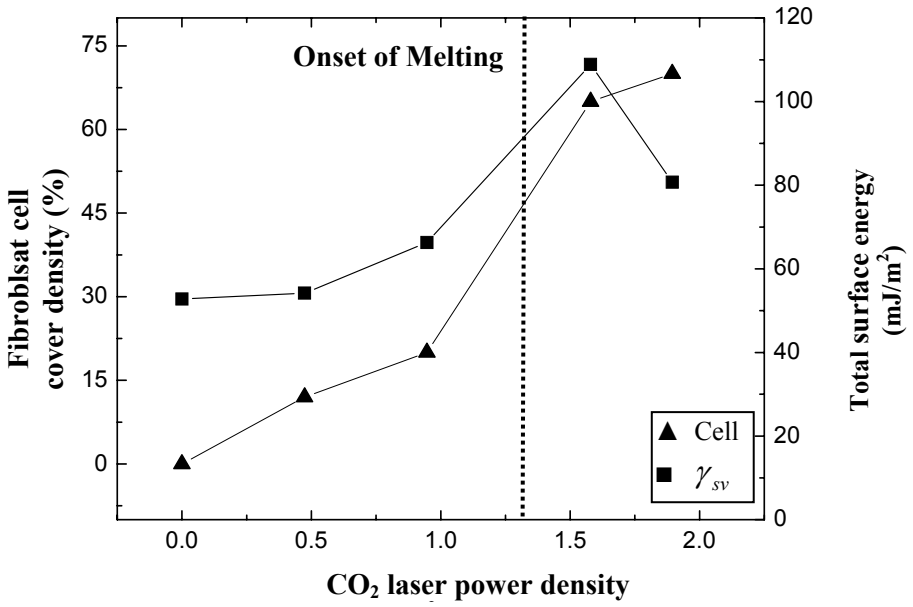

Fig. 10.6. Human skin fibroblast cell attachment as a function of the MgO-PSZ surface energy (γ_s, wettability) and power density of CO_2 laser treatment.

All cell types, other than those that grow in suspension, are in contact with substrates having certain topography. Topography can influence cells in a wide variety of the ways by confining the channels of diffusion for the access of nutrients and the escape of their waste products. The shapes taken up by the cells reacting to the surrounding topography may introduce strains into the cytoskeleton, in some parts of the cell, which could in turn influence ion channels as observed in the stretch receptors of a variety of organisms. Currently, the topographical reactions of cells usually refer to their movements, shape, orientation and proliferation [325]. In this study, it was found that a small number of fibroblasts cells spread and directed themselves along the line of the few cracks (see Fig. 10.1(e)). This indicates that the topography of the MgO-PSZ influence both the spreading and orientation of the cells. The skin fibroblast behaviour in relation to grooves has been studied by the Meyle *et al* [326]. Ponsonnet *et al* [325] have found that and fibroblast cells aligning themselves along the groove axis. Moreover, it has been shown by Dunn and Brown [327] that fibroblasts on grooved substrates could form actin fibre terminations (suggestive of focal adhesion) both on the ridges and in the grooves, and that orientation and elongation appear to be the result of inhibition of the cell's marginal expansion in any direction other than that of the grooves. The finding reveals that the more fibroblast cells on rougher MgO-PSZ compared with the smoother samplers (see Fig. 10.5). This fact is in contradiction with the previous studies by Ponsonnet *et al* [325] that the higher the roughness of the NiTi, the lower the fibroblast cell proliferation, indicating other properties plays more important role than the surface roughness in the fibroblast cell adhesion and growth on the MgO-PSZ. Since the wettability characteristics and surface roughness changed simultaneously

after CO_2 laser treatment, it is reasonable to postulate that the wettability characteristics is the main mechanism and its effects is much more important than the surface roughness on the fibroblast cell adhesion and growth.

10.4. Osteoblast Cell Response on CO_2 Laser Treated MgO-PSZ

This hFOB human osteoblast cell line was established by transfection of limb tissue obtained from a spontaneous miscarriage. The cells have the ability to differentiate into mature osteoblasts expressing the normal osteoblast phenotype and provide a homogenous, rapidly proliferating model system for study normal human osteoblast differentiation, osteoblast physiologym and hormonal, growth factor, and other cytokine effects on osteoblast function and differentiation. It overcomes disadvantages of earlier *in vitro* model systems, as there were unknown species-specific phenotype characteristics of animal osteoblast cultures and very slow rate proliferation as well as short lifetime of primary cultures derived from normal human bone [328].

10.4.1. The General Effect of CO_2 Laser Treatment on Osteoblast Attachment

Fig. 10.7(a) shows that no osteoblast cells were observed on the untreated MgO-PSZ after 24 h cell incubation, whereas a few cells attached on the CO_2 laser treated MgO-PSZ (Fig. 10.7(b)).

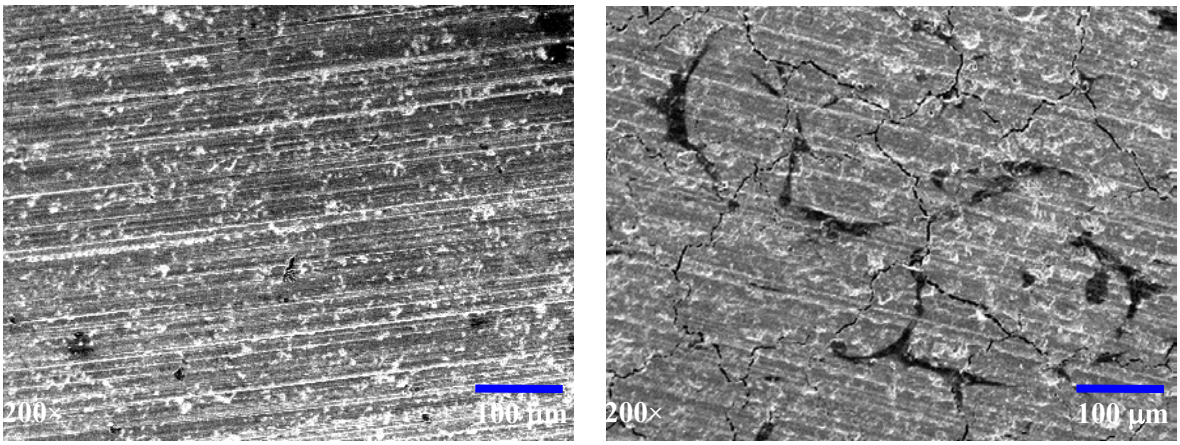

(a) (b)

Fig. 10.7. SEM image of hFOB human osteoblast cells after 24 hours on the (a) untreated MgO-PSZ and (b) CO_2 laser treated MgO-PSZ at power densities of 1.6 kW/cm^2.

It is quite clear that the osteoblast cell attachment on the MgO-PSZ was influenced by the CO_2 laser treatment, indicating the surface properties generated by the CO_2 laser treatment were more favourable for the osteoblast cell attachment. The cells on the CO_2 laser treated samples showed the filopodia and spread well (Fig. 10.7(b)), denoting the good cell attachment.

Moreover, it is evident from Fig. 10.8 that the osteoblast cells had different morphologies at different regions of the CO_2 laser treated track. Fig. 10.8(a) shows that the osteoblast cells at the edge underwent initial spreading and the individual cell was found to cover the area about 30 to 40 μm as shown in Fig. 10.8(b). Short filopodia protruded and elongated about 5 to 10 μm from the osteoblast cell (Fig. 10.8(b)). Elongation direction of the short filopodia implies the direction of the migration process. Conversely, the osteoblast cells at the centre reached to a stage where they grew and spread to cover a region of 60-150 μm (Fig. 10.8(a)).

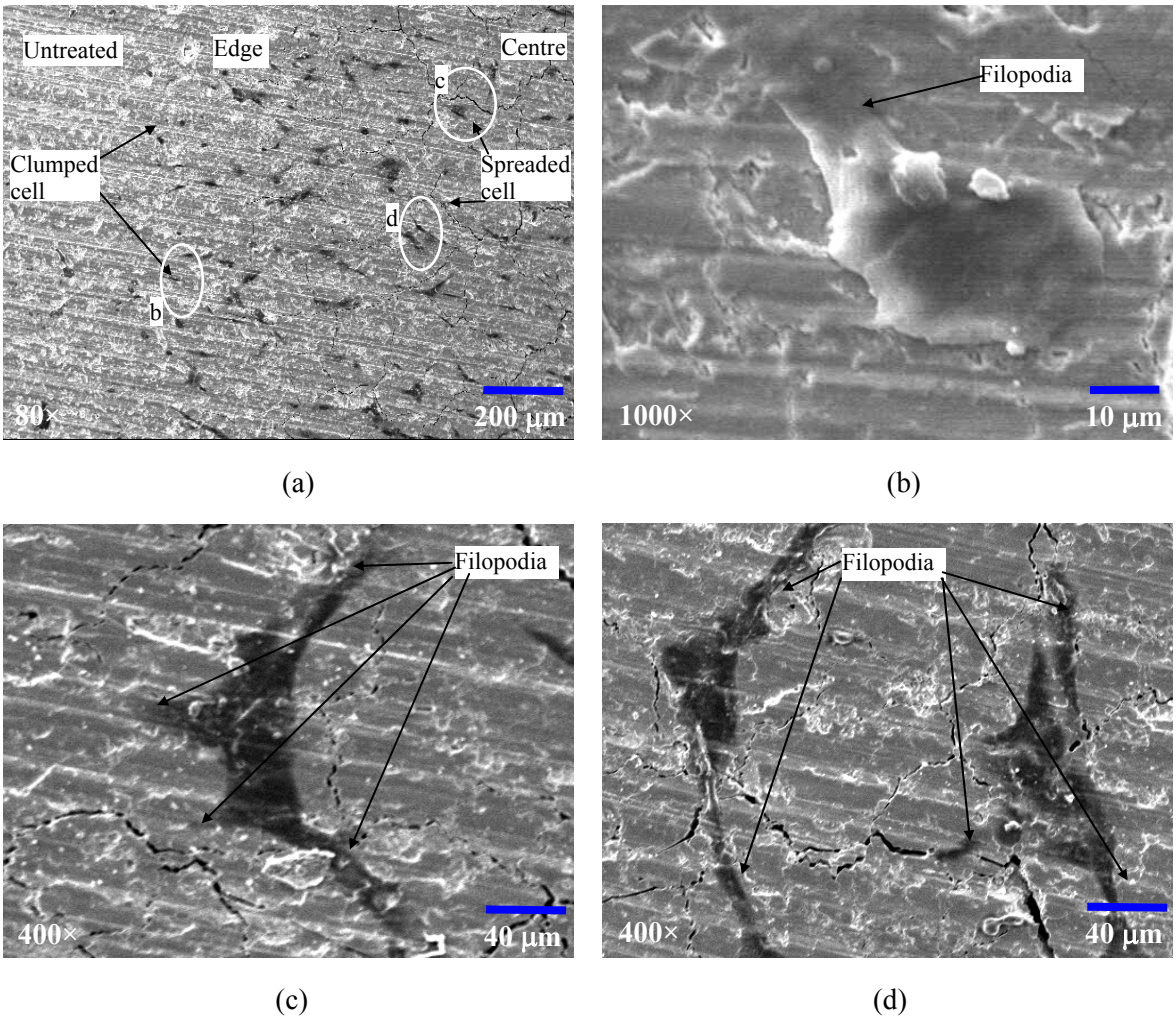

Fig. 10.8. SEM image of hFOB human osteoblast cells after 24 h on (a) at the interface region, (b) the circled area at the edge, (c) (d) the circled area at the centre of the CO_2 laser treated MgO-PSZ with 1.6 kW/cm^2 power density.

One typical osteoblast cell (Fig. 10.8(c)), had spread completely and flattened, with the cytoplasmic spread to cover an area about 30-50 μm as well as forming four filopodias, two of them elongated to 50–60 μm. Likewise, another two osteoblast cells (Fig. 10.8(d)), had a flat cytoplasm with two filopodias elongated to 50–60 μm. The morphologies of these osteoblast cells display the final stage

of cell attachment. In general, osteoblast cells in the centre spread better and reach a higher stage of the cell attachment than those at the edge of the CO_2 laser treated track. Since the CO_2 laser treatment exerted a higher photo-chemical effect at the centre than on the edge due to intensity distribution of the CO_2 laser TEM_{01} beam mode (Fig. 6.12), it could be concluded that the osteoblast cell spreading and attachment is influenced by the level of the CO_2 laser treatment.

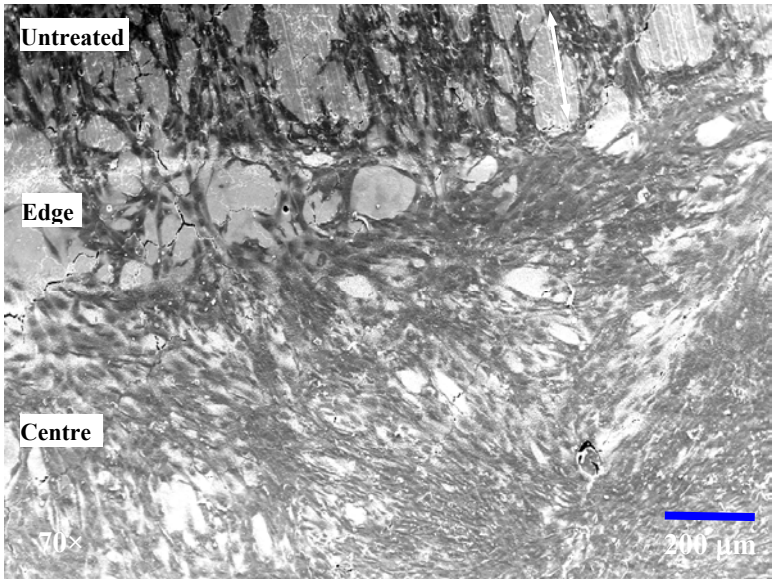

Fig. 10.9. The SEM image of the hFOB osteoblast cells on the different region of the CO_2 laser treated sample (at power density of 1.6 kw/cm^2 edge)

Fig. 10.9 shows the different osteoblast cell adhesion across the untreated region and the CO_2 laser treated track on the sample treated with a power density of 1.6 kW/cm^2. Few osteoblast cells were observed on the untreated region near the edge of the CO_2 laser treated track. At the edge of the track, some surface area was uncovered by the osteoblast cells, whereas the osteoblast cells covered almost the whole centre area of the track. This confirms that osteoblast cell adhesion is influenced by the degree of the CO_2 laser treatment. What is more, it is also noted that the direction of osteoblast cell spreading on the untreated region, which is parallel to the groove, is different from the direction of osteoblast cell spreading on the CO_2 laser treated region (see Fig. 10.9).

10.4.2. The Effects of Power Density Variation

After a 7-day incubation period, the hFOB osteoblast cells grew well and formed a layer on all the samples (Fig. 10.10). The degree of osteoblast cell adhesion and growth in terms of cell coverage area varied with the CO_2 laser power density. The cover density is defined by the ratio of the osteoblast cell adhesion area to the whole surface area and is used as an indication of the osteoblast cell adhesion and growth.

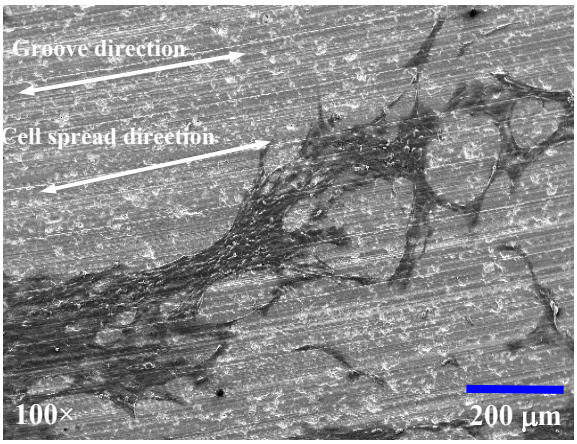

(a)

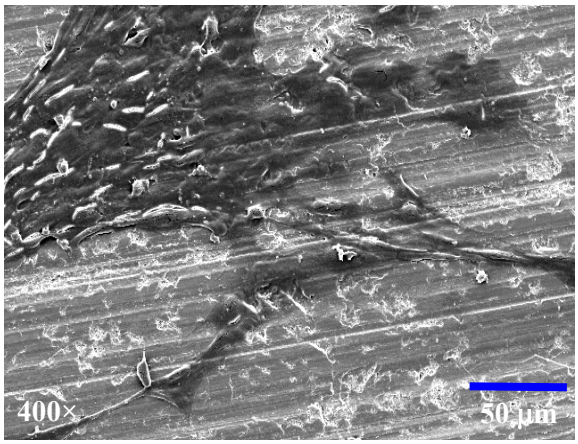

(a-1)

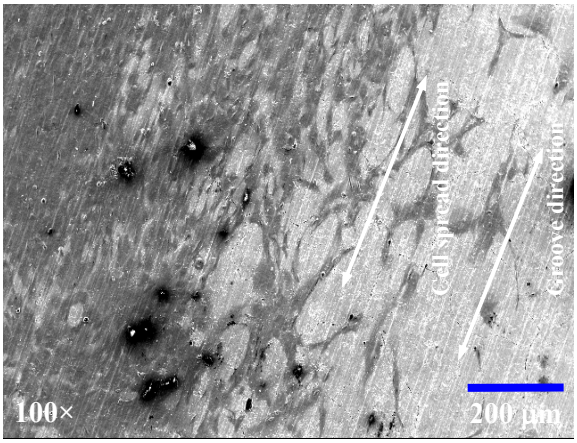

(b)

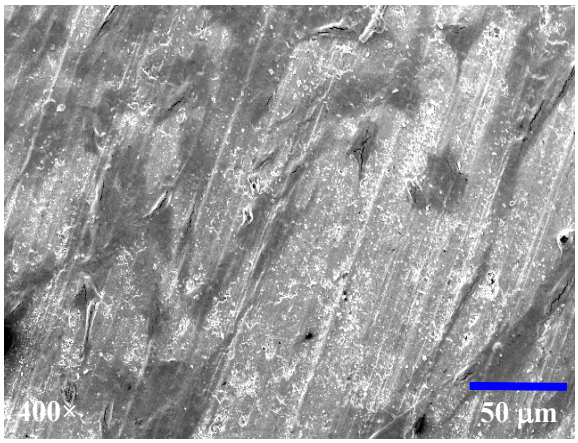

(b-1)

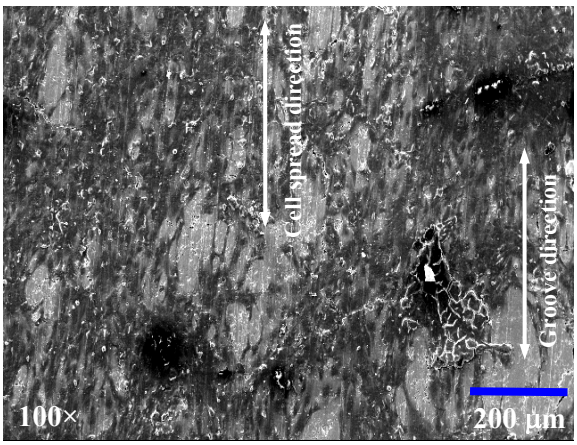

(c)

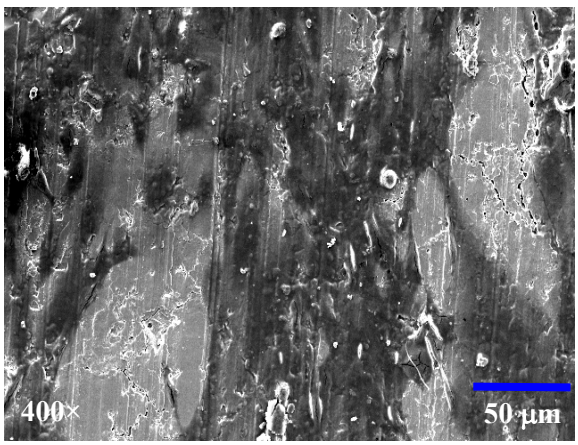

(c-1)

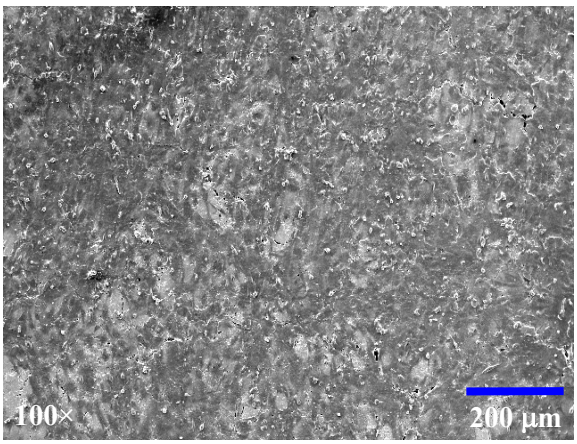

(d)

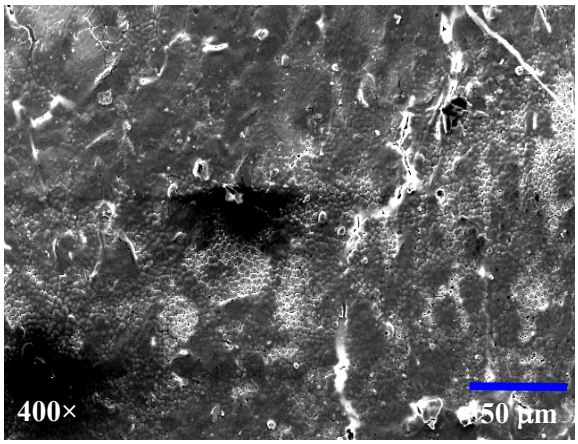

(d-1)

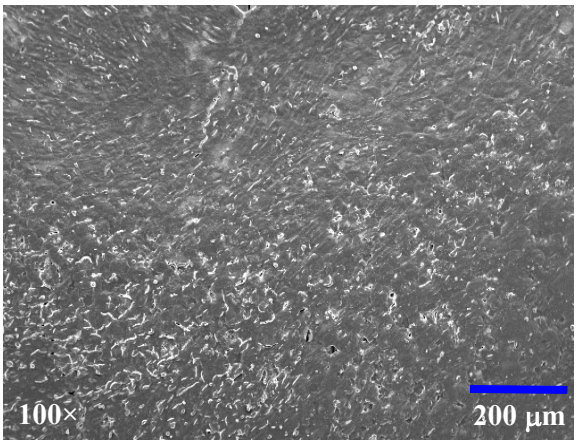

(e)

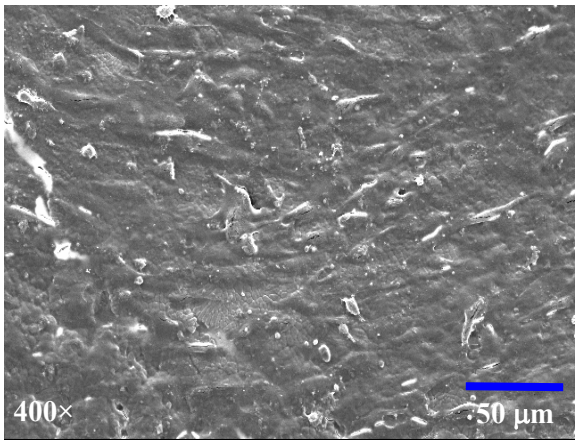

(e-1)

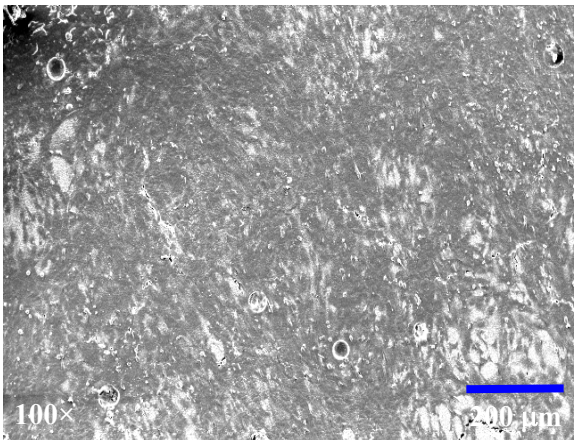

(f)

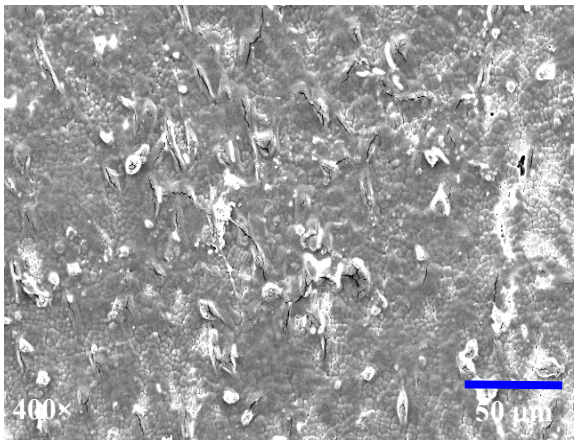

(f-1)

Fig. 10.10. SEM image of hFOB human osteoblast cells on the (a) untreated MgO-PSZ and CO_2 laser treated MgO-PSZ at power densities of (b) 0.5 kW/cm^2, (c) 0.9 kW/cm^2, (d) 1.6 kW/cm^2, (e) 1.9 kW/cm^2, (f) 2.5 kW/cm^2.

The osteoblast cells covered about 30 % of the area on the untreated surface as shown in Fig. 10.10(a), whereas the osteoblast cells covered more area on the CO_2 laser treated MgO-PSZ. Following CO_2 laser treatment, there was a cover density about 50 % at 0.6 kW/cm^2 (see Fig. 10.10(b)), 70 % at 0.9 kW/cm^2 (see Fig. 10.10(c)), 90% at 1.6 kW/cm^2 (see Fig. 10.10(d)), 95% at 1.9 kW/cm^2 (see Fig. 10.10(e)), and 90% at 2.5 kW/cm^2 (see Fig. 10.10(f)).

Thus, it has been found that the CO_2 laser power density used in the treatment had a significant influence on the cover density of the osteoblast cells. For instance, a power density of 0.6 kW/cm^2 exerted a marked increase in the osteoblast cell cover density of about 17 % on the CO_2 laser treated MgO-PSZ over the untreated sample. A power density of 0.9 kW/cm^2 generated double cover density, while the higher power densities of 1.6, 1.9 and 2.5 kW/cm^2 brought about triple cover density on the CO_2 laser treated MgO-PSZ, compared with the untreated one (see Fig. 10.11). Generally, the osteoblast cell coverage area was found to increase as power density increased when it is lower than 1.9 kW/cm^2.

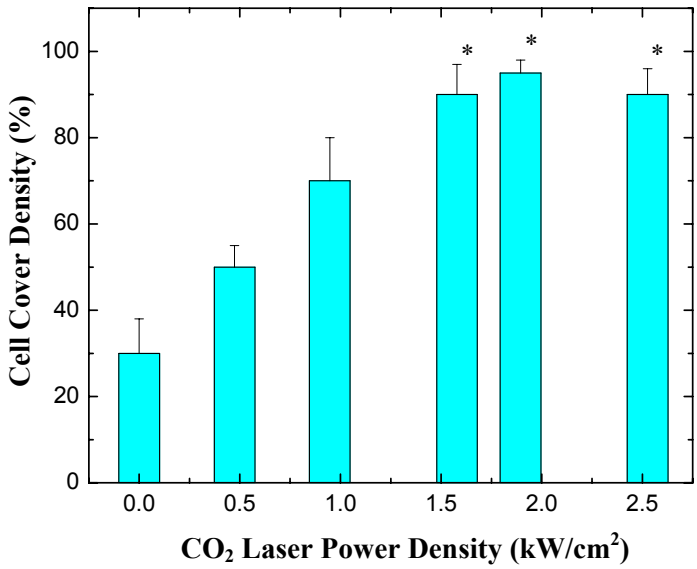

Fig. 10.11. The relationship between the cover density of the hFOB human osteoblast cells and CO_2 laser power density. (There was significant statistical difference between the untreated and CO_2 laser treated MgO-PSZ samples, and no statistical difference amongst the samples CO_2 laser treated at 1.6, 1.9 and 2.6 kW/cm^2 $^*p<0.05$)

Fig. 10.12 shows the number of osteoblast cells after 14-days on the untreated MgO-PSZ is less than the CO_2 laser treated MgO-PSZ. Generally, the number of osteoblast cells increased with the increasing power density when it is lower than 1.9 kW/cm^2. The osteoblast cell proliferation analysis in Fig. 10.12 shows the similar result of that the cells number on the MgO-PSZ generally increased with the power density. It is certain that the levels of power density of the CO_2 laser treatment influence the hFOB human osteoblast cell adhesion and growth, implying that this

technique is able to improve and control the response of the cells to the MgO-PSZ. It is found that both cell growth in 7 day investigated by the SEM and cell proliferation 14 day counted by the hematocytometer shows that a similar trend of the cell growth on the MgO-PSZ depends on the power density. The SEM investigation after 7-days shows 3-fold difference, while cell proliferation by counting the number of the cell after 14-days indicates a 71 % difference in cell growth between the untreated specimen and CO_2 laser treated MgO-PSZ (1.6 kW/cm^2). This could be explained by the fact that the osteoblast cells are anchorage cells and their growth will be constrained by the availability of the surface area. Since the results of the SEM analysis is more distinguish in term of cell growth than that of cell proliferation analysis and indicate the initial osteoblast cell adhesion that is critical for the evaluation of the implants, the following discussion uses the SEM analysis result to investigate the surface properties' effects on cell adhesion and growth.

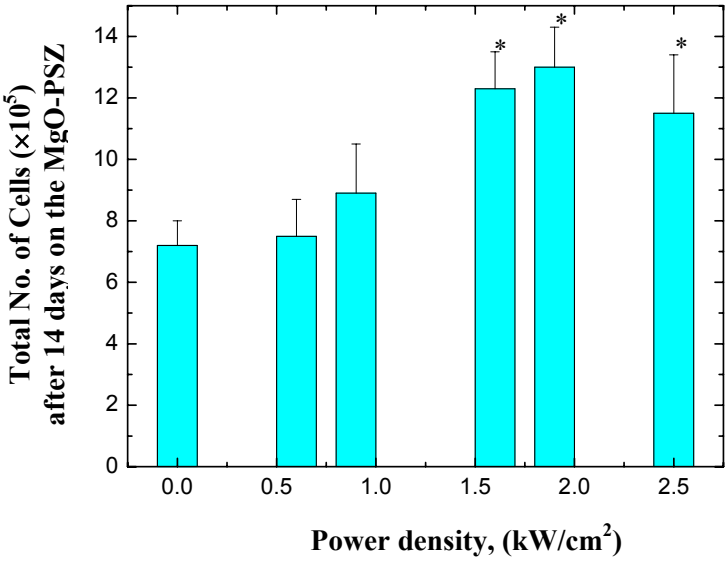

Fig. 10.12. Total number of osteoblast cells on the untreated and CO_2 laser treated MgO-PSZ after 14 days. (There was significant statistical difference between the untreated sample and the samples CO_2 laser treated at 1.6, 1.9 and 2.6 kW/cm^2, and no statistical difference amongst the untreated sample and the samples CO_2 laser treated at 0.6 and 0.9 kW/cm^2 $^*p<0.05$)

10.4.3. The Effect of Wettability Characteristics on Osteoblast Adhesion

The modifications of the wettability characteristics, attributed to surface changes of the MgO-PSZ generated by the CO_2 laser treatment, are primarily determined by the change in surface energy, especially γ_{sv}^{p}. The result of the one-day cell culture on the MgO-PSZ showed that there were no osteoblast cells attached on the untreated MgO-PSZ with low wettability characteristics (γ_{sv} = 52.8; γ_{sv}^{p} = 10.1; γ_{sv}^{d} = 42.7 mJ/cm^2), whereas some cells already attached and spread on the CO_2 laser

treated MgO-PSZ (power density of 1.6 kW/cm^2) with high wettability characteristics (γ_{sv} = 108.9; γ_{sv}^{p} = 60.7; γ_{sv}^{d} = 48.2 mJ/cm^2). The difference in wettability characteristics and surface energy must be mechanism determining the difference in osteoblast cell attachment.

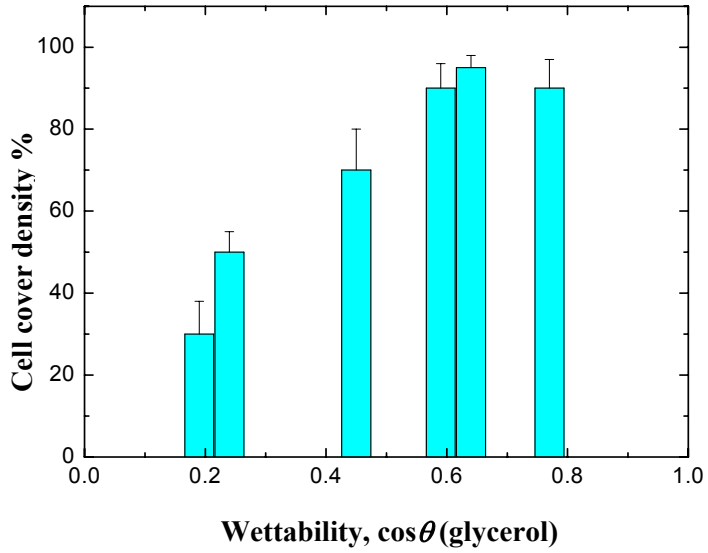

(a)

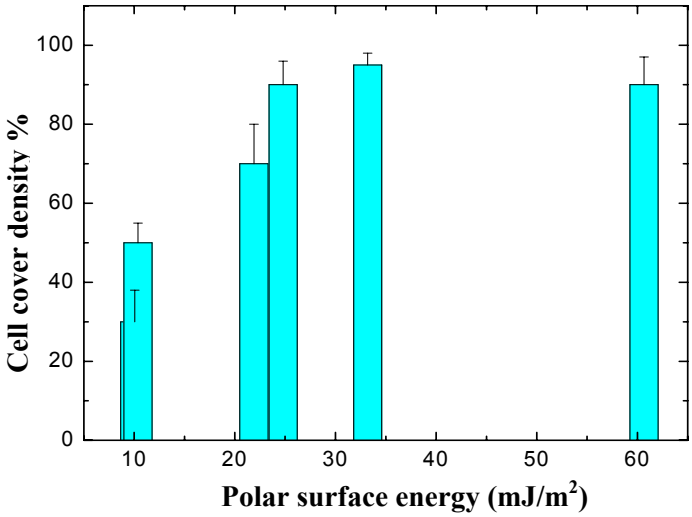

(b)

Fig. 10.14 The relationship between the cover density of the hFOB human osteoblast cells and (a) wettability characteristics and (b) polar surface energy

The CO_2 laser used in the experiment is a TEM_{01} multi-mode. From the Fig. 6.12, it can see that the level of CO_2 laser beam interaction is higher in the centre than that at the edge of the CO_2 laser beam. Thus, the level of the CO_2 laser treatment at the centre region is higher than that at the edge of the CO_2 laser treated track. Consequently, the modification level of surface energy would be higher at the centre than that at the edge of the CO_2 laser treated track. The different wettability

characteristics generated by CO_2 laser treatment across the track brought about the different levels of osteoblast spreading between cells at the edge and cells at the centre (see Fig. 10.8). Moreover, the difference in the short-term osteoblast cell morphology between the cells as shown in Fig. 10.8 and difference in the osteoblast cell cover density at the edge and at the centre of the CO_2 laser track as shown in Fig. 10.9 were associated with lower surface energy at the edge and higher surface energy at the centre.

The various CO_2 laser power densities brought about the different extent changes in wettability characteristics and surface energy and in turn resulted in the different osteoblast cell response. The value of cos θ (glycerol) was used to express the wettability characteristics of the MgO-PSZ. The higher the cos θ is, the higher the wettability characteristics is. As is evident from Fig. 10.14(a), the osteoblast cell cover density increases generally as the wettability characteristics increases. It was noticed that the cos θ ranged between 0.6 and 0.8 did not present great disparity in cell cover density, implying after a certain value, further increase in the wettability characteristics would not improve better cell response. Thus, a medium value of wettability characteristics could be optimal for cell response. The change in wettability characteristics was primarily influenced by the surface energy of the MgO-PSZ, especially polar component. As described in previous, the γ_{sv}^{d} were similar, whereas the γ_{sv}^{p} were significantly different for the untreated and CO_2 laser treated MgO-PSZ at various power densities and in turn resulted in the different osteoblast cell cover density (see Fig. 10.14(b)).

10.4.4. The Effects of Topography

The CO_2 laser treatment generated a consistently rougher surface on the MgO-PSZ compared with the untreated sample and R_a increased with the power density. As shown in Fig. 10.13, the CO_2 laser treated MgO-PSZ with rougher surface has higher osteoblast cell cover density compared with the smooth untreated sample. This is in agreement with some reports that the rougher surface of titanium promoted more osteoblast-like cell attachment [329]. Even so, there is no linear relationship between the osteoblast cell cover density and R_a. As one can see from Fig. 10.13, when R_a changes slightly from the 0.295 to 0.333 μm, the cell cover density almost doubled and MgO-PSZ with R_a of 0.717 μm already has the relatively 90% cell cover density.

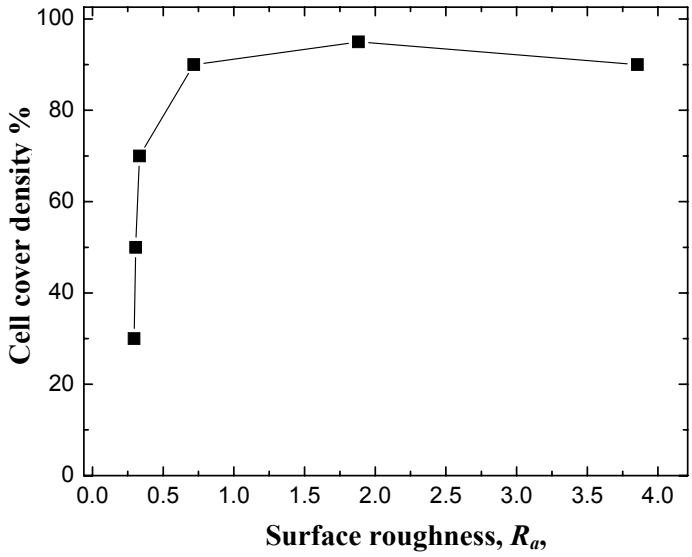

Fig. 10.13. The relationship between the cover density of the hFOB human osteoblast cells and surface roughness, R_a

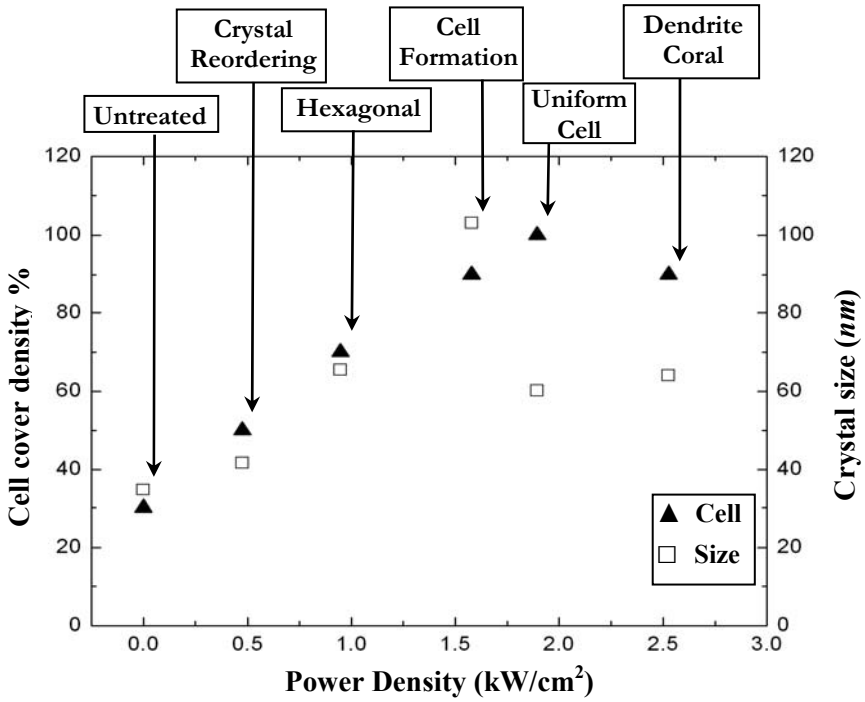

Fig. 10.14.The relationship between the cover density of the hFOB human osteoblast cells, microstructures and crystal size

Furthermore, the different microstructures and increase in the crystal sizes were postulated to be the factors influencing the osteoblast cell cover density as shown in Fig. 10.14. The degrees of the cell adhesion improved markedly when obvious microstructure change happened on the MgO-PSZ.

Relatively high osteoblast cell cover densities were found on the hexagonal (70%), cell formation (90%), uniform cell (100%) and dendrite and coral (90%) (see Fig. 10.14). A number of reasons have been suggested for an increased differentiation of osteoblasts on microstructured surface, such as the influence of surface structure on cell shape or that the surface topography creates a specific bio-chemical microenvironment around each cell [330]. Fig. 10.14 shows that the crystal sizes in all CO_2 laser treated MgO-PSZ are larger than the untreated sample. The osteoblast cell cover density generally increased with the increased crystal size when the power density was lower than 1.9 kW/cm^2, indicating that crystal size could possibly influence the osteoblast cell adhesion.

10.4.5. Discussion of Osteoblast Cell Response

As with fibroblast cells (see Section 10.3.5), it is also without doubt that the different responses of osteoblast cells on the MgO-PSZ are associated with the various wettability characteristics and surface topography brought about by the CO_2 laser treatment.

This study shows that the marked difference in initial osteoblast cell attachment and spreading attributed to the difference in wettability characteristics between the untreated and CO_2 laser treated MgO-PSZ. It has been found that the influence of the surface properties, in particular the surface energy of the substratum, remains even after protein adsorption at the surface of the substratum [329,331]. The work on polymers and glass revealed that cell spreading and substratum surface free energy showed a characteristic sigmoid relationship both in the presence and in the absence of serum proteins; good spreading only occurred when surface energy higher than approximately 57 mJ/cm^2 [106]. This explains that osteoblast cell attachment did not appear on the untreated MgO-PSZ with the surface energy of 52.8 mJ/cm^2 (see Fig. 10.7) and cell did not spreading well at the edge of the CO_2 laser treated track where had low surface energy (see Fig. 10.8).

Moreover, the different spreading of osteoblast cells across the CO_2 laser treated track also resulted from the different wettability characteristics across the track. The modification level of wettability characteristics was higher at the centre compared with the edge of the CO_2 laser treated track. As a function of substratum surface energy, cell spreading only appears when the surface energy is higher than the 50 mJ/cm^2 and increases with surface energy until the value of the surface energy reaches 100 mJ/cm^2 as shown in the Fig 3.4. The critical parameter for osseoconduction is the initial number of well-attached osteoblastic cells to the bone substitute [331]. It is clear that the difference in initial osteoblast cell adhesion resulted in the difference in the 7-days cell adhesion growth between the untreated region and CO_2 laser treated region (see Fig. 10.10). It is likely that the more flatten cells at the centre of the CO_2 laser treated track produced more collagen than less flatted cells [331] at the edge of the track and untreated region.

The 7–day osteoblast cell adhesion and growth as well as 14 days proliferation on the MgO-PSZ shows that the different wettability characteristics generated with various CO_2 laser power densities are the main mechanism accounting for the different osteoblast cell adhesion and growth. It has been found that the cell adhesion and growth increased with the wettability characteristics when the wettability characteristics changed from a lower value to a moderate value ($\cos\theta$ from 0.2 to 0.65). The finding agrees with previous studies showing the influence of wettability on various cells attachment and spreading [329,331-333]. These studies showed good cell attachment and spreading on high-energy substrata and poor cell attachment and spreading on low-energy substrata, which accounts for the minimal energetic state of a system in equilibrium. While the further increase in the wettability characteristics did not bring about the higher osteoblast cell adhesion and growth on the MgO-PSZ, indicating a moderate wettability characteristic could be optimal for the osteoblast cell response. This is similar with the finding that the highest levels of cell attachment was found on a moderately hydrophilic surface using a model surface [334].

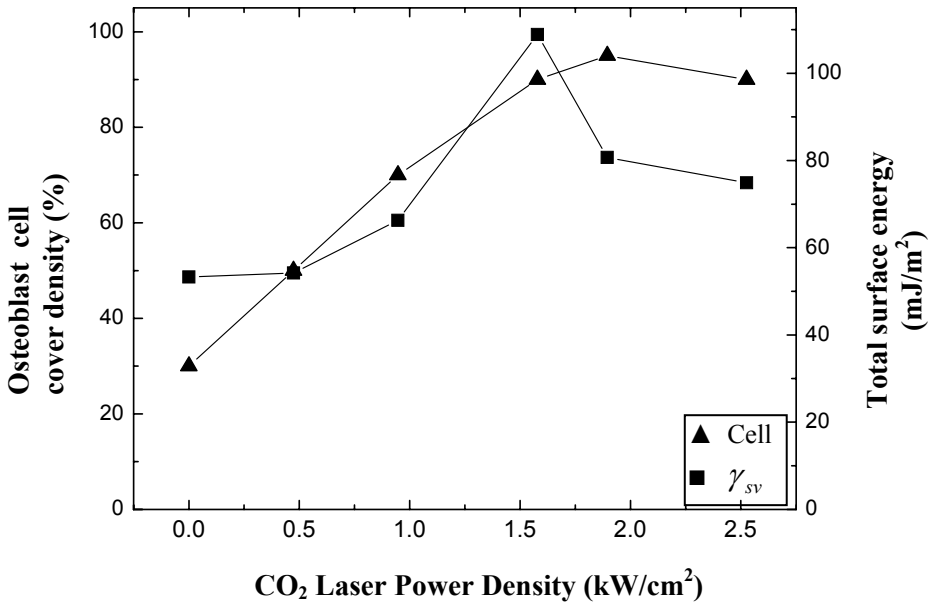

Fig. 10.15. hFOB osteoblast cell attachment as a function of the MgO-PSZ surface energy (γ_{sv},) and power density of CO_2 laser treatment.

As one can see from Fig. 10.15, CO_2 laser treatment resulted in higher surface energy and better attachment of human skin fibroblast cells on the MgO-PSZ surface than on the untreated MgO-PSZ. The fibroblast cell adhesion, closely correlated with the γ_{sv}, shows a similar change with the γ_{sv} depending on the CO_2 laser power density. It was noted that the change in surface energy of the MgO-PSZ mostly are attributed to the γ_{sv}^{p} instead of γ_{sv}^{d}. The results indicated that γ_{sv}^{p} influenced the behaviour of the osteoblasts on MgO-PSZ surfaces more strongly compared to γ_{sv}^{d}, which was

probably attributed that the composition and the culture medium all are polar, and thus cells and MgO-PSZ should interact mainly in polar force. The finding in the behaviour of osteoblastic cells at the surface of hydroxyapatite [331] and at the surface of titanium [329] demonstrated that γ_{sv}^{p} play a critical role.

The osteoblast cell spreading oriented with the grooved on the untreated surface, indicating that the orientation of the osteoblast cell could be influenced by the surface topography. It found that the extent of the cell cover density varied with the different microstructures of the MgO-PSZ (see Fig. 10.14). A number of reasons have been suggested for an increased differentiation of osteoblasts on microstructured surface, such as the influence of surface structure on cell shape or that the surface topography creates a specific biochemical microenvironment around each cell [330]. Surface microtopography has been cited as an important factor influencing protein-surface and cell-surface interactions [63]. Curved surfaces, pits, protrusions, cavities, etc., that have sizes and radii comparable with those of the biological entities (proteins ~1-10 nm, cells 1-100 μm) will induce biological interactions different from those on a flat surface [63]. Generally, the MgO-PSZ with crystal size ranged between 60 and 100 nm exhibited better osteoblast cell adhesion than those with crystal size ranged between 30 and 50 nm. It is most likely that the greater nano-surface area created by the larger crystal size may promote interactions (such as adsorption, configuration, bioactivity, etc), of select serum proteins(s), which, subsequently, enhance osteoblast adhesion. The study of osteoblast adhesion on nanophase ceramics has elucidated that a critical grain size (between 49 and 67 nm for alumina and between 32 and 56 nm for titania) played a crucial role in medicating osteoblast adhesion to nanophase ceramics by creating greater surface area and promoting interaction of protein [195]. However, Fig. 10.14 shows that a linear relationship does not exist between the cell cover density and crystal size.

The finding that the osteoblast cell growth better on the rougher surface compared with the smooth MgO-PSZ is similar with the some reports that the rougher surface promote more osteoblast-like cell attachment [329]. However, effects of the surface roughness As shown in Fig. 10.13, the CO_2 laser treated MgO-PSZ with rougher surface has higher osteoblast cell cover density compared with the smooth untreated sample. However, the changes in R_a are considerable in the range from 0.717 to 3.854 μm only generate a minor 10% difference in the cell coverage density. The MgO-PSZ surface with R_a of 3.854 μm even had a slightly lower cover density than that surface with R_a of 1.882 μm. In contrast to this, Deligianni *et al* [335] concluded that the increased surface roughness of HA ranged between 0.73 and 4.68 μm improved the short- and longer-term response of bone marrow cells *in vitro*. It noted that the CO_2 laser treatment bring about the increase in the topography and surface energy synchronously, thus, it is impossible to quantitatively analyse the effect of the change in one of the surface properties while the other property remains constant.

Therefore, a simple conclusion would be difficult to elucidate the relation between the amplitude of surface roughness the cell behaviours, because the surface roughness is only one of the factors affecting cell behaviours. Indeed, Hallab *et al* [336] demonstrated that surface free energy was a more important surface characteristic than surface roughness for cellular adhesion strength and proliferation. Schakenraad *et al* [106] found that, despite the great number of parameters interfering with cellular adhesion and spreading, the solid surface energy apparently is a dominated factor in cellular attachment to a polymer surface and remains so, even if the solid surface has been covered by a protein layer. Thus, it is reasonable to postulate that the surface roughness does influence human osteoblast cell response, however, its effects is less than the surface energy.

10.5. Comparison of Fibroblast and Osteoblast Cell Response to the MgO-PSZ Following CO_2 Laser Treatment

The adhesion and growth of the fibroblast cells and osteoblast cells is influenced by the CO_2 laser power density as shown in Fig. 10.16, indicating that the CO_2 laser process could be able to improve and control the response of the cells to the MgO-PSZ, possibly the other bioinert ceramics. It has shown that the fibroblast cell presents a similar response as the osteoblast cell response depending on the power density of CO_2 laser treatment. The similar responses of the fibroblast and osteoblast cell are also found on the bioglass-coated zirconia [197]. Both fibroblast and osteoblast cell adhesion and growth increased with the increasing CO_2 laser power density (see Fig. 10.16). As discussed above, the cell response is mostly determined by the wettability characteristics and surface topography. As shown in Fig. 10.16, the various CO_2 power densities generated different surface roughness, O_2 surface content, crystal size, microstructures and polar surface energy. It has found that the surface roughness, O_2 surface content and surface energy are the factors influencing the wettability characteristics of the MgO-PSZ. As is evident from see Fig. 10.16, both fibroblast and osteoblast cell adhesion and growth, influenced by the wettability characteristics, increased as wettability characteristics increased from the low value to the moderate value ($\cos\theta$ ranged between 0.2 and 0.6). Further increase in the wettability characteristics did not cause better cell response. Both cell shows optimal response on the MgO-PSZ with moderate wettability ($\cos\theta$ ranged between 0.6 and 0.8). The finding agrees with the previous reports that the maximum cell adhesion and cell adhesion strength appeared at a moderately hydrophilic surface on polymer surface with wettability gradient [337] and highest levels of cell attachment was found on a moderately hydrophilic surface using a model surface [334].

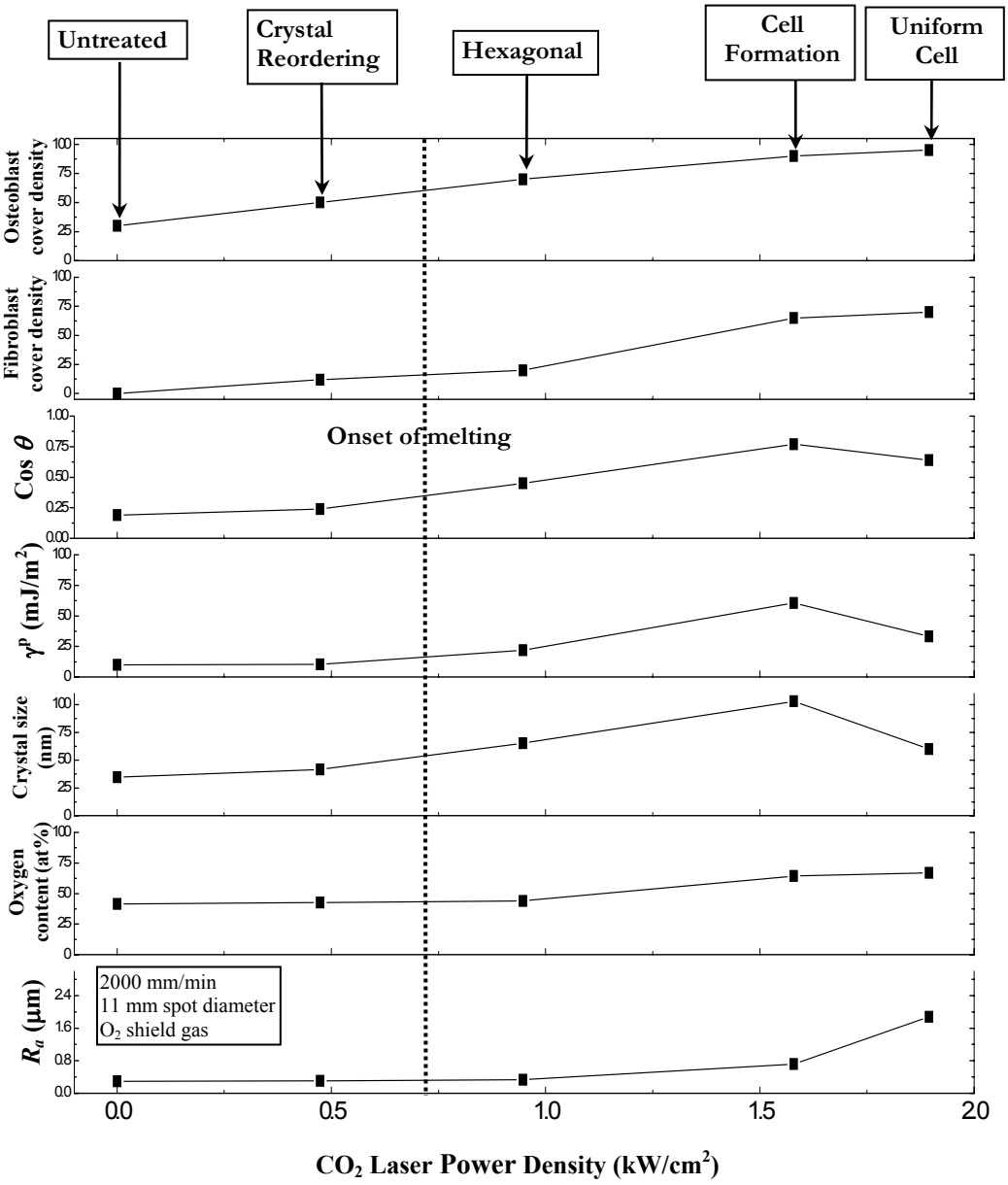

Fig. 10.16. Relationship between fibroblast and osteoblast cell adhesion and the wettability characteristics (cos θ for glycerol), γ_{sv}^{p}, the crystal size, the surface oxygen content, R_a and the microstructures of the untreated and CO_2 laser treated MgO-PSZ.

The fibroblast cell presented oriented spreading along the grooves of the certain cracks and the osteoblast cell presented oriented spreading along the grooves of the untreated region, suggesting that the topography of the cells influenced the migration of both cells. It has been shown that cells are highly sensitive to surface morphology and this interaction affects several cellular shape and migration (cell shape and predominant type, migration, adhesion and tissue organization) [338]. In this study, the cell adhesion and growth of the fibroblast and osteoblast cells increased as the surface roughness increased (see Fig. 10.16). However, previous reports revealed that osteoblast-

like cells adhere better to rough surfaces with irregular morphologies than on smooth surfaces [339] and conversely, fibroblasts prefer smooth surfaces over roughened ones [186]. Thus, it indicated that the effects of the surface roughness on the fibroblast cell adhesion and growth are expressed by the minor contribution to the wettability characteristics instead of the topography. While, the effects of the surface roughness on the osteoblast cell adhesion and growth are expressed by the minor contribution to the wettability characteristics as well as the topography. The fibroblast and osteoblast cell shows similar results indicated that the wettability characteristics is the main mechanism governing the both cell response and play more information role than the surface topography.

10.6. Summary

In this study a MgO-PSZ bioceramic was modified using a CO_2 laser, with the aim being to acquire the surface properties favouring interface interaction at implant and bone tissue. Human skin fibroblast cells and hFOB human osteoblast cells were used examine *in vitro* cell response on MgO-PSZ following CO_2 laser treatment. The conclusion can be drawn as follows:

1. The favourable responses of fibroblast cells were found on the CO_2 laser treated MgO-PSZ compared with the untreated samples. The fibroblast cells increased as wettability characteristics increased from a low value to a medium value. The topography presented by the certain groove could cause the orientation of fibroblast cell spreading. It found that the effects of wettability characteristic were far more important than the surface roughness on the fibroblast cell adhesion and growth.
2. The osteoblast cell spreading and adhesion of osteoblast cells changed with different surface properties generated by the CO_2 laser treatment with various power densities. The modification of fibroblast cell adhesion is most similar to wettability changes caused by the CO_2 laser induced different surface energy. The topography influences the osteoblast cell orientation, adhesion and growth. The wettability characteristics plays more important role than the surface roughness.
3. The fibroblast cell presents a similar response as the osteoblast cell response depending on the power density of CO_2 laser treatment. The analysis revealed that the wettability characteristics was the primary mechanism governing the cell response and moderate wettability value brought about the optimal response. The γ_{sv}^{p} instead of γ_{sv}^{d} generated the different wettability characteristics and in turn influenced the cell response.

Conclusions

In order to improve the bioactivity and biointegration of the selected magnesia partially stabilised zirconia (MgO-PSZ) bioceramic, work has been conducted using a CO_2 laser to treat the surface of the MgO-PSZ and investigates the changes in the surface properties of the MgO-PSZ. More specifically, the laser's ability to modify the wettability characteristics of the material and induce functional groups, which thereby allows the bone-like apatite formation, protein adsorption and cell response of this bioinert ceramic to be manipulated, was studied. Valuable inroads have been made as a result of this work for establishing the laser as a novel and viable technique for improving the biocompatibility of implant materials.

Effects of CO_2 Laser Radiation on the Surface of the MgO-PSZ

Experiments were performed with a 3 kW continuous wave (CW) CO_2 laser and the general effects thereof on the surface of the MgO-PSZ were observed. All treated samples displayed cracks and craters to some extent on the glaze layer after a single pass of the CO_2 laser beam. The effects of the CO_2 laser radiation on the MgO-PSZ varied with laser power density and traverse speed. From X-ray diffraction (XRD) and energy disperse X-ray (EDX) analyses it was found that rapid heating caused by the CO_2 laser treatment induced only microstructural and phase changes in the surface of the MgO-PSZ. Furthermore, variations in the CO_2 laser operating parameters (power density and traverse speed) were seen to affect significantly the microstructure obtained within the laser-treated areas on the MgO-PSZ. With a relatively high power density of 2.5 kW/cm^2 and a traverse speed of 2000 mm/min speed, the mostly structures described as "coral" and a few dendritic structures were found in the centre of CO_2 laser treated track. While a cellular structure was observed at the midway point and a hexagonal structure appeared at the far edges. Such different solidification characteristics within the same track caused by CO_2 laser radiation were explained with the theories of constitutional supercooling and the morphology. The different thermal gradient/ solidification rate (G/R) ratio and convection in the melted pool caused the microstructures analysed above. With relatively high traverse speed of laser beam pass, further increase of cooling rate eliminated the coalescence and growth of cells and produced a uniform microcrystalline structure in the region of centre. Complex heat transfer in the regions of craters and cracks results in the variation of microstructures.

Laser Induced Wettability Characteristics Modification

There is a growing amount of published work that testifies to the potential of lasers for altering the surface properties of some engineering materials and certain bio-polymers in order to improve their

wettability characteristics. However, so far no work has been conducted on the laser process for the wettability modification of bioceramics. The results of this work are a clear indication that CO_2 laser surface treatment of the MgO-PSZ brought about a reduction in the contact angle, θ, formed between the MgO-PSZ and the control liquids, thus modifying the wettability characteristics of the material. The extent of the wettability characteristics modification was controlled by manipulation of the various CO_2 laser parameters. The main conclusions could be made as follows:

1. The increase in γ_{sv}^{p} results from the melting and solidification of the MgO-PSZ surface with various microstructures. The maximum value of γ_{sv}^{p} was obtained when the CO_2 laser induced solidified microstructure was of cell formation.
2. The increase in the surface O_2 content of the MgO-PSZ resulting from surface oxidation followed CO_2 laser treatment was identified as further promoting the action of wetting. Whilst surface roughness was found to contributed to the changes of wettability characteristics.
3. Further analysis revealed that the surface energy was the primary influential factor governing changes in θ. Meantime, the surface O_2 content was shown to influence to a lesser extent, whilst surface roughness was found to play a minor role in inducing changes in the wettability characteristics.
4. Surface energy changes with the microstructure in terms of crystal size and phase change. The larger crystal size and higher tetragonal phase generated by the CO_2 laser treatment bring about the higher surface energy of the MgO-PSZ.

Laser Induced Hydroxyl Group and Apatite Formation

The biological activity of most orthopaedic and dental biomaterials is related to their ability to promote the formation of a neoformed layer of carbonate apatite crystals analogous to bone mineral. This layer also associates specific bone proteins and is the starting point of bone reconstruction. A fourier transform infrared spectrometer (FTIR) was therefore used to analyse OH groups on the MgO-PSZ following the CO_2 laser irradiation. The bioactivity of the CO_2 laser modified MgO-PSZ was investigated in stimulated human fluids (SBF) with ion concentrations almost equal to those in human blood plasma. This analysis established that treatment could improve the bioactivity of the MgO-PSZ surface by generating functional group to facilitate the formation of bonelike apatites.

The analysis revealed that the CO_2 laser parameters employed were influential. After 14 days SBF soaking, the apatite formed on the MgO-PSZ with a relatively high amount of hydroxyl groups generated by the CO_2 laser treatment with a power density of 1.6 and 1.9 kW/cm^2, while no apatite was observed on the untreated samples. It exhibits that the Zr-OH groups on the MgO-PSZ surface is the functional groups to facilitate the apatite formation.

The surface melting on the MgO-PSZ induced by CO_2 laser processing provides the Zr^{4+} ion and OH^- ion. The incorporation of Zr^{4+} ion and OH^- ion creates the Zr-OH group on the surface. However, the power density at 2.5 kW/cm^2 could generate the explosive evaporation and in turn cause the loss of the water and the OH bond.

It was found that there was correlation between the OH group and γ_{sv}^{p} of the MgO-PSZ. The improvement of γ_{sv}^{p} probably possibly depends on the relative density of OH groups on the MgO-PSZ following CO_2 laser treatment.

Laser Manipulation of Protein Adsorption

The particular properties of surfaces, as well as the specific properties of individual proteins from the surrounding fluid contribute to the organisation of the absorbed protein layer. The nature of this layer in turn determines the cellular response to the adsorbed surfaces. In order to understand the fundamental interaction between the proteins and MgO-PSZ and provide useful information for the subsequent cellular interactions, ellipsometry was used to investigate the albumin and fibronectin adsorption on the untreated and CO_2 laser modified MgO-PSZ bioceramic.

It was clear that the CO_2 laser treatment brought about the lower amount the adsorbed albumin layer and higher amount of the adsorbed fibronectin layer on the modified MgO-PSZ compared with the untreated sample. Such interactions would benefit to the osteoblast cell adhesion since albumin is the no-cell adhesive protein while fibronectin is the cell adhesive protein.

The surface roughness and wettability characteristics influenced the adsorption of the protein adsorption. The albumin adsorption decreased, while the fibronectin increased with the increased surface roughness and wettability characteristics of the MgO-PSZ. The effect of the surface roughness is correlated with the wettability characteristics and less than that of the wettability characteristics on the protein adsorption. Moreover, the considerable change in the γ_{sv}^{p} and thereof its effect on protein adsorption implied that the albumin and fibronectin adsorption on the MgO-PSZ surfaces was probably due to the polar and chemical interactions.

Laser Augmentation of Cell Response

Numerous *in vitro* experiments have shown that cell behaviour is influenced by the physicochemical properties of polymer surfaces such as wettability, chemistry and roughness. In particularly hydrophobicity, or wettability, is an important determinant of cell adhesion. In this work favourable responses of fibroblast cells were found on the CO_2 laser treated MgO-PSZ when compared with the untreated samples. The fibroblast cells increased as wettability characteristics increased from a low value to a medium value. The topography presented by the certain groove could cause the orientation of fibroblast cell spreading. It was found that the effects of the changes

in the wettability characteristic were far more important than the surface roughness changes on the fibroblast cell adhesion and growth.

The osteoblast cell spreading and adhesion of osteoblast cells changed with different surface properties generated by the CO_2 laser treatment with various power densities. The modification of fibroblast cell adhesion is most similar to wettability changes caused by the CO_2 laser induced different surface energy. The topography influences the osteoblast cell orientation, adhesion and growth. The wettability characteristics plays more important role than the surface roughness.

The fibroblast cell presents a similar response as the osteoblast cell response depending on the power density of CO_2 laser treatment. The analysis revealed that the wettability characteristics were the primary mechanism governing the cell response and moderate wettability value brought about the optimal response. The γ_{sv}^{p} instead of γ_{sv}^{d} generated the different wettability characteristics and in turn influenced the cell response.

Future Work Recommendations

The work detailed in this report establishes the CO_2 laser as a feasible tool for modifying the surface properties of the magnesia partially stabilised zirconia (MgO-PSZ), especially the wettability characteristics and hydroxyl groups, and in turn, effecting the bone-like apatite formation, protein adsorption and cell responses on this bioinert material. Further study in the following areas is suggested to take the work detailed in this thesis forward.

In vitro Evaluation of Cell Functions. The following functions of osteoblasts on the untreated and CO_2 laser treated MgO-PSZ will be investigated in intro cellular models.

- Alkaline phosphatase assay
- Assay for osteocalcin and fibronectin
- Detection of type I collagen
- Quantification of extracellular calcium

It will provide the evidence of long-terms functions of the osteoblasts cultured on the untreated and CO_2 laser treatment MgO-PSZ, thus revealing the effects of the CO_2 laser treatment on the functions of the osteoblast in vitro.

Extension of Protein Adsorption and Cell Response Mechanisms. Extension of the generic laser modification of the protein adsorption and cell response to more materials, including metals, would give a greater understanding and a larger applications base of the mechanisms identified. Also, further insight into the mechanisms identified could be acquired by establishing the correlation, for different lasers and a number of materials, between the operating parameters and the degree of protein adsorption and cell response modification.

In vivo Evaluation of Osseointegration. The untreated and CO_2 laser treated MgO-PSZ were evaluated in an animal model. After certain time of implantation in animal, histomorphometry and SEM microanalysis were performed on the sections to determine the osseointegration rate. Thus, it could analyse the relationships between the osseointegration rate and surface properties of the MgO-PSZ and thereof, deduce the predominant factors for the osseointegration. The results could provide the feedback to the laser processing.

The Effects of Laser Wavelength. The aims of this work is to compare the differences in modification of the hydroxyl groups and wettability characteristics of the MgO-PSZ with the predominant materials processing lasers: the CO_2; the Nd:YAG; the excimer; and the high power diode laser, possible other lasers. The selected industrial lasers emit across a wide range of

wavelengths, with the output from the CO_2 laser, the Nd:YAG laser, and the diode laser ranging from the far infrared to the near infrared range of the spectrum respectively, while the excimer laser emits in the ultraviolet region of the spectrum. Thus it will be possible to design any wavelength dependent changed to the wettability. By manipulating the laser power densities and traverse speeds, one can obtain the same energy density of each of the lasers incident upon the surface so as to compare the effects of each laser on the hydroxyl groups and wettability characteristics of the MgO-PSZ.

Interface Analysis. An examination of the interface between the CO_2 laser treated surface and the bulk MgO-PSZ substrate would be of great interest. Firstly, it would allow the operating parameters to be further refined and the absolute outer limits to be established. But, perhaps more importantly, such an analysis would give insight into the CO_2 laser beam-material interaction mechanisms.

Mathematical Model. The development of an accurate analysis procedure for many laser applications, including the laser surface treatment of the MgO-PSZ, is extremely complicated due to the multitude of process parameters involved. Once the inter-relationships between laser process parameter, hydroxyl groups, apatite formation, wettability characteristics and protein adsorption and cell response has been established, it will be essential to build an analytical mathematic model. In this way, the development of a suitable model to predict such changes can not only eliminate the need to perform experiments with every possible range of operating parameters, but can also provide information outside the range of operating parameters currently possible. Only through mathematical modelling of the inter-relationships can the technique be fully controllable, thereby allowing the apatite formation, protein adsorption and cell response to thereof to be manipulated. In addition, mathematical modelling will facilitate an analysis of the technique in terms of the inter-relationships produced by more traditional means.

Process Optimisation. The process of inducing the hydroxyl groups and modifying the wettability characteristic and in consequently, manipulating the apatite formation, protein adsorption, cell response of the MgO-PSZ will be optimised by gaining a creative understanding of the fundamental mechanisms of laser beam interaction. To examine the effects of beam mode and shape, the CO_2, the Nd:YAG and the excimer lasers beams will be characterised using a laser beam analyser. The absorption characteristics of the MgO-PSZ with the different sources of laser radiation used in the work will also be investigated through the application of Beer-Lambert's Law. The density and length of cracks, thermal shock cracking and size and density of craters will be analysed. The pyrometer will be use to measure the surface temperature of the MgO-PSZ samples to determine the onset of melting during the laser processing. In this way, it will be possible to establish the temperature curve (heating and cooling rate) during the laser processing and thus preclude or

minimise crack formation on the surface of the MgO-PSZ. The ultimate result of the work will be the generation of a detailed and practical operation window for the process.

Laser Treatment of Other Bioceramic and Biometals for Improved Biocompatibility. Experiments will be conducted on the yittria stabilised tetragonal zirconia polycrystals (Y-TZP) and alumina so as to determine the presence or absence of genetic processing characteristics in terms of bioceramic materials. In addition, it will explore the ability of laser surface processing for improved the biocompatibility of the biometals.

Process Implementation. It is likely that the technique will have presented itself as being workable and from the work above it will have been completely characterised. Thus it will be possible develop the technique to a stage from which actual process large scale implementation can take place. This will basically entail the development of prototypes and process marketing.

Commercial Viability Evaluation. The overall commercial possibilities of laser surface process of the biomateials must be assessed. Firstly, the possible markets for the process must be identified, leading to the development of a market entry and exploitation strategy. Secondly, the assessment must incorporate an economic comparison of the laser surface modification of biomaterials with existing methods.

References

1. Steen, W. M. (1991). *Laser material processing*, Springer-Verleg, London.
2. Smallman, R. E. (1999). *Modern physical metallurgy and materials engineering: science, process, applications*, Butterworth-Heinemann, Boston.
3. Ratner, B. D. (1996). *Biomaterials science : an introduction to materials in medicine*, Academic Press, San Diego.
4. J. Li and G.W. Hastings. (1998). *Oxide Bioceramics: Inert Ceramic Materials in Medicine and Dentistry*, Chapman & Hall, London ; New York.
5. Hench, L. L. (1991). "Bioceramic: from concept to clinic." *Journal of American Ceramic Society*, 74, 1487-1510.
6. Li, P., Ye, X., Kangasniemi, I., de Blieck-Hogervorst, J. M., Klein, C. P. and de Groot, K. (1995). "In vivo calcium phosphate formation induced by sol-gel-prepared silica." *Journal of Biomedical Materials Research*, 29(3), 325-328.
7. Tanahashi, M., Yao, T., Kokubo, T., Minoda, M., Miyamoto, T., Nakamura, T. and Yamamuro, T. (1995). "Apatite coated on organic polymers by biomimetic process: improvement in its adhesion to substrate by glow-discharge treatment." *Journal of Biomedical Materials Research*, 29(3), 349-357.
8. Li, P., Ohtsuki, C., Kokubo, T., Nakanishi, K., Soga, N., Nakamura, T. and Yamamuro, T. (1993). "Process of formation of bone-like apatite layer on silica gel." *Journal of Materials Science: Materials in Medicine*, 4(2), 127-131.
9. Puleo, D. A. and Nanci, A. (1999). "Understanding and controlling the bone-implant interface." *Biomaterials*, 20(23-24), 2311-2321.
10. McFarland, C. D., Mayer, S., Scotchford, C., Dalton, B. A., Steele, J. G. and Downes, S. (1999). "Attachment of cultured human bone cells to novel polymers." *Journal of Biomedical Materials Research*, 44(1), 1-11.
11. Anselme, K. (2000). "Osteoblast adhesion on biomaterials." *Biomaterials*, 21(7), 667-681.
12. Puleo, D. A. (1996). "Biochemical surface modification of Co---Cr---Mo." *Biomaterials*, 17(2), 217-222.
13. Vogler, E. A. (1998). "Structure and reactivity of water at biomaterial surfaces." *Advances in Colloid and Interface Science*, 74(1-3), 69-117.
14. Lawrence, J. and Li, L. (2001). *Laser modification of the wettability characteristics of engineering materials*, Professional Engineering, London.
15. Charschan, S. S. (1972). *Lasers in industry*, Von Nostrad Reinhold, New York.

16. Mead, R. D., Tidwell, S. C., Kangas, K. W., Brown, A. J. W. and Lowenthal, D. D. (1992). "Diode-end-pumped, Q-switched Nd:YLF laser." *OSA Proceedings on Advanced Solid-State Lasers, Vol.13. 17-19 Feb. 1992*, Sante Fe, NM, USA, 194-196.
17. Pedraza, A. J. (1992). "Excimer laser modification of materials surfaces and interfaces." *International Conference on Beam Processing of Advanced Materials, Nov 2-5 1992*, Chicago, IL, USA, 69.
18. Pedraza, A. J. and Lowndes, D. H. (1998). "Surface engineering using excimer lasers." *Proceedings of the SPIE - The International Society for Optical Engineering, High-Power Laser Ablation, 27-30 April 1998*, 3343, 829-39.
19. Bachmann, F. (2003). "Industrial applications of high power diode lasers in materials processing." *Applied Surface Science*, 208-209, 125-136.
20. von Neumann, J. (1987). "Notes on the photon-disequilibrium-amplification scheme" *IEEE Journal of Quantum Electronics*, 23(6), 659-71.
21. Hall, R. N., Fenner, G. E., Kingsley, J. D., Soltys, T. J. and Carlson, R. O. (1962). "Stimulated emission of radiation from GaAs p-n junction." *Physics. Review. Letter.*, 366-369.
22. Steen, W. M. (2003). "Laser material processing - An overview." *Journal of Optics A: Pure and Applied Optics*, 5(4), 3-7.
23. Powell, J. (1985). "Laser cladding with pre-placed powder." *Proceedings of the conference on surface engineering with lasers*, London, UK, 177-189.
24. Weerasinghe, V. M. and Steen, W. M. (1987). "Laser cladding with blown powder." *Metal Construction*, 19(10), 581-585.
25. Steen, W. M., Weerasinghe, V. M. and Monson, P. (1986). "Some aspects of the formation of laser clad tracks." *Proceedings of the SPIE - The International Society for Optical Engineering, High Power Lasers and their Industrial Applications. Divisional Meeting of the Quantum Electronics Division/ European Physical Society, 15-18 April 1986*, 650, 226-34.
26. Ayers, J. D. and Schaefer, R. J. (1979). "Consolidation of plasma-sprayed coatings by laser remelting." *Proceedings of the Society of Photo-Optical Instrumentation Engineers, Laser Applications in Materials Processing, 27-28 Aug. 1979*, 198, 57-64.
27. Pangborn, R. J. and Beaman, D. R. (1980). "Laser glazing of sprayed metal coatings." *Journal of Applied Physics*, 51(11), 5992-3.
28. Dallaire, S. and Cielo, P. (1982) "Surface processing by a pulsed laser." *Surface Engineering: Surface Modification of Materials.*, Les Arc, France, 318-329.
29. Mazumder, J. and Allen, S. D. (1979). "Laser chemical vapor deposition of titanium carbide." *Proceedings of the Society of Photo-Optical Instrumentation Engineers, Laser Applications in Materials Processing, 27-28 Aug. 1979*, San Diego, CA, USA, 73-80.

30. Allen, S. D. (1979). "Laser chemical vapor deposition-applications in materials processing." *Proceedings of the Society of Photo-Optical Instrumentation Engineers, Laser Applications in Materials Processing, 27-28 Aug. 1979*, 198, 49-56.

31. Tagaki, S. (1990). "Laser physical vapour deposition." Industrial laser handbook, D. A. Belforte, M. Levitt, and L. Berude, eds., Penwell Books, Tulsa, 106-108.

32. Weitoa, W., Streiff, R. and Maocai, W. (1989). "Effect of laser surface modification on high-temperature oxidation and corrosion behaviour of alloys and coatings." *Materials Science & Engineering A: Structural Materials: Properties, Microstructure and Processing*, 120(1), 499-507.

33. Wilson, J. and Hawkes, J. F. B. (1987). *Lasers: principles and applications*, Prebtice Hall, London.

34. Draper, C. W. and Poate, J. M. (1985). "Laser surface alloying." *International Metals Reviews*, 30(2), 85-108.

35. Snow, D. B., Breinan, E. M. and Kear, B. H. (1980). "Rapid solidification processing of superalloys using high power lasers." *Superalloys 1980, Proceedings of the 4th International Symposium on Superalloys.*, Champion, PA, USA, 189-203.

36. Schubert, E. and Bergmann, H. W. (1993). "Surface modification of ceramic materials using excimer lasers." *Surface Engineering*, 9(1), 77-81.

37. Li, L., Modern, P. and Steen, W. M. (1992). "Laser fixing and sealing of radioactive contamination on concrete surfaces." *Proceedings of LAMP' 92: Science and applications*, Nagaoka, Japan, 843-848.

38. Armstrong, J. V., McLoughlin, M., Lunney, J. G. and Coey, J. M. D. (1991). "Thermal diffusivity and laser melting of $YBa_2Cu_3O_7$ superconductor." *Superconductor Science & Technology*, 4(3), 89-92.

39. Bradley, L., Li, L. and Stott, F. H. (1999). "Characteristics of the microstructures of alumina-based refractory materials treated with CO_2 and diode lasers." *Applied Surface Science*, 138-139, 233-239.

40. Lee, S. Z. and Gahr, K.-H. Z. (1992). "Surface treatments of Al_2O_3-ceramics by CO_2-lasers." *Materialwissenschaft und Werkstofftechnik*, 23(4), 117-123.

41. Bradley, L., Li, L. and Stott, F. H. (1999). "Flame-assisted laser surface treatment of refractory materials for crack-free densification." *Materials Science and Engineering A*, 278(1-2), 204-212.

42. Triantafyllidis, D., Li, L. and Stott, F. H. (2002). "Surface treatment of alumina-based ceramics using combined laser sources." *Applied Surface Science*, 186(1-4), 140-144.

43. Triantafyllidis, D., Li, L. and Stott, F. H. (2003). "Mechanisms of porosity formation along the solid/liquid interface during laser melting of ceramics." *Applied Surface Science*, 208-209, 458-462.

44. Zaplatynsky, I. (1982). "Performance of laser glazed zirconia thermal barrier coatings in cyclic oxidation and corrostion burner rig test." *Thin Solid Films*, 95, 275-284.

45. Longa, Y. and Takemoto, M. (1992). "High-temperature corrosion of laser-glazed alloys in Na_2SO_4-V_2O_5." *Corrosion (Houston)*, 48(7), 599-607.

46. Adamski, A. and McPherson, R. (1986). "Laser sealing of ceramic surface layers." *Proceedings of the 11th international thermal spraying conference, May 1986,* Los Angelse, USA, 555-564.

47. Mordike, B. L. and Sivakumar, R. (1986) "Laser surface melting of ZrO_2 protective layers." *Proceedings of ECLAT, May 1986,* Berlin, Germany, 373-381.

48. Sivakumar, R. and Mordike, B. L. (1988). "Laser melting of plasma sprayed ceramic coatings." *Journal of Surface Engineering*, 4, 127-140.

49. Galasso, F. S. and Veltri, R. (1983). "Observation of laser interactions with ceramics." *Ceramics Bulletin*, 62, 253-258.

50. Jasmin, K. M., West, D. R. F. and Steen, W. M. (1988). "Laser sealing of plasma-sprayed calcia-stabilized zirconia." *Journal of Materials Science Letters*, 7(12), 1307-1309.

51. Havrda, M. (1986). "The generation of a crack-free ZrO_2-SiO_2 coating using a CO_2 laser." *Proceedings of the 11th international thermal spraying conference, May 1986,* Los Angeles, USA, 569-588.

52. Rosengren, A., Pavlovic, E., Oscarsson, S., Krajewski, A., Ravaglioli, A. and Piancastelli, A. (2002). "Plasma protein adsorption pattern on characterized ceramic biomaterials." *Biomaterials*, 23(4), 1237-1247.

53. Hulbert, S. F. (1993). "The use of alumina and zirconia in surgical implants." An introduction to bioceramics, L. L. Hench and J. Wilson, eds., World Scient, Singapore, 25-40.

54. Piconi, C. and Maccauro, G. (1999). "Zirconia as a ceramic biomaterial." *Biomaterials*, 20(1), 1-25.

55. Saikko, V. (1994). "Wear of polyethylene acetabular cups against zirconia femoral heads studies with a hip joint simulator." *Wear*, 176(2), 207-212.

56. Oka, M., Kumar, P., Ikeuchi, K., Yamamuro, T. and Nakamura, T. (1992). "Low wear rate of UHMWPE against zirconia." Bioceramics, T. Yamamuro, T. Kokubo, and T. Nakamura, eds., Kyoto, Japan, 373-379.

57. Willmann, G. (2000). "Ceramic acetabular cups for total hip replacement." *Biomedical Engineering*, 45(12), 370-376.

58. MaColm, I. J. (1983). *Ceramic science for materials technologists*, L.Hill, Glasgow.

59. Sodhi, R. N. S. (1996). "Application of surface analytical and modification techniques to biomaterial research." *Journal of Electron Spectroscopy and Related Phenomena*, 81(3), 269-284.

60. Benson, R. S. (2002). "Use of radiation in biomaterials science." *Nuclear Instruments and Methods in Physics Research, Section B: Beam Interactions with Materials and Atoms*, 191(1-4), 752-757.

61. Chu, P. K., Chen, J. Y., Wang, L. P. and Huang, N. (2002). "Plasma-surface modification of biomaterials." *Materials Science and Engineering: R: Reports*, 36(5-6), 143-206.

62. Cui, F. Z. and Luo, Z. S. (1999). "Biomaterials modification by ion-beam processing." *Surface and Coatings Technology*, 112(1-3), 278-285.

63. Kasemo, B. and Gold, J. (1999). "Implant surfaces and interface process." *Advance Dental Research*, 13, 8-20.

64. Duncan, A. C., Weisbuch, F., Rouais, F., Lazare, S. and Baquey, C. (2002). "Laser microfabricated model surfaces for controlled cell growth." *Biosensors and Bioelectronics*, 17(5), 413-426.

65. Ringeisen, B. R., Chrisey, D. B., Pique, A., Young, H. D., Modi, R., Bucaro, M., Jones-Meehan, J. and Spargo, B. J. (2002). "Generation of mesoscopic patterns of viable Escherichia coli by ambient laser transfer." *Biomaterials*, 23(1), 161-166.

66. Prina Mello, A., Bari, M. A. and Prendergast, P. J. (2002). "A comparison of excimer laser etching and dry etching process for surface fabrication of biomaterials." *Journal of Materials Processing Technology*, 124(3), 284-292.

67. Cotell, C. M. (1993). "Pulsed laser deposition and processing of biocompatible hydroxylapatite thin films." *Applied Surface Science*, 69(1-4), 140-148.

68. Ball, M. D., Downes, S., Scotchford, C. A., Antonov, E. N., Bagratashvili, V. N., Popov, V. K., Lo, W.-J., Grant, D. M. and Howdle, S. M. (2001). "Osteoblast growth on titanium foils coated with hydroxyapatite by pulsed laser ablation." *Biomaterials*, 22(4), 337-347.

69. Suchanek, W. and Yoshimura, M. (1998). "Processing and properties of hydroxyapatite-based biomaterials for use as hard tissue replacement implants." *Journal of Materials Research*, 13(1), 94-117.

70. D'Alessio, L., Ferro, D., Marotta, V., Santagata, A., Teghil, R. and Zaccagnino, M. (2001). "Laser ablation and deposition of Bioglass 45S5 thin films." *Applied Surface Science*, 183(1-2), 10-17.

71. D'Alessio, L., Teghil, R., Zaccagnino, M., Zaccardo, I., Ferro, D. and Marotta, V. (1999). "Pulsed laser ablation and deposition of bioactive glass as coating material for biomedical applications." *Applied Surface Science*, 138-139, 527-532.

72. Serra, P. and Morenza, J. L. (1998). "Fluence dependence of hydroxyapatite laser ablation plumes." *Thin Solid Films*, 335(1-2), 43-48.

73. Hontsu, S., Matsumoto, T., Ishii, J., Nakamori, M., Tabata, H. and Kawai, T. (1997). "Electrical properties of hydroxyapatite thin films grown by pulsed laser deposition." *Thin Solid Films*, 295(1-2), 214-217.

74. Wu, P. K., Ringeisen, B. R., Callahan, J., Brooks, M., Bubb, D. M., Wu, H. D., Pique, A., Spargo, B., McGill, R. A. and Chrisey, D. B. (2001). "The deposition, structure, pattern deposition, and activity of biomaterial thin-films by matrix-assisted pulsed-laser evaporation (MAPLE) and MAPLE direct write." *Thin Solid Films*, 398-399, 607-614.
75. Chrisey, D. B., Pique, A., Modi, R., Wu, H. D., Auyeung, R. C. Y. and Young, H. D. (2000). "Direct writing of conformal mesoscopic electronic devices by MAPLE DW." *Applied Surface Science*, 168(1-4), 345-352.
76. Villermaux, F., Tabrizian, M., Yahia, L. H., Meunier, M. and Piron, D. L. (1997). "Excimer laser treatment of NiTi shape memory alloy biomaterials." *Applied Surface Science*, 109-110, 62-66.
77. Yue, T. M., Yu, J. K. and Man, H. C. (2001). "The effect of excimer laser surface treatment on pitting corrosion resistance of 316LS stainless steel." *Surface and Coatings Technology*, 137(1), 65-71.
78. Yue, T. M., Yu, J. K., Mei, Z. and Man, H. C. (2002). "Excimer laser surface treatment of Ti-6Al-4V alloy for corrosion resistance enhancement." *Materials Letters*, 52(3), 206-212.
79. Mirzadeh, H., Katbab, A. A. and Burford, R. P. (1995). "CO_2-laser graft copolymerization of HEMA and NVP onto ethylene-propylene rubber (EPR) as biomaterial-(III)." *Radiation Physics and Chemistry*, 46(4-6), 859-862.
80. Mirzadeh, H., Katbab, A. A., Khorasani, M. T., Burford, R. P., Gorgin, E. and Golestani, A. (1995). "Cell attachment to laser-induced AAm- and HEMA-grafted ethylene-propylene rubber as biomaterial: in vivo study." *Biomaterials*, 16(8), 641-648.
81. Cheang, P., Khor, K. A., Teoh, L. L. and Tam, S. C. (1996). "Pulsed laser treatment of plasma-sprayed hydroxyapatite coatings." *Biomaterials*, 17(19), 1901-1904.
82. Davies, J. T. and Rideal, E. K. (1963). *Interfacial phenomena*, Academic Press, New York.
83. Jaycock, M. J. and Parfitt, G. D. (1981). *Chemistry of Interfaces*, John Wiley & Sons,, Chichester.
84. Zisman, W. A. (1963). "Influence of constitution on adhesion." *Industrial & engineering chemistry*, 55, 19-38.
85. Zisman, W. A. (1964). "Relationship of equilibrium contact angle to liquid and solid constitution." Contact angle, wettability and adhesion. advanced in chemistry series 43, R. F. Gould, ed., American Chemical Society, Washington D C, 1-51.
86. Chidambaram, P. R., Edwards, G. R. and Olson, D. I. (1992). "Thermodynamic criterion to predict wettability at metal-alumina interfaces." *Metallurgical Transactions B (Process Metallurgy)*, 23(2), 215-222.
87. Pask, J. A. and Tiomisa, A. P. (1991). "Wetting, surface energies, adhesion and interface reaction thermodynamics." Engineered materials handbook: ceramics and glasses, S. J. Schneider, ed., ASM International, 251-279.

88. Adam, N. K. and Elliott, G. E. P. (1958). "The effects of high temperature variations on contact angle measurements of vitreous enamels." *Journal of the Chemical Society*, 18, 2206-2215.

89. Fowkes, F. M. (1964). "Attractive forces at interface." *Industrial Engineering Chemistry*, 56, 40-52.

90. Dann, J. R. (1970). "Forces involved in the adhesive process. I. Critical surface tensions of polymeric solids as determined with polar liquids." *Journal of Colloid and Interface Science*, 32(2), 302-20.

91. Girifalco, L. A. and Good, D. J. (1957). "A theory for the estimation of surface and interfacial energies. i: derivation and application to interfacial tension." *Journal of Physical Chemistry*, 61, 904-909.

92. Good, R. J. and Girifalco, L. A. (1960). "A theory of the estimation of surface and interfacial energies. III: Estimation of surface energies of solids from contact angle data." *Journal of Physical Chemistry*, 64(5), 561-565.

93. Baier, R. E. "Blood vessels. problems arising at the borders of natural and artificial blood vessels." *Proceedings 8th Scientific Conference of Gesellschaft Deutscher Naturforscher und*, Berlin, 159-162.

94. Baier, R. E. and Dutton, R. C. (1969). "Initial events in interactions of blood with a foreign surface." *Journal of Biomedical Material Research*, 3, 191.

95. Baier, R. E. (1972). *The role of surface energy in thrombosis*, Acadamic, Medical.

96. Baier, R. E. (1970). "Surface properties influencing biological adhesion." Adhesion in Biological Systems, R. S. Manly, ed., Academic Press, New York, 15-48.

97. van Oss, C. J., Gillman, C. F. and Neumann, A. W. (1975). "Phagocytic engulfment and cell adhesiveness as cellular surface phenomena." Phagocytic engulfment and cell adhesiveness, Dekker, Marcel, New York, 7-152.

98. van Oss, C. J., Zingg, W., Hum, O. S. and A.W., N. (1977). "Platelet activation on agar/agarose gel surfaces: variation correlated with casting technique and hydrophobic/hydrophilic balance as reflected in contact angle measurements." *Thrombosis Research*, 11, 183-191.

99. Vogler, E. A. (1993). "Interfacial Chemistry in Biomaterial Science." Wettability (Surfactant Science Series 49), J. Berg, ed., Marcel Dekker, New York, 184-250.

100. Nuzzo, R. G., Dubois, L. H. and Allara, D. L. (1990). "Fundamental studies of microscopic wetting on organic surfaces. I. Formation and structural characterization of a self-consistent series of polyfunctional organic monolayers." *Journal of the American Chemical Society*, 112(2), 558-69.

101. Laibinis, P. E., WHitesides, G. M., Allara, D. L., Tao, Y.-T., Parikh, A. N. and Nuzzo, R. G. (1991). "Comparison of the structures and wetting properties of self-assembled monolayers of n-alkanethiols on the coinage metal surfaces, Cu, Ag, Au." *Journal of the American Chemical Society*, 113(19), 7152-7167.

102. Derjaguim, B. V. and Landau, L. D. (1941). "Theory of the stability of strongly charged lyophobic sols and of the adhesion of strongly charged particles in solution of electrolytes." *Acta Physic Chimica*, 633-662.

103. Verway, E. J. W. and Overbeek, J. H. G. (1948). *Theory of stability of lyophobic colliods*, Elsevier, Amsterdam.

104. van Oss, C. J., Good, R. J. and Chaudhury, M. K. (1986). "The role of van der Waals forces and hydrogen bonds in hydrophobic interactions between biopolymers and low energy surfaces." *nterface Science*, 111, 378-379.

105. Stewart, M. G., Moy, E., Chang, G., Zingg, W. and Neumann, A. W. (1989). "Thermodynamic model for cell spreading." *Colloids Surfaces*, 42, 215-232.

106. Schakenraad, J. M., Busscher, H. J., Wildevuur, C. R. H. and Arends, J. (1986). "Influence of substratum surface free energy on growth and spreading of human fibroblasts in the presence and absence of serum proteins." *Journal of Biomedical Materials Research*, 20(6), 773-784.

107. Campbell, C. E. and von Recum, A. M. (1987). "Microtopography and soft tissue response." *Journal of Invest Surgery*, 2, 51-74.

108. Duval, J. L., Letort, M. and Sigot-Luizard, M. F. (1990). "Fundamental study of cell migration and adhesion towards different biomaterials with organotypic culture method." *Advances in Biomaterials*, 93-98.

109. Jeffrey, J. S. and James, S. F. (1990). "Chemically modified polymeric resins for high-performance liquid chromatography." *Journal of Chromatography A*, 522, 95-105.

110. Bischoff, R. and Bischoff, G. (1998). "Chemical surface modifications of silicone biomaterials." *Journal of Biomechanics*, 31(1), 58.

111. Iwaki, M. (2001). "Ion surface treatments on organic materials." *Nuclear Instruments and Methods in Physics Research Section B: Beam Interactions with Materials and Atoms*, 175-177, 368-374.

112. Fuji, M., Takei, T., Watanabe, T. and Chikazawa, M. (1999). "Wettability of fine silica powder surfaces modified with several normal alcohols." *Colloids and Surfaces A: Physicochemical and Engineering Aspects*, 154(1-2), 13-24.

113. Zhou, X. B. and De Hosson, J. T. M. (1996). "Reactive wetting of liquid metals on ceramic substrates." *Acta Materialia*, 44(2), 421-426.

114. MacDonald, D. E., Deo, N., Markovic, B., Stranick, M. and Somasundaran, P. (2002). "Adsorption and dissolution behavior of human plasma fibronectin on thermally and chemically modified titanium dioxide particles." *Biomaterials*, 23(4), 1269-1279.

115. Kurdi, J., Ardelean, H., Marcus, P., Jonnard, P. and Arefi-Khonsari, F. (2002). "Adhesion properties of aluminium-metallized/ammonia plasma-treated polypropylene: Spectroscopic analysis (XPS, EXES) of the aluminium/polypropylene interface." *Applied Surface Science*, 189(1-2), 119-128.

116. Carrino, L., Moroni, G. and Polini, W. (2002). "Cold plasma treatment of polypropylene surface: a study on wettability and adhesion." *Journal of Materials Processing Technology*, 121(2-3), 373-382.

117. Cho, J. S., Beag, Y.-W., Han, S., Kim, K.-H., Cho, J. and Koh, S.-K. (2000). "Hydrophilic surface formation on materials and its applications." *Surface and Coatings Technology*, 128-129, 66-70.

118. Kim, K.-H., Cho, J.-S., Choi, D.-J. and Koh, S.-K. (2001). "Hydrophilic group formation and cell culturing on polystyrene Petri-dish modified by ion-assisted reaction." *Nuclear Instruments and Methods in Physics Research Section B: Beam Interactions with Materials and Atoms*, 175-177, 542-547.

119. Haddadi-Asl, V. and Burford, R. P. (1996). "Radiation graft modification of ethylene-propylene rubber--III. Effect on water uptake, wettability and biocompatibility." *Radiation Physics and Chemistry*, 47(6), 907-912.

120. Brun, C., Chambaudet, A., Mavon, C., Berger, F., Fromm, M. and Jaffiol, F. (2000). "Modifications of polypropylene surface properties by alpha ionizing radiation." *Applied Surface Science*, 157(1-2), 85-91.

121. Mathieson, I. and Bradley, R. H. (1996). "Improved adhesion to polymers by UV/ozone surface oxidation." *International Journal of Adhesion and Adhesives*, 16(1), 29-31.

122. Nie, H.-Y., Walzak, M. J., Berno, B. and McIntyre, N. S. (1999). "Atomic force microscopy study of polypropylene surfaces treated by UV and ozone exposure: modification of morphology and adhesion force." *Applied Surface Science*, 144-145, 627-632.

123. Benson, R. S. (2002). "Use of radiation in biomaterials science." *Nuclear Instruments and Methods in Physics Research Section B: Beam Interactions with Materials and Atoms*, 191(1-4), 752-757.

124. Kilduff, J. E., Mattaraj, S., Pieracci, J. P. and Belfort, G. (2000). "Photochemical modification of poly(ether sulfone) and sulfonated poly(sulfone) nanofiltration membranes for control of fouling by natural organic matter." *Desalination*, 132(1-3), 133-142.

125. Lee, J. H., Khang, G., Lee, J. W. and Lee, H. B. (1998). "Interaction of different types of cells on polymer surfaces with wettability gradient." *Journal of Colloid and Interface Science*, 205(2), 323-330.

126. Podgorski, L., Chevet, B., Onic, L. and Merlin, A. (2000). "Modification of wood wettability by plasma and corona treatments." *International Journal of Adhesion and Adhesives*, 20(2), 103-111.

127. Vallet, M., Berge, B. and Vovelle, L. (1996). "Electrowetting of water and aqueous solutions on poly(ethylene terephthalate) insulating films." *Polymer*, 37(12), 2465-2470.

128. Kapplel. (1998). "Excimers help ceramic stick together." Opto and Laser Europe, 34.

129. Lawrence, J., Li, L. and Spencer, J. T. (1999). "The effects of high-power diode laser radiation on the wettability, adhesion and bonding characteristics of an alumina/silica-based oxide and vitreous enamel." *Surface and Coatings Technology*, 115(2-3), 273-281.

130. Lawrence, J. and Li, L. (1999). "Wettability characteristics of an Al_2O_3/SiO_2-based ceramic modified with CO_2, Nd:YAG, excimer and high-power diode lasers." *Journal of Physics D (Applied Physics)*, 32(10), 1075-1082.

131. Lawrence, J., Li, L. and Spencer, J. T. (1999). "Diode laser modification of ceramic material surface properties for improved wettability and adhesion." *Applied Surface Science*, 138-139, 388-393.

132. Lawrence, J. (2003). "Identification of the principal elements governing the wettability characteristics of ordinary Portland cement following high power diode laser surface treatment." *Materials Science and Engineering A*, 356(1-2), 162-172.

133. Heitz, J., Arenholz, E., Kefer, T., Bauerle, D., Hibst, H. and Hagemeyer, A. (1992). "Enhanced adhesion of metal films on PET after UV-laser treatment." *Applied Physics A (Solids and Surfaces)*, A55(4), 391-392.

134. Henari, F. and Blau, W. (1995). "Excimer-laser surface treatment of metals for improved adhesion." *Applied Optics*, 34(3), 581-584.

135. Olfert, M., Mueller, R. E., Duley, W., North, T., Hood, J. and Sakai, D. (1996). "Enhancement of adhesion in coated steels through excimer laser surfacing." *Journal of Laser Applications*, 8(2), 79-87.

136. Critchlow, G. W., Cottam, C. A., Brewis, D. M. and Emmony, D. C. (1997). "Further studies into the effectiveness of CO_2 laser treatment of metals for adhesive bonding." *International Journal of Adhesion and Adhesives*, 17(2), 143-150.

137. Song, W., Zhu, P. and Cui, K. (1996). "Effect of Ni content on cracking susceptibility and microstructure of laser-clad Fe-Cr-Ni-B-Si alloy." *Surface & Coatings Technology*, 80(3), 279-282.

138. Lawrence, J. and Li, L. (2000). "Wettability characteristics of carbon steel modified with CO_2, Nd:YAG, excimer and high power diode lasers." *Applied Surface Science*, 154-155, 664-669.

139. Lawrence, J. and Li, L. (2002). "On the mechanisms of wetting characteristics modification for selected metallic materials by means of high power diode laser radiation." *Journal of Laser Applications*, 14(2), 107-113.

140. Petit, S., Laurens, P., Amouroux, J. and Arefi-Khonsari, F. (2000). "Excimer laser treatment of PET before plasma metallization." *Applied Surface Science*, 168(1-4), 300-303.

141. Watanabe, H., Takata, T. and Tsuge, M. (1993). "Polymer surface modification due to excimer laser radiation - chemical and physical changes in the surface structure of poly(ethylene terephthalate)." *Polymer International*, 31(3), 247-254.

142. Andrew, J. E., Dyer, P. E., Forter, D. and Key, P. H. (1983). "Direct etching of polymeric materials using a XeCl laser." *Applied Physics Letter*, 43, 717.

143. Watanabe, H. and Takata, T. (1994). "Direct excimer laser etching of polymeric materials." *Journal of Adhesion Science and Technology*, 6, 1425.

144. Laurens, P., Sadras, B., Decobert, F., Arefi-Khonsari, F. and Amouroux, J. (1998). "Enhancement of the adhesive bonding properties of PEEK by excimer laser treatment." *International Journal of Adhesion and Adhesives*, 18(1), 19-27.

145. Laurens, P., Ould Bouali, M., Meducin, F. and Sadras, B. (2000). "Characterization of modifications of polymer surfaces after excimer laser treatments below the ablation threshold." *Applied Surface Science*, 154-155, 211-216.

146. Song, Q. and Netravali, A. N. (1998). "Excimer laser surface modification of ultra-high-strength polyethylene fibers for enhanced adhesion with epoxy resins: Part1. Effect of laser operating parameters." *Journal of Adhesion Science and Technology*, 12(9), 957-982.

147. Song, Q. and Netravali, A. N. (1998). "Excimer laser surface modification of ultra-high-strength polyethylene fibres for enhanced adhesion with epoxy resins: Part 2. Effect of treatment environment." *Journal of Adhesion Science and Technology*, 9, 983-987.

148. Song, Q. and Netravali, A. N. (1999). "Effects of a pulsed XeCl excimer laser on ultra-high strength polyethylene fiber and its interface with epoxy resin." *Journal of Adhesion Science and Technology*, 13(4), 501-516.

149. Viville, P., Beauvois, S., Lambin, G., Lazzaroni, R., Bredas, J. L., Laude, L. and Kolev, K. (1996). "Excimer laser-induced surface modifications of biocompatible polymer blends." *Applied Surface Science*, 96-98, 558-562.

150. Dadbin, S. (2002). "Surface modification of LDPE film by CO_2 pulsed laser irradiation." *European Polymer Journal*, 38(12), 2489-2495.

151. Lawrence, J. and Li, L. (2001). "Modification of the wettability characteristics of polymethyl methacrylate (PMMA) by means of CO_2, Nd:YAG, excimer and high power diode laser radiation." *Materials Science and Engineering A*, 303(1-2), 142-149.

152. Dadsetan, M., Mirzadeh, H., Sharifi-Sanjani, N. and Daliri, M. (2001). "Cell behavior on laser surface-modified polyethylene terephthalate in vitro." *Journal of Biomedical Materials Research*, 57(2), 183-189.

153. Yaszemski, M. J., Payne, R. G., Hayes, W. C., Langer, R. and Mikos, A. G. (1996). "Evolution of bone transplantation: molecular, cellular and tissue strategies to engineer human bone." *Biomaterials*, 17(2), 175-185.

154. Friedman, R. J., Black, J., Galante, J. O., Jacobs, J. J. and Skinner, H. B. (1993). "Current concepts in orthopaedic biomaterials and implant fixation." *Journal of Bone and Joint Surgery - Series A*, 75(7), 1086-1109.

155. Hastings, G. W. and Mahmud, F. A. (1993). "Intelligent orthopaedic materials." *Journal of Intelligent Material Systems and Structures*, 4(4), 452-456.

156. Dalton, B. A., McFarland, C. D., Gengenbach, T. R., Greisser, H. J. and Steele, J. G. (1998). "Polymer surface chemistry and bone cell migration." *Journal of Biomaterials Science, Polymer Edition*, 9(8), 781-799.

157. Healy, K. E., Thomas, C. H., Rezania, A., Kim, J. E., McKeown, P. J., Lom, B. and Hockberger, P. E. (1996). "Kinetics of bone cell organization and mineralization on materials with patterned surface chemistry." *Biomaterials*, 17(2), 195-208.

158. von Recum, A. F. and van Kooten, T. G. (1995). "The influence of micro-topography on cellular response and the implications for silicone implants." *Journal of Biomaterials Science. Polymer Edition*, 7(2), 181-198.

159. Kokubo, T., Kim, H.-M. and Kawashita, M. (2003). "Novel bioactive materials with different mechanical properties." *Biomaterials*, 24(13), 2161-2175.

160. Rey, C. (1998). "Orthopedic biomaterials, bioactivity, biodegradation; a physical-chemical approach." *Journal of Biomechanics*, 31(1), 182.

161. Uchida, M., Kim, H.-M., Kokubo, T., Miyaji, F. and Nakamura, T. (2001). "Bonelike apatite formation induced on zirconia gel in a simulated body fluid and its modified solutions." *Journal of the American Ceramic Society*, 84(9), 2041-2044.

162. Uchida, M., Kim, H.-M., Kokubo, T., Tanaka, K. and Nakamura, T. (2002). "Structural dependence of apatite formation on zirconia gels in a simulated body fluid." *Journal of the Ceramic Society of Japan*, 110(8), 710-715.

163. Uchida, M., Kim, H.-M., Kokubo, T., Nawa, M., Asano, T., Tanaka, K. and Nakamura, T. (2002). "Apatite-forming ability of a zirconia/alumina nano-composite induced by chemical treatment." *Journal of Biomedical Materials Research*, 60(2), 277-282.

164. Uchida, M., Kim, H. M., Miyaji, F., Kokubo, T. and Nakamura, T. (2002). "Apatite formation on zirconium metal treated with aqueous NaOH." *Biomaterials*, 23(1), 313-317.

165. Carlsson, T., Rostlund, B., Albrektson, T., Albrektson, P. and Branemark, I. (1986). "Osseointegration of titanium implants." *Acta Orthopedic Scand*, 57(4), 285-289.

166. Cooper, L. F., Masuda, T., Yliheikkila, P. K. and Felton, D. A. (1998). "Generalizations regarding process and phenomenon of osseointegration. Part II. In vitro studies." *International Journal of Oral Maxillofacial Implants*, 13, 163-174.

167. Hench, L. L. (1998). "Biomaterials: a forecast for the future." *Biomaterials*, 19(16), 1419-1423.

168. Grzesik, W. J. and Robey, P. G. (1994). "Bone matrix RGD glycoproteins: immunolocalization and interaction with human primary osteoblastic bone cells in vitro." *Journal of Bone And Mineral Research: The Official Journal of The American Society For Bone And Mineral Research*, 9(4), 487-496.

169. Zigmond, S. H. (1996). "Signal transduction and actin filament organization." *Current Opinion in Cell Biology*, 8(1), 66-73.

170. Boyan, B. D., Hummert, T. W., Dean, D. D. and Schwartz, Z. (1996). "Role of material surfaces in regulating bone and cartilage cell response." *Biomaterials*, 17(2), 137-146.

171. Chesmel, K. D., Clark, C. C., Brighton, C. T. and Black, J. (1995). "Cellular responses to chemical and morphologic aspects of biomaterial surfaces. II. The biosynthetic and migratory response of bone cell populations." *Journal of Biomedical Materials Research*, 29(9), 1101-1110.

172. Naji, A. and Harmand, M.-F. (1990). "Study of the effect of the surface state on the cytocompatibility of a Co-Cr alloy using human osteoblasts and fibroblasts." *Journal of Biomedical Materials Research*, 24(7), 861-871.

173. Anselme, K., Bigerelle, M., Noel, B., Dufresne, E., Judas, D., Iost, A. and Hardouin, P. (2000). "Qualitative and quantitative study of human osteoblast adhesion on materials with various surface roughnesses." *Journal of Biomedical Materials Research*, 49(2), 155-166.

174. Bowers, K. T., Keller, J. C., Randolph, B. A., Wick, D. G. and Michaels, C. M. (1992). "Optimization of surface micromorphology for enhanced osteoblast responses in vitro." *International Journal of Oral Maxillofac Implants*, 7(3), 302-310.

175. Martin, J. Y., Schwartz, Z., Hummert, T. W., Schraub, D. M., Simpson, J., Lankford, J. J., Dean, D. D., Cochran, D. L. and Boyan, B. D. (1995). "Effect of titanium surface roughness on proliferation, differentiation, and protein synthesis of human osteoblast-like cells (MG63)." *Journal of Biomedical Materials Research*, 29(3), 389-401.

176. Michaels, C. M., Keller, J. C., Stanford, C. M. and Solursh, M. (1989). "In vitro cell attachment of osteoblast-like cells to titanium." *Journal of Dental Research*, 68, 278-286.

177. Lincks, J., Boyan, B. D., Blanchard, C. R., Lohmann, C. H., Liu, Y., Cochran, D. L., Dean, D. D. and Schwartz, Z. (1998). "Response of MG63 osteoblast-like cells to titanium and titanium alloy is dependent on surface roughness and composition." *Biomaterials*, 19(23), 2219-2232.

178. Ong, J. L., Carnes, D. L., Cardenas, H. L. and Cavin, R. (1997). "Surface roughness of titanium on bone morphogenetic protein-2 treated osteoblast cells in vitro." *Implant Dentistry*, 6(1), 19-24.

179. Groessner-Schreiber, B. and Tuan, R. S. (1992). "Enhanced extracellular matrix production and mineralization by osteoblasts cultured on titanium surfaces in vitro." *Journal of Cell Science*, 101(1), 209-217.

180. Bigerelle, M., Anselme, K., Noel, B., Ruderman, I., Hardouin, P. and Iost, A. (2002). "Improvement in the morphology of Ti-based surfaces: a new process to increase in vitro human osteoblast response." *Biomaterials*, 23(7), 1563-1577.

181. Chesmel, K. D., Clark, C. C., Brighton, C. T. and Black, J. (1995). "Cellular responses to chemical and morphologic aspects of biomaterial surfaces. II. The biosynthetic and migratory response of bone cell populations." *Journal of Biomedical Materials Research*, 29, 1101-1110.

182. Anselme, K., Bigerelle, M., Noel, B., Dufresne, E., Judas, D., Lost, A. and Hardouin, P. (2000). "Qualitative and quantitative study of human osteoblast adhesion on materials with various surface roughnesses." *Journal of Biomedical Materials Research*, 49(2), 155-166.

183. Meyer, U., Szulczewski, D. H., Moeller, K., Heide, H. and Jones, D. B. (1993). "Attachment kinetics and differentiation of osteoblasts on different biomaterials." *Cells and Materials*, 3(2), 129-140.

184. Webb, K., Hlady, V. and Tresco, P. A. (2000). "Relationships among cell attachment, spreading, cytoskeletal organization, and migration rate for anchorage-dependent cells on model surfaces." *Journal of Biomedical Material Research*, 49, 362-368.

185. Shelton, R. M., Rasmussen, A. C. and Davies, J. E. (1988). "Protein adsorption at the interface between charged polymer substrata and migrating osteoblasts." *Biomaterials*, 9(1), 24-29.

186. Kononen, M., Hormia, M., Kivilahti, J., Hautaniemi, J. and Thesleff, I. (1992). "Effect of surface processing on the attachment orientation, and proliferation of human gingival fibroblasts on titanium." *Journal of Biomedical Material Research*, 26, 1325-1341.

187. Kasemo, B. and Lausmaa, J. (1986). "Surface science aspects on inorganic biomaterials." *Critical Review of Biocomptability*, 2, 335-380.

188. Tamada, Y. and Ikada, Y. (1993). "Cell adhesion to plasma-treated polymer surfaces." *Polymer*, 34(10), 2208-2212.

189. Anker, M., Johansson, A., Rindlav, A., Hjertberg, T. and Thomsen, P. (1996). "Cell interactions with modified fluoropolymer surfaces." *Proceedings of the 5th World Biomaterials Congress. Part 1 (of 2), May 29-Jun 2 1996*, Toronto, Canada, 21.

190. Lee, S. J., Lee, Y. M., Khang, G., Kim, I. Y., Lee, B. and Lee, H. B. (2002). "Effect of poly(3-hydroxybutyrate-co-3-hydroxyvalerate) surface with different wettability on fibroblast behaviour." *Macromolecular research*, 10(3), 150-157.

191. Roberson, S., Sehgal, A., Fahey, A. and Karim, A. (2003). "Time-of-flight secondary ion mass spectrometry (TOF-SIMS) for high-throughput characterization of biosurfaces." *Applied Surface Science*, 203-204, 855-858.

192. Svorcik, V., Tomasova, P., Dvorankova, B., Hnatowicz, V., Ochsner, R. and Ryssel, H. (2003). "Fibroblasts adhesion on ion beam modified polyethylene." *Nuclear Instruments and Methods in Physics Research Section B: Beam Interactions with Materials and Atoms*, 215(3-4), 366-372.

193. Mirzadeh, H. and Dadsetan, M. (2003). "Influence of laser surface modifying of polyethylene terephthalate on fibroblast cell adhesion." *Radiation Physics and Chemistry*, 67(3-4), 381-385.

194. Fujimori, S. (1995). "Surface characterization of titanium plates with different surface treatments and cellular proliferation and expression of osteoblast-like cells in vitro on their surface." *Journal of Dental Materials*, 14, 155-168.

195. Webster, T. J., Siegel, R. W. and Bizios, R. (1999). "Osteoblast adhesion on nanophase ceramics." *Biomaterials*, 20(13), 1221-1227.

196. Webster, T. J., Siegel, R. W. and Bizios, R. (2001). "Enhanced surface and mechanical properties of nanophase ceramics to achieve orthopaedic/dental implant efficacy." *Key Engineering Materials*,192-195, 321-324.

197. Bosetti, M., Verne, E., Ferraris, M., Ravaglioli, A. and Cannas, M. (2001). "In vitro characterisation of zirconia coated by bioactive glass." *Biomaterials*, 22(9), 987-994.

198. Sumner, D. R., Turner, T. M., Purchio, A. F., Gombotz, W. R., Urban, R. M. and Galante, J. O. (1995). "Enhancement of bone ingrowth by transforming growth factor-beta." *The Journal of Bone And Joint Surgery. American Volume*, 77(8), 1135-1147.

199. Piattelli, A., Scarano, A., Corigliano, M. and Piattelli, M. (1996). "Effects of alkaline phosphatase on bone healing around plasma-sprayed titanium implants: a pilot study in rabbits." *Biomaterials*, 17(14), 1443-1449.

200. Liu, S. Q., Ito, Y. and Imanishi, Y. (1993). "Cell growth on immobilized cell growth factor: 5. Interaction of immobilized transferrin with fibroblast cells." *International Journal of Biological Macromolecules*, 15(4), 221-226.

201. Liu, Z. (1991). "Surface modification of materials using high power lasers and an arc image intensifier," PhD Thesis, University of Liverpool.

202. Antou, G., Montavon, G., Hlawka, F., Cornet, A., Coddet, C. and Machi, F. (2003). "Modification of ceramic thermal spray deposit microstructures implementing in situ laser remelting." *Surface and Coatings Technology*, 172(2-3), 279-290.

203. Spalding, I. (1987). "Modern laser application." *Proceedings of the Institution of Mechanical Engineers, Part B: Management and Engineering Manufacture*, 201(B3), 165-174.

204. Sivakumar, R. and Mordike, B. L. (1988). "Laser melting of plasma sprayed ceramic coatings." *Surface Engineering*, 4(2), 127-40.

205. Liu, Q., An, S. and Qiu, W. (1999). "Study on thermal expansion and thermal shock resistance of MgO-PSZ." *Solid State Ionics*, 121(1-4), 61-65.

206. Grain, C. F. (1967). "Phase relations in the ZrO_2-MgO system." *Journal of American Ceramic Society*, 50(6), 288.

207. Pei, Y. T., Ouyang, J. H. and Lei, T. C. (1996). "Laser cladding of ZrO_2--(Ni alloy) composite coating." *Surface and Coatings Technology*, 81(2-3), 131-135.

208. Chwa, S. O. and Ohmori, A. (2001). "The influence of surface roughness of sprayed zirconia coatings on laser treatment." *Surface and Coatings Technology*, 148(1), 87-94.

209. Wei, W.-C. J. and Lin, Y.-P. (1998). "Processing character of MgO-partially stabilized zirconia (PSZ) in size grading prepared by injection molding." *Journal of the European Ceramic Society*, 18(14), 2107-2116.

210. Duwez, P., Willens, R. H. and Klenert, W. (1960). "Continuous series of metastable solid solutions in silver-copper alloys." *Journal of Applied Physics*, 31(6), 1136-1137.

211. Elder, S. P. and Abbaschian, G. J. (1979). "Supercooling and rapid solidification using EM levitation." Principles of Solidification and Materials Processing, S. M. Trivedi and J. M. Marten, eds., Academic Press, New York, 299-354.

212. Mehrabian, R., Kear, B. H. and Cohen, M. (1980). "Supercooling and rapid solidification microstructures in metals and alloys." Rapid Solidification Processing, Principles and Technologies II,, R. Mehrabian, B. H. Kear, and M. Cohen, eds., Claitors Publishing, Baton Rouge, 89-126.

213. Kurz, W. and Fusher, D. J. (1986). *Fundamentals of Solidification*, Trans Tech Publications, Aedermansdorf.

214. Flemings, M. C. (1974). *Solidification processing*, McGraw-Hill, New York.

215. Mordike, S. (1990). "State-of-the-art of surface engineering with high energy beams." *Transactions of the Powder Metallurgy Association of India*, 17, 81-93.

216. Pollinger, J. P. and Messing, G. L. (1984). "Microstructural analysis of rapidly solidified alumina." *Materials Science Research*, 17, 505-517.

217. Rutter, J. W. and Chalmers, B. (1953). "A prismatic substructure formed during solidification of metals." *Canadian Journal of Physics*, 31, 15-39.

218. Chalmers, B. (1956). "Structures formed during solidification in terms of composition." *Transactions of AIME*, 200, 132-146.

219. Chalmers, B. (1964). *Principles of solidification*, John Wiley & Sons, New York.

220. Walton, D., Tiller, W. A., Rutter, J. W. and Winegard, W. C. (1955). "Solidification and cellular growth in a binary alloy." *Transactions of AIME*, 203, 1023-1031.

221. Tiller, W. A. and Rutter, J. W. (1956). "The effect of growth conditions upon the solidification of a binary alloy." *Canadian Journal of Physics*, 34, 96-121.

222. Plaskett, T. S. and Winegard, W. C. (1956). "Cellular growth in tin alloys." *Canadian Journal of Physics*, 37, 1555-1557.

223. Esquivel, O., Mazumder, J., Bass, M. and Copely, S. M. (1980). "Microstructural formation according to the theory of constitutional supercooling." Rapid solidification processing, principles and technologies II, R. Mehrabian, B. H. Kear, and M. Cohen, eds., Claitors Publishing, Baton Rouge, 150-173.

224. Ashbrook, R. L. (1983). *Rapid solidification technology: source book*, ASM International, Metals Park.

225. Mehrabian, R. (1982). "Rapid solidification." *International Metals Reviews*, 27(4), 185-209.

226. Chadwick, G. A. (1967). "Constitutional supercooling and microsegregation." Fractional solidification, M. Zief and W. R. Wilcox, eds., Academic Press, New York, 120-128.

227. Holmes, E. L., Rutter, J. W. and Winegard, W. C. (1957). "Growth conditions for stability of a cellular solid-liquid Interface." *Canadian Journal of Physics*, 35, 1223-1227.

228. Plaskett, T. S. and Winegard, W. C. (1950). "Analysis of stability of a cellular solid-liquid interface." *Transactions of AIME*, 51, 222-234.

229. Flemmings, M. C. (1968). *Surfaces and interfaces*, Syracuse University Press, Syracuse.

230. Flemmings, M. C. (1971). *Surfaces*, ASM International, Metals Park.

231. Flemmings, M. C., Poirer, D. R., Barone, R. V. and Brody, H. D. (1970). "Mechanical characteristics of solidified structures." *Journal of the Iron and Steel Institution*, 208, 208-214.

232. Jones, H. (1983). *Rapid solidification of metals and alloys*, Institute of Metallurgists, London.

233. Biloni, H., Bolling, G. F. and Cole, G. S. (1966). "Preferred growth directions in a solidified binary alloy." *Transactions of the Metallic Society*, 236, 930-938.

234. Chadwick, G. A. (1967). *Fractional solidification*, Dekker, New York.

235. Morris, L. R. and Winegard, W. C. (1969). "Preferred growth directions in a binary alloy of cellular and dendritic structures." *Journal of Crystal Growth*, 5, 361-370.

236. Mulins, W. W. (1964). "Stability of planner interface during solidification of a dilute binary alloy." *Journal of Applied Physics*, 35(2), 444-451.

237. Sekerka, R. F. (1965). "A stability function for explicit evaluation of the mulins-sekerka interface stability criterion." *Journal of Applied Physics*, 36(1), 264-273.

238. Breinan, E. M. and Kear, B. H. (1983). "Rapid solidification laser processing at high power density." Laser materials processing, M. Bass, ed., 241.

239. Kear, B. H., Greenwald, L. E. and Breinan, M. (1979). "Laser glazing - a new process for production and control of rapidly chilled metallurgical microstructures." *Metals Technology*, 121-130.

240. Ouyang, J. H., Nowotny, S., Richter, A. and Beyer, E. (2001). "Characterization of laser clad yttria partially-stabilized ZrO_2 ceramic layers on steel $16MnCr_5$." *Surface and Coatings Technology*, 137(1), 12-20.

241. Bradley, L., Li, L. and Stott, F. H. (1999). "Characteristics of the microstructures of alumina-based refractory materials treated with CO_2 and diode lasers." *Applied Surface Science*, 138-139, 233-9.

242. Lee, S. Z. and Gahr, K.-H. Z. (1992). "Surface treatments of Al_2O_3 ceramics by CO_2 lasers." *Material Wissenschaft und Werkstofftechnik*, 23(4), 117-23.

243. Shieh, J. H. and Wu, S. T. (16). "Rapid solidification of a plasma-sprayed ceramic coating melted by a CO2 laser." *Applied Physics Letters*, 59(12), 1512-14.

244. Rivindram, K., Srinivasan, J. and Marathe, A. G. (1994). "Finite element study on the role of convection in laser surface melting." *Numerical Heat Transfer*, 26(5), 601-618.

245. Morvan, D., Cipriani, F. D. and Bournot, P. (1994). "Thermocapillary convection during laser surface melting." *International Journal of Heat and Mass Transfer,* 37(14), 1973-1983.

246. Mazumder, J. and Steen, W. M. (1980). "Heat transfer model for CW laser processing." *Journal of Applied Physics,* 51(2), 941-947.

247. Biswalit, B. and Date, A. W. (1979). "Numerical modelling of melting and solidification Processes." Principles of solidification and materials processing, S. M. Trivedi and J. M. Marten, eds., Academic Press, New York, 490-526.

248. Chaim, R., Heuer, A. H. and Aronov, V. (1990). "Surface microstructure changes on laser treatment of MgO-partially stabilised zirconia." *Journal of the American Ceramic Society,* 73, 1519-1523.

249. Shih, C. H. S., Molian, P. A., McCallum, R. W. and Balachandran, U. (1994). "Laser surface refinement of $YBa_2Cu_3O_x$ superconductor." *Journal of Materials Science,* 29(6), 1629-1635.

250. Shieh, Y. N., Rawlings, R. D. and West, D. R. F. (1994). "Laser processing of ceramics of the $SiO_2Al_2O_3$ system." *Journal of Materials Science,* 29(6), 5285-5292.

251. McCallum, R. W., Kramer, M. J. and Weir, S. T. (1993). "Phase diagram effects in rapid thermal processing of $REBa_2Cu_3O_{7-d.}$" *IEEE Transaction on Applied Superconductivity,* 3(1), 1147-1149.

252. Neumann, A. W., Absolom, D. R., Zingg, W. and van Oss, C. J. (1979). "Surface thermodynamics of leukocyte and platelet adhesion to polymer surfaces." *Cell Biophysics,* 1, 79-92.

253. Neumann, A. W., Hope, C. J., Ward, C. A., Herbert, M. A., Dunn, G. W. and Zingg, W. (1975). "Role of surface thermodynamics in thromboresistance of biomaterials." *Journal of Biomedical Materials Research,* 9(2), 127-142.

254. Agathopoulos, S. and Nikolopoulos, P. (1995). "Wettability and interfacial interactions in bioceramic-body-liquid systems." *Journal of Biomedical Materials Research,* 29(4), 421-429.

255. Lawrence, J., Li, L. and Spencer, J. T. (1998). "A two-stage ceramic tile grout sealing process using a high power diode laser--Grout development and materials characteristics." *Optics & Laser Technology,* 30(3-4), 205-214.

256. Lawrence, J. and Li, L. (1999). "Wettability characteristics of a modified mild steel with CO_2, Nd:YAG, excimer and high power diode lasers." *Journal of Physics D (Applied Physics),* 32(18), 2311-2318.

257. Kinloch, A. J. (1987). A*dhesion and Adhesives: Science and Technology,* Chapman and Hall.

258. Ueki, M., Naka, M. and Okamoto, I. (1986). "Wettability of some metals against zirconia ceramics." *Journal of Materials Science Letters,* 5(12), 1261-1262.

259. Li, J. (1993). "Microscopic approach of adhesion and wetting of liquid metal on solid ionocovalent oxide surface." *Xiyou Jinshu/Rare Metals,* 12(2), 84-96.

260. Wenzel, R. N. (1936). "Resistance of solid surfaces to wetting by water." *Industrial Engineering Chemistry*, 28, 988-994.

261. Feng, A., McCoy, B. J., Munir, Z. A. and Cagliostro, D. (1998). "Wettability of transition metal oxide surfaces." *Materials Science and Engineering A*, 242(1-2), 50-56.

262. Zhang, X. M., Yue, T. M. and Man, H. C. (1997). "Enhancement of ceramic-to-metal adhesive bonding by excimer laser surface treatment." *Materials Letters*, 30(5-6), 327-332.

263. Lawrence, J. (2002). "On the predominant mechanisms active during the high-power diode-laser modification of the wettability characteristics of an SiO_2/Al_2O_3 based ceramic material." *Proceedings of the Royal Society of London, Series A (Mathematical, Physical and Engineering Sciences)*, 458(2026), 2445-63.

264. Chattoraj, D. K. and Birdi, K. S. (1984). A*dsorption and the gibbs surface excess*, Plenum Press, New York.

265. Scherrer, P. (1918). "Estimation of size and internal structure of colloidal particles by means of Rontgen rays." *Gottinger Nachrichten*, 2, 98-100.

266. Lu, K. (1995). "Interfacial structural characteristics and grain-size limits in nanocrystalline materials crystallized from amorphous solids." *Physical Review B*, 51, 18-27.

267. Man, H. C., Zhang, X. M., Yue, T. M. and Lau, W. S. (1997). "Excimer laser surface modification of engineering ceramics for adhesive bonding." *Journal of Materials Processing Technology*, 66(1-3), 123-129.

268. Christensen, A. and Carter, E. A. (1998). "First-principles study of the surfaces of zirconia." *Physical Review B (Condensed Matter)*, 58(12), 8050-64.

269. Uchida, M., Kim, H.-M., Kokubo, T., Nawa, M., Tanaka, K. and Nakamura, T. (2001). "Apatite-forming ability of zirconia gels with different structures." *14th International Symposium on Ceramics in Medicine-Annual Meeting of the International Society for Ceramics in Medicine Bioceramics'01 (ISCM), Nov 14-17 2001*, Palm Springs, CA, 637-640.

270. Uchida, M., Kim, H.-M., Kokubo, T., Fujibayashi, S. and Nakamura, T. (2003). "Structural dependence of apatite formation on titania gels in a simulated body fluid." *Journal of Biomedical Materials Research*, 64(1), 164-170.

271. Morterra, C., Cerrato, G., Ferroni, L. and Montanaro, L. (1994). "Surface characterization of yttria-stabilized tetragonal ZrO_2 Part 1. Structural, morphological, and surface hydration features." *Materials Chemistry and Physics*, 37(3), 243-257.

272. Uchida, M., Kim, H.-M., Kokubo, T., Tanaka, K. and Nakamura, T. (2002). "Structural dependence of apatite formation on zirconia gels in a simulated body fluid." *Nippon Seramikkusu Kyokai Gakujutsu Ronbunshi/Journal of the Ceramic Society of Japan*, 110(1284), 710-715.

273. Qian, Z. and Shi, J. L. (1998). "Characterization of pure and doped zirconia nanoparticles with infrared transmission spectroscopy." *Nanostructured Materials*, 10(2), 235-244.

274. Yang, X. C., Riehemann, W., Dubiel, M. and Hofmeister, H. (2002). "Nanoscaled ceramic powders produced by laser ablation." *Materials Science and Engineering B,* 95(3), 299-307.

275. Cochez, M., Ferriol, M., Bourson, P. and Aillerie, M. (2002). "Influence of the dopant concentration on the OH- absorption band in Fe-doped $LiNbO_3$ single-crystal fibers." *Optical Materials,* 21(4), 775-781.

276. Zeng, D. W., Yung, K. C. and Xie, C. S. (2003). "UV Nd:YAG laser ablation of copper: chemical states in both crater and halo studied by XPS." *Applied Surface Science,* 217(1-4), 170-180.

277. Lee, B.-S., Hung, Y.-L. and Lan, W.-H. (2003). "Compositional and morphological changes of human dentin after Er:YAG laser irradiation." *International Congress Series,* 1248, 143-152.

278. Jung, K. T. and Bell, A. T. (2000). "The effects of synthesis and pretreatment conditions on the bulk structure and surface properties of zirconia." *Journal of Molecular Catalysis A: Chemical,* 163(1-2), 27-42.

279. Malicsko, L. and Watterich, A. (2002). "Changes of OH- bands induced by laser irradiation in LiNbO3:Fe single crystals." *Nuclear Instruments and Methods in Physics Research Section B: Beam Interactions with Materials and Atoms,* 191(1-4), 106-109.

280. Tsyganenko, A. A. and Filimonov, V. N. (1972). "Infrared spectra of surface hydroxyl groups and crystalline structure of oxides." *Spectroscopy Letters,* 5(12), 477-87.

281. Takeda, S., Yamamoto, K., Hayasaka, Y. and Matsumoto, K. (1999). "Surface OH group governing wettability of commercial glasses." *Journal of Non-Crystalline Solids,* 249(1), 41-46.

282. Takeda, S., Fukawa, M., Hayashi, Y. and Matsumoto, K. (1999). "Surface OH group governing adsorption properties of metal oxide films." *Thin Solid Films,* 339(1-2), 220-224.

283. Janczuk, B., Bruque, J. M., Gonzalez-Martin, M. L. and del Pozo, J. M. (1993). "Determination of components of cassiterite surface free energy from contact angle measurements." *Journal of Colloid and Interface Science,* 161(1), 209-222.

284. Gonzalez-Martin, M. L., Labajos-Broncano, L., Janczuk, B. and Bruque, J. M. (1999). "Wettability and surface free energy of zirconia ceramics and their constituents." *Journal of Materials Science,* 34(23), 5923-6.

285. Janczuk, B., Gonzalez-Martin, M. L. and Bruque, J. M. (1994). "Influence of mixture anionic and non-ionic surfactants on the surface free energy of cassiterite." *Journal of Materials Science,* 29(12), 3177-3184.

286. Feng, B., Chen, J. Y., Qi, S. K., He, L., Zhao, J. Z. and Zhang, X. D. (2002). "Characterization of surface oxide films on titanium and bioactivity." *Journal of Materials Science: Materials in Medicine,* 13(5), 457-464.

287. Deligianni, D. D., Katsala, N., Ladas, S., Sotiropoulou, D., Amedee, J. and Missirlis, Y. F. (2001). "Effect of surface roughness of the titanium alloy Ti-6Al-4V on human bone marrow cell response and on protein adsorption." *Biomaterials,* 22(11), 1241-1251.

288. Castner, D. G. and Ratner, B. D. (2002). "Biomedical surface science: Foundations to frontiers." *Surface Science*, 500(1-3), 28-60.

289. Horbett, T. A. and Klumb, L. A. (1996). *Cell culturing: surface aspects and considerations*, Marcel Dekker, New York.

290. Kanagaraja, S., Lundstrom, I., Nygren, H. and Tengvall, P. (1996). "Platelet binding and protein adsorption to titanium and gold after short time exposure to heparinized plasma and whole blood." *Biomaterials*, 17(23), 2225-2232.

291. Nygren, H., Tengvall, P. and Lundstrom, I. (1997). "The initial reactions of TiO_2 with blood." *Journal of Biomedical Materials Research*, 34(4), 487-492.

292. Walivaara, B., Askendal, A., Lundstrom, I. and Tengvall, P. (1996). "Blood protein interactions with titanium surfaces." *Journal of Biomaterials Science, Polymer Edition*, 8(1), 41-48.

293. Hong, J., Andersson, J., Ekdahl, K. N., Elgue, G., Axen, N., Larsson, R. and Nilsson, B. (1999). "Titanium is a highly thrombogenic biomaterial: Possible implications for osteogenesis." *Thrombosis and Haemostasis*, 82(1), 58-64.

294. Ducheyne, P. and Qiu, Q. (1999). "Bioactive ceramics: the effect of surface reactivity on bone formation and bone cell function." *Biomaterials*, 20(23-24), 2287-2303.

295. Puleo, D. A. and Bizios, R. (1992). "Mechanisms of fibronectin-mediated attachment of osteoblasts to substrates in vitro." *Bone And Mineral*, 18(3), 215-226.

296. Taborelli, M., Eng, L., Descouts, P., Ranieri, J. P., Bellamkonda, R. and Aebischer, P. (1995). "Bovine serum albumin conformation on methyl and amine functionalized surfaces compared by scanning force microscopy." *Journal of Biomedical Materials Research*, 29, 707-714.

297. Ranieri, J. P., Bellamkonda, R., Jacob, J., Vargo, T. G., Gardella, J. A. and Aebischer, P. (1993). "Selective neuronal cell attachment to a covalently patterned monoamine on fluorinated ethylene propylene films." *Journal of Biomedical Materials Research*, 27(7), 917-925.

298. Janocha, B., Hegemann, D., Oehr, C., Brunner, H., Rupp, F. and Geis-Gerstorfer, J. (2001). "Adsorption of protein on plasma-polysiloxane layers of different surface energies." *Surface and Coatings Technology*, 142-144, 1051-1055.

299. Ying, P., Yu, Y., Jin, G. and Tao, Z. (2003). "Competitive protein adsorption studied with atomic force microscopy and imaging ellipsometry." *Colloids and Surfaces B: Biointerfaces*, 32(1), 1-10.

300. Altankov, G., Grinnell, F. and Groth, T. (1996). "Fibronectin matrix formation and signaling via integrins on biomaterials." *Proceedings of the 5th World Biomaterials Congress. Part 1 (of 2), May 29-Jun 2 1996*, Toronto, Canada, 281.

301. Altankov, G. and Groth, T. (1994). "Reorganization of substratum-bound fibronectin on hydrophilic and hydrophobic materials is related to biocompatibility." *Journal of Materials Science: Materials in Medicine*, 5(9-10), 732-737.

302. Altankov, G. and Groth, T. (1996). "Fibronectin matrix formation and the biocompatibility of materials." *Journal of Materials Science: Materials in Medicine*, 7(7), 425-429.

303. Galli, C., Collaud Coen, M., Hauert, R., Katanaev, V. L., Groning, P. and Schlapbach, L. (2002). "Creation of nanostructures to study the topographical dependency of protein adsorption." *Colloids and Surfaces B: Biointerfaces*, 26(3), 255-267.

304. Galli, C., Collaud Coen, M., Hauert, R., Katanaev, V. L., Wymann, M. P., Groning, P. and Schlapbach, L. (2001). "Protein adsorption on topographically nanostructured titanium." *Surface Science*, 474(1-3), 180-184.

305. Thomes, B., Timmons, R. and Eberhart, R. (1998). "Surface roughness & surface chemistry effects on protein adsorption." *Proceedings of the 17th Southern Biomedical Engineering Conference, Feb 6-8 1998*, San Antonio, TX, USA, 47.

306. Olsson, J., Carlen, A., Burns, N. L. and Holmberg, K. (1995). "Modified pellicle formation and reduced in vitro bacterial adherence after surface treatment with different siloxane polymers." *Colloids and Surfaces B: Biointerfaces*, 5(3-4), 161-169.

307. Serro, A. P., Fernandes, A. C., Saramago, B. and Norde, W. (1999). "Bovine serum albumin adsorption on titania surfaces and its relation to wettability aspects." *Journal of Biomedical Materials Research*, 46(3), 376-381.

308. MacDonald, D. E., Marcovic, B., Allen, M., Somasundaran, P. and Boskey, A. L. (1998). "Surface analysis of human plasma fibronectin adsorbed to commercially pure titanium materials." *Journal of Biomedical Materials Research*, 41(1), 120-130.

309. Francois, P., Vaudaux, P., Taborelli, M., Tonetti, M., Lew, D. P. and Descouts, P. (1997). "Influence of surface treatments developed for oral implants on the physical and biological properties of titanium. Part2. Adsorption isotherms and biological activity of immobilized fibronectin." *Clinical Oral Implant Research*, 8, 217-225.

310. Grinnell, F. and Feld, M. K. (1982). "Fibronectin adsorption on hydrophilic and hydrophobic surfaces detected by antibody binding and analyzed during cell adhesion in serum-containing medium." *The Journal Of Biological Chemistry*, 257(9), 4888-4893.

311. Feng, B., Weng, J., Yang, B. C., Chen, J. Y., Zhao, J. Z., He, L., Qi, S. K. and Zhang, X. D. (2002). "Surface characterization of titanium and adsorption of bovine serum albumin." *Materials Characterization*, 49(2), 129-137.

312. Wan, H., Williams, R. L., Doherty, P. J. and Williams, D. F. (1997). "Study of cell behaviour on the surfaces of multifilament materials." *Journal of Materials Science: Materials in Medicine*, 8(1), 45-51.

313. Lee, J. H., Jung, H. W., Kang, I.-K. and Lee, H. B. (1994). "Cell behaviour on polymer surfaces with different functional groups." *Biomaterials*, 15(9), 705-711.

314. Horbett, T. A., Waldburger, J. J., Ratner, B. D. and Hoffman, A. S. (1988). "Cell adhesion to a series of hydrophilic-hydrophobic copolymers studies with a spinning disc apparatus." *Journal of Biomedical Materials Research,* 22(5), 383-404.

315. Suggs, L. J., Shive, M. S., Garcia, C. A., Anderson, J. M. and Mikos, A. G. (1999). "In vitro cytotoxicity and in vivo biocompatibility of poly(propylene fumarate-co-ethylene glycol) hydrogels." *Journal of Biomedical Materials Research,* 46(1), 22-32.

316. Jenney, C. R. and Anderson, J. M. (1999). "Effects of surface-coupled polyethylene oxide on human macrophage adhesion and foreign body giant cell formation in vitro." *Journal of Biomedical Materials Research,* 44(2), 206-216.

317. Chuang, W.-Y., Young, T.-H., Yao, C.-H. and Chiu, W.-Y. (1999). "Properties of the poly(vinyl alcohol)/chitosan blend and its effect on the culture of fibroblast in vitro." *Biomaterials,* 20(16), 1479-1487.

318. Li, J. and Hastings, G. W. (1998). "Oxide bioceramics: inert ceramic materials in medicine and dentistry." Handbook of biomaterial properties, J. Black and G. W. Hastings, eds., Chapman & Hall, London, 340-353.

319. Hasenbein, M. E., Andersen, T. T. and Bizios, R. (2002). "Micropatterned surfaces modified with select peptides promote exclusive interactions with osteoblasts." *Biomaterials,* 23(19), 3937-3942.

320. Puleo, D. A. and Bizios, R. (1992). "Formation of focal contacts by osteoblasts cultured on orthopedic biomaterials." *Journal of Biomedical Materials Research,* 26(3), 291-301.

321. Grinnell, F. and Hays, D. G. (1978). "Induction of cell spreading by substratum-adsorbed ligands directed against the cell surface." *Experimental Cell Research,* 116(2), 275-284.

322. Burridge, K., Fath, K., Kelly, T., Nuckolls, G. and Turner, C. (1988). "Focal adhesions: transmembrane junctions between the extracellular matrix and the cytoskeleton." *Annual Review of Cell Biology,* 4, 487-525.

323. Ruardy, T. G., Schakenraad, J. M., Van der Mei, H. C. and Busscher, H. J. (1995). "Adhesion and spreading of human skin fibroblasts on physicochemically characterized gradient surfaces." *Journal of Biomedical Materials Research,* 29(11), 1415-1423.

324. Lee, S. J., Khang, G., Lee, Y. M. and Lee, H. B. (2003). "The effect of surface wettability on induction and growth of neurites from the PC-12 cell on a polymer surface." *Journal of Colloid and Interface Science,* 259(2), 228-235.

325. Ponsonnet, L., Comte, V., Othmane, A., Lagneau, C., Charbonnier, M., Lissac, M. and Jaffrezic, N. (2002). "Effect of surface topography and chemistry on adhesion, orientation and growth of fibroblasts on nickel-titanium substrates." *Materials Science and Engineering: C,* 21(1-2), 157-165.

326. Meyle, J., Gultig, K., Wolburg, H. and Von Recum, A. F. (1993). "Fibroblast anchorage to microtextured surfaces." *Journal of Biomedical Materials Research,* 27(12), 1553-1557.

327. Dunn, G. A. and Brown, A. F. (1986). "Alignment of fibroblasts on grooved surfaces described by a simple geometric transformation." *Journal Of Cell Science,* 83, 313-340.

328. Heinrich, G., Grogler, T., Singer, R. F. and Rosiwal, S. M. (1997). "CVD diamond coated titanium alloys for biomedical and aerospace applications." *Surface and Coatings Technology,* 94-95(1-3), 514-520.

329. Feng, B., Weng, J., Yang, B. C., Qu, S. X. and Zhang, X. D. (2003). "Characterization of surface oxide films on titanium and adhesion of osteoblast." *Biomaterials,* 24(25), 4663-4670.

330. Chehroudi, B., Qu, J.-L. and Brunette, D. M. (1996)"Effects of implant surface topography on osteogenesis." *Proceedings of the 5th World Biomaterials Congress. May 29-Jun 2 1996,* Toronto, Canada, 119.

331. Redey, S. A., Nardin, M., Bernache-Assolant, D., Rey, C., Delannoy, P., Sedel, L. and Marie, P. J. (2000). "Behavior of human osteoblastic cells on stoichiometric hydroxyapatite and type A carbonate apatite: Role of surface energy." *Journal of Biomedical Materials Research,* 50(3), 353-364.

332. Scotchford, C. A., Cooper, E., Leggett, G. J. and Downes, S. (1998). "Growth of human osteoblast-like cells on alkanethiol on gold self-assembled monolayers: The effect of surface chemistry." *Journal of Biomedical Materials Research,* 41(3), 431-442.

333. Price, R. L., Waid, M. C., Haberstroh, K. M. and Webster, T. J. (2003). "Selective bone cell adhesion on formulations containing carbon nanofibers." *Biomaterials,* 24(11), 1877-1887.

334. Webb, K., Hlady, V. and Tresco, P. A. (1998). "Relative importance of surface wettability and charged functional groups on NIH 3T3 fibroblast attachment, spreading, and cytoskeletal organization." *Journal of Biomedical Materials Research,* 41(3), 422-430.

335. Deligianni, D. D., Katsala, N. D., Koutsoukos, P. G. and Missirlis, Y. F. (2001). "Effect of surface roughness of hydroxyapatite on human bone marrow cell adhesion, proliferation, differentiation and detachment strength." *Biomaterials,* 22(1), 87-96.

336. Hallab, N. J., Bundy, K. J., O'Connor, K., Moses, R. L. and Jacobs, J. J. (2001). "Evaluation of metallic and polymeric biomaterial surface energy and surface roughness characteristics for directed cell adhesion." *Tissue Engineering,* 7(1), 55-71.

337. Lee, J. H., Lee, S. J., Khang, G. and Lee, H. B. (2000). "The effect of fluid shear stress on endothelial cell adhesiveness to polymer surfaces with wettability gradient." *Journal of Colloid and Interface Science,* 230(1), 84-90.

338. Rodil, S. E., Olivares, R., Arzate, H. and Muhl, S. (2003). "Properties of carbon films and their biocompatibility using in-vitro tests." *Diamond and Related Materials,* 12(3-7), 931-937.

339. Bowers, K. T., Keller, J. C., Randolph, B. A., Wick, D. G. and Michaels, C. M. (1992). "Optimization of surface micromorphology for enhanced osteoblast responses in vitro." *The International Journal 0f Oral & Maxillofacial Implants,* 7(3), 302-310.

Appendix A

The Properties of Magnesia Partially Stabilised Zirconia (MgO-PSZ)

Chemical Resistance	
Acids - concentrated	Fair
Acids - dilute	Good
Alkalis	Good-Poor
Halogens	Fair
Metals	Good-Fair
Mechanical Properties	
Compressive strength (MPa)	1500-2000
Hardness - Vickers (kgf mm^{-2})	1200
Shear strength (MPa)	414
Tensile modulus (GPa)	200
Tensile strength (MPa)	>300
Physical Properties	
Apparent porosity (%)	0
Density (g cm^{-3})	5.74
Water absorption - saturation (%)	0
Thermal Properties	
Specific heat @25C (J K^{-1} kg^{-1})	400-500
Thermal conductivity @20C (W m^{-1} K^{-1})	1.5-2.5
Thermal expansivity, 20-1000C ($x10^{-6}$ K^{-1})	5-10
Upper continuous use temperature (C)	1000